Yukon

Exploration & Geology Technical Papers

2023

Yukon Geological Survey staff.

Left to right: Patrick Sack, Carolyn Relf, Sydney van Loon, David Moynihan, Rosie Cobbett, Tyler Ambrose, Justin Emberley, Sarah Ellis, Panya Lipovsky, Brett Elliot, Chad Cote, Moya Painter, Bailey Staffen, Julie Minor, Diane Skipton, Maurice Colpron, Leyla Weston, Derek Cronmiller, Amanda O'Connor, Yury Klyukin.

Yukon

Exploration & Geology

Technical Papers

2023

Edited by

L.H. Weston and Purple Rock Inc.

Yukon Geological Survey

Energy, Mines and Resources

Government of Yukon

Front cover photograph: Yukon Geological Survey fly camp on the shores of a small lake in the Rackla Range of the southern Wernecke Mountains. The rocks are carbonate of the Mesoproterozoic Pass Mountain Formation (Pinguicula Group). View to the west.
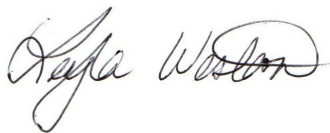(Photo by Tyler Ambrose, Yukon Geological Survey.)

Preface

The annual Yukon Exploration and Geology (YEG) volumes—YEG Overview and YEG Technical Papers—are the main publications of the Yukon Geological Survey (YGS; Energy, Mines and Resources, Government of Yukon). Individual YEG technical papers, with colour images, are available in digital format only. The YEG Overview is available in digital format and in a limited colour print run. All YGS publications can be downloaded from our website, https://data.geology.gov.yk.ca/.

The Yukon Exploration and Geology 2023 volumes contain up-to-date information on mining and mineral exploration activity, studies by industry and results of recent geological field studies. Information in this volume comes from prospectors, exploration and government geologists, mining companies and students, all of whom are willing to contribute to public geoscience for the benefit of the scientific community, the public and the mineral industry of the Yukon. Their work is appreciated.

This year marks a new chapter for Yukon Exploration and Geology. In September 2023, Karen MacFarlane, former Head of Technical Services for the YGS and Chief Editor of YEG retired. Karen started with YGS in 2009 and single-handedly edited and laid out 13 volumes of YEG. Her tireless effort and dedication to this volume over the last several years cannot be overstated. As a previous YEG editor, I have immense gratitude to Karen for the past 13 years during which I had the pleasure of enjoying the holiday season without having to work. After a long hiatus, I am back at it this year, but thankfully not alone. I have had the great pleasure to work with Nicole Barlow, Moretta Shuert and the team at Purple Rock Inc., whose hard work and professionalism have made the transition truly seamless. I do hope they'll stay!

I hope you enjoy the volume. Input or suggestions that you may have to improve future YEG publications are welcomed. Please contact us at (867) 393-7187, or by email at geology@yukon.ca.

Leyla Weston

Yukon Exploration and Geology Technical Papers 2023

Table of Contents

Shear-wave velocities from broadband HVSR measurements for geothermal resource assessment near Burwash Landing, Yukon

Fernando Berumen-Borrego[*], Hersh Gilbert, Jan Dettmer,
Jeremy M. Gosselin and Pejman Shahsavari
Department of Earth, Energy, and Environment, University of Calgary, Calgary, Alberta, Canada

Abstract

As Canada pursues net-zero CO_2 emissions targets, geothermal energy represents a promising solution, especially in northern Yukon communities such as Burwash Landing. Currently, Burwash Landing relies on importing diesel for power and heating and would benefit from a reliable source of renewable energy. Our study uses horizontal-to-vertical spectral ratio (HVSR) measurements from nine temporary broadband seismometers to refine shear-wave velocity models for the upper 500 m of the crust. These models constrain layering and structure within shallow sediments, depth to bedrock, and discontinuities within the bedrock. These results provide reliable estimates of the thickness of sedimentary cover overlying bedrock. Bedrock depths vary from 50 to 450 m, deepening to the northeast of the Denali fault, and follows a power-law increase with depth through sediments. These insights improve the geological understanding around this portion of the Denali fault and contribute to constructing comprehensive models for the development of geothermal energy in the region.

Introduction

Canada's commitment to net-zero CO_2 emissions by 2050 emphasizes the potential for geothermal energy to make a crucial contribution, especially for northern communities such as Burwash Landing, Yukon. Located along the Alaska Highway in southwest Yukon, the community of Burwash Landing is within the Traditional Territory of *the Lhù'ààn Mân' Ku Dań*, the Kluane Lake People, and home to the Kluane First Nation. Burwash Landing is located near the Denali fault, which is a crustal-scale, strike-slip fault and major geological terrane boundary (Colpron and Nelson, 2021). Geothermal gradients near Burwash Landing are estimated to be approximately 40°C/km (Witter, 2020). Both the seismogenic layer thicknesses and Curie point depth mapping (Li et *al.*, 2017; Biegel et

al., 2023) suggest that the Denali and Duke River fault systems have elevated crustal temperatures and could potentially host viable geothermal resources (Li et *al.*, 2017; Biegel et *al.*, 2023). Based on the inferred geothermal gradient, temperatures near 40 to 45°C are expected at a depth of 1 km close to the Denali fault near Burwash Landing (Li et *al.*, 2017; Biegel et *al.*, 2023).

The Yukon Geological Survey (YGS) investigated this region to evaluate the potential for harnessing warm fluids near the surface (Witter, 2020; Finley et *al.*, 2022; Tschirhart et *al.*, 2022). This earlier work relied upon magnetotelluric (Tschirhart et *al.*, 2022), gravity, magnetic, and low-frequency electromagnetic data

[*] fernando.berumenborr@ucalgary.ca

(Witter, 2020) to measure structural changes in the crust across the Denali fault (Fig. 1). However, the frequency ranges of the data and the scale of model resolution used in these studies were focused on structures at depths of approximately 0.2 to 1 km and greater. Our study contributes to this knowledge base by examining horizontal-to-vertical spectral ratio (HVSR) measurements from ambient seismic noise recorded by nine broadband seismometers that were deployed around Burwash Landing in summer 2021 (Fig. 1). The HVSR method is recognized for its effectiveness to infer shallow seismic velocity structures (Fäh et *al*., 2003; Arai and Tokimatsu, 2004; Havenith et *al*., 2007; Sánchez-Sesma et *al*., 2011; Cipta et *al*., 2018; Piña-Flores et *al*., 2021). The models presented here are based on a transdimensional Bayesian inversion to infer shear-wave velocity (V_S) beneath each station with associated uncertainties. The approach also avoids subjective model parameterization choices by allowing for the modelling of an unknown number of subsurface layers. This method increases the reliability and adaptability of our models (Dettmer et *al*., 2013; Cipta et *al*., 2018), a crucial feature given the limited geological data within the area. Our observations reveal significant variations in HVSR characteristics and basement depth across the Denali fault. Understanding these variations is crucial for refining our interpretations of the Denali fault and aids in refining interpretations from other geophysical methods. Additionally, we find that stations located on a thick sedimentary layer exhibit a power-law increase in V_S through this layer, a pattern observed in other basins and associated with sediment compaction and saturation (Scherbaum et *al*., 2003; Havenith et *al*., 2007; Molnar et *al*., 2010; Cipta et *al*., 2018).

Unlike its more seismically active central section in Alaska, the eastern extension of the Denali fault that extends through the Yukon, including near Burwash Landing, exhibits lower seismicity (Elliott and Freymueller, 2020). This makes seismic ambient noise methods such as HVSR particularly valuable. The approach was initially developed for seismic site effects studies (Kanai and Tanaka, 1961). The HVSR method has proven effective indicating ground shaking amplification during strong earthquakes that closely aligns with ambient noise estimates. Our work contributes new constraints on geological structures near Burwash Landing, which informs responsible geothermal resource development and natural (seismic) hazard mitigation.

Geological setting

The Denali fault, a large Cenozoic dextral strike-slip fault, extends more than 2100 km from northwestern British Columbia to southwestern Alaska, and plays a central role in interactions between the Insular and Intermontane superterranes (*e.g.*, Gabrielse et *al*., 2006; Elliott and Freymueller, 2020; Colpron and Nelson, 2021). The eastern segment of the Denali fault exhibits both strike-slip and reverse motions, as revealed by earthquake focal mechanism estimates (Gosselin et *al*., 2023). Displacement estimates for the Denali fault range from 370 to 480 km during the Cenozoic (Lowey, 1998; Waldien et *al*., 2021).

Near Burwash Landing, northeast of the Denali fault, basement rocks correspond to the Upper Cretaceous Kluane Schist, consisting of a quartz-mica schist with serpentinite and carbonate inclusions. This unit transitions from greenschist to lower amphibolite facies northwestward (Mezger et *al*., 2001; Israel et *al*., 2011). Southwest of the Denali fault, the basement comprises rocks from the Carboniferous to Upper Triassic Wrangellia terrane, which includes volcanic units of the Station Creek Formation and sedimentary units corresponding to the Hasen Creek Formation (Israel et *al*., 2005, 2006). These units are unconformably overlain by the Nikolai Basalt, which is unconformably overlain by marine clastic rocks of the Tatamagouche succession. The structural setting consists of various styles of folding and cut by steep faults, including the Denali fault, Duke River and Bock's Creek faults (Fig. 1; Israel et *al*., 2005, 2006). To the northeast of the Kluane Range, Quaternary to present sedimentary deposits accumulate and thicken toward Kluane Lake (Fig. 1; Kennedy, 2013).

Our HVSR-based study provides new insights into the depth to bedrock, offering a more detailed understanding of the thickness of the unconsolidated sedimentary layer, particularly in regions where well data are limited. For example, a well drilled to a depth of 384 m in Burwash Landing only encountered Quaternary sediments, whereas another well near station BL05 hit bedrock at a depth of 49 m. Comparing our HVSR results to these wells increases confidence in our shear-wave velocity models.
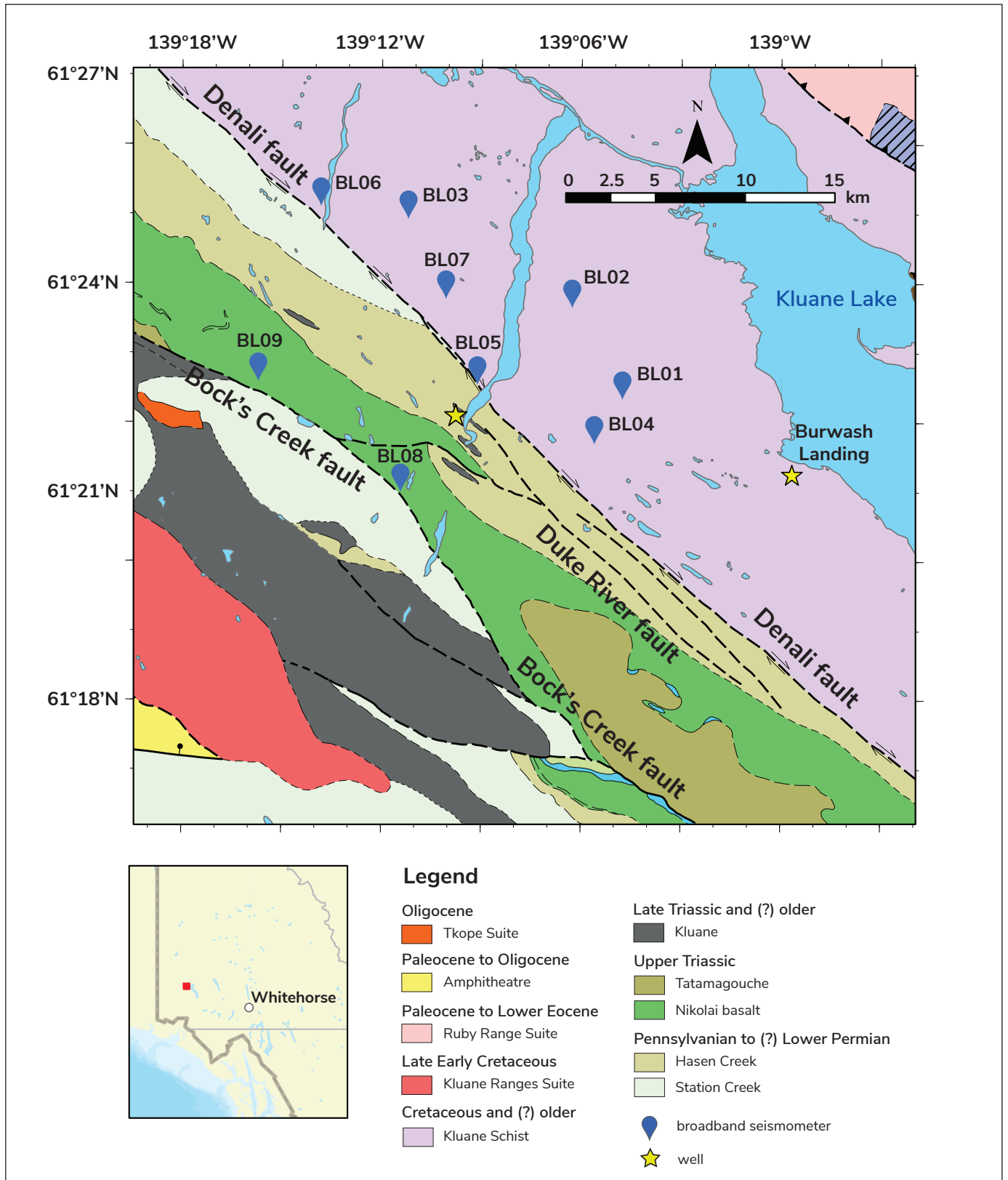
Figure 1. *Bedrock geology map of the Burwash Landing area (Colpron, 2022). Faults are shown by black dashed lines. Three-component seismometers are shown as blue pins. Wells drilled near the Duke River fault and Burwash Landing are shown as yellow stars.*

Horizontal-to-vertical spectral ratio method and data processing

The horizontal-to-vertical spectral ratio (HVSR) method, popularized by Nakamura (1989, 2008, 2019), is recognized for its efficiency in field acquisition and simplicity in processing ambient seismic noise. This noise, encompassing low-frequency signals from natural origins such as storms and ocean waves, and higher-frequency signals from anthropogenic activities, is a useful source for creating site-specific, shear-wave velocity profiles (Bonnefoy-Claudet et al., 2006). The lowest frequency peak observed on HVSR curves corresponds to the fundamental resonance frequency, f_0, at each site. Assuming HVSR is representative of resonance of horizontally polarized shear waves, the fundamental resonance frequency can be related to the shear velocity at the site by $f_0 = V_s / 4h$, where V_s is the average shear-wave velocity of the sedimentary column and h is its thickness (Nakamura, 2008, 2019). Recent studies suggest HVSR is attributed to, and can be modelled as, the ellipticity of ground motion caused by Rayleigh (surface) wave propagation (e.g., Cipta et al., 2018), or by a combination of these wave phenomena (Sánchez-Sesma et al., 2011; Molnar et al., 2022).

The HVSR curves are computed by taking the square-root of the product of the Fourier amplitude spectra of the north-south and east-west components ($H_{NS}(\omega)$ and $H_{EW}(\omega)$) and dividing them by the Fourier spectrum of the vertical component ($V(\omega)$), as expressed by

$$HVSR(\omega) = \frac{\sqrt{H_{NS}(\omega) \times H_{EW}(\omega)}}{V(\omega)}. \qquad (1)$$

Our HVSR measurements involve the following steps: defining an appropriate time window length; applying smoothing techniques to individual time windows; averaging horizontal spectra; removing noisy windows; and completing spectral ratio computations. This conventional processing using SESAME (Site EffectS assessment using AMbient Excitations) geophysics ensures both reliability and scientific rigour (SESAME, 2004). We used the open-source hvsrpy software (Vantassel, 2020) because of its capability to process multiple stations in parallel over several days, as well as its ability to reject time windows based on frequency-domain analysis (Cheng et al., 2020; Cox et al., 2020).

Individual time windows should be at least 10 times longer than the fundamental resonance period at a specific site (SESAME, 2004). The longest resonance period observed was approximately 3.25 s long beneath station BL07. Therefore, an entire day of data was used, segmented into time windows of 180 s each, yielding a total of 480 windows to ensure statistically meaningful results. Our choice of window length balances the need for spectral resolution and reliable statistics, enabling low resonance frequencies to be analyzed. The use of 480 windows exceeds the 20-window minimum suggested by Picozzi et al. (2005).

The logarithmic frequency-sampled smoothing filter proposed by Konno and Ohmachi (1998) was applied to minimize spectral variance. For the filter coefficient, we followed recommendations from SESAME (2004) and Cox et al. (2020) and used a value of 40. The geometric mean was used for averaging the horizontal spectra. The geometric mean tends to yield the least biased estimates, and its stability increases as the number of time windows grows (Cox et al., 2022; Molnar et al., 2022).

We used the frequency-domain window-rejection algorithm included in hvsrpy for effective time-window selection (Cox et al., 2020). The algorithm iteratively removes windows that deviate from a computed average frequency by more than a specified number of standard deviations. In this study, the rejection threshold was set at 1.75 standard deviations to preserve a reasonable number of time windows and eliminate significant outliers.

The final step in our HVSR processing involves the computation of mean μ and standard deviation σ of HVSR curves. The software hvsrpy uses log-normal statistics to compute these curves. Let ω denote a sampled frequency, and n be the number of time windows considered. For a given ω, the mean and standard deviation of HVSR at each frequency are calculated as

$$\mu(n, \omega) = exp^{\left(\frac{1}{n}\sum_{i=1}^{n} \ln(HVSR(\omega))\right)} \qquad (2)$$

and

$$\sigma_\omega(n, \omega) = \sqrt{\frac{1}{n-1}\sum_{i=1}^{n}(\ln(HVSR(\omega)) - \ln(\mu(n, \omega)))^2}. \quad (3)$$

Once these values are determined, *hvsrpy* outputs $\mu(n, \omega)$, as well as the upper and lower bound curves, are calculated using

$$\mu \pm \sigma\,(n, \omega) = exp^{\left(\ln(\mu(n,\omega)) \pm \sigma_\omega(n,\omega)\right)}. \qquad (4)$$

This approach assumes that the natural logarithm of the HVSR values at different frequencies follow a normal distribution and are independently and identically distributed. An advantage of *hvsrpy* is its ability to output the standard deviation of the mean HVSR curve. The measure of the standard deviation of the HVSR curve allows for the incorporation of noise level estimates in the subsequent transdimensional inversion (Dettmer et a*l*., 2013; Dosso et a*l*., 2014; Cipta et a*l*., 2018).

Our HVSR curves all feature a prominent peak corresponding to the f_0 beneath each station (Fig. 2b–d). Based on the frequency of these peaks, we classified the stations into three groups that show a strong correlation with depth to bedrock (Fig. 2a–d). Group one, comprising stations BL01, BL02, BL03, BL04 and BL07, exhibits low-frequency peaks ranging from approximately 0.3 to 0.4 Hz with amplitudes between approximately 1.8 and 3.5. These stations are situated to the northeast of the Denali fault, where a thick layer of sediments extends beyond a depth of 384 m at the well drilled in Burwash Landing. Group two, including stations BL05 and BL06, exhibit peaks at approximately 7.5 Hz with amplitudes under 2.5, indicative of a thinner sediment layer near the Denali fault, as confirmed by the well drilled near the Duke River. Lastly, group three, featuring stations BL08 and BL09, show peaks around 11 Hz with amplitudes of approximately 2.5, and are situated near the Bock's Creek fault.

Transdimensional inversion

To effectively solve non-linear inversion problems and include uncertainty quantification, we use Bayesian inference. Within the Bayesian framework, the solution to the inverse problem is given by the posterior probability density (PPD) of model parameters, which are connected by Bayes' theorem to the likelihood function—the probability to observe the data given a certain model—and *a priori* information, which is data independent, such as model parameterization. For nonlinear inverse problems, the PPD can be effectively

sampled using Markov chain Monte Carlo (MCMC) methods (Mosegaard and Tarantola, 1995; Dettmer et a*l*., 2013; Cipta et a*l*., 2018).

Spatial parameterization plays a crucial role in the ability of a model to accurately represent a system, particularly when model parameterization (e.g., number or thickness of layers) is not well known. Transdimensional inversions provide a robust approach to addressing this challenge. Instead of constraining to a unique parameterization, this method relaxes the selection to a set of parameterizations, avoiding subjective choices (Green 1995, 2003; Malinverno, 2002; Dettmer et a*l*., 2013). This approach simultaneously considers multiple models, with a distinct number of layers and other parameters, while avoiding the need for explicitly specifying velocity structure and allowing for arbitrary layering.

In transdimensional methods, the PPD is commonly sampled using reversible-jump MCMC algorithms (Green, 1995, Dettmer et a*l*., 2013; Dosso et a*l*., 2014; Cipta et a*l*., 2018). A structured strategy for parameterizing subsurface variations accommodating both smooth transitions and sharp discontinuities without explicit assumptions is used here (Bodin and Sambridge, 2009; Cipta et a*l*., 2018). Models transition through the addition or subtraction of interfaces using a birth-death scheme (Geyer and Møller, 1994). For a birth step, an interface is created from a uniformly sampled depth, splitting a pre-existing layer. Elastic parameters for the new layer are randomly modified using a Gaussian distribution, centred on the current model state. Conversely, during death steps, interfaces are randomly eliminated, and the new state is randomly selected from one of the original layers. Elastic parameters also undergo perturbation steps using a Cauchy proposal targeting individual parameters leading to occasional large shifts, enhancing convergence rates (Dettmer et a*l*., 2009).

To perform forward computations, we use the Geopsy tool (*gpell*) that computes Rayleigh wave ellipticity curves for homogeneous layered models (Wathelet et a*l*., 2004; Wathelet, 2008). Attempting to match observed HVSR curves to these ellipticity calculations assumes that the HVSR peaks are exclusively due to Rayleigh wave ellipticity. Even though we expect this to be a valid assumption, any contribution to HVSR signals from other sources of energy, such as scattering
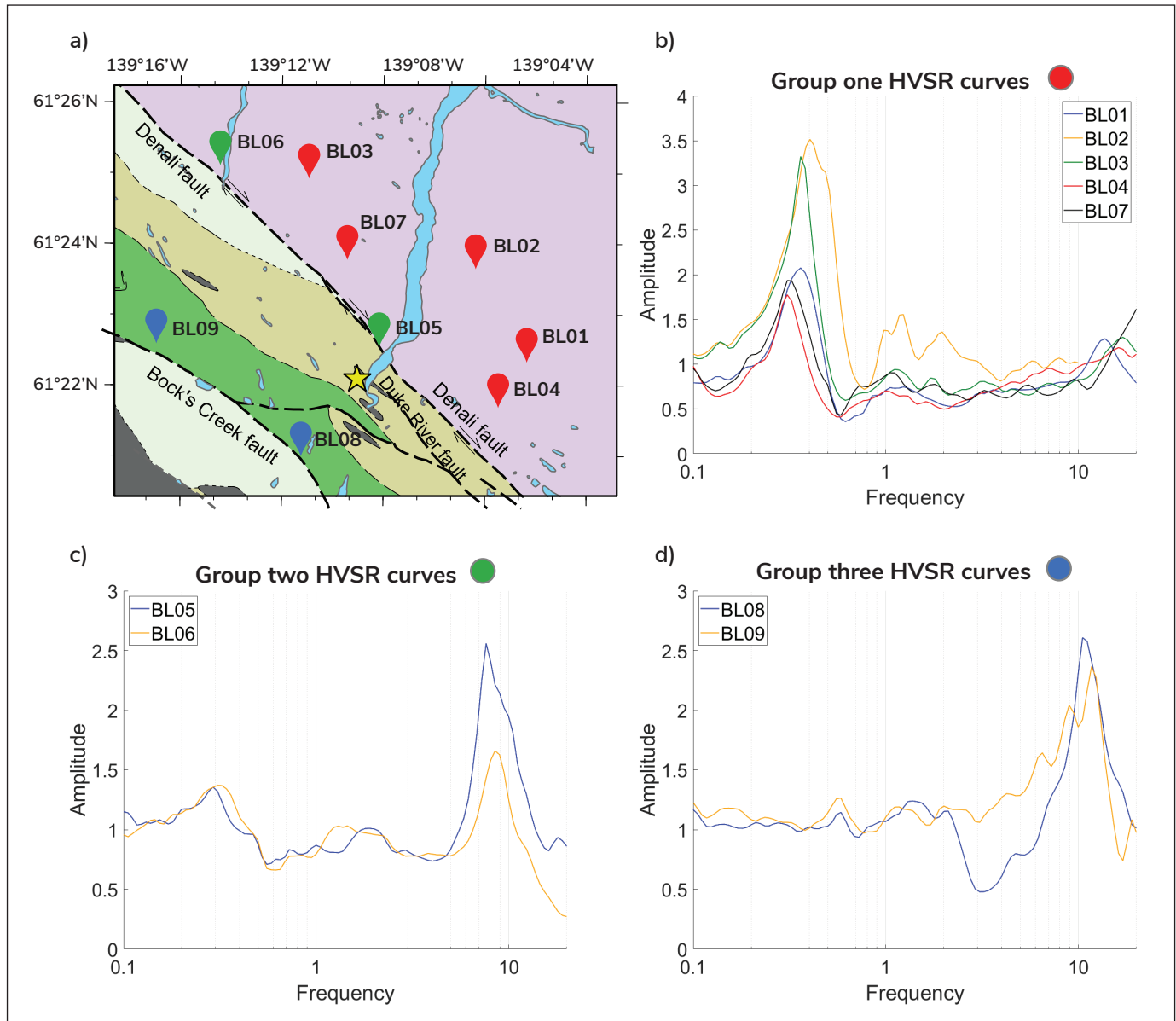
Figure 2. *Measured HVSR curves.* **a)** *Bedrock geology map denoting station locations, which are colour-coded based on their HVSR peak group classification. Group one stations are denoted by red pins, Group two stations with green pins, and Group three stations correspond to the blue pins. Subplots for each group show the corresponding HVSR curves* **b)–d)**.

or body waves, would not be accurately represented and would be a source of theory error in our analysis. We invert for the number of layers k as well as for V_S, V_P/V_S, ρ and thickness h in each layer. The log likelihood function of the history of the entire sampling chain was used to determine convergence for these inversions. Following Dettmer et al. (2013) and Cipta et al. (2018), the likelihood function is given by

$$L(\vec{d}|k,\vec{m}_k) = exp\left(-\frac{1}{2}(\vec{d} - \vec{d}(k,\vec{m}_k))^T C_d^{-1}(\vec{d} - \vec{d}(k,\vec{m}_k))\right). \quad (5)$$

We assume a Gaussian-distributed residual error distribution, which is a conservative choice supported by the central limit theorem. Here, $C_d = \sigma_\omega^2 * I$, where I is the identity matrix and σ_ω represents the standard deviation of the noise from equation 3, $d = [HVSR(\omega_0), HVSR(\omega_1), \ldots , HVSR(\omega_i)]$. The modelled data vector, $\vec{d}(k,\vec{m}_k)$, reflects HVSR values at specific frequencies $\omega_0, \omega_1, \ldots , \omega_i$ for a given model.

Results

Our results demonstrate the effectiveness of transdimensional inversion of HVSR curves in determining shear-wave velocity profiles beneath broadband stations near Burwash Landing. These profiles, with reasonable uncertainties that increase with depth, align with the expected behaviour in diffusive wave fields such as Rayleigh wave propagation (Cipta et *al*., 2018). With minimal prior parameter information, the algorithm effectively models subsurface characteristics fitting observations within noise standard deviations (Fig. 3).

As described above, we categorized stations into three groups based on their HVSR curve resonance frequencies and proximity to the Denali fault (Fig. 2a–d). The models for station BL04 exhibited high uncertainty and poor resolution, likely due to hydrological effects because the water table was high (*i.e.*, near the surface) near this site. As a result, we do not report on BL04 further. Group one stations display low-frequency peaks (~0.3 to 0.4 Hz) with significant amplitudes (~1.8 and 3.5). This group comprises stations BL01, BL02, BL03, BL04, and BL07, situated over a thick section of Quaternary sediments (Fig. 4a–c, f and 5a–c, f). Here, we observed a distinct power-law increase in shear-wave velocity as a function of depth, which we attribute to sediment compaction. For instance, BL02 shows a gradual velocity increase from approximately 250 m/s to 600 m/s at 300 m depth, then a sharp transition to more than 1000 m/s, marking the boundary with the basement rocks. Station BL03 follows a similar pattern, with velocities rising from 250 to 900 m/s up to 400 to 420 m depth before jumping to approximately 1300 m/s. Station BL01 and BL07 reveal gradual velocity increases, and BL01 had a higher uncertainty in resolving bedrock depth. The sediment-bedrock interface depths vary within the group, emphasizing the lateral heterogeneity of the area and providing insights into its structural complexity.

Group two stations exhibit low-frequency peaks and higher frequencies of 7.75 and 7.51 Hz for stations BL05 and BL06, respectively. These stations are located over a package of thinner Quaternary sediments overlying bedrock (Fig. 4d, e and 5d, e). For BL05 and BL06, we noted power-law increases in velocity to approximately 700 m/s at depths of 90 to 100 m and 170 m, respectively, before sharply increasing to

bedrock velocities of approximately 1000 to 1100 m/s. Another notable jump in velocity was observed within the bedrock to more than 2000 m/s at a depth of approximately 350 to 380 m.

Group three, comprising stations BL08 and BL09, presents single high-frequency peaks (~11 Hz) with amplitudes of approximately 2.5. The depth-to-bedrock estimates for these stations are about 1000 m for BL08 and 40 to 50 m for BL09 (Fig. 4g, h and 5g, h). Both stations exhibit gradual increases in velocity through the sediments, with sharp transitions to higher velocities in basement rocks. Station BL08 shows an increase to 700 m/s before a jump to approximately 1100 m/s, and another increase at approximately 260 m depth. The V_S profile for BL09 indicates a gradual increase to 500 m/s, then a sharp rise to 900 m/s at 40 to 50 m depth.

Our study across the station groups reveals varied patterns in shear-wave velocity changes through Quaternary sediments. Whereas a power-law increase in velocity due to compaction and/or saturation was observed for some stations, others exhibited more gradual velocity increases. Notably, at the sediment-bedrock interface, a sharp increase in velocity is seen consistently across the stations. Furthermore, the depth to this interface increases toward the northeast, reflecting sediment thickness variations in the region. These new constraints on the sediment-bedrock boundary, highlighted by the lateral heterogeneity observed across the station groups, are crucial for refining geological models of the region and aid in assessing geothermal potential. Reliable estimates of elastic properties in the shallow subsurface are necessary in enhancing the interpretation of other geophysical data, which often rely on initial (*i.e.*, starting) models (*e.g.*, Witter, 2020).

Discussion

Our results showcase the efficiency of HVSR transdimensional inversion in estimating the 1D velocity structure beneath stations near Burwash Landing. These estimates highlight significant variability in bedrock depth, ranging from 50 to 450 m, with depths sharply increasing to the northeast of the Denali fault. This approach proves effective even in areas with reduced seismicity and limited prior subsurface knowledge, such as the Burwash Landing region.
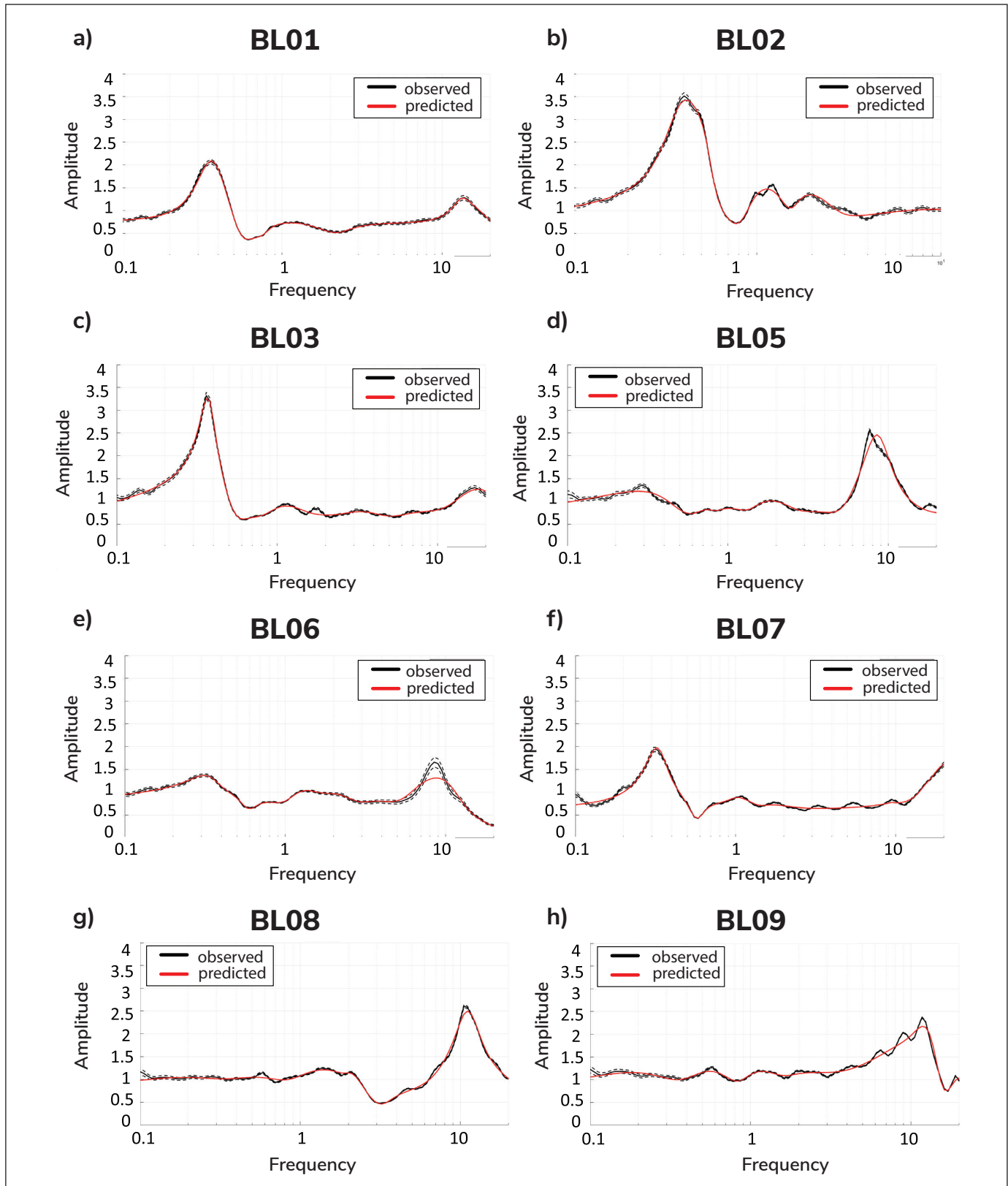
Figure 3. *Data fit curves.* ***a)–h)*** *Measured HVSR curves (solid black curves) and standard deviations (dashed black curves) are reasonably fit in all stations analyzed. The red curves show the HVSR for models with maximum a posteriori probability for stations BL01 to BL09.*
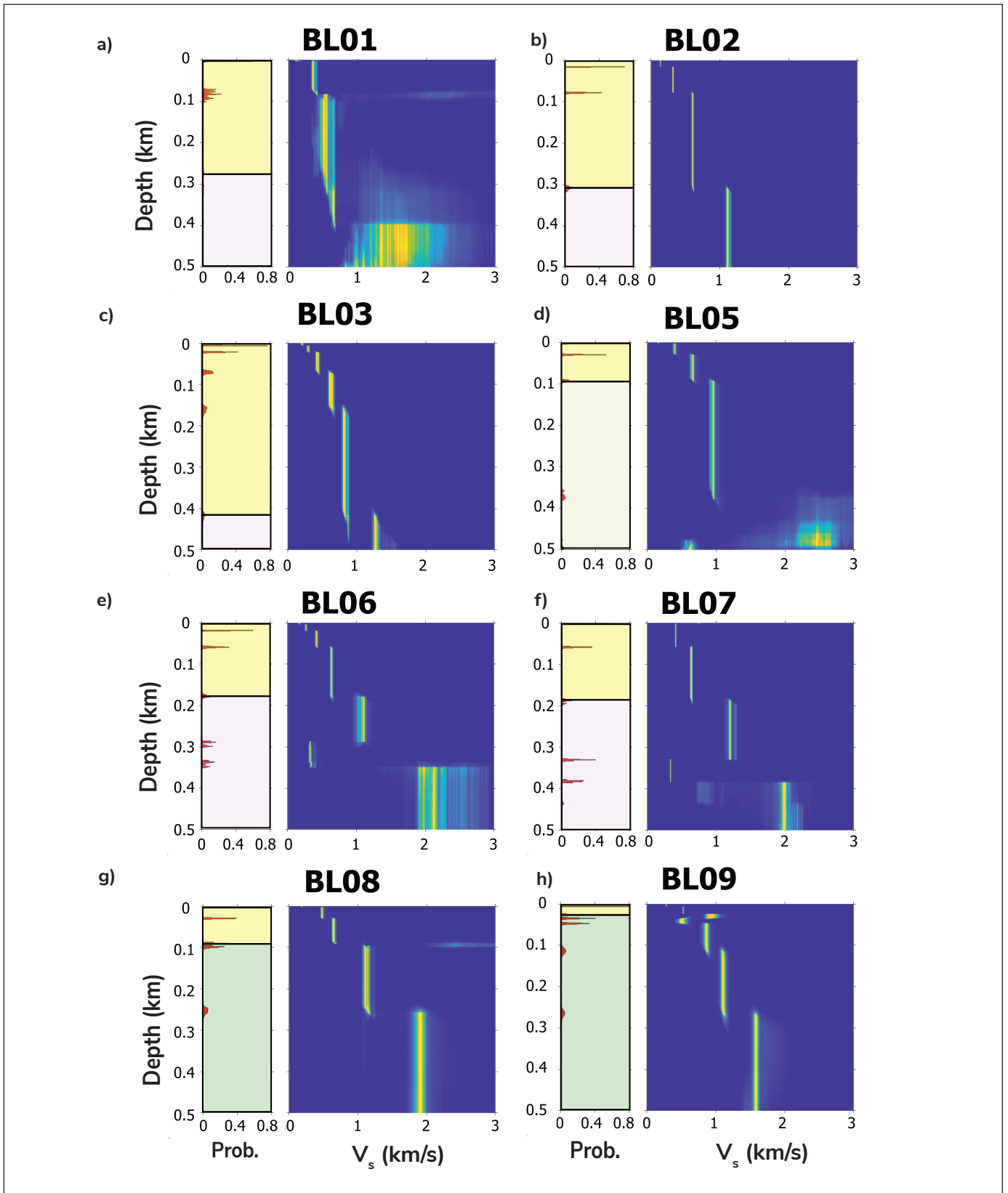
Figure 4. *Interface probability (left) and shear-wave velocity profiles (right) for the upper 500 m for stations BL01 to BL09 **a)**–**h)**. The yellow shaded region in the interface probability plots is interpreted to correspond to sedimentary cover whereas the purple, brown and green mark the corresponding bedrock units as indicated in Figure 1.*
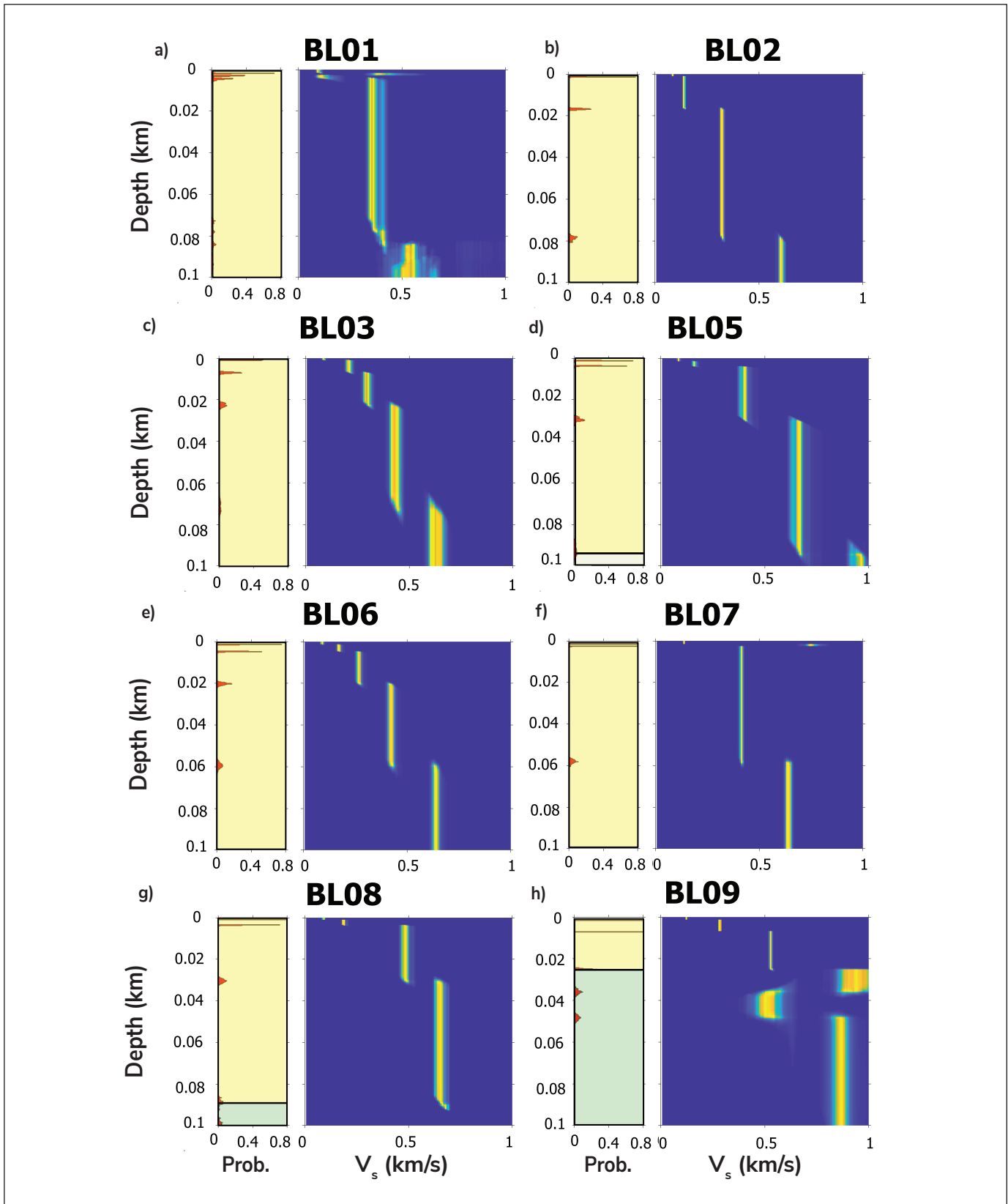
Figure 5. *Interface probability (left) and shear-wave velocity profiles (right) for the upper 100 m for stations BL01 to BL09* **a)**–**h)**. *The yellow shaded region in the interface probability plots is interpreted to correspond to sedimentary cover whereas the brown and green mark the corresponding bedrock units as indicated in Figure 1.*

A key aspect of our results is its agreement with the limited bedrock depth observations from nearby wells. For station BL05 near the Duke River fault, we have estimated bedrock to be close to 90 to 100 m deep. Our estimate of bedrock depth agrees with findings from drilling operations near this location in 2022 that encountered bedrock at a depth of only 49 m (M. Colpron, pers. comm., 2022). Earlier estimates of the depth to bedrock around BL05 used extremely low frequency – electromagnetics (ELF-EM), which suggested close to 200 m of overlying sediments at this location (Witter, 2020). For a gravity profile crossing the Denali fault (Fig. 1), Witter (2020) found that a model consisting of a layer of low-density sediments approximately 200 m thick atop a basement layer of increased densities fit the observed gravity variations well. Our HVSR results for this location indicate the presence of a shallow low V_S layer closer to approximately 100 m thick or less. These seismic constraints highlight the need to develop a revised model of the upper crust that can fit both the observed ELF-EM, gravity, magnetic and seismic observations while incorporating observational constraints from wells. Future efforts will be devoted to jointly modelling all available geophysical measurements to find a single model that can consistently match all observations.

Focusing on the upper 100 m, we find that at stations BL02, BL03, BL05, and possibly BL06, the pattern in which V_S increases with depth follows a power-law relationship between seismic velocities and depth (Fig. 5b–e). Seismic velocities exhibiting a power-law dependence on depths have been found in other sedimentary basins and have been attributed to sediment compaction or saturation. Scherbaum *et al.* (2003) inverted HVSR curves to determine shallow shear velocity profiles near Cologne, Germany. Testing inversions using a model in which seismic velocities are parameterized to follow a power-law increase with depth, this study found velocities that agree well with observations based on downhole measurements (Scherbaum *et al*., 2003). Using HVSR and dispersion curves, Havenith *et al*. (2007) observed a similar power-law increase in V_S within a basin of the Upper Rhine Graben while investigating the region bordering Switzerland, France and Germany. More recently, Molnar *et al*. (2010) used a Bayesian approach to estimate shear-wave velocities near Vancouver, British Columbia, from dispersion curves and found that a V_S profile parameterized using a power-law gradient to a

depth of at least 110 m fit observations from the Fraser River delta.

The differing pattern of sediment V_S variations as a function of depth (*i.e.*, presence of power-law depth trend) suggests differing shallow structure within the overburden underlying the different groups of stations. The abrupt changes in velocities observed at shallow depths of less than 100 m for BL08 and BL09 (Fig. 5g, h) are suggestive of a thin layer of sedimentary cover atop basement rocks with faster V_S. The sediments within the thin shallow layer may not be subjected to sufficiently high pressures to be compacted so that the velocity of the layer increases, as observed for stations in group one.

The observed changes in shallow structures between the stations surrounding the Denali fault support earlier observations of structural changes at greater depths identified by other geophysical investigations of the region that used gravity and magnetic methods (Witter, 2020). Differences in V_S for the basement structures between stations in groups one, two and three provide support for variations in densities observed in gravity modelling across the boundary between the Kluane Schist and Station Creek Formation. Magnetotelluric observations provide further support for differences we observe in the shallow structure and suggest these extend to greater depths based on the identification of a conductive anomaly at depths greater than approximately 200 m to the northeast of the Denali fault (Tschirhart *et al*., 2022). Comparable to the lateral extent of stations in group one, this conductive anomaly extends from the Denali fault to the northeast. The alignment of these observations from diverse geophysical methods suggests that structural differences across the Denali fault extend from near-surface to depths of 1 km or more.

In summary, our study not only enhances the accuracy of depth to bedrock estimates but also provides insight into the sedimentary and tectonic dynamics, and the link to a deeper structure in the Burwash Landing area. The integration of HVSR results with other geophysical methods advances our understanding of geothermal resources in the area. Our work also underscores the adaptability of transdimensional inversion of HVSR curves. Despite sparse prior knowledge regarding the seismic structure in the Burwash Landing area, the transdimensional inversions provide estimates of shear-

wave velocities while avoiding subjective modelling choices. The incorporation of Bayesian inference is crucial, offering detailed uncertainty estimates and a more robust approach to non-linear problems compared to deterministic methods.

Conclusions

As part of a broader comprehensive geothermal investigation, we deployed nine broadband seismometers along the crustal-scale, right-lateral eastern Denali fault near Burwash Landing. Using data from this temporary network of seismic sensors, we have demonstrated that resonant frequencies of HVSR curves can be reliably fit using V_S models consisting of low-velocity layers atop higher-velocity basement, as suggested by Nakamura (1989, 2008, 2019). The velocity models presented here provide insights into the characteristics of the underlying geological structure near Burwash Landing. Our observations can be divided into three distinct groups based on their measured resonant frequency. We estimated depth to bedrock to be between 250 to 450 m below the surface for stations within group one with f_0 = ~0.3 to 0.4 Hz (Fig. 2b). For stations in group two, which exhibit f_0 = ~7.5 Hz (Fig. 2c), we estimated depth to bedrock to be approximately 90 to 100 m. Stations in group three, which exhibit f_0 >10 Hz (Fig. 2d), have depth to bedrock estimates of approximately 50 to 100 m. These new constraints of the shallow crust can contribute to refining the models produced using other geophysical methods (e.g., Witter, 2020; Tschirhart et al., 2022).

Several studies have emphasized the importance of incorporating higher order Rayleigh modes when fitting observed HVSR curves, particularly when low-velocity zones are present (Arai and Tokimatsu, 2004; Bonnefoy-Claudet et al., 2006). The joint inversion of HVSR curves and surface-wave dispersion curves has been used to mitigate the trade-off between layer thickness and velocity inherit to HVSR analysis (Parolai et al., 2005; Hobiger et al., 2012). Future efforts will be devoted toward integrating dispersion measured from a temporary, dense seismic array that was recently deployed in the region.

Acknowledgments

References

Arai, H. and Tokimatsu, K., 2004. S-wave velocity profiling by inversion of Microtremor H/V Spectrum. Bulletin of the Seismological Society of America, vol. 94, issue 1, p. 53–63. https://doi.org/10.1785/0120030028

Biegel, K., Gosselin, J. and Dettmer, J., 2023. Preliminary double-difference relocation earthquake catalogue for southwestern Yukon centred along the Denali fault zone. *In*: Yukon Exploration and Geology 2022, K.E. MacFarlane (ed.), Yukon Geological Survey, p. 1–18, plus digital appendices.

Bodin, T. and Sambridge, M., 2009. Seismic tomography with the reversible jump algorithm. Geophysical Journal International, vol. 178, issue 3, p. 1411–1436. https://doi.org/10.1111/j.1365-246x.2009.04226.x

Bonnefoy-Claudet, S., Cotton, F. and Bard, P.-Y., 2006. The nature of Noise Wavefield and its applications for site effects studies. Earth-Science Reviews, vol. 79, issue 3–4, p. 205–227. https://doi.org/10.1016/j.earscirev.2006.07.004

Cheng, T., Cox, B.R., Vantassel, J.P. and Manuel, L., 2020. A statistical approach to account for azimuthal variability in single-station HVSR measurements. Geophysical Journal International, vol. 223, issue 2, p. 1040–1053. https://doi.org/10.1093/gji/ggaa342

Cipta, A., Cummins, P., Dettmer, J., Saygin, E., Irsyam, M., Rudyanto, A. and Murjaya, J., 2018. Seismic velocity structure of the Jakarta Basin, Indonesia, using trans-dimensional Bayesian inversion of horizontal-to-vertical spectral ratios. Geophysical Journal International, vol. 215, issue 1, p. 431–449. https://doi.org/10.1093/gji/ggy289

Colpron, M. (compiler), 2022. Yukon Bedrock Geology Map. Yukon Geological Survey, Open File 2022-1, 1 000 000 scale map and legend.

Colpron, M. and Nelson, J.L., 2021. Northern Cordillera: Canada and Alaska. Encyclopedia of Geology (Second Edition), p. 93–106. https://doi.org/10.1016/b978-0-12-409548-9.12502-3

Cox, B.R., Cheng, T., Vantassel, J.P. and Manuel, L., 2020. A statistical representation and frequency-domain window-rejection algorithm for single-station HVSR measurements. Geophysical Journal International, vol. 221, issue 3, p. 2170–2183. https://doi.org/10.1093/gji/ggaa119.

Dettmer, J., Dosso, S.E. and Holland, C.W., 2009. Model selection and Bayesian inference for high-resolution seabed reflection inversion. The Journal of the Acoustical Society of America, vol. 125, issue 2, p. 706–716. https://doi.org/10.1121/1.3056553

Dettmer, J., Holland, C.W. and Dosso, S.E., 2013. Transdimensional uncertainty estimation for dispersive seabed sediments. Geophysics, vol. 78, issue 3. https://doi.org/10.1190/geo2012-0358.1

Dosso, S.E., Dettmer, J., Steininger, G. and Holland, C.W., 2014. Efficient trans-dimensional Bayesian inversion for geoacoustic profile estimation. Inverse Problems, vol. 30, issue 11, 114018. https://doi.org/10.1088/0266-5611/30/11/114018

Elliott, J. and Freymueller, J.T., 2020. A block model of present-day kinematics of Alaska and Western Canada. Journal of Geophysical Research: Solid Earth, vol. 125, issue 7. https://doi.org/10.1029/2019jb018378

Fäh, D., Kind, F. and Giardini, D., 2003. Inversion of local S-wave velocity structures from average H/V ratios, and their use for the estimation of site-effects. Journal of Seismology, vol. 7, issue 4, p. 449–467. https://doi.org/10.1023/b:jose.0000005712.86058.42

Finley, T., Salomon, G., Stephen, R., Nissen, E., Cassidy, J. and Menounos, B., 2022. Preliminary results and structural interpretations from drone lidar surveys over the Eastern Denali fault, Yukon. *In*: Yukon Exploration and Geology 2021, K.E. MacFarlane (ed.), Yukon Geological Survey, p. 83–105. https://doi.org/10.13140/RG.2.2.11124.01925

Gabrielse, H., Murphy, D.C. and Mortensen, J.K., 2006. Cretaceous and Cenozoic dextral orogen-parallel displacements, magmatism, and paleogeography, north-central Canadian Cordillera. *In*: Paleogeography of the North American Cordillera: Evidence For and Against Large-Scale Displacements, J.W. Haggart, R.J. Enkin and J.W.H. Monger (eds.), Geological Association of Canada Special Paper, vol. 46, p. 255–276.

Geyer, C.J. and Møller, J., 1994. Simulation Procedures and Likelihood Inference for Spatial Point Processes. Scandinavian Journal of Statistics, vol. 21, issue 1, p. 359–373.

Gosselin, J.M., Biegel, K., Hamidbeygi, M. and Dettmer, J., 2023. Improvements in the regional earthquake focal mechanism catalogue for southwestern Yukon. *In*: Yukon Exploration and Geology 2022, K.E. MacFarlane (ed.), Yukon Geological Survey, p. 63–76 plus digital appendices.

Green, P.J., 1995. Reversible jump Markov chain Monte Carlo Computation and Bayesian model determination. Biometrika, vol. 82, issue 4, p. 711–732. https://doi.org/10.1093/biomet/82.4.711

Green, P.J., 2003. Trans-dimensional Markov chain Monte Carlo Computation. *In*: Highly Structured Stochastic Systems, P.J. Green, N.L. Hjort and S. Richardson (eds.), p. 179–198. https://doi.org/10.1093/oso/9780198510550.003.0017

Havenith, H.-B., Fäh, D., Polom, U. and Roulle, A., 2007. S-wave velocity measurements applied to the seismic microzonation of Basel, Upper Rhine Graben. Geophysical Journal International, vol. 170, p. 346–358. https://doi.org/10.1111/j.1365-246X.2007.03422.x

Hobiger, M., Cornou, C., Wathelet, M., Giulio, G.D., Knapmeyer-Endrun, B., Renalier, F., Bard, P.-Y., Savvaidis, A., Hailemikael, S., Le, B.N., Ohrnberger, M. and Theodoulidis, N., 2012. Ground structure imaging by inversions of Rayleigh wave ellipticity: Sensitivity analysis and application to European Strong-motion sites. Geophysical Journal International, vol. 192, p. 207–229. https://doi.org/10.1093/gji/ggs005

Israel, S., Murphy, D., Bennett, V., Mortensen, J. and Crowley, J., 2011. New insights into the geology and mineral potential of the Coast Belt in southwestern Yukon. *In:* Yukon Exploration and Geology 2010, K.E. MacFarlane, L.H. Weston and C. Relf (eds.), Yukon Geological Survey, p. 101–123.

Israel, S., Tizzard, A.M. and Major, J., 2005. Geological Map of the Duke River Area (Parts of NTS 115G/2, 3, 5, 6, 7). Yukon Geological Survey Open File 2005–11.

Israel, S., Tizzard, A. and Major, J., 2006. Bedrock geology of the Duke River area, parts of NTS 115G/2, 3, 4, 6 and 7, southwestern Yukon. *In:* Yukon Exploration and Geology 2005, D.S. Emond, G.D. Bradshaw, L.L. Lewis and L.H. Weston (eds.), Yukon Geological Survey, p. 139–154.

Kanai, K. and Tanaka, T., 1961. On Microtremors VIII. Bulletin of Earthquakes Research Institute, vol. 39, p. 97–114.

Kennedy, K.E., 2013. Surficial Geology of Burwash Landing and Destruction Bay (parts of NTS 115G/2, 6 and 7) Yukon. Yukon Geological Survey Open File, 2013–14.

Konno, K. and Ohmachi, T., 1998. Ground-motion characteristics estimated from spectral ratio between horizontal and vertical components of microtremor. Bulletin of the Seismological Society of America, vol. 88, issue 1, p. 228–241. https://doi.org/10.1785/bssa0880010228

Li, C.-F., Lu, Y. and Wang, J., 2017. A global reference model of Curie-point depths based on EMAG2. Scientific Reports, vol. 7, article number 45129, https://doi.org/10.1038/srep45129

Lowey, G., 1998. A new estimate of the amount of displacement on the Denali Fault system based on the occurrence of carbonate megaboulders in the Dezadeash Formation (Jura-Cretaceous), Yukon, and the Nutzotin Mountains sequence (Jura-Cretaceous), Alaska. Bulletin of Canadian Petroleum Geology, vol. 46, issue 3, p. 379–386.

Malinverno, A., 2002. Parsimonious Bayesian Markov Chain Monte Carlo inversion in a nonlinear geophysical problem. Geophysical Journal International, vol. 151, issue 3, p. 675–688. https://doi.org/10.1046/j.1365-246x.2002.01847.x

Mezger, J.E., Chacko, T. and Erdmer, P., 2001. Metamorphism at a late Mesozoic accretionary margin: A study from the coast belt of the North American Cordillera. Journal of Metamorphic Geology, vol. 19, issue 2, p. 121–137. https://doi.org/10.1046/j.0263-4929.2000.00300.x

Molnar, S., Dosso, S.E. and Cassidy, J.F., 2010. Bayesian inversion of microtremor array dispersion data in southwestern British Columbia. Geophysical Journal International, vol. 183, p. 923–940. https://doi.org/10.1111/j.1365-246X.2010.04761.x

Molnar, S., Sirohey, A., Assaf, J., Bard, P.-Y., Castellaro, S., Cornou, C., Cox, B., Guillier, B., Hassani, B., Kawase, H., Matsushima, S., Sánchez-Sesma, F.J. and Yong, A., 2022. A review of the Microtremor horizontal-to-vertical spectral ratio (MHVSR) method. Journal of Seismology, vol. 26, issue 4, p. 653–685. https://doi.org/10.1007/s10950-021-10062-9

Mosegaard, K. and Tarantola, A., 1995. Monte Carlo sampling of solutions to inverse problems. Journal of Geophysical Research: Solid Earth, vol. 100, issue B7, p. 12431–12447. https://doi.org/10.1029/94jb03097

Nakamura, Y., 1989. A method for dynamic characteristics estimation of subsurface using microtremor on the ground surface. Railway Technical Research Institute, vol. 30, issue 1, p. 25–33.

Nakamura, Y., 2008. On the H/V Spectrum. The 14th World Conference on Earthquake Engineering, Beijing, China, 12–17 October 2008.

Nakamura, Y., 2019. What is the Nakamura method? Seismological Research Letters, vol. 90, issue 4, p. 1437-1443. https://doi.org/10.1785/0220180376

Parolai, S., Picozzi, M., Richwalski, S.M. and Milkereit, C., 2005. Joint inversion of phase velocity dispersion and H/V ratio curves from seismic noise recordings using a genetic algorithm, considering higher modes. Geophysical Research Letters, vol. 32, issue 1. https://doi.org/10.1029/2004gl021115

Picozzi, M., Parolai, S. and Richwalski, S.M., 2005. Joint inversion of H/V ratios and dispersion curves from seismic noise: Estimating the s-wave velocity of bedrock. Geophysical Research Letters, vol. 32, issue 11. https://doi.org/10.1029/2005gl022878

Piña-Flores, J., Cárdenas-Soto, M., Sarabia-González, A., García-Jerez, A., Sierra-Álvarez, C.A., Sáenz-Castillo, M.A., Luzón, F. and Sánchez-Sesma, F.J., 2021. Imaging the structure of the Sun Pyramid (Teotihuacán, Mexico) from passive seismic methods. Engineering Geology, vol. 281, no. 105969. https://doi.org/10.1016/j.enggeo.2020.105969

Sánchez-Sesma, F.J., Rodríguez, M., Iturrarán-Viveros, U., Luzón, F., Campillo, M., Margerin, L., García-Jerez, A., Suarez, M., Santoyo, M.A., and Rodríguez-Castellanos, A., 2011. A theory for Microtremor H/V spectral ratio: Application for a layered medium. Geophysical Journal International, vol. 186, issue 1, p. 221–225. https://doi.org/10.1111/j.1365-246x.2011.05064.x

Scherbaum, F., Hinzen, K.-G. and Ohrnberger, M., 2003. Determination of shallow shear wave velocity profiles in the Cologne/Germany area using ambient vibrations, Geophysical Journal International, vol. 152, p. 597–612.

SESAME, 2004. Guidelines for the Implementation of the H/V Spectral Ratio Technique on Ambient Vibrations: Measurements, Processing and Interpretation. SESAME European Research Project WP12 - Deliverable D23.12, European Commission – Research General Directorate Project No. EVG1-CT-2000-00026 SESAME, 62 p.

Tschirhart, V., Colpron, M., Craven, J., Ghalati, F.H., Enkin, R.J. and Grasby, S.E., 2022. Geothermal exploration in the Burwash Landing Region, Canada, using three-dimensional inversion of passive electromagnetic data. Remote Sensing, vol. 14, issue 23, no. 5963. https://doi.org/10.3390/rs14235963

Vantassel, J., 2020. jpvantassel/hvsrpy: latest (Concept). Zenodo. https://doi.org/10.5281/zenodo.3666956

Waldien, T.S., Roeske, S.M. and Benowitz, J.A., 2021. Tectonic underplating and dismemberment of the Maclaren-Kluane schist records Late Cretaceous terrane accretion polarity and ~480 km of Post-52 ma dextral displacement on the Denali fault. Tectonics, vol. 40, issue 10. https://doi.org/10.1029/2020tc006677

Wathelet, M., 2008. An improved neighborhood algorithm: Parameter conditions and dynamic scaling. Geophysical Research Letters, vol. 35, issue 9. https://doi.org/10.1029/2008gl033256

Wathelet, M., Jongmans, D. and Ohrnberger, M., 2004. Surface-wave inversion using a direct search algorithm and its application to ambient vibration measurements. Near Surface Geophysics, vol. 2, issue 4, p. 211–221. https://doi.org/10.3997/1873-0604.2004018

Witter, J., 2020. Early-stage exploration for geothermal energy resources along the Denali fault near Duke River, Yukon. Yukon Geological Survey, Open File 2020–3, 62 p.

Permafrost-related landslides following a 2017 wildfire, Dempster Highway, Yukon (parts of NTS 116G/9 and 116H/12)

Heather C. Clarke*
Simon Fraser University

Derek C. Cronmiller
Yukon Geological Survey

Brent C. Ward
Simon Fraser University

Katelyn A. Groeneveld
Simon Fraser University

Abstract

The Yukon is experiencing impacts of climate change, marked by elevated annual air temperatures, alterations in precipitation patterns and increased wildfire activity. These changes can lead to permafrost degradation, impacting highways and community infrastructure. In July 2017, a wildfire burned a slope in permafrost terrain above the Dempster Highway in the Yukon. In the years following the wildfire, two types of permafrost-related landslides have been observed on the slope. Active layer detachment activity was highest in the first year after the landslide, possibly influenced by warm temperatures and rainfall events. Retrogressive thaw flow slides formed in 2019 in areas of ice-rich permafrost and are still active in 2023. Deposition of sediment and influx of water has resulted in flooding near the highway, further degrading the permafrost in the valley bottom. This study characterizes the landslide timing and morphology following a wildfire on permafrost terrain, and investigates potential triggers and controls.

Introduction

Background

Northern regions are experiencing impacts due to climate change at a faster and more extreme rate than the rest of the world (Vincent, 2020). Over the last 50 years, the Yukon has seen an increase in mean annual air temperature of approximately 2°C, with the greatest increase in temperature occurring in winter (Perrin and Jolkowski, 2022). Temperatures are predicted to continue to increase, as are the intensity, frequency and annual amount of precipitation (Perrin and Jolkowski, 2022).

One of the major impacts of climate change in the Yukon is the alteration of permafrost conditions. Permafrost, defined as ground that remains below 0°C continuously for two or more years, plays a critical role in regulating various geomorphological processes and supporting unique ecosystems (Smith *et al.*, 2022). Thaw of permafrost and associated ground ice can lead to surface subsidence and slope instability, which modifies terrain and drainage patterns (Lewkowicz, 1990). Permafrost also plays a critical role in the global climate system: long-term climate warming can release carbon stored in near-surface permafrost as well as impact the

* heather_clarke@sfu.ca

amount and distribution of snow cover, which insulates and modifies the temperature of the underlying ground. The feedback loops triggered by thawing permafrost, such as the release of methane and carbon dioxide, further contribute to the amplification of global climate change (Jorgenson et a*l*., 2010; Schuur et a*l*., 2015). The geotechnical and environmental problems associated with permafrost degradation are increasingly important issues in the Yukon (Perrin and Jolkowski, 2022).

Permafrost distribution is primarily controlled by mean annual air temperature; other important factors include depth and duration of snow cover, slope angle, slope aspect, geology, surface water conditions and vegetation cover. Because of this, permafrost stability is threatened not only by the increasing mean annual air temperature, but also by factors including the alteration of precipitation patterns and increased frequency and severity of wildfires in the north (Smith et a*l*., 2022). Although wildfire activity varies annually, there is a regional trend in historical data from 1959 to 2015 of increased area burned per year and an increased number of large fires per year (Hanes et a*l*., 2019; Perrin and Jolkowski, 2022). The number and intensity of fires is expected to increase in Canada due to climate change (Wotton et a*l*., 2017); this will have significant impacts on permafrost conditions. Following fires, ground temperatures and active layer thicknesses increase, especially in more severely burned areas (Lipovsky et a*l*., 2005; Coates, 2008; Holloway et a*l*., 2020; Smith et a*l*., 2022). Wildfires destroy the insulating organic layer, reduce snow interception by trees due to the decrease in vegetation canopy, lower ground surface albedo by charring the organic mat, and diminish evapotranspiration (Lipovsky et a*l*., 2005; Smith et a*l*., 2022). The duration and extent of permafrost degradation after a fire can persist for years, depending on the burn intensity and the pre-fire vegetation cover (Holloway et a*l*., 2020). Measurements taken at burned and unburned sites in permafrost regions have shown the mean annual ground surface temperatures at burned sites were 1–7°C higher than at unburned sites (Holloway et a*l*., 2020).

In 2017, a wildfire initiated by a lightning strike burned 86 128 ha near the Dempster Highway in the Yukon during the span of three weeks from late June to mid-July (Yukon Wildland Fire Report, 2017). In the weeks and years following the fire, landslide activity was observed on a slope parallel to the highway, with one slide crossing the highway and forcing closure of the road until debris could be cleared. The purpose of this study is to characterize the timing and morphology of the landslides and explore potential relationships between permafrost characteristics, geology, weather conditions and ground disturbance. This work will contribute to the growing body of research on how climate change is impacting communities and infrastructure in permafrost regions.

Study area

Location and physiography

The study area encompasses the slopes parallel to KM 240 to KM 250 on the northwest side of the Dempster Highway, Yukon (Fig. 1), a 740 km all-season gravel highway beginning approximately 40 km south of Dawson City, Yukon, and traversing northeast across the Arctic Circle to the town of Inuvik, Northwest Territories. The study area overlaps with the Traditional Territories of the Tr'ondëk Hwëch'in and Vuntut Gwitchin First Nations. The highway here is part of the Ogilvie maintenance section and is bounded by the Ogilvie River on the southeast and a slope on the northwest. The Ogilvie River drains to the northeast, becoming the Peel River at its confluence with the Blackstone River 40 km northeast of the study area. The elevation ranges from 480 m above sea level (masl) near the Ogilvie River, up to 850 masl at the top of the slope.

The Eagle Lowland physiographic region is part of the Foreland fold and thrust belt, composed of deformed sedimentary rocks deposited on or adjacent to the stable North American craton (Smith et a*l*., 2004). Bedrock comprises uplifted sedimentary rocks from the Monster assemblage that were deposited during the Cretaceous (Dixon, 1992). These rocks include coarsening-upward cycles up to 30 m thick of dark grey to black shale with interbeds of siltstone and fine-grained sandstone (Dixon, 1992). The topography of the Eagle Lowland slopes is strongly influenced by bedrock structure and lithology, which influences slope angles and forms benches and terraces through differential erosion of rock types.
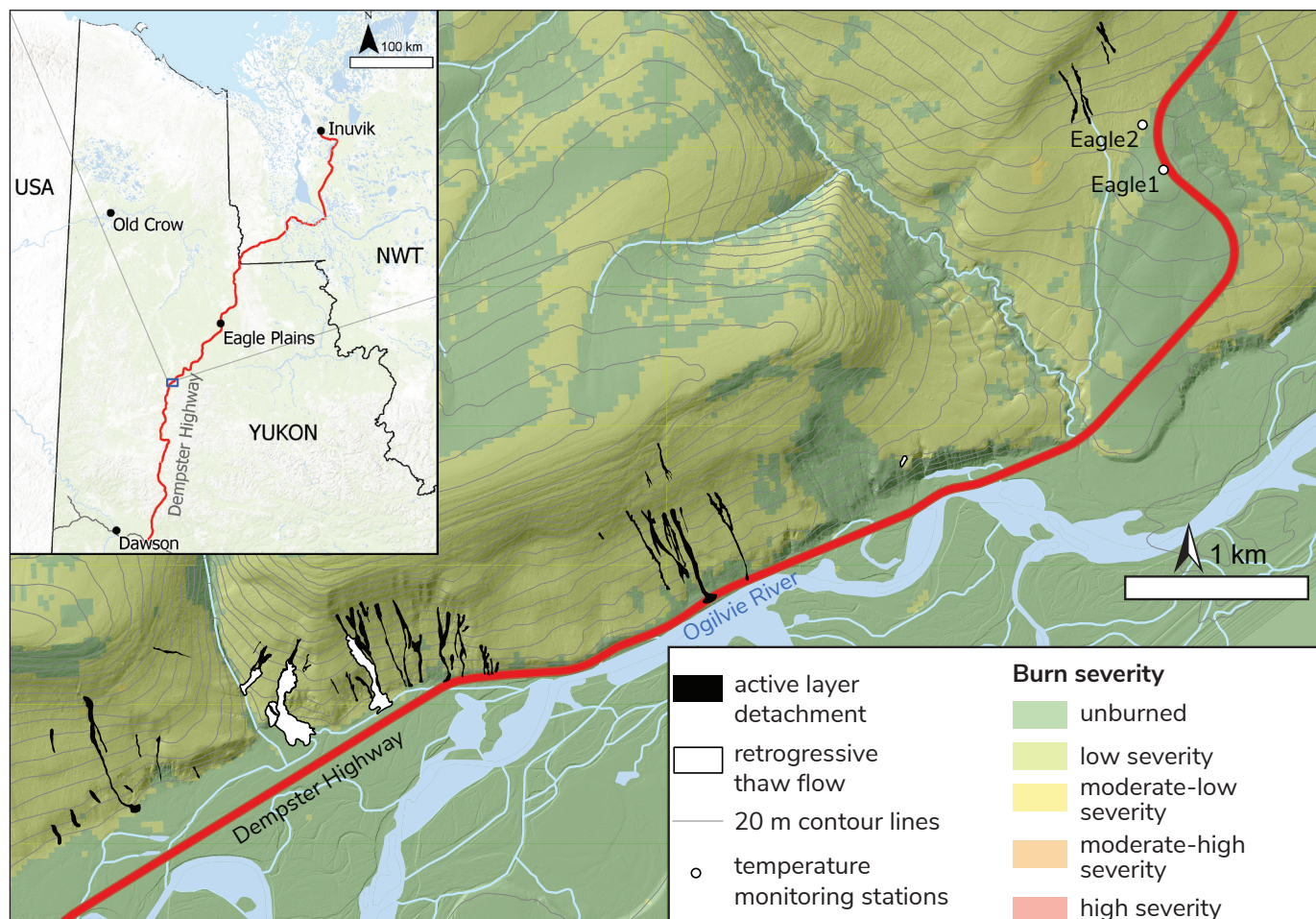
Figure 1. *Study area location with outlines of permafrost-related landslides from 2017 to 2023. Colour scale represents burn severity from the 2017 wildfire. Inset map shows regional location of study area. Dempster Highway represented by red line in both maps. The Ogilvie floodplain temperature monitoring site is not shown.*

Glacial history and surficial geology

The study area remained unaffected by glacial ice during the Quaternary; however, major rivers in the watershed were influenced by regional glaciation to the east. During this period, advancement of the Laurentide Ice Sheet northwest across the northern Mackenzie Mountains impounded the east-flowing Bonnet Plume basin and resulted in the formation of Glacial Lake Hughes during the Last Glacial Maximum (Duk-Rodkin and Hughes, 1995; Kennedy et a*l.*, 2010). The glacial lake extended westward from the Bonnet Plume basin to the Ogilvie River valley and drained north via the Eagle River into the Bell basin (Duk-Rodkin and Hughes, 1995). The study area lies just beyond the mapped limits for Glacial Lake Hughes.

Continental glaciation also modified global circulation patterns and caused sea level to lower during glacial periods. During the Last Glacial Maximum, the exposed continental shelf between eastern Russia and Alaska, USA, formed the Bering Land Bridge, connecting the two continents. This unglaciated region is known as Beringia and was characterized by a cold and arid climate comprising tundra, steppe tundra and forest-tundra ecosystems (Guthrie, 2001). In the study area, the Ogilvie River system has incised the terrain, forming valleys and floodplains composed of fluvial materials. On the slope above the highway, aeolian accumulations of silt have formed thick packages of loess on slope breaks. Extensive weathering of the bedrock has resulted in the accumulation of colluvial blankets and veneers covering the slope.

Climate and vegetation

The study area is in the Taiga Cordillera Ecoregion, which is characterized by a subarctic continental climate with long, cold winters and short, cool summers (Smith et al., 2004). Strong temperature inversions occur in this mountainous region due to topographic shading and cold-air drainage, causing the valleys to be considerably colder in the winter than the surrounding ridges and plateaus (Burn, 1994). Weather systems coming from the Gulf of Alaska lose most of their moisture on the St. Elias Mountains before reaching central Yukon; however, moderate precipitation occurs primarily as summer rainfall from June to August (Burn et al., 2015). Annual precipitation is predicted to increase by 11% between 2021 and 2050 based on the representative concentration pathway (RCP) 8.5 emissions scenario, where greenhouse gas emissions continue to increase at current rates (Climate Atlas of Canada, 2019). Under the same scenario, summer and winter precipitation is expected to increase by 10 and 11%, respectively, with more heavy precipitation days (more than 10 mm in 24 hours) annually (Climate Atlas of Canada, 2019).

The closest weather station to the study site is located at the Ogilvie Highway maintenance camp at KM 194 of the Dempster Highway (Environment Canada, 2023). There are large gaps in the record from this station during the past two decades; however, from 1988 to 2006, the mean annual air temperature at the station was –9°C. The coldest month was January, with average monthly temperatures as low as –40°C, and the warmest month was July, with average monthly temperatures as high as 15°C (Environment Canada, 2023). Data from the weather station reveal an upward trend in the mean annual air temperature consistent with regional model predictions of a 1.3°C and 3.2°C increase in mean summer and winter temperatures, respectively, from 2021 to 2050 under the RCP 8.5 emissions scenario (Climate Atlas of Canada, 2019).

Vegetation in the study area features an open canopy forest of single and mixed-species canopies including black spruce (*Picea mariana*), white spruce (*P. glauca*) and aspen (*Populus tremuloides*). Canopy gaps are commonly filled with willow (*Salix* spp.) and alder (*Alnus* spp.), as well as shrubs and sedges such as dwarf birch (*Betula* spp.) and Labrador tea (*Rhododendron groenlandicum*). Willow, alder, balsam poplar (*P. balsamifera*) and aspen are present in the

fluvial plain. Low-shrub tundra communities including dwarf birch, willows, and lichens are found on the upper slope and ridge.

Permafrost

Permafrost is continuous in the study area. Perennially frozen ground is present everywhere except locally under lakes, river channels and other bodies of water (Smith et al., 2004). Ground ice content in permafrost regions influences the ground thermal regime and is an important factor in how the landscape will respond to permafrost degradation (French, 2017). Models have predicted that the study area has 10–20% ground ice content by volume in the upper 5 m of permafrost as either ice wedges or segregated ice (Heginbottom et al., 1995; O'Neill et al., 2022). These models are useful for regional and circumpolar estimations; however, the scale is not intended for site-specific conditions. More work is needed to better understand and predict ground-ice content at a local scale.

Landslide types

Two types of permafrost-related landslides occur in the study area: active layer detachments (ALDs) and retrogressive thaw flows (RTFs). Active layer detachments are rapid mass movements that occur when the active layer (the uppermost layer that freezes and thaws seasonally) becomes detached from the underlying permafrost (Lewkowicz, 1990; Lewkowicz and Harris, 2005a, b). The permafrost table serves as the failure plane for ALDs and controls the depth of scour. The initiation of ALDs involves a reduction of effective stress at the transition between the active layer and the permafrost table due to an increase in pore water pressure (Lewkowicz, 1990). Increased pore water pressure, which is commonly a result of precipitation or heat, can induce rapid thaw of ice-rich sediment at the transition layer (French, 2017). Other factors that influence the occurrence of ALDs include soil moisture conditions, slope form and steepness, surficial materials, depth of the active layer, and vegetation cover (Lipovsky et al., 2005). Active layer detachments in the Yukon commonly involve flow or slide styles of movement and initiate on moderate to steep slopes. Wildfires can contribute to ALD initiation by rapidly thawing and deepening the active layer and melting ice at the transition layer, resulting in an increase in pore water pressure at the permafrost

table (Lewkowicz and Harris, 2005a; Coates, 2008). Destroying the vegetation reduces root strength in the organic mat and can lead to changes in permafrost conditions, impacting slope stability for months and years following a wildfire (Holloway et a*l.*, 2020).

Retrogressive thaw flows are characterized by a steep, bowl-shaped headscarp of thawing ice-rich sediments or massive ice, and a low-angle tongue of landslide debris (Lantuit and Pollard, 2007). Initiation of RTFs commonly occurs when ground ice is exposed by processes such as fluvial erosion, subsidence, active layer detachments, wildfire, increased air temperatures, and human-induced ground disturbance (Kokelj et a*l.*, 2015). As ice within permafrost melts, the structural integrity of the slope decreases and the headwall can retrogress upslope as further permafrost is exposed (Burn and Lewkowicz, 1990; Kokelj et a*l.*, 2015). Retrogressive thaw flows deposit saturated material at the base of the headwall, which can be transported downslope by slides and flows at rates that are dependent on slope angle, sediment characteristics, and ground-ice content (Kokelj et a*l.*, 2015). Retrogressive thaw flows farther north on the Dempster Highway had 20 year average retreat rates of 7.2–26.6 m/year (Lacelle et a*l.*, 2015). The Takhini River retrogressive thaw slump (near Whitehorse) had a 6 year average rate of 8 m/year (Calmels et a*l.*, 2021). Retrogressive thaw flows can undergo polycyclic cycles of stabilization and re-exposure for up to 50 years following the initial event (French, 1974). Both types of permafrost landslides can

damage infrastructure and contribute large amounts of sediment and water into nearby terrestrial and aquatic ecosystems, altering ground temperatures and inducing change in vegetation growth (Jones et a*l.*, 2021).

Methodology

Initial site investigations by the Yukon Geological Survey occurred in fall 2021 and fall 2022. In fall 2022, thermistors were installed in three locations (Table 1, Fig. 2): two in the study area, one in an unburned site (Eagle1) and the other in a burned site (Eagle2); and a third in an unburned site on the Ogilvie River floodplain (Ogilvie floodplain), approximately 4 km southeast of the study area. In 2023, fieldwork took place during three separate trips in June, August and September. Field observations were made at multiple landslides and samples were collected for geochronology, ice-content measurements and geotechnical analysis. The most active RTF during field investigations in 2023 was RTF1. To gain insight into the ice content of the headwall of RTF1, six sediment samples were taken from four stratigraphic units in the headwall. Volumetric excess ice content (E_i, expressed as a percentage) was estimated using equation 1 (Kokelj and Burn, 2003):

$$E_i = \frac{(W_V 1.09)}{(S_V + (W_V 1.09)} \qquad (1)$$

where W_v is the volume of supernatant water, S_v is the volume of saturated sediment, and 1.09 represents the expansion of water when it freezes. Gravimetric ice

Table 1. *Site characteristics of temperature monitoring stations in the study area. The locations of Eagle1 and Eagle2 are shown in Figure 1; Ogilvie floodplain is approximately 4 km south of study area.*

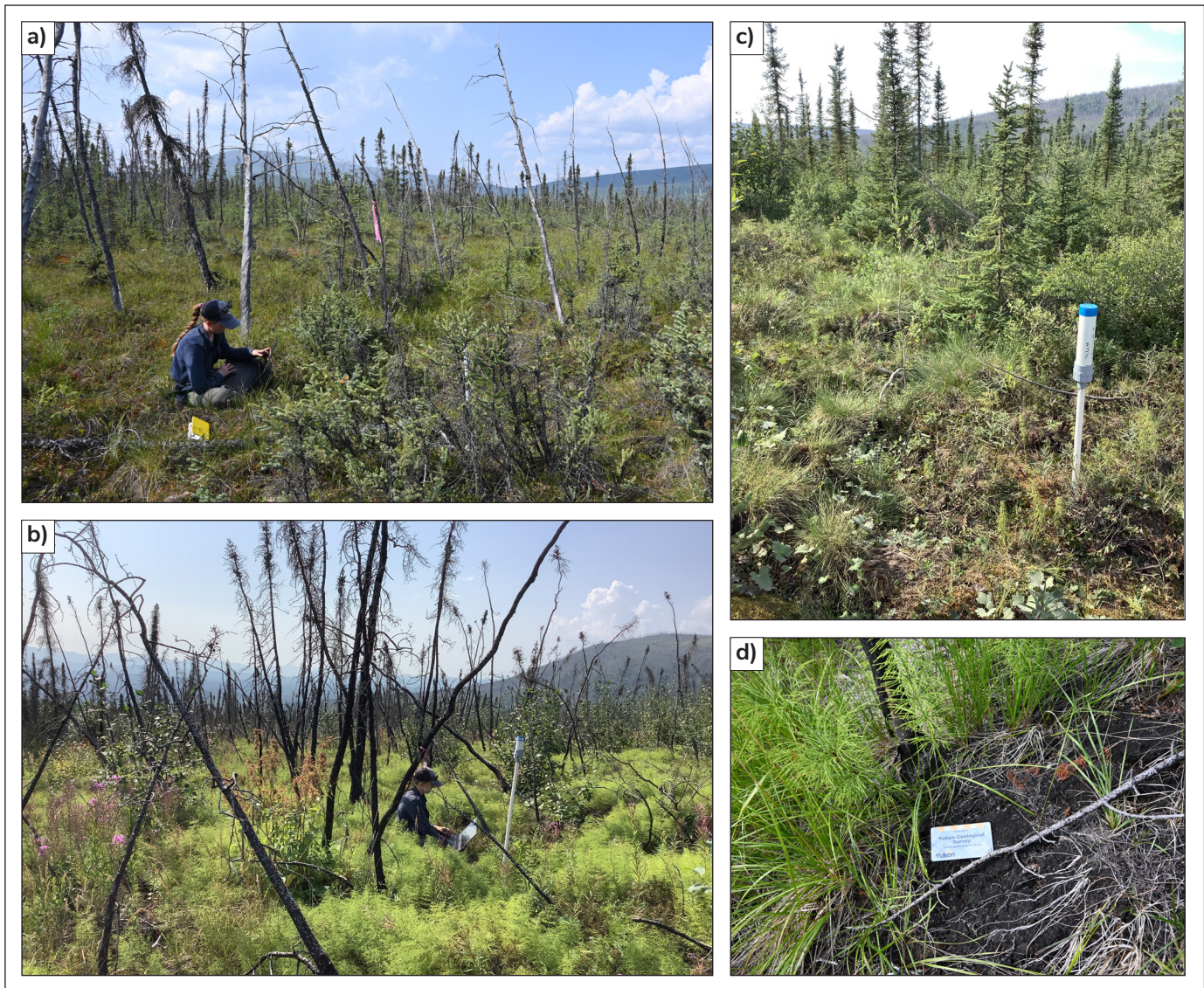| Site	Eagle1	Eagle2	Ogilvie floodplain
Burn condition	unburned	burned	unburned
Permafrost	absent	present	present
Vegetation type	black spruce forest	burnt black spruce forest	mixed spruce and aspen
Depth of sensors (cm)	0, 50, 150	0, 50, 150, 200	0, 50, 100, 135
Core log	0–20 cm: organics	0–15 cm: burned organics	0–45 cm: organics, fibric to mesic
	20–110 cm: silt	15–200 cm: sandy silt	45–50 cm: ice
	110–150 cm: bedrock		50–100 cm: sandy silt w/ ice lenses up to 5 mm thick
			100–140 cm: silt grading to sand

Figure 2. *Temperature monitoring stations in the study area:* **a)** *Ogilvie floodplain station,* **b)** *Eagle2 station (burned),* **c)** *Eagle1 station (unburned) and* **d)** *charred organic mat at Eagle2.*

content (W_d) was estimated using equation 2, based on Reynolds and Topp (2008),

$$W_d = \frac{m_i}{m_{ds}} \qquad (2)$$

where m_i is the ice weight (measured as weight loss after drying) and m_{ds} is dry soil weight.

Aerial photos from unmanned aerial vehicle (UAV) surveys from each field visit along with 2020 lidar data (Government of Yukon, 2023) were used to track changes in landslide morphology over time. Agisoft Metashape was used to create structure-from-motion orthomosaics and digital elevation models (DEMs) of the landslides following a workflow designed by the United States Geological Survey (USGS; Over et al., 2021). The orthomosaics and DEMs were loaded into ArcGIS Pro and used to delineate retrogressive thaw flow headscarp movement from 2021 to 2023.

Timing of the landslides was investigated using air photos from the Government of Yukon air photo library dating from 1949 to 2007 (Yukon Energy, Mines and Resources, 2023) and PlanetLab satellite imagery from 2017 to 2023 (Planet Labs PBC, 2017–2023). The temporal resolution of satellite imagery varied between 1 and 3 days and was often cloud covered for multiple consecutive days. The initiation date for each landslide

was assigned using the first day that there was visible evidence of the landslide. It is important to note that nine new landslides were visible after a particularly long span of cloud-covered imagery between July 14 and 21, 2018. The exact initiation dates for these landslides were difficult to determine due to the cloudy imagery, so they were all assigned a July 22 initiation date. Landslide scars were delineated by polygons in ArcGIS Pro (Fig. 1) and points were used in initiation zones to calculate landslide characteristics.

Spectral differences between healthy vegetation and recently burned vegetation can be used to calculate a burn severity index. Healthy vegetation strongly reflects near-infrared light (NIR) and weakly reflects shortwave infrared (SWIR) light compared to burned vegetation. A normalized burn ratio (NBR; equation 3) was calculated using Landsat 8 imagery taken before and after the fire. The difference between the pre and post-fire NBR (differenced NBR, or dNBR) was used to calculate the burn severity of the fire (equation 4), which was then classified according to Key and Benson (2006), which is the USGS standard.

$$NBR = \frac{NIR - SWIR}{NIR + SWIR} \qquad (3)$$

$$dNBR = pre\text{-}fire\ NBR - post\text{-}fire\ NBR \qquad (4)$$

Results

Wildfire effects on permafrost depth and temperature

The study area experienced mostly low burn severity, with 30 to 100 m^2 patches of moderate to low-severity burn (Fig. 1). Ground temperature data from thermistors show that the depth to permafrost is approximately 100 cm in the Ogilvie floodplain (Fig. 3a). The burned site (Eagle2) reaches permafrost at a depth of 180 cm (Fig. 3b). The unburned borehole (Eagle1) does not reach permafrost, but it has a shallower depth than the other sites, extending only 150 cm below surface (Fig. 3c). Using second-order polynomial trendlines it can be inferred that the unburned Eagle1 site would reach permafrost at approximately 160 cm. The zone of zero amplitude is near 170 cm and the permafrost temperature is approximately –1°C. The inferred zone of zero amplitude for the burned site is much deeper, at approximately 210 cm; however, the permafrost

temperature is also approximately –1°C. This indicates that although permafrost temperatures are likely to be similar between Eagle1 and Eagle2, Eagle1 reaches permafrost approximately 50 cm closer to surface than Eagle2 (burned). When comparing similar depths, the unburned and burned sites have similar average temperatures. The Ogilvie floodplain data has the shallowest depth to permafrost, and the zone of zero amplitude has a temperature of approximately –4°C. The measurements taken at 0 cm at all locations are likely inflated due to the influence of solar radiation on the sections of pipe that are above ground.

Active layer detachments

A total of 31 ALDs were identified in the study area between 1949 and 2013. This is likely an under-representation because the spatial and temporal resolution of the historical record is lower than that of more recent data. No obvious fire triggers were evident for these landslides, so they are interpreted to represent a background landslide rate. No landslides were identified between 2013 and 2016. The occurrence of 41 ALDs was identified during the period from the wildfire in 2017 and the end of 2018; one additional ALD was identified in 2020 (Fig. 4). This represents a fortyfold increase in landslides per year in the two years after the wildfire compared to the background landslide rate. Figure 5a and b show active layer detachment events relative to precipitation and temperature data from the Eagle Plains weather station. In 2017, the first ALD occurred 3 days after the wildfire and more than 50% of the total slides occurred during a two-week period in early August 2017, beginning just 20 days after the area was burned. During this two-week period, the weather station recorded increased precipitation (20% of the total summer rainfall) and average daily temperatures were 2°C higher than the average August temperature from 1980 to 2006.

In summer 2018, there were 16 ALDs. Almost all landslides occurred in July, with most initiating between July 13 and 25. The satellite imagery is cloud covered from July 14 to 21, coinciding with increased precipitation recorded at Eagle Plains. Landslides with the assigned date of July 22 may have occurred earlier during this eight-day cloudy period. Similar to 2017, these landslides became visible following high rainfall days. Daily average temperature reached its summer peak from July 22 to 25, coinciding with the initiation of
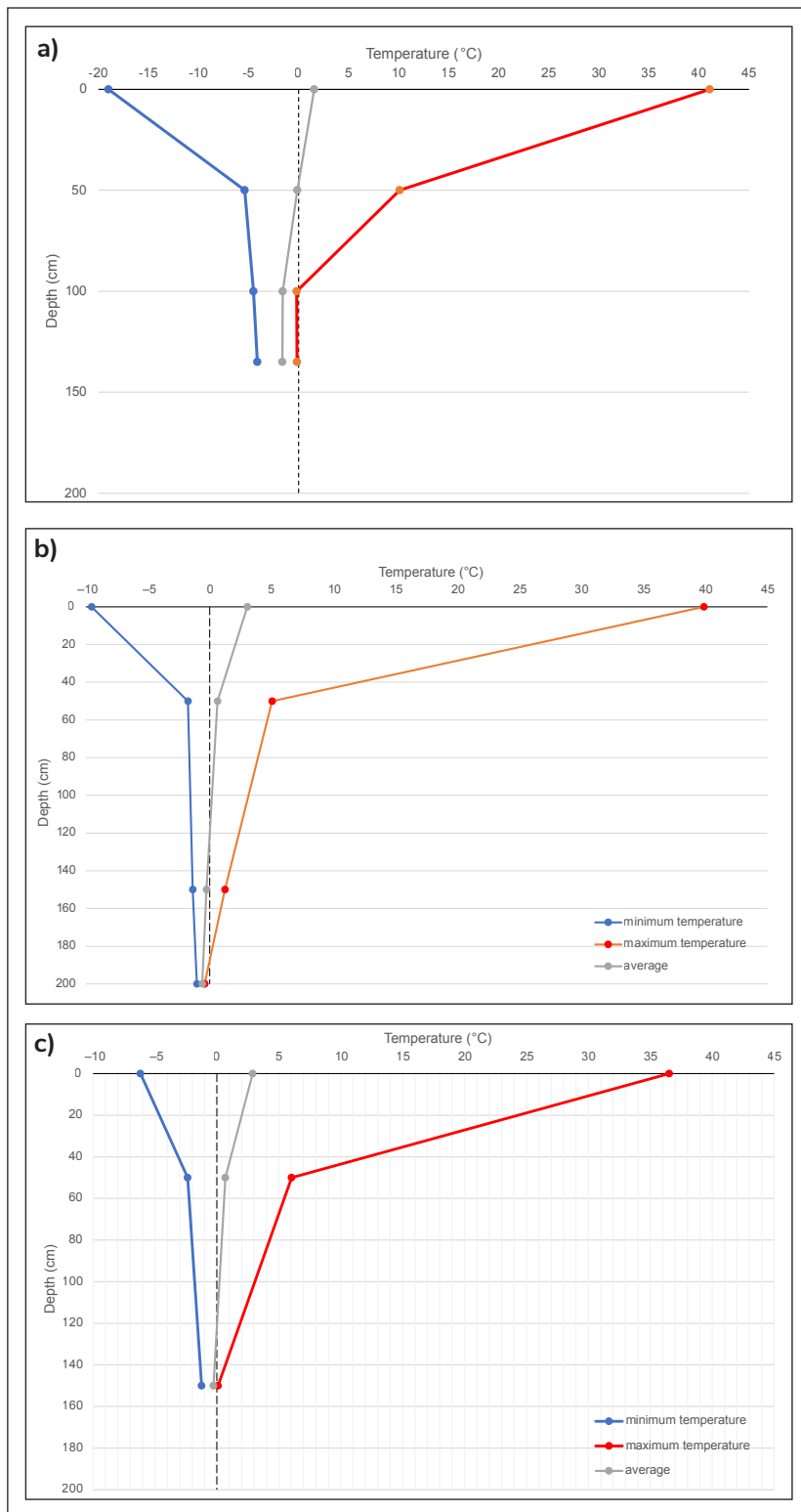
Figure 3. *Temperature envelopes plotted for **a)** Ogilvie floodplain, **b)** Eagle2 (burned) and **c)** Eagle1 (unburned) stations. Depth at which the red line crosses 0°C is the depth to permafrost. None of the borehole depths are deep enough to measure the permafrost temperature at the zone of zero amplitude where the minimum and maximum lines converge.*

three ALDs. From 2019 to 2023, only one ALD has been identified in the study area.

Active layer detachment characteristics are summarized in Table 2 and representative photos are shown in Figure 6. All ALDs within the study area occur on south and southwest-facing slopes. The landslide failure surfaces are relatively planar and parallel to topography; however, deep V-shaped, post-landslide incisions made by surface water erosion have modified this profile. The depths of the headscarps and initiation zones are relatively uniform, ranging from approximately 1 to 2 m. The runout distances of the ALDs range from 25 to 530 m, with the most extensive reaching the bottom of the slope. Two of the most extensive ALDs occurred in 2018, depositing debris on the highway and right of way that resulted in road closures (Fig. 6c). Those landslides that travelled to the bottom of the slope appear to have scoured deeper into the lower slope, entraining more material and forming levees of coarse debris on the sides of the landslide scars. Many of the ALDs experienced multiple stages of failure, with upslope retrogressions occurring in the days following the initial failure. Slope angles at the initiation point ranged from 9 to 45 degrees. Field investigations revealed that the initiation of ALDs commonly occurred in either shale-dominant colluvium or sandstone-dominant colluvium. Some headscarps exposed highly weathered shale bedrock at or below the failure plane. Bedrock exposed in the headscarps is classified as highly weathered according to the classification of rock weathering by Deere and Patton (1971), when more than half the rock material is decomposed and fresh rock is present as a discontinuous framework.
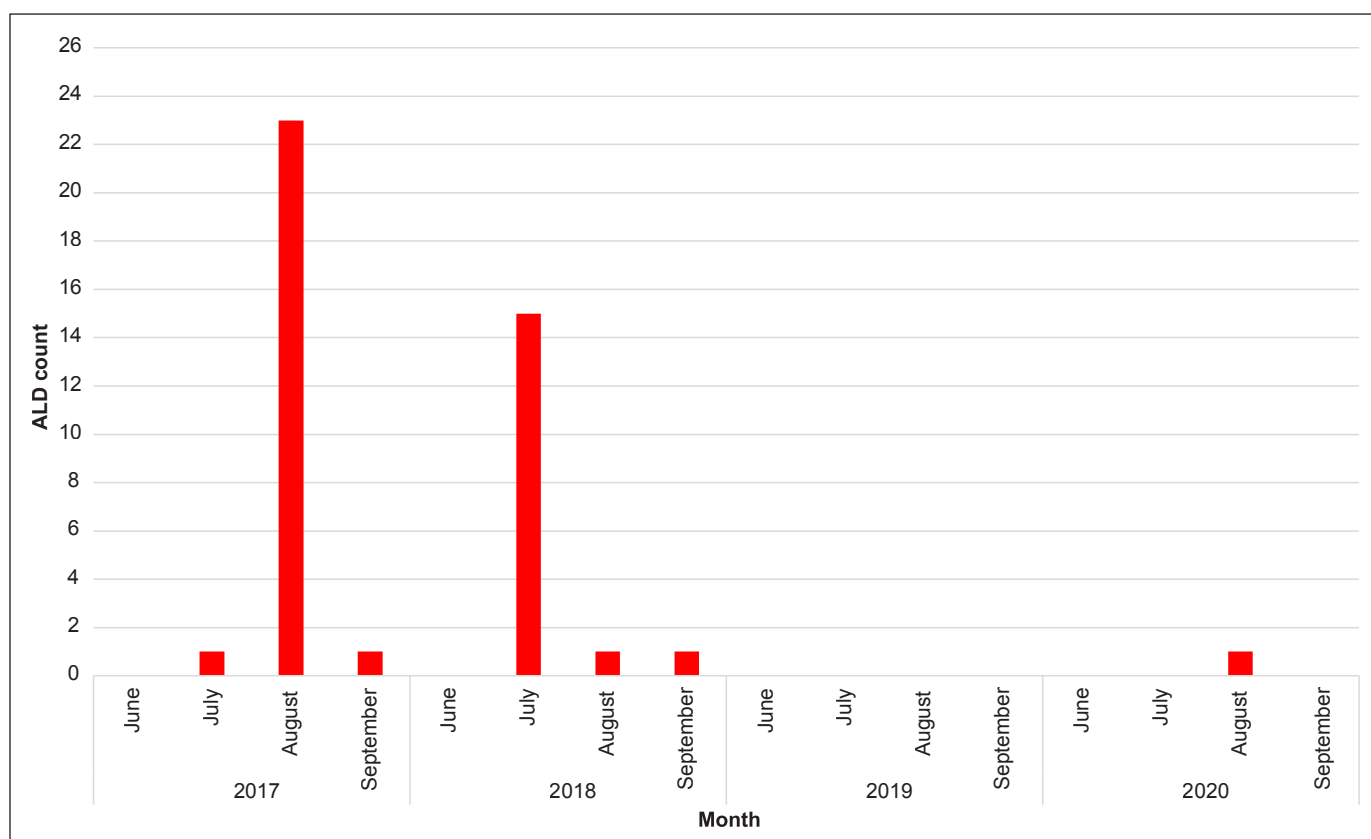
Figure 4. *Active layer detachment (ALD) events in the study area from 2017 to 2020. No ALDs were identified from 2021 to 2023.*

Retrogressive thaw flows

Six RTFs were identified in the study area; all were initiated after the 2017 wildfire. The exact initiation timing of the RTFs is difficult to constrain due to poor spatial resolution of available imagery and the slow nature of the slide progression. Retrogressive thaw flows appear to have started transporting sediment downslope during summer 2019 and all six are clear in lidar data obtained during summer 2020. Five of six RTFs are within close proximity in the west end of the study area; the sixth is near the east end of the study area (Fig. 7a). At the eastern end of the study area, RTF6 was the only landslide that did not appear to form in the path left by an ALD and had the lowest initiation slope angle (Fig. 7b). In 2023, the RTFs ranged in area from 1150 to 39 400 m^2. The average slope angle from the estimated initiation point is 14 degrees. Sediment transport and deposition from three RTFs reaches the bottom of the slope, causing blockages in backchannels and creeks that traverse the area between the slope and highway. This is shown in UAV imagery and was also observed on the ground as the waterways were

found to have changed from the first field visit in early June to the last visit in late September (Fig. 7c). Four of the RTFs had massive ice bodies exposed in their headwalls. The two that did not have exposed ice were not as active throughout the 2023 site visits and exhibited patches of vegetation regrowth in the form of mosses and shrubs.

RTF1

In 2023, the largest and most active RTF in the study area was RTF1 (Fig. 7a). RTF1 was the only site selected for ice content sample collection because it has the most extensive exposures of stratigraphy and visibly ice-rich permafrost. This landslide has grown more than 200% in area (from headscarp to extent of deposition) and has retrogressed approximately 50 m/year between 2021 and 2023 (Fig. 8a). Detailed stratigraphy of RTF1 as well as the other RTFs is forthcoming in future work; however, the focus for this study is the variation in ice content between different surficial materials. The stratigraphy of the headwall and sidewalls of RTF1 is
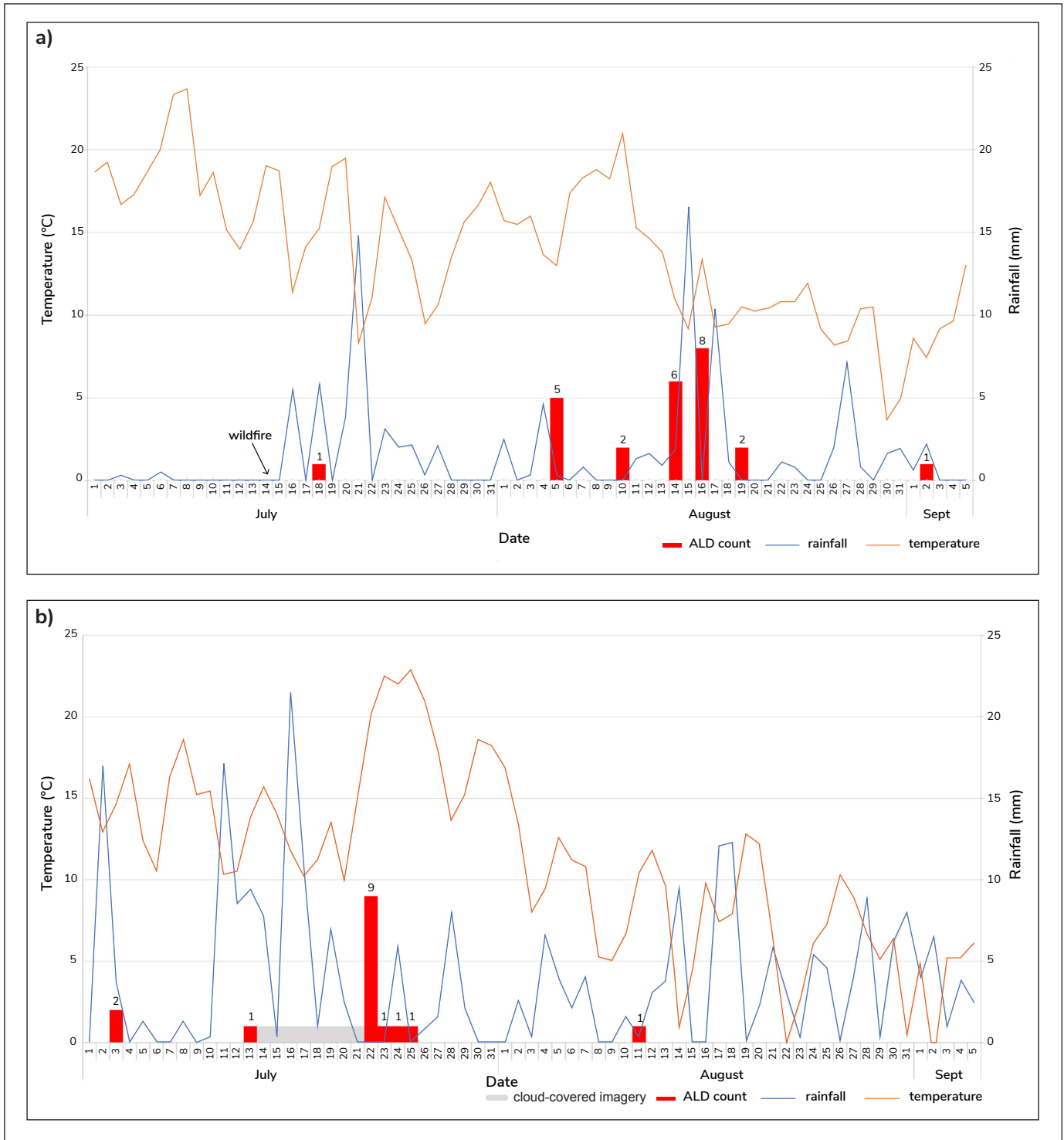
Figure 5. Active layer detachment initiation dates for **a)** 2017 and **b)** 2018, plotted with temperature and rainfall data from the Eagle Plains weather station. Note: July 14 to 21, 2018, satellite imagery is cloud covered; active layer detachment events plotted on July 22 may have occurred up to eight days earlier.

Table 2. *Characteristics of active layer detachment and retrogressive thaw flows.*

Landslide type		Landslide area (m²)	Initiation elevation (masl)	Initiation slope (degrees)
Active layer detachment	mean	4389	622	27
	maximum	21 031.4	769	45
	minimum	318.3	519	9
	total	184 365		
Retrogressive thaw flow slide	mean	12 549	542	14
	maximum	39 401	521	24
	minimum	1150	562	4
	total	75 296		

complex and spatially variable (Fig. 8b, c). Colluvium and loess are the predominant materials; both range in clast content and amounts of organic matter. The colluvium units are up to 5 m thick and the loess packages range from 0.3 to 1.4 m. The headwalls also have extensive wedge ice, with exposures of up to 3 m vertical and 7 m horizontal in some sections. Most of the exposed headwall and sidewalls are frozen from 1 to 2 m below ground surface. Ice content of selected units is described in Table 3. The sample with the highest excess ice content is sample 2a from the lower part of a silty colluvium unit, with 65% volumetric excess-ice content and 121% gravimetric water content. Samples taken from unit 4 have the lowest ice content.

Discussion

Significance of bedrock

Initial observations indicate that there are important associations between ALDs and bedrock lithology in the study area. Because the region is unglaciated, bedrock is pervasively weathered on most slopes, resulting in thick blankets of bedrock-derived colluvium. The breakdown of the sedimentary rocks into finer materials such as silt and clay can decrease pore space, reducing water drainage through the slope. High ice content is more commonly associated with finer materials than with coarse materials (Jorgenson et a*l.*, 2008; French, 2017; O'Neill et a*l.*, 2019). Investigations

of ALD initiation zones commonly revealed either sandstone-dominant colluvium or shale-dominant colluvium. In sandstone-dominant colluvium, ALDs initiate only on slopes greater than 30 degrees; whereas initiation angles ranged from 11 to 34 degrees in shale-dominant colluvium. The relatively high hydraulic conductivity of the sandstone compared to the low hydraulic conductivity of the shales may impact slope stability (Deere and Patton, 1971) and influence the permafrost conditions of the slope. Another factor to consider is the role of ice formation within weathered shale bedrock. Fine-grained sedimentary rocks allow segregated ice to form within fractures and bedding planes. This contributes to slope instability in two ways: ice formation within bedrock results in fracturing along the planes of weakness (Dyke, 1984); and increasing the ice content can lead to increased pore water pressure if the permafrost degrades (Eigenbrod et al., 1996).

Significance of topography in RTF formation

The national and global-scale model estimations for ground ice content are useful conceptual tools, but do not capture local-scale factors. As a result, initial observations from the field area indicate that ground ice content is significantly higher in some areas of the slope than the estimated 20% from the models (Heginbottom et al., 1995; O'Neill et al., 2022). The
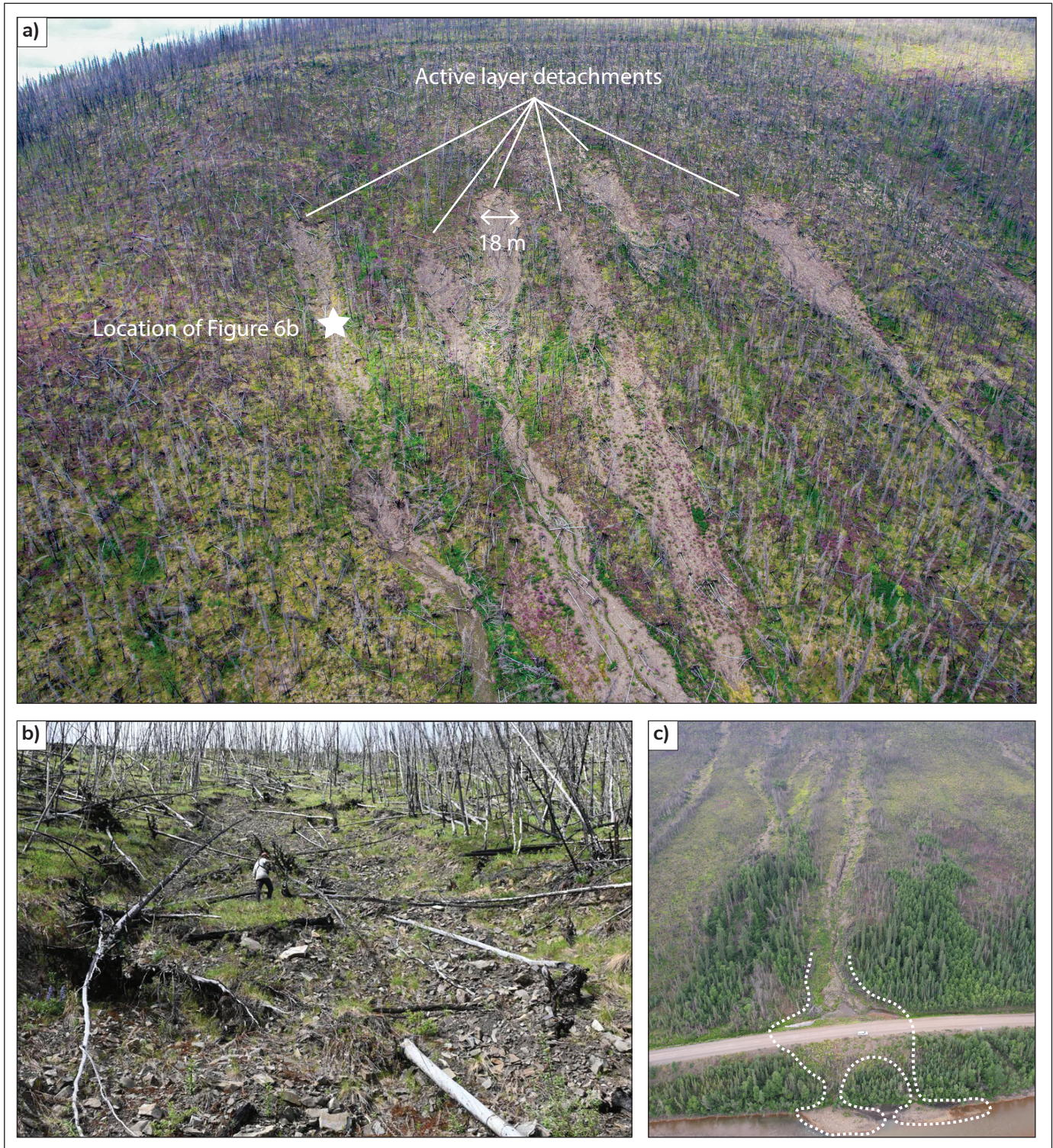
Figure 6. *Field images of active layer detachments (ALDs) in the study area:* **a)** *multiple parallel ALD scars initiating at approximately the same elevation, with varying run-out lengths. Photo taken in August 2023;* **b)** *upslope view of ALD indicated in a) with person for scale. Photo taken in June 2023;* **c)** *run out of one 2018 ALD, which crossed the Dempster Highway in 2018 and caused closures; white truck for scale, run out delineated by white dashed line. Photo taken in 2019.*

Figure 7. a) *View facing east of retrogressive thaw flow (RTF) locations in the study area in September 2023.* **b)** *View looking east showing RTF6, the only RTF in the east end of the study area. Photo taken June 2023.* **c)** *Sedimentation from RTF1 fills and blocks a creek at the base of the slope, resulting in flooding of the forest floor. Photo taken September 2023.*

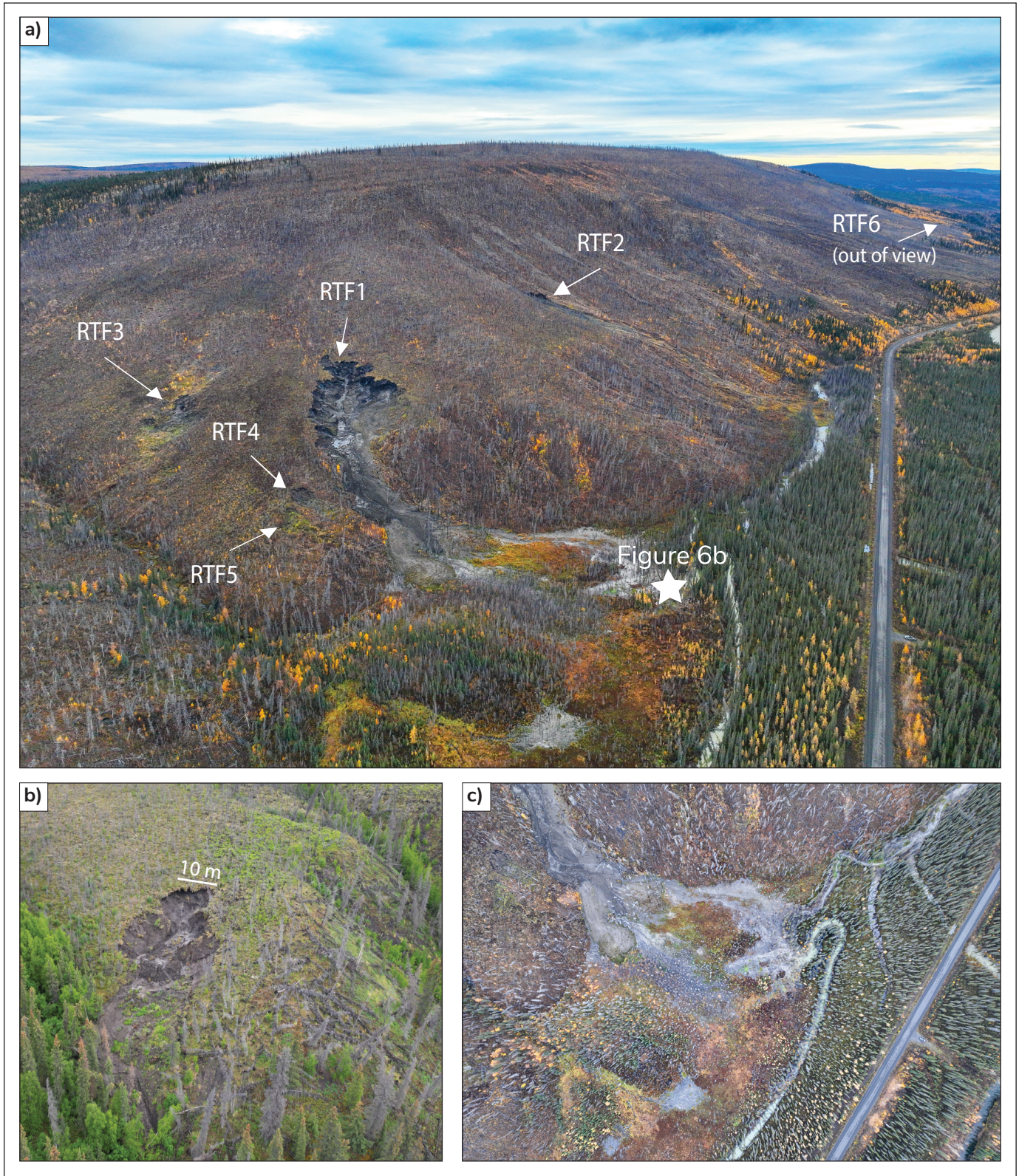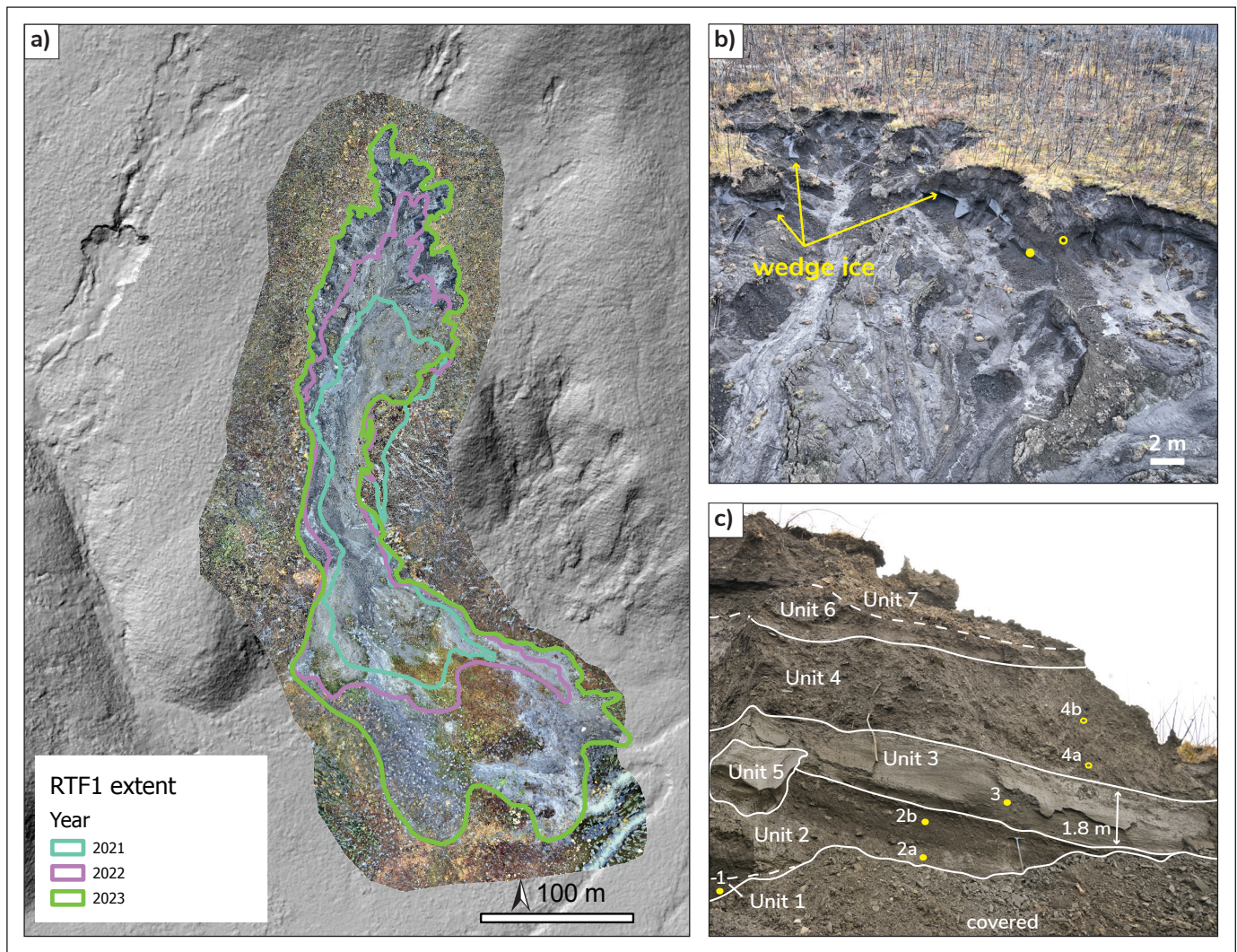Figure 8. a) *Growth of RTF1 from 2021 to 2023 shown on 2023 orthomosaic overlying hillshade derived from lidar data (Government of Yukon, 2023).* b) *Oblique view of the RTF1 headscarp in September 2023 showing wedge ice and locations of ice content sampling. The solid yellow circle indicates the locations of samples 1 to 3 and the hollow yellow circle indicates the location of samples 4a and b.* c) *Close-up view of units sampled for ice content. Samples 4a and b (hollow yellow circles) were collected on the other side of the exposed rib. Photo taken September 2023.*

models generally account for the first 5 m below surface in their estimations and may not be able to account for multiple surficial materials within that depth. The headwalls and sidewalls of RTFs in the study area commonly expose ground ice, including metre-scale wedge ice at depths up to 8 m. The surficial material units also vary in composition and thickness within sites, each with varying ice contents. Retrogressive thaw flow formation in the study area is dependent on high ground-ice content to mobilize sediment and continue upslope retrogression; therefore, RTF formation appears to be a reasonable indicator for the presence of high ice content and fine-grained materials in certain areas of the slope. The RTFs formed on gently sloping terrain situated between steep upper and lower slopes. A possible reason for high ice content across this landform is the preferential accumulation of loess and colluvium, which supply ideal conditions for ice-wedge formation and preservation.

Wildfire, precipitation and temperature influences on landslide timing

The timing and frequency of the landslides in the study area are strong indicators that slope stability was impacted by the 2017 wildfire. Most of the ALDs

Table 3. Ice content analysis of samples collected from RTF1, the largest and most active retrogressive thaw flow in the study area; sample locations are indicated in Figure 8b, c.

Unit	Sample number	Unit thickness (cm)	Material	Frozen	Volumetric excess-ice content (%)	Gravimetric water content (%)
1	1	30 (lower contact covered)	silt	yes	39	64
2	2a	200	silty colluvium	yes	65	121
2	2b			yes	44	43
3	3	180	silt	yes	9	31
4	4a	470	organic-rich colluvium	yes	no supernatant water	20
4	4b			yes	3	8
5	n/a	variable: 10–300	wedge ice	yes	approximately 100	not measured
6	n/a	40	organic-rich silt	no	not sampled	not sampled
7	n/a	170	colluvium	no	not sampled	not sampled

occurred within weeks of the wildfire. During this period, the permafrost likely experienced rapid changes due to the direct heat from the fire and the increased absorption of incoming solar radiation caused by decreased shade, insulation and albedo. Active layer detachments in the summers of 2017 and 2018 may have also been influenced by precipitation and warm air temperatures. In 2018, peak annual rainfall was followed by peak summer temperatures, following which nine ALDs were identified. Air temperature and rainfall patterns in the summer of 2019 were similar to 2017 and 2018; however, even with distinct peaks in either temperature or precipitation, no new landslides were identified. This suggests that wildfire impacts had the strongest influence on slope stability in the study area relative to air temperatures and rainfall events. One small ALD took place in 2020 and shows no clear association with either precipitation or temperature. No RTFs were identified in the study area from 1949 to 2017; however, six RTFs initiated in the study area during the six years following the wildfire, and in 2023 all of them exhibited some degree of activity.

Hazard cascades

The study area is a unique example of the cascading effects of hazards in permafrost regions (Fig. 9). Here, a slope containing ice-rich permafrost experienced a wildfire, which decreased slope stability and resulted in numerous ALDs. The resultant exposure of permafrost triggered the initiation of RTFs in subsequent years, all of which are still active today. The RTFs have deposited large amounts of sediment and caused an influx of water at the base of the slope, altering drainage patterns and flooding the forest next to the highway. The impacts of increased water in the area are yet to be fully realized; however, it could lead to further degradation of permafrost and subsidence in the valley bottom near the road.

Degradation of permafrost is a negative cycle of its own in which carbon and methane previously stored in frozen ground are released into the atmosphere, where they contribute to the amplification of climate change. The impacts of permafrost-related landslides in the study area go beyond the burn area and the

Figure 9. *Cascading impacts of wildfire in permafrost terrain in the study area. Wildfire leads to active layer detachments (black arrows), which expose ice-rich permafrost, resulting in retrogressive thaw flow (white hatched lines show headscarps) that deposit large volumes of sediment and water at the base of the slope (white dotted outlines), and further degrade permafrost in the valley bottom. Photo taken in 2023.*

visible outline of the landslide scars. These processes and feedback loops highlight the fragility of northern communities and infrastructure in a changing climate.

Conclusions

This study investigated permafrost-related landslides following a 2017 wildfire on a slope along the Dempster Highway in the Yukon. A 39% increase in ALDs was observed within the two years following the fire, suggesting the burn significantly influenced slope stability. Increased precipitation and air temperatures appear to have contributed to slope instability in both 2017 and 2018. No RTFs were identified between 1949 and 2016, although the spatial and temporal resolution of the historical data may not be sufficient to detect these types of landslides. Six RTFs were identified after the wildfire in areas that were burned and/or disturbed by ALDs. Retrogressive thaw flow development is not discernible until summer 2019. The largest RTF retrogressed 100 m between 2021 and 2023. The ALDs and RTFs in the study area have brought debris onto the highway and increased sediment and water volume at the base of the slope, potentially causing further permafrost degradation. Results from this study indicate that wildfire on permafrost slopes can initiate a

cascading hazard effect that can be further influenced by local precipitation and warm summer temperatures. Further research is needed to quantify the predictive relationship between bedrock lithology, surficial material and permafrost characteristics with respect to landslide initiation.

Acknowledgments

References

Burn, C.R., 1994. Permafrost, tectonics, and past and future regional climate change, Yukon and adjacent Northwest Territories. Canadian Journal of Earth Sciences, vol. 31, no. 1, p. 182–191. https://doi.org/10.1139/e94-015

Burn, C.R. and Lewkowicz, A.G., 1990. Canadian landform examples – 17: Retrogressive thaw slumps. Canadian Geographic, vol. 34, p. 967–981.

Burn, C.R., Moore, J., O'Neill, H.B., Hayley, D., Trimble, J., Calmels, F., Orban, S.N., Idrees, M., 2015. Permafrost characterization of the Dempster Highway, Yukon and Northwest Territories. *In:* Proceedings, 68th Canadian Geotechnical Conference and 7th Canadian Permafrost Conference, Paper 703, 21-23 September 2015, Quebec City, QC, Canadian Geotechnical Society, Richmond, BC, 8 p.

Calmels, F., Roy, L.P., Laurent, C., Amyot, F., Cubley, J. and Lipovsky, P., 2021. Assessment and Monitoring of a New Retrogressive Thaw Slump at km 1456 of the Alaska Highway: A Rare Opportunity. YukonU Research Centre, Yukon University, Whitehorse, 72 p. https://www.yukonu.ca/sites/default/files/inline-files/PGR_2021_01_Tak_Slump_NTAI_0.pdf

Climate Atlas of Canada, 2019. Climate Change in Canada, version 2. Prairie Climate Centre, University of Winnipeg, Winnipeg, Manitoba, https://climateatlas.ca [accessed November 25, 2023].

Coates, J., 2008. The impact of forest fire on permafrost slopes Klondike area, Yukon Territory. MSc thesis, University of Ottawa, Ontario, Canada, 218 p. https://doi.org/10.20381/ruor-18782

Deere, D. and Patton, F., 1971. Slope stability in residual soils. *In:* Proceedings of the 4th Panamerican Conference on Soil Mechanics and Foundation Engineering, vol. 1: State-of-the-Art Papers. American Society of Civil Engineers, New York, p. 87–170.

Dixon, J., 1992. Stratigraphy of Mesozoic strata, Eagle Plain area, northern Yukon. Geological Survey of Canada, Bulletin 408, 58 p. https://doi.org/10.4095/133639

Duk-Rodkin, A. and Hughes, O.L., 1995. Quaternary geology of the northeastern part of the central Mackenzie Valley Corridor, District of Mackenzie, Northwest Territories. Geological Survey of Canada Bulletin 458, 45 p.

Dyke, L., 1984. Frost heaving of bedrock in permafrost regions. Environmental and Engineering Geosciences, vol. 21, no. 4, p. 389–405. https://doi.org/10.2113/gseegeosci.xxi.4.389

Eigenbrod, K.D., Knutsson, S. and Sheng, D., 1996. Pore-water pressures in freezing and thawing fine-grained soils. Journal of Cold Regions Engineering, vol. 10, no. 2, p. 77–92. https://doi.org/10.1061/(ASCE)0887-381X(1996)10:2(77)

Environment Canada, 2023. Environment and Climate Change Canada Historical Climate Data. https://climate.weather.gc.ca/ [accessed November 10, 2023]

French, H.M., 1974. Active thermokarst processes, eastern Banks Island, western Canadian Arctic. Canadian Journal of Earth Sciences, vol. 11, no. 6, p. 785–794. https://doi.org/10.1139/e74-078

French, H.M., 2017. The Periglacial Environment, Fourth Edition. Wiley-Blackwell, New Jersey, 544 p.

Government of Yukon, 2023. Lidar collection. https://maps.mcelhanney.com/Vertisee/YukonGovLidar/ [accessed January 2023].

Guthrie, R.D., 2001. Origin and causes of the mammoth steppe: A story of cloud cover, woolly mammal tooth pits, buckles, and inside-out Beringia. Quaternary Science Reviews, vol. 20, p. 549–574. https://doi.org/10.1016/S0277-3791(00)00099-8

Hanes, C.C., Wang, X., Jain, P., Parisien, M.-A., Little, J.M. and Flannigan, M.D., 2019. Fire-regime changes in Canada over the last half century. Canadian Journal of Forest Research, vol. 49, no. 3, p. 256–269. https://doi.org/10.1139/cjfr-2018-0293

Heginbottom, J.A., Dubreuil, M.A. and Harker, P.A., 1995. Canada, Permafrost. *In*: The National Atlas of Canada (5th edition), Natural Resources Canada, Geomatics Canada, MCR Series no. 4177, 1 sheet. https://doi.org/10.4095/294672

Holloway, J., Lewkowicz, A., Douglas, T., Li, X., Turetsky, M., Baltzer, J. and Jin, H., 2020. Impact of wildfire on permafrost landscapes: A review of recent advances and future prospects. Permafrost and Periglacial Processes, vol. 31, no. 3, p. 371–382. https://doi.org/10.1002/ppp.2048

Jones, M.K.W., Pollard, W.H. and Giguère, N., 2021. Daily Field Observations of Retrogressive Thaw Slump Dynamics in the Canadian High Arctic. Arctic, vol. 74, p. 339–354.

Jorgenson, M.T., Romanovsky, V., Harden, J., Shur, Y., O'Donnell, J., Schuur, E.A.G., Kanevskiy, M. and Marchenko, S., 2010. Resilience and vulnerability of permafrost to climate change. Canadian Journal of Forest Research, vol. 40, no. 7, p. 1219–1236. https://doi.org/10.1139/X10-060

Jorgenson, T., Yoshikawa, K., Kanevskiy, M., Shur, Y., Romanovsky, V., Marchenko, S., Grosse, G., Brown, J. and Jones, B., 2008. Permafrost Characteristics of Alaska. *In*: The Ninth International Conference on Permafrost, Fairbanks, Alaska, p. 121–122.

Kennedy, K.E., Froese, D.G., Zazula, G.D. and Lauriol, B., 2010. Last Glacial Maximum age for the northwest Laurentide maximum from the Eagle River spillway and delta complex, northern Yukon. Quaternary Science Reviews, vol. 29, no. 9–10, p. 1288–1300. https://doi.org/10.1016/j.quascirev.2010.02.015

Key, C. and Benson, N., 2006. Landscape Assessment (LA). *In*: D.C. Lutes, R.E. Keane, J.F. Caratti, C.H. Key, N.C. Benson, S. Sutherland and L.J. Gangi. FIREMON: Fire effects monitoring and inventory system. Gen. Tech. Rep. RMRS-GTR-164-CD. Fort Collins, CO: U.S. Department of Agriculture, Forest Service, Rocky Mountain Research Station, p. LA-1-55

Kokelj, S.V. and Burn, C.R., 2003. Ground ice and soluble cations in near-surface permafrost, Inuvik, Northwest Territories, Canada. Permafrost and Periglacial Processes, vol. 14, no. 3, p. 275–289. https://doi.org/10.1002/ppp.458

Kokelj, S.V., Tunnicliffe, J., Lacelle, D., Lantz, T.C. and Fraser, R.H., 2015. Retrogressive thaw slumps: From slope process to the landscape sensitivity of northwestern Canada. *In*: Proceedings, 68th Canadian Geotechnical Conference and 7th Canadian Permafrost Conference, Paper 104, 21–23 September 2015, Quebec City, QC, Canadian Geotechnical Society, Richmond, BC, 8 p.

Lacelle, D., Brooker, A., Fraser, R.H. and Kokelj, S.V., 2015. Distribution and growth of thaw slumps in the Richardson Mountains–Peel Plateau region, northwestern Canada. Geomorphology, vol. 235, p. 40–51. https://doi.org/10.1016/j.geomorph.2015.01.024

Lantuit, H. and Pollard, W., 2007. Fifty years of coastal erosion and retrogressive thaw slump activity on Herschel Island, Southern Beaufort Sea, Yukon Territory, Canada. Geomorphology, vol. 95, p. 84–102. https://doi.org/10.1016/j.geomorph.2006.07.040

Lewkowicz, A., 1990. Morphology, frequency and magnitude of active layer detachment slides, Fosheim Peninsula, Ellesmere Island, N.W.T. Nordicana, vol. 54, p. 111–118.

Lewkowicz, A.G. and Harris, C., 2005a. Morphology and geotechnique of active-layer detachment failures in discontinuous and continuous permafrost, northern Canada. Geomorphology, vol. 69, p. 275–297. https://doi.org/10.1016/j.geomorph.2005.01.011

Lewkowicz, A.G. and Harris, C., 2005b. Frequency and magnitude of active-layer detachment failures in discontinuous and continuous permafrost, northern Canada. Permafrost and Periglacial Processes, vol. 16, p. 115–130. https://doi.org/10.1002/ppp.522

Lipovsky, P.S., Coates, J., Lewkowicz, A.G., Trochim, E., 2005. Active-layer detachments following the summer 2004 forest fires near Dawson City, Yukon. *In:* Yukon Exploration and Geology 2005, D.S. Emond, G.D. Bradshaw, L.L. Lewis and L.H. Weston (eds.), Yukon Geological Survey, p. 175-194.

O'Neill, H.B., Wolfe, S.A. and Duchesne, C., 2019. New ground ice maps for Canada using a paleogeographic modelling approach. The Cryosphere, vol. 13, no. 3, p. 753–773. https://doi.org/10.5194/tc-13-753-2019

O'Neill, H.B., Wolfe, S.A. and Duchesne, C., 2022. Ground ice map of Canada version 1.1. Geological Survey of Canada, Open File 8713, p. 7 (1 sheet). https://doi.org/10.4095/330294

Over, J.-S.R., Ritchie, A.C., Kranenburg, C.J., Brown, J.A., Buscombe, D.D., Noble, T., Sherwood, C.R., Warrick, J.A. and Wernette, P.A., 2021. Processing coastal imagery with Agisoft Metashape Professional Edition, version 1.6—Structure from motion workflow documentation. United States Geological Survey, Open-File Report 2021-1039, 46 p. https://doi.org/10.3133/ofr20211039

Perrin, A. and Jolkowski, D., 2022. Yukon Climate Change Indicators and Key Findings 2022. YukonU Research Centre, Yukon University, Whitehorse, 126 p.

Planet Labs PBC, 2017–2023. Planet Application Program Interface: In Space for Life on Earth. https://www.planet.com/ [accessed July 2023].

Reynolds, W.D. and Topp, G.C., 2008. Soil water analyses: principles and parameters. *In*: Soil Sampling and Methods of Analysis, 2nd ed., M.R. Carter and E.G. Gregorich (eds.), Canadian Society of Soil Science, Pinawa, MB, Canada, p. 913-937.

Schuur, E., McGuire, A.D., Schädel, C., Grosse, G., Harden, J., Hayes, D.J., Hugelius, G., Koven, C., Kuhry, P., Lawrence, D., Natali, S., Olefeldt, D., Romanovsky, V., Schaefer, K., Turetsky, M., Treat, C. and Vonk, J., 2015. Climate change and the permafrost carbon feedback. Nature, vol. 2015, p. 171–179. https://doi.org/10.1038/nature14338

Smith, C.A.S., Meikle, J.C. and Roots, C.F. (eds), 2004. Ecoregions of the Yukon Territory: Biophysical properties of Yukon landscapes. Agriculture and Agri-Food Canada, PARC Technical Bulletin no. 04-01, Summerland, British Columbia, 313 p.

Smith, S.L., O'Neill, H.B., Isaksen, K., Noetzli, J. and Romanovsky, V.E., 2022. The changing thermal state of permafrost. Nature Reviews Earth and Environment, vol. 3, p. 10–23. https://doi.org/10.1038/s43017-021-00240-1

Vincent, W.F., 2020. Arctic climate change: Local impacts, global consequences, and policy implications. *In*: The Palgrave Handbook of Arctic Policy and Politics, K.S. Coates and C. Holroyd (eds.), Springer International Publishing, Palgrave Macmillan, Cham, p. 507–526. https://doi.org/10.1007/978-3-030-20557-7_31

Wotton, B.M., Flannigan, M.D. and Marshall, G.A., 2017. Potential climate change impacts on fire intensity and key wildfire suppression thresholds in Canada. Environmental Research Letters, vol. 12, no. 9, 12 p. https://doi.org/10.1088/1748-9326/aa7e6e

Yukon Energy, Mines and Resources, 2023. Air photo library. Yukon Energy, Mines and Resources. https://yukon.ca/en/science-and-natural-resources/research-and-monitoring/find-air-photos-yukon [accessed July 2023].

Yukon Wildland Fire Report, 2017. Map compiled by Wildland Fire Management, Department of Community Services, Government of Yukon, 3 p. https://yukon.ca/en/2017-yukon-wildfire-map [accessed October 2023].

Seismicity near the eastern Denali fault from temporary and long-term seismic recordings

Jongwon Han
Department of Earth and Environmental Sciences, Korea University, Seoul, Republic of Korea

Jan Dettmer*, Jeremy M. Gosselin, Hersh Gilbert and Katherine Biegel
Department of Geoscience, University of Calgary, Calgary, Alberta, Canada

Seongryong Kim
Department of Earth and Environmental Sciences, Korea University, Seoul, Republic of Korea

Abstract

We studied earthquakes near Burwash Landing, Yukon. Using data from temporary and permanent seismic stations, we enhanced the understanding of both regional and local earthquakes. The study used deep learning and template matching to effectively detect earthquakes, even from noisy data. Following detection, seismic parameters, earthquake location, and magnitude were estimated and refined. The analysis revealed 103 local earthquakes, with 28 located in an area of geothermal resource potential. Notable small-magnitude earthquakes were observed near Bock's Creek fault. No earthquakes were observed on the Denali fault during the study period. The existence of active faults strike-parallel to the Denali fault suggests that local permeable structures may exist in the area. Regional observations detected 46 432 regional earthquakes in 13 years, but none along a section of the Denali fault near Burwash Landing, Yukon, which we interpret as a seismic gap.

Introduction

Southwestern Yukon exhibits complex active tectonism and significant earthquake activity due to plate boundary interactions between the Pacific and North American plates (Fig. 1). Major plate boundary structures in the region include the Queen Charlotte–Fairweather fault system, which has a primarily right-lateral strike-slip motion resulting from the oblique convergence of the Pacific Plate with the North American Plate and the Yakutat microplate (Leonard et *al*., 2007). The convergence is partitioned between the Aleutian Trench subduction zone, and a series of right-lateral, crustal strike-slip faults that includes the Denali fault zone (DFZ). Together, these features exemplify the diverse tectonic regime.

The Denali fault is a crustal-scale, dextral, strike-slip fault resulting from terrane accretion. It extends more than 2000 km from British Columbia through Yukon and central Alaska to the Bering Sea. The Denali fault has experienced right-lateral displacement of 400–480 km (Lowey, 1998; Waldien et *al*., 2021). Grantz (1966) partitions the Denali fault into three parts: the western segment in west-central Alaska, the central (McKinley) segment in eastern Alaska, and the eastern segment in southwestern Yukon. During the Holocene, fault activity was predominantly concentrated on the central McKinley segment, with additional activity on the southern Totschunda fault (Lanphere, 1978). The Denali fault has been a focus of recent seismic studies following the 2002 magnitude 7.9 Denali earthquake,
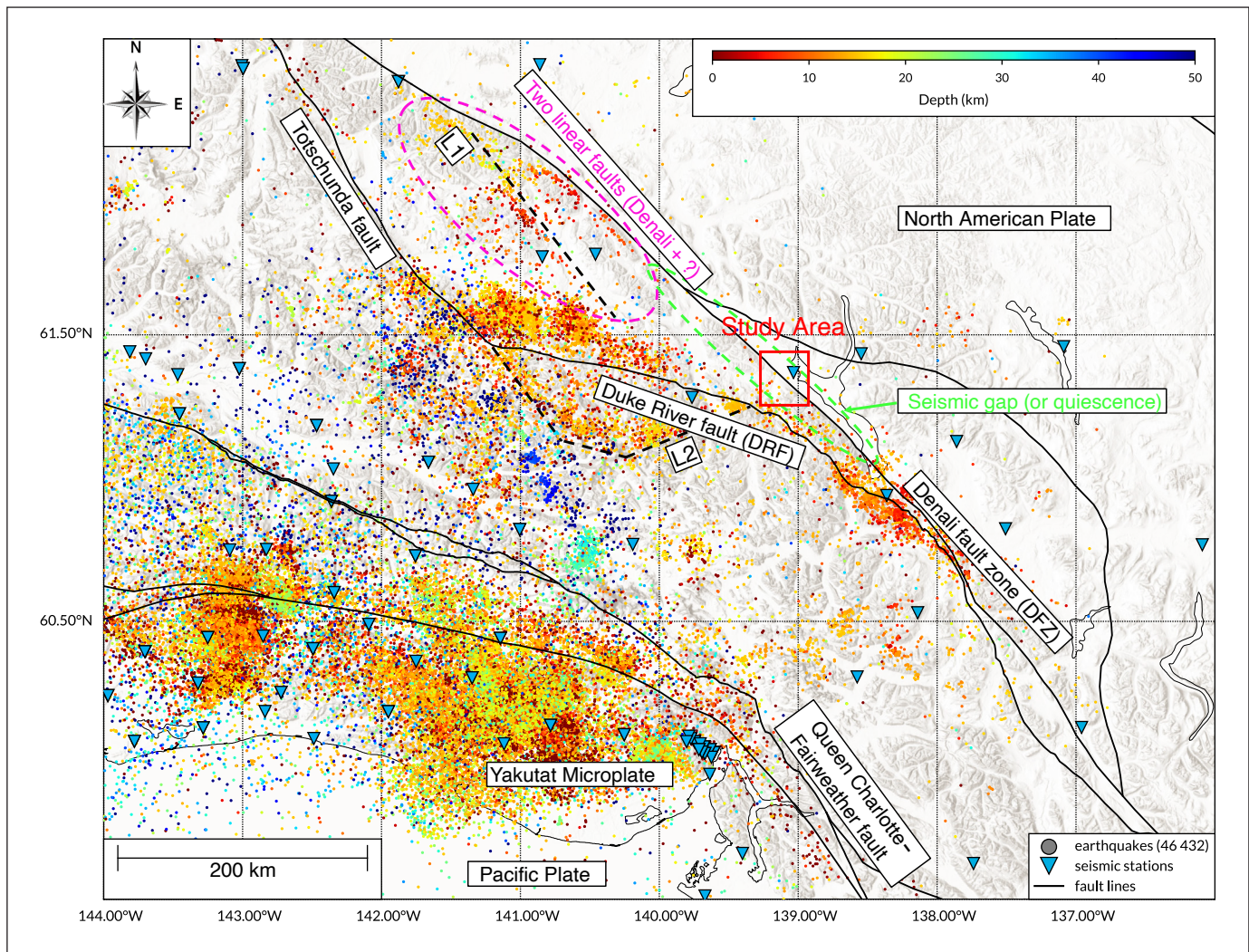
* jan.dettmer@ucalgary.ca

Figure 1. *Regional distribution of earthquakes recorded between 2010 and 2023 near the study area (red rectangle) based on network data. The colour scale indicates event depths and highlights the predominantly shallow deformation along the Denali fault zone (DFZ). The dashed line labelled L1 represents the newly discovered linear seismic trend from this study; L2 is a lineament confirmed in previous studies (Biegel et al., 2023; Gosselin et al., 2023). Areas of particular interest are highlighted by dashed ellipses.*

which highlighted the current seismic potential and complex rupture behaviour of past large events (Eberhart-Phillips et *al.*, 2003).

Knowledge of the regional patterns of seismicity in southwestern Yukon was previously limited by sparse seismic network coverage, which has improved in recent years. The enhanced monitoring capabilities have facilitated a new understanding of regional seismicity and crustal stress regimes. Advances in seismic station deployment have expanded detection capabilities and improved precision in earthquake location and characterization, providing insight into the tectonic processes that shape the region (Meighan et *al.*, 2013;

Ruppert and West, 2020; Biegel et *al.*, 2023; Gosselin et *al.*, 2023).

Regional seismicity is influenced by several fault systems including the Chugach-St. Elias, Fairweather, Denali and Teslin faults. These faults contribute to a complex pattern of seismicity, with events predominantly featuring reverse and dextral strike-slip mechanisms (L2 in Fig. 1; Gosselin et *al.*, 2023). Notably, seismicity near the Duke River fault (DRF) zone exhibits mostly reverse faulting within a predominantly transpressive regional context, underscoring the diverse nature of fault behaviour in the area (Doser, 2014). In the St. Elias region, a combination of thrust and strike-slip fault

characteristics underscore the area (Plafker et a*l*., 1978; Fletcher and Freymueller, 2003; Elliott et a*l*., 2010). The St. Elias Mountains, a wide mountain range formed from multiple accreted terranes, are a testament to ongoing subduction processes, marking a zone of significant crustal seismicity between the Fairweather and Denali faults.

Recent research has focused on understanding the broader implications of these tectonic interactions. For instance, the behaviour of the Denali fault system is indicative of not just local, but also regional geodynamic processes. Specifically, the eastern segment of the Denali fault was hypothesized to serve as a regional stress boundary that influences seismic activity and deformation patterns of the adjacent areas (Choi et a*l*., 2021). This perspective is critical for assessing the seismic hazard of the region and for understanding the broader tectonic framework of southwestern Yukon. The tectonic history and current dynamics of the Denali fault system offer insights into the potential for natural resource development in the region.

Southwestern Yukon is of particular interest for potential geothermal resource development (Majorowicz and Grasby, 2014); however, understanding the dynamic geological processes that characterize the resources and natural hazards is important for exploration and development. Regionally, the estimation of shallow Curie point depths (Li et a*l*., 2017; Witter et a*l*., 2018), shallow seismogenic crustal thickness (Biegel et a*l*., 2023), and the mapping of radiogenic rocks and warm water springs, suggest significant geothermal potential in the region (Colpron, 2019). Locally, near Burwash Landing, shallow conductors were recently inferred from magnetotelluric data, which may be evidence for crustal fluid circulation in the vicinity of the Denali fault (Tschirhart et a*l*., 2022). In this study, we present preliminary investigations of seismic patterns regionally (throughout southwestern Yukon) and locally near the eastern Denali fault (in the vicinity of Burwash Landing). The goal of this research is to improve knowledge of past and current regional tectonics, fault structure, and local behaviour near Burwash Landing, for the purpose of characterizing geothermal resource potential.

This paper presents preliminary results from a deep-learning–based earthquake detection algorithm (Mousavi et a*l*., 2020) and a template-matching method (Chamberlain et a*l*., 2018) used to detect earthquakes below the noise thresholds of conventional analysis techniques. Regionally, we present the distribution of 46 432 earthquakes between 2010 and 2023, many of which are additions to the existing regional catalogue. Locally, we analyzed data from recent temporary seismic instrument deployments near Burwash Landing to identify 103 earthquakes. Specifically, we present 28 new earthquake locations, with associated magnitude estimates, near the Denali fault (DF). These newly identified events were detected from 8 weeks of recordings on a high-density linear nodal geophone array operated by the University of Calgary between June and August 2022. Notably, these events were detected over this short period in an area where earthquakes had not previously been observed in the decades-long record of regional seismic networks. Using magnitude-frequency analysis and waveform similarity clustering, we estimated source parameters of the earthquakes to characterize seismic events in the area. We also compared the local results to the long-term regional distribution of earthquakes from similar analyses of data from permanent stations in the region.

Our results show that the eastern Denali fault is seismically quiescent near Burwash Landing. However, other portions of the Denali fault exhibit significant seismicity. We interpreted these observations as the presence of a seismic gap on the eastern Denali fault with potential for future earthquakes. Active deformation on strike-parallel faults is evidence of permeable structures that may enable warm fluid mobility in the subsurface and improve prospects for geothermal potential. In combination with geophysical knowledge from recent studies, the improved understanding of seismicity from this work highlights geological complexity at regional and local scales. This further underscores the significance of the region for geothermal resource potential and the need for natural hazard assessments.

Method and data

Deep-learning–based earthquake detection and phase picker

We used EQTransformer (EQT), a deep-learning model for detecting earthquakes and identifying their seismic phases from continuous waveform data (Mousavi

et al., 2020). This model combines a long short-term memory (LSTM) network with a deep convolutional neural network (CNN) architecture comprising 56 layers. The LSTM is useful in handling sequential data (specifically processing longer sequences). The deep CNN architecture in EQT uses convolutional layers coupled with max pooling, a common approach in deep-learning models to reduce the spatial dimensions of data while retaining important features. To address the potential degradation issues associated with deep CNNs, especially when strong downsampling is involved, EQT uses residual connections within the CNN. These connections help preserve information throughout the network, ensuring the integrity of the input data from beginning to end.

EQTransformer incorporates an attention mechanism, a feature that enhances the model's ability to extract core features by focusing on local aspects (e.g., individual seismic phases) and the overall context (e.g., an entire wave packet containing body and surface waves). This mechanism plays a crucial role in estimating probabilities in three key areas of the model: earthquake full waveform, P-wave phase and S-wave phase detection. The output from each of these areas is processed through a sigmoid layer, which produces a probability distribution on [0,1]. These probabilities are used as threshold values to classify input signals as earthquakes. For practical application, specific threshold values used in a previous study (Mousavi et al., 2020) were set for the detection of P-waves, S-waves and earthquakes at 0.3, 0.1 and 0.1, respectively.

The original model was trained on the STanford EArthquake Dataset (STEAD), which consists of approximately 1 000 000 records of local earthquakes and 300 000 noise signals (Mousavi et al., 2019). Generally, instead of starting learning from scratch, retraining based on an existing model can yield a training model optimized for the research area. In this study, we also conducted transfer learning using earthquake origin information and phase-picking data from Biegel et al. (2023), which led to the development of a model that is finely tuned for our research area near Burwash Landing. The model's comprehensive structure, with 372 000 parameters across its 56-layer network, highlights its complexity and capability in earthquake detection and phase identification.

Template-matching–based earthquake detection

In recent research, initial earthquake catalogues have been constructed through a deep learning–based approach, followed by detecting additional earthquakes based on the similarity of event waveforms (i.e., template-matching techniques; Chamberlain et al., 2018). The template-matching technique uses an event waveform as a template to search for similar waveforms in continuous data. This technique is effective for detecting earthquakes using continuous seismic data and a template waveform. It relies on the similarity of waveforms from different events recorded on the same seismograph, provided these events originate from nearby locations, have similar rupture mechanisms and share similar paths from their sources to the receivers. The advantage of template matching is its ability to detect earthquakes in noisy data, where traditional methods fail.

A significant drawback of the template-matching technique is computational cost, exacerbated by the increasing number of templates and the volume of continuous data that must be analyzed. Recent technical advancements, particularly in the use of graphics processing units (GPUs), have been instrumental in mitigating this issue, as pointed out by Beaucé et al. (2017). The use of GPUs enhanced the efficiency of the template-matching technique, enabling the detection of up to 20 times more events than traditional processing technologies while significantly reducing computation time. This is a considerable improvement in earthquake detection capability, particularly in identifying small-scale events that were previously undetectable with older methods. In this study, we used the match and locate method (Liu et al., 2020) to calculate waveform similarity within a GPU setting.

Estimation of earthquake source parameters

After detecting earthquakes, the initial locations are determined using HYPOELLIPSE (Lahr, 1999), a software program designed for earthquake location using 1D seismic velocity model. Central to this method is the calculation of seismic wave traveltimes, which depends on a 1D seismic velocity model. The program calculates earthquake locations by iteratively refining the estimated hypocentre location and origin

time using the arrival times of P-waves and S-waves recorded at multiple stations. HYPOELLIPSE uses least squares inversion to minimize the difference between observed and calculated arrival times, thereby optimizing the hypocentre estimate. In this study, we used a 1D velocity model presented in Fogleman et al. (1993). Following initial location, we relocated events with the double-difference method (Waldhauser and Ellsworth, 2000), which improves the accuracy of hypocentres for earthquakes that occur in proximity to each other. It compares differences in traveltimes and waveform similarities between pairs of earthquakes recorded by the same seismic station. By focusing on these relative time differences instead of absolute traveltimes, the method effectively minimizes the effects of heterogeneous velocity structures in the Earth's crust. Using the waveform similarities, the method groups the earthquakes based on cross-correlation coefficients (CC) between event pairs and uses this information during the iterations for locating hypocentres. This leads to more precise hypocentre locations, especially in regions with complex geological structures. Finally, we converted all waveforms to Wood-Anderson amplitudes (Uhrhammer and Collins, 1990), and estimated local magnitudes based on the equation suggested by Fogleman et al. (1993).

Data

We analyzed data from 34 temporary seismic stations (nodal geophones) that form two linear arrays crossing the Denali fault near Burwash Landing (Fig. 2) on transects that follow Burwash Creek and the Duke River. The stations operated from June 14 to August 22, 2022. The geophones have a natural frequency of 5 Hz, making them ideal for detecting local earthquakes of small magnitude. To investigate earthquakes at the regional scale, we used data from permanent International Federation of Digital Seismograph Network (FDSN) stations, accessed through Incorporated Research Institutions for Seismology (IRIS; see data and resources section). Regional earthquake data processing followed the same steps using the framework suggested by Han et al. (2023). All data were bandpass filtered to a range of 1–45 Hz. For the template matching and waveform similarity clustering analyses, which targeted the S-wave phase, a narrower bandpass filter range of 2–15 Hz was applied.

Results and discussion

Local seismicity near Burwash Landing

We studied an area near Burwash Landing, Yukon (Fig. 2). Notably, this is an area that has shown few earthquakes in the past 15 years, despite significant improvements in instrumentation coverage (Fig. 2). The earthquakes presented here were identified by applying the deep-learning model to geophone data, followed by detection of micro-earthquakes using template matching. All earthquakes detected by the deep-learning picker were used as template waveforms and applied as continuous waveforms to estimate CC. Following each earthquake detection, initial locations were determined using HYPOELLIPSE (Lahr, 1999), and then redetermined using HypoDD (Waldhauser and Ellsworth, 2000) using the estimated CCs. This process identified 103 earthquakes, ranging in magnitude from 0.6 to 3.1. We located 75 earthquakes within the study area (Fig. 3). Using magnitude-frequency analysis, the magnitude of completeness of the presented catalogue was determined to be 1.1, and the b-value was found to be 0.94 (Fig. 4), which is similar to global averages.

Although the short observation period limits the interpretation of earthquake trends from these data alone, we identified three spatially distinct groups (Fig. 3). Group 2 (Fig. 5) occurred near Burwash Landing and includes earthquakes close to, but not on, the Denali fault. These events are not reported by the United States Geological Survey (USGS) catalogue (see data and resources section for more details). Group 2a includes earthquakes related to the DRF. Group 2b includes events we interpreted to be on Bock's Creek fault (BCF), and on faults that appear to accommodate deformation connecting BCF to other faults previously inferred from digital elevation models (Witter, 2020) and lidar surveys (Finley et al., 2022). In the Group 2a area, fault plane solutions from catalogued earthquakes outside deployment time for our data have northwest strikes (Doser, 2014; Gosselin et al., 2023) and reverse fault motion; however, the DRF is a southwest-dipping thrust fault, and the observed earthquakes appear on the footwall, suggesting that they may occur in an unmapped fault developing between the DRF and DF, similar to the BCF.
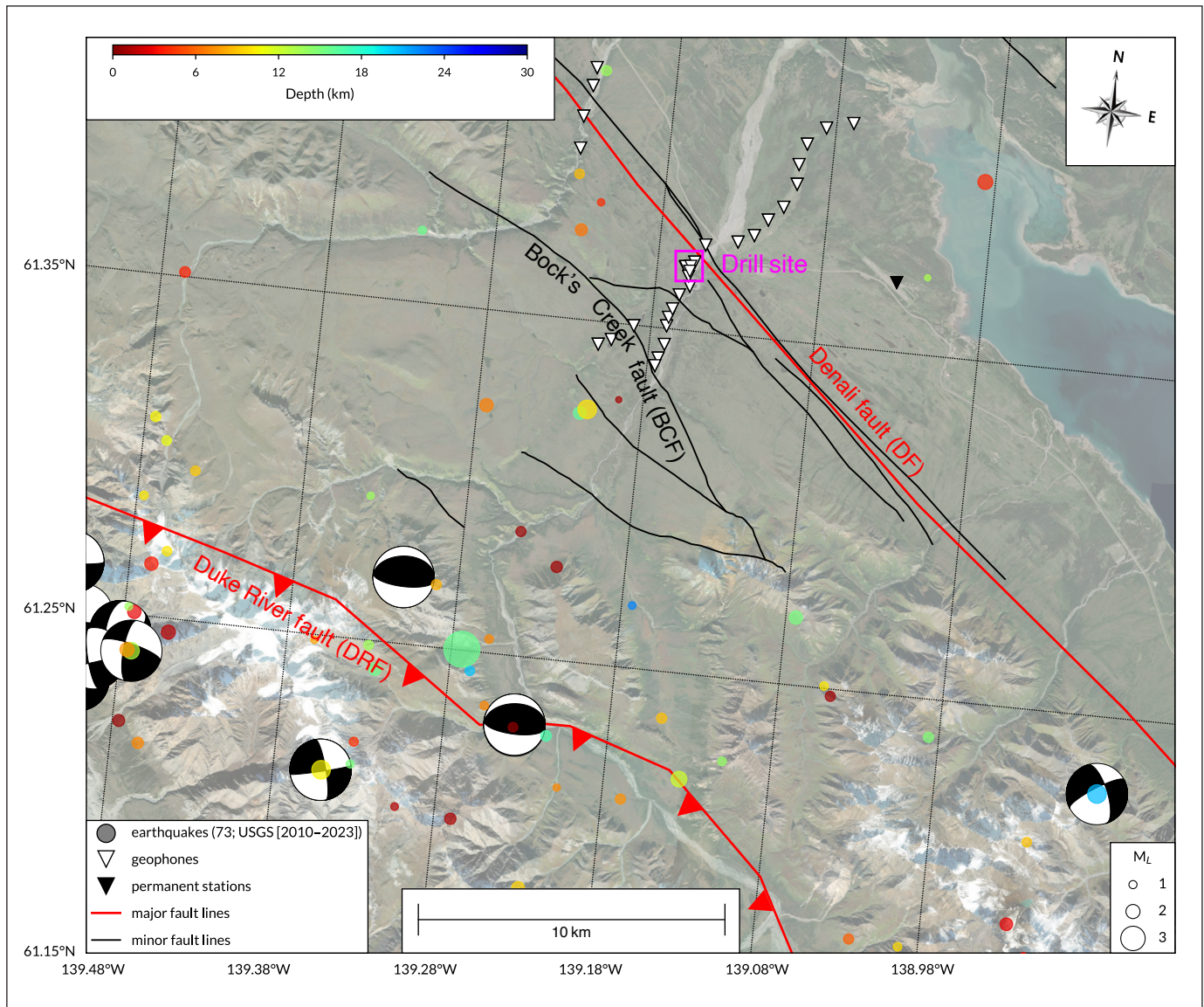
Figure 2. Distribution of geophone array stations (white triangles) and earthquakes reported by the United States Geological Survey between 2010 and 2023 within the study area. Note the absence of earthquakes along the Denali fault (DF). A small number of earthquakes were observed near Bock's Creek fault (BCF). M_L: Richter local magnitude of earthquakes observed. The drill site marks the location of an approximately 200 m deep exploratory well installed by the Yukon Geological Survey. The focal mechanisms for earthquakes contained in the USGS catalogue are also shown.

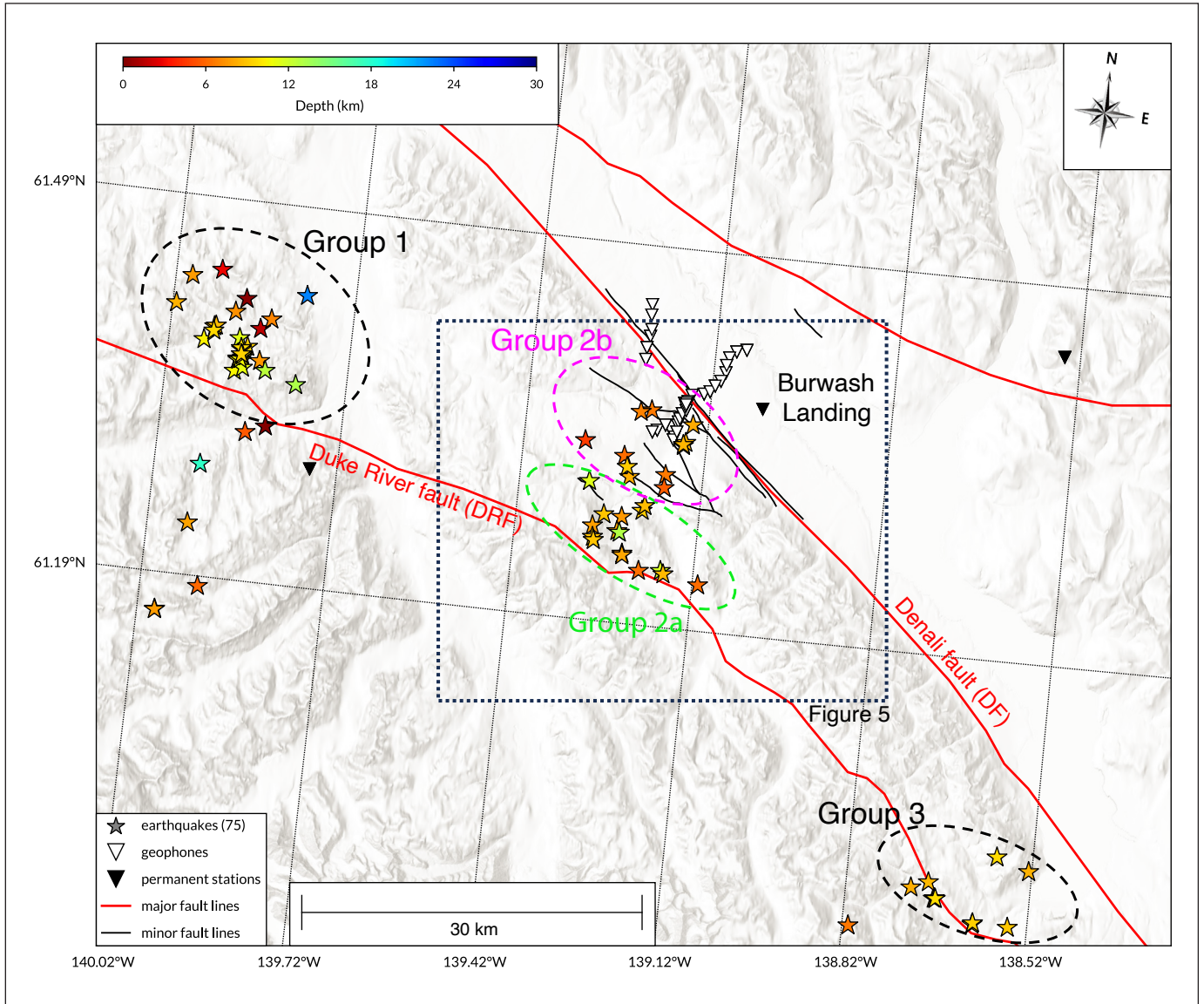**Figure 3.** *Earthquakes (stars) detected in the study area as part of this study. Colours of stars indicate earthquake depths. Seismicity clusters in three groups are highlighted by ellipses. The dashed rectangle outlines the area presented in further detail in Figure 5.*
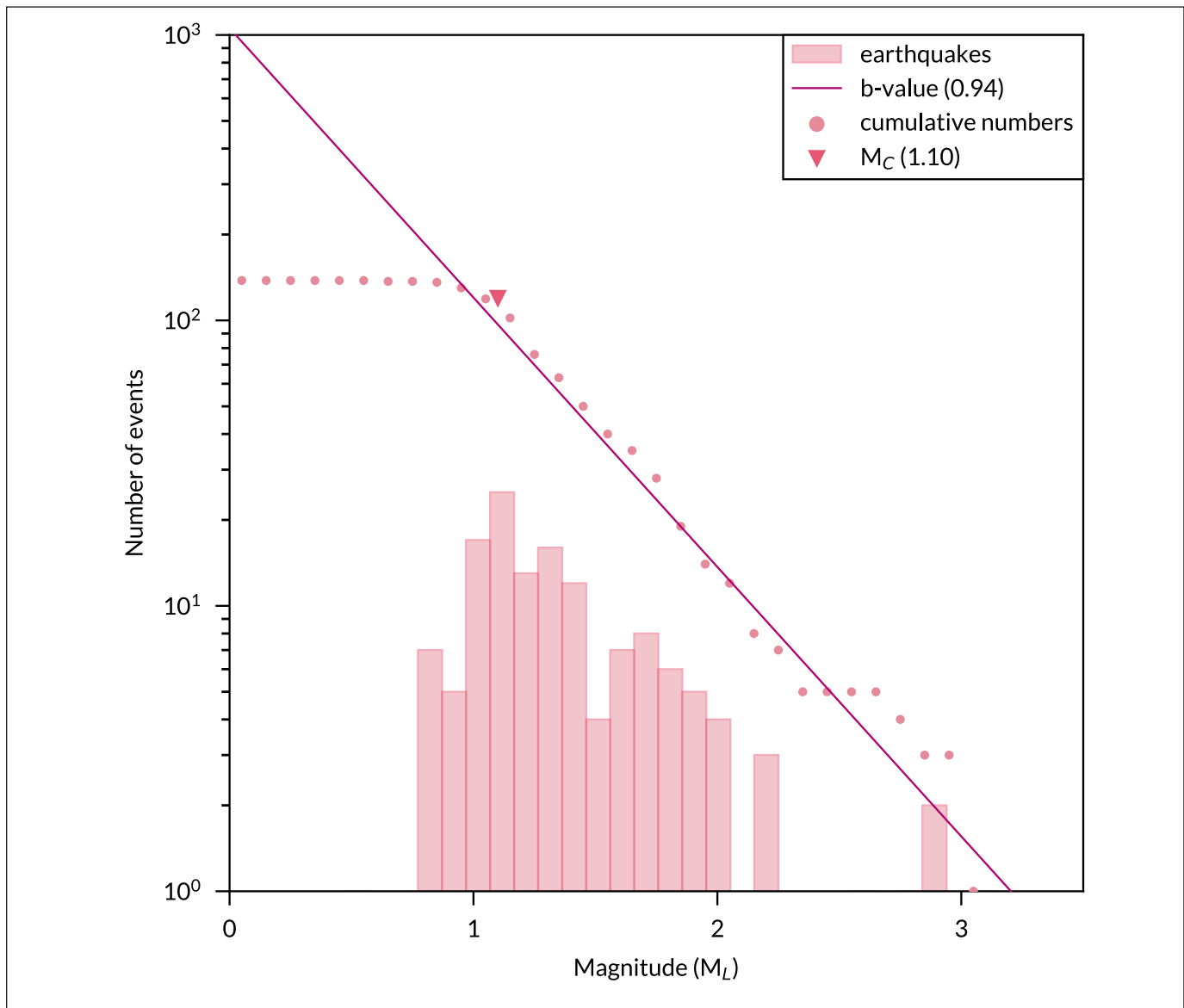
Figure 4. *Gutenberg-Richter analysis of the local earthquake catalogue showing a power-law distribution of earthquake frequency with magnitude (M_L) that is typical of global active tectonic settings. The magnitude of completeness (M_C) value is also shown.*

To cluster these earthquakes, an event dendrogram was determined by analyzing waveform similarity using station 32 from the temporal seismic array, which provided the most phase information among the detected results (Fig. 6). The earthquake clusters were divided into eight groups (C1–C8). Waveform-similarity–based analysis identified earthquake clusters C3 and C4, which are related to Group 2b (Fig. 7). Cluster C4 is distributed closer to the geophone array compared to C3, with differing waveform characteristics (Fig. 7). The C3 events are located to the southwest of the seismic network, suggesting a

possible origin from a minor fault between strands of BCF (Fig. 7). The two events of C3 may be located on the same portion of BCF or, alternatively, come from an unmapped fault connecting these fault strands (Fig. 7). This possible unmapped fault may be related to those previously identified by the inversion of three passive electromagnetic datasets (Tschirhart et al., 2022). Although the precision of our interpretations is limited by the scarcity of data and the aperture of the seismic network, this study confirms active deformation, with earthquakes occurring on smaller fault structures in the area. The absence of microearthquakes on the Denali

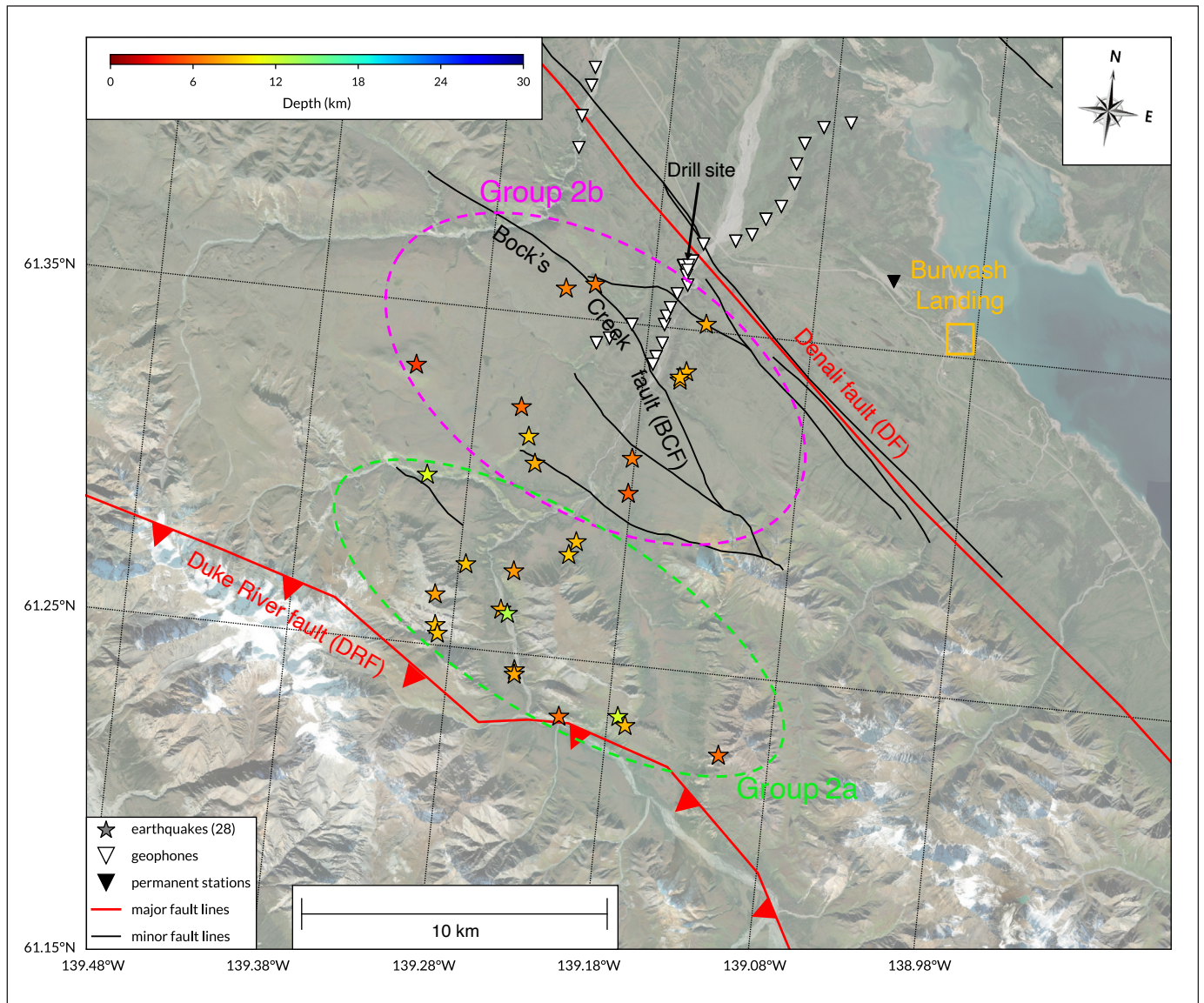**Figure 5**. *Detailed view of earthquakes near Burwash Landing, Yukon. Group 2a occurs on the footwall of the Duke River fault (DRF), and may have originated from an unmapped fault between the DRF and the Denali fault (DF). Group 2b is of particular interest because it includes 13 earthquakes consistent with recently mapped faults, the Bock's Creek fault (BCF) and other related fault structures (Witter, 2020; Finley et al., 2022).*
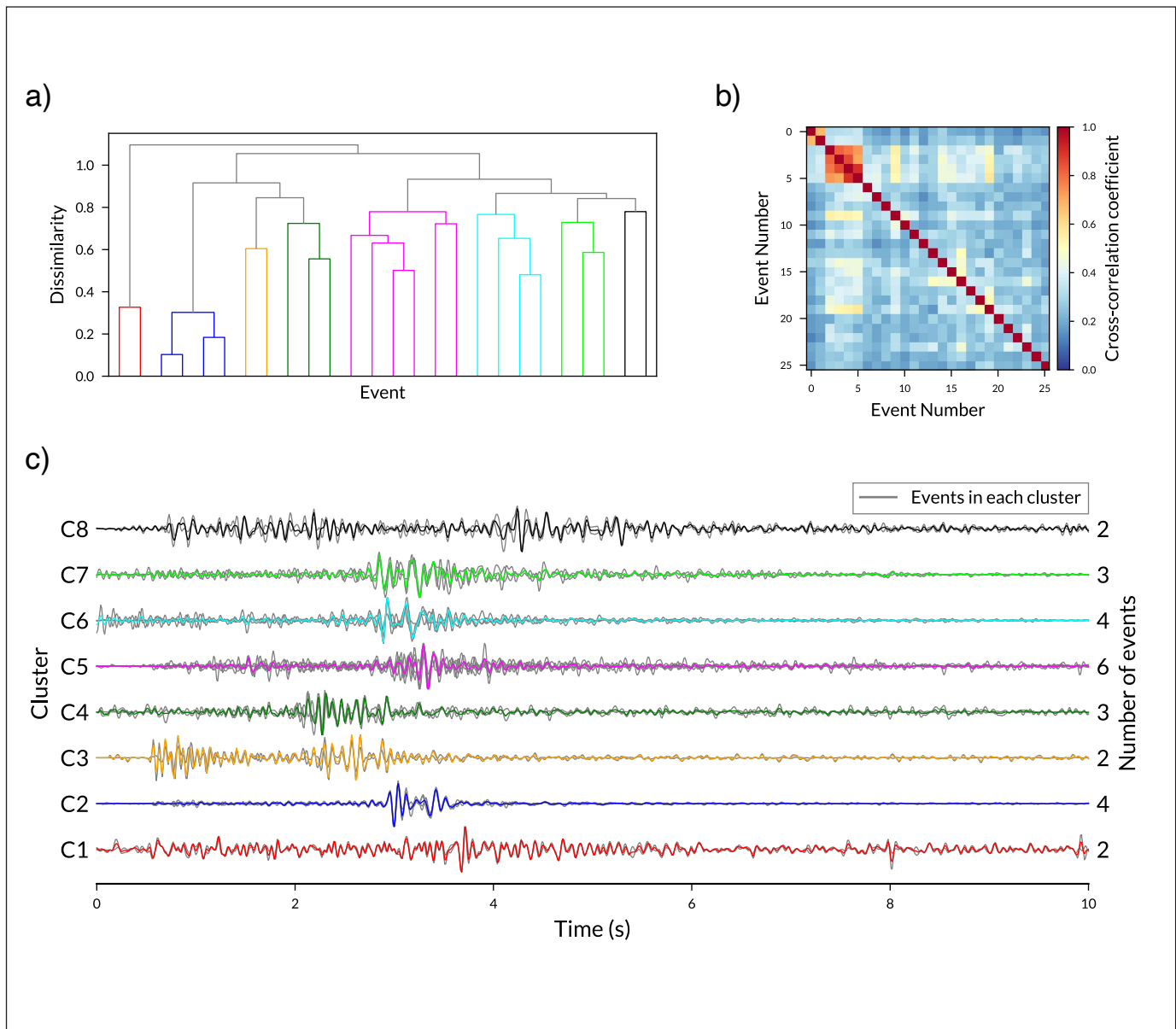
Figure 6. *Analysis of waveform similarity for the earthquake events shown in Figure 5:* ***a)*** *dendrogram of earthquakes based on waveform similarity;* ***b)*** *cross-correlation coefficient matrix between event pairs;* ***c)*** *individual (grey lines) and stacked (coloured lines) waveforms of clustered earthquakes.*

fault is peculiar and provides evidence of a seismic gap, considering that regional networks have also not detected earthquakes in this location.

Regional seismicity

We also present an extended catalogue of more than 40 000 earthquakes at the regional scale, based on continuous seismic data of permanent stations, that significantly extends the USGS catalogue (see data and resources section for more details). Detection and

phase picking were conducted in the same manner as previously discussed (Han *et al.*, 2023). Phase association was calculated using a Bayesian-Gaussian mixture model (Zhu *et al.*, 2022). The results show 46 432 regional earthquakes between 2010 and 2023 (Fig. 1). A detailed interpretation of this catalogue is not the focus of this report. Broadly speaking, the distribution of these earthquakes supports the interpretation proposed by Biegel *et al.* (2023) and identifies linear structures not previously reported. Most important to this study is the observed lack of
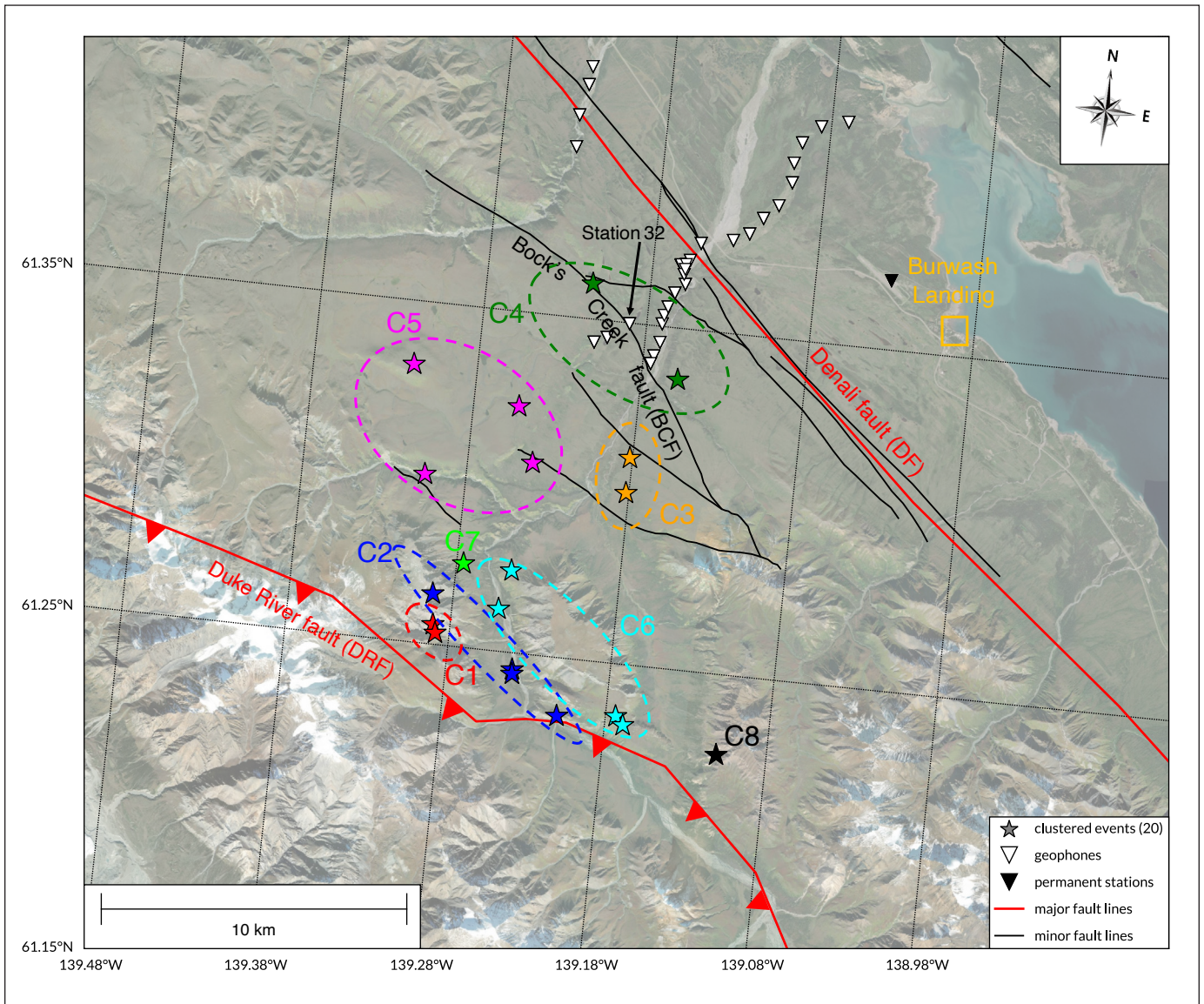
Figure 7 Map of clustered events in Figure 6. The events in each cluster (C1–C8) exhibit highly similar waveforms suggesting that these earthquakes occur on the same structures.

seismicity in the vicinity of the DFZ in a 50–100 km long fault section near Burwash Landing, which may present a seismic gap with increased potential for future earthquakes.

A second observation of interest is located farther northwest (Fig. 1). Here, a distinct linear trend parallel to the Denali fault is observed that was not previously reported (L1 in Fig. 1). The newly interpreted parallel fault segment southwest of the main Denali fault appears to connect to the DRF zone as discussed in Gosselin et al. (2023).

Conclusion

This paper presents a detailed seismic analysis of southwestern Yukon, highlighting the seismicity near Burwash Landing. Using a combination of data collected from temporary seismic stations operated during summer 2022 and long-term data from permanent stations, we offer new insights into the seismicity of this geologically complex region. Key findings include the identification of 46 432 regional earthquakes from a decade-long period and 103 local earthquakes from a three-month period. The study effectively used advanced seismic detection techniques

such as deep-learning–based earthquake detection and template matching to enhance earthquake catalogue completeness and accuracy. The application of HYPOELLIPSE and HypoDD provided refined hypocentre locations and magnitude estimations, contributing to a more comprehensive understanding of the seismic behaviour in the area. Regionally, we have identified new linear seismic structures and added to the existing knowledge of the tectonic framework through this study. While the study had limitations, such as the short observation period and small aperture of the temporary array, the research significantly advances our understanding of the seismicity and tectonic processes near the eastern Denali fault and Burwash Landing area. Specifically, we observed no seismicity associated with the eastern Denali fault, which we interpreted as a seismic gap. Additionally, we observed that active deformation occurs on strike-parallel fault structures which may increase rock permeability. These observations highlight the significance of the region in terms of both geothermal resource potential and the need for natural hazard assessments.

Data and resources

Seismograms from permanent stations used in this study were collected from the Incorporated Research Institutions for Seismology Data Management Centre (IRIS, 2023). The earthquake catalogue used is published by the United States Geological Survey (USGS, 2023). All maps were obtained from ArcGIS REST API services (ArcGIS, 2023). The local and regional earthquake catalogues, including local magnitudes for the local catalogue, are available as a data supplement to this paper in comma-separated values format.

Acknowledgments

References

ArcGIS (2023): ArcGIS REST services directory. Version 10.91. https://server.arcgisonline.com/arcgis/rest [accessed December 2023].

Beaucé, E., Frank, W.B. and Romanenko, A., 2017. Fast matched filter (FMF): An efficient seismic matched-filter search for both CPU and GPU architectures. Seismological Research Letters, vol. 89, no. 1, p. 165–172. https://doi.org/10.1785/0220170181

Biegel, K., Gosselin, J. and Dettmer, J., 2023. Preliminary double-difference relocation earthquake catalogue for southwestern Yukon centred along the Denali fault zone. *In*: Yukon Exploration and Geology 2022, K.E. MacFarlane (ed.), Yukon Geological Survey, p. 1–18, plus digital appendices.

Chamberlain, C.J., Hopp, C.J., Boese, C.M., Warren-Smith, E., Chambers, D., Chu, S.X., Michailos, K. and Townend, J., 2018. EQcorrscan: Repeating and near-repeating earthquake detection and analysis in Python. Seismological Research Letters, vol. 89, no. 1, p. 173–181. https://doi.org/10.1785/0220170151

Choi, M., Eaton, D.W. and Enkelmann, E., 2021. Is the eastern Denali fault still active? Geology, vol. 49, no. 6, p. 662–666. https://doi.org/10.1130/G48461.1

Colpron, M., 2019. Potential radiogenic heat production from granitoid plutons in Yukon. Yukon Geological Survey, Open File 2019-16, 1 map and data.

Doser, D.I., 2014. Seismicity of southwestern Yukon, Canada, and its relation to slip transfer between the Fairweather and Denali fault systems. Tectonophysics, vol. 611, p. 121–129. https://doi.org/10.1016/j.tecto.2013.11.018

Eberhart-Phillips, D., Haeussler, P.J., Freymueller, J.T., Frankel, A.D., Rubin, C.M., Craw, P., Ratchkovski, N.A., Anderson, G., Carver, G.A. and Crone, A.J., 2003. The 2002 Denali fault earthquake, Alaska: A large magnitude, slip-partitioned event. Science, vol. 300, p. 1113–1118. https://doi.org/10.1126/science.1082703

Elliott, J.L., Larsen, C.F., Freymueller, J.T. and Motyka, R.J., 2010. Tectonic block motion and glacial isostatic adjustment in southeast Alaska and adjacent Canada constrained by GPS measurements. Journal of Geophysical Research: Solid Earth, vol. 115, no. B9, article B09407, 21 p. https://doi.org/10.1029/2009JB007139

Finley, T., Salomon, G., Stephen, R., Nissen, E., Cassidy, J. and Menounos, B., 2022. Preliminary results and structural interpretations from drone lidar surveys over the Eastern Denali fault, Yukon. *In*: Yukon Exploration and Geology 2021, K.E. MacFarlane (ed.), Yukon Geological Survey, p. 83–105.

Fletcher, H.J. and Freymueller, J.T., 2003. New constraints on the motion of the Fairweather fault, Alaska, from GPS observations. Geophysical Research Letters, vol. 30, no. 3, article 1139, 4 p. https://doi.org/10.1029/2002GL016476

Fogleman, K.A., Lahr, J.C., Stephens, C.D. and Page, R.A., 1993. Earthquake locations determined by the southern Alaska seismograph network for October 1971 through May 1989: United States Geological Survey, Open-File Report 93–309, 54 p. https://doi.org/10.3133/ofr93309

Gosselin, J.M., Biegel, K., Hamidbeygi, M. and Dettmer, J., 2023. Improvements in the regional earthquake focal mechanism catalogue for southwestern Yukon. *In*: Yukon Exploration and Geology 2022, K.E. MacFarlane (ed.), Yukon Geological Survey, p. 63–76 plus digital appendices.

Grantz, A., 1966. Strike-slip faults in Alaska: United States Geological Survey, Open-File Report 66–53, 82 p. https://doi.org/10.3133/ofr6653

Han, J., Seo, K.J., Kim, S., Sheen, D.-H., Lee, D. and Byun, A.-H., 2023. Research catalog of inland seismicity in the southern Korean Peninsula from 2012 to 2021 using deep learning techniques. Seismological Research Letters. https://doi.org/10.1785/0220230246

IRIS, 2023: Incorporated Research Institutions for Seismology Data Management Centre. https://www.iris.edu [accessed October 2023].

Lahr, J.C., 1999. HYPOELLIPSE: A computer program for determining local earthquake hypocentral parameters, magnitude, and first-motion pattern: United States Geological Survey, Open-File Report 99–23, version 1.1, 119 p. and software. https://pubs.usgs.gov/of/1999/ofr-99-0023/

Lanphere, M.A., 1978. Displacement history of the Denali fault system, Alaska and Canada. Canadian Journal of Earth Sciences, vol. 15, no. 5, p. 817–822. https://doi.org/10.1139/e78-086

Leonard, L.J., Hyndman, R.D., Mazzotti, S., Nykolaishen, L., Schmidt, M. and Hippchen, S., 2007. Current deformation in the northern Canadian Cordillera inferred from GPS measurements. Journal of Geophysical Research: Solid Earth, vol. 112, no. B11, article B11401, 15 p. https://doi.org/10.1029/2007JB005061

Li, C.-F., Lu, Y. and Wang, J., 2017. A global reference model of Curie-point depths based on EMAG2. Scientific Reports, vol. 7, article 45129. https://doi.org/10.1038/srep45129

Liu, M., Li, H., Zhang, M. and Wang, T., 2020. Graphics processing unit-based match and locate (GPU-M&L): An improved match and locate method and its application. Seismological Research Letters, vol. 91, no. 2A, p. 1019–1029. https://doi.org/10.1785/0220190241

Lowey, G.W., 1998. A new estimate of the amount of displacement on the Denali fault system based on the occurrence of carbonate megaboulders in the Dezadeash Formation (Jura-Cretaceous), Yukon, and the Nutzotin Mountains sequence (Jura-Cretaceous), Alaska. Bulletin of Canadian Petroleum Geology, vol. 46, no. 3, p. 379–386.

Majorowicz, J. and Grasby, S.E., 2014. Geothermal energy for northern Canada: Is it economical? Natural Resources Research, vol. 23, no. 1, p. 159–173. https://doi.org/10.1007/s11053-013-9199-3

Meighan, L.N., Cassidy, J.F., Mazzotti, S. and Pavlis, G.L., 2013. Microseismicity and tectonics of southwest Yukon Territory, Canada, using a local dense seismic array. Bulletin of the Seismological Society of America, vol. 103, no. 6, p. 3341–3346. https://doi.org/10.1785/0120130068

Mousavi, S.M., Ellsworth, W.L., Zhu, W., Chuang, L.Y. and Beroza, G.C., 2020. Earthquake transformer—an attentive deep-learning model for simultaneous earthquake detection and phase picking. Nature Communications, vol. 11, article 3952. https://doi.org/10.1038/s41467-020-17591-w

Mousavi, S.M., Sheng, Y., Zhu, W. and Beroza, G.C., 2019. Stanford Earthquake Dataset (STEAD): A global data set of seismic signals for AI. IEEE access. https://doi.org/10.1109/ACCESS.2019.2947848

Plafker, G., Hudson, T., Bruns, T. and Rubin, M., 1978. Late Quaternary offsets along the Fairweather fault and crustal plate interactions in southern Alaska. Canadian Journal of Earth Sciences, vol. 15, no. 5, p. 805–816. https://doi.org/10.1139/e78-085

Ruppert, N.A. and West, M.E., 2020. The impact of USArray on earthquake monitoring in Alaska. Seismological Research Letters, vol. 91, no. 2A, p. 601–610. https://doi.org/10.1785/0220190227

Tschirhart, V., Colpron, M., Craven, J., Ghalati, F.H., Enkin, R.J. and Grasby, S.E., 2022. Geothermal exploration in the Burwash Landing region, Canada, using three-dimensional inversion of passive electromagnetic data. Remote Sensing, vol. 14, no. 23, article 5963. https://doi.org/10.3390/rs14235963

Uhrhammer, R.A. and Collins, E.R., 1990. Synthesis of Wood-Anderson seismograms from broadband digital records. Bulletin of the Seismological Society of America, vol. 80, no. 3, p. 702–716.

USGS, 2023: Earthquake catalog. Earthquake Hazards Program. USGS. https://earthquake.usgs.gov/earthquakes/search/ [accessed November 2023].

Waldhauser, F. and Ellsworth, W.L., 2000. A double-difference earthquake location algorithm: Method and application to the northern Hayward fault, California. Bulletin of the Seismological Society of America, vol. 90, no. 6, p. 1353–1368. https://doi.org/10.1785/0120000006

Waldien, T., Roeske, S. and Benowitz, J., 2021. Tectonic underplating and dismemberment of the Maclaren-Kluane schist records Late Cretaceous terrane accretion polarity and ~480 km of post-52 Ma dextral displacement on the Denali fault. Tectonics, vol. 40, no. 10, article e2020TC006677. https://doi.org/10.1029/2020TC006677

Witter, J.B., 2020. Early-stage exploration for geothermal energy resources along the Denali fault near Duke River, Yukon. Yukon Geological Survey, Open File 2020-3, 62 p.

Witter, J.B., Miller, C.A., Friend, M. and Colpron, M., 2018. Curie point depths and heat production in Yukon, Canada. *In:* Proceedings, 43rd Workshop on Geothermal Reservoir Engineering, Stanford University, Standford, California, February 12-14, 2018 SGP-TR-213, p. 12–14.

Zhu, W., McBrearty, I.W., Mousavi, S.M., Ellsworth, W.L. and Beroza, G.C., 2022. Earthquake phase association using a Bayesian Gaussian mixture model. Journal of Geophysical Research: Solid Earth, vol. 127, no. 5, article e2021JB023249. https://doi.org/10.1029/2021JB023249

Surficial geochemical data extracted from assessment reports: Development and initial release of the database

Yury Klyukin*
Yukon Geological Survey

Abstract

The Yukon archive of assessment reports contains a significant amount of data; however, accessing these data is challenging due to the absence of a centralized storage system. This paper introduces the Geochemical Assessment Report Data Extracted database (GARDEd), which is specifically designed to store these data. Initially, GARDEd was constructed using data from assessment reports from a 75 km radius of the Casino deposit in the Yukon, but this spatial limit was subsequently removed. The initial release of the database contains geochemical data describing more than 300 000 surficial samples from more than 300 assessment reports submitted after 2004.

The structure of GARDEd follows the data model developed by the British Columbia Geological Survey for storing surficial geochemical sample data acquired from their assessment reports. This paper outlines the structure of the database and discusses the workflow for extracting the data. The paper also describes a custom Python tool developed to automate data extraction from digital assessment reports.

Introduction

The Yukon Geological Survey (YGS) stores a significant amount of geological information gathered by exploration companies in compliance with the Quartz Mining Act. This information is primarily contained in assessment reports (AR). Since 1920 (Fig. 1), more than 8000 hardrock assessment reports have been collected, with more than 6000 of these containing geochemical data on surficial samples (e.g., soil, rock, stream sediment, and vegetation). The sheer volume and historical depth of these data provide valuable insight into the mineral potential of the Yukon.

Exploration companies rely on data from ARs to search for exploration targets. Furthermore, regional and local studies such as those conducted by Grunsky and Caritat (2020) and Wang and Zuo (2022) rely on

similar datasets to test and develop models to identify geochemical anomalies in their areas of interest. To aid exploration companies, YGS has initiated the development of a database that will consolidate geochemical data extracted from assessment reports.

The primary objective of this paper is to introduce the Geochemical Assessment Report Data Extracted database (GARDEd), which was created by extracting and compiling data from more than 300 assessment reports (Fig. 1). This paper details the structure of GARDEd and provides instructions for accessing the database when it is released in early 2024. The paper also introduces a toolset that was used to extract data from the reports. The toolset is still in development but is available upon request from geology@yukon.ca.
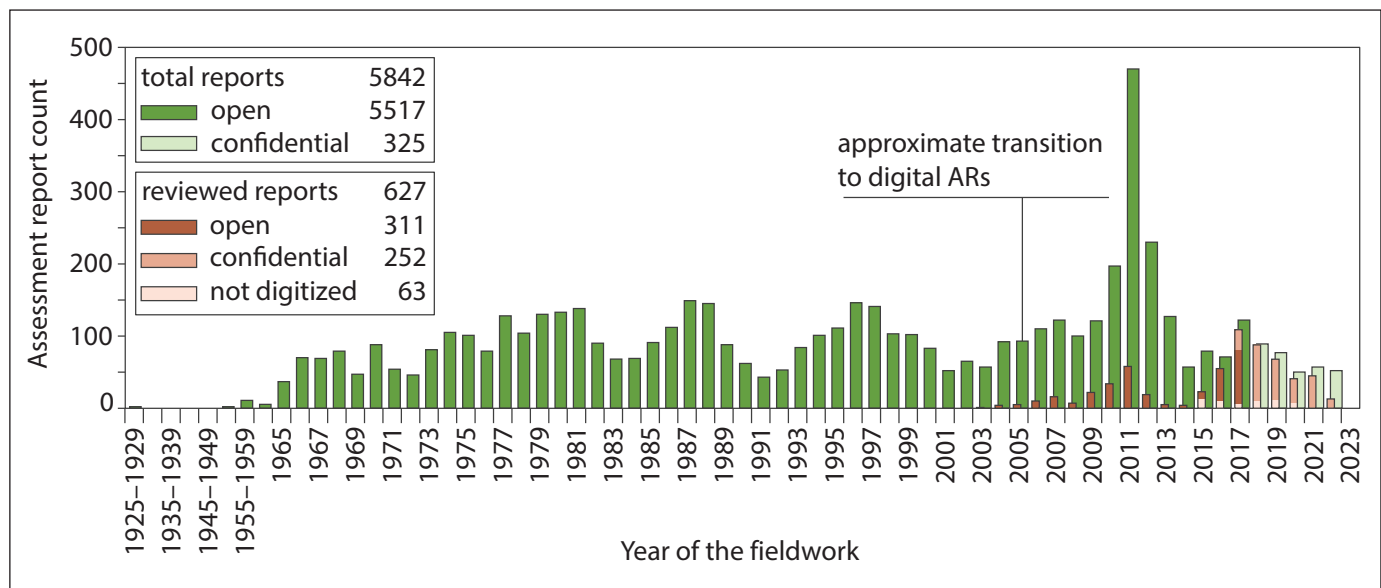
* yury.klyukin@yukon.ca

Figure 1. *Histogram showing the number of assessment reports (AR) that contain surficial geochemical data, plotted against the year of submission. The bin size for ARs between 1925 and 1964 is 5 years, while the rest have a bin size of 1 year. Prior to 2005, most reports are scanned copies. After 2005, reports began to be submitted in electronic formats, which has facilitated data extraction efforts.*

Database structure

The structure of GARDEd is based on the work of Han et al. (2019) and Norris and Fortin (2019), who developed a data model for storing surficial geochemical sample data from assessment reports submitted to the British Columbia Geological Survey. The database described in this document closely follows the original data model by Norris and Fortin (2019), with minor modifications, which are outlined below. GARDEd is released as a Geopackage, an open standard for storing geospatial data in the SQLite file format.

GARDEd consists of tables with the prefixes "code_" and "data_". The tables with the data_ prefix store sample data and assay certificates, whereas the tables with the code_ prefix store metadata about analytical techniques and assay certificates (Fig. 2). Detailed descriptions of all fields are provided in the GARDEd manual, which will be included in the release of the database in early 2024.

The data_sample table is a central table in the database. It stores information about the sample type, description, original coordinates, and additional metadata as described in the assessment report. A notable modification made to Norris and Fortin's (2019) database model is the direct storage of the coordinates,

which have been converted to decimal degrees (WGS 84) in the data_sample table. This differs from the dynamically generated table described in Norris and Fortin (2019). The converted coordinates are stored in two formats: as a Geopackage point geometry column, and as separate latitude and longitude fields (Fig. 2). The data_source_info table contains details on how the data were captured from the assessment reports. Analytical data are stored in the data_analyte table, whereas metadata extracted from assay certificates are stored in the data_cert table.

Tables with the code_ prefix store details on how samples were analyzed. The code_lab table records the names and acronyms of laboratories. The code_method table stores analytical method details described in assay certificates. The code_prep table reports on the sample preparation techniques used during the analytical process. The unit associated with each analytical result is stored as a text value in the unit_id field. In cases where assessment reports did not specify units, the units have been inferred by the author of this paper. In the Geopackage, these units are marked with the 'infer_' prefix.

The initial release of GARDEd is further complemented by the inclusion of comma-separated value (CSV) files, which can be used directly in GIS software. These files
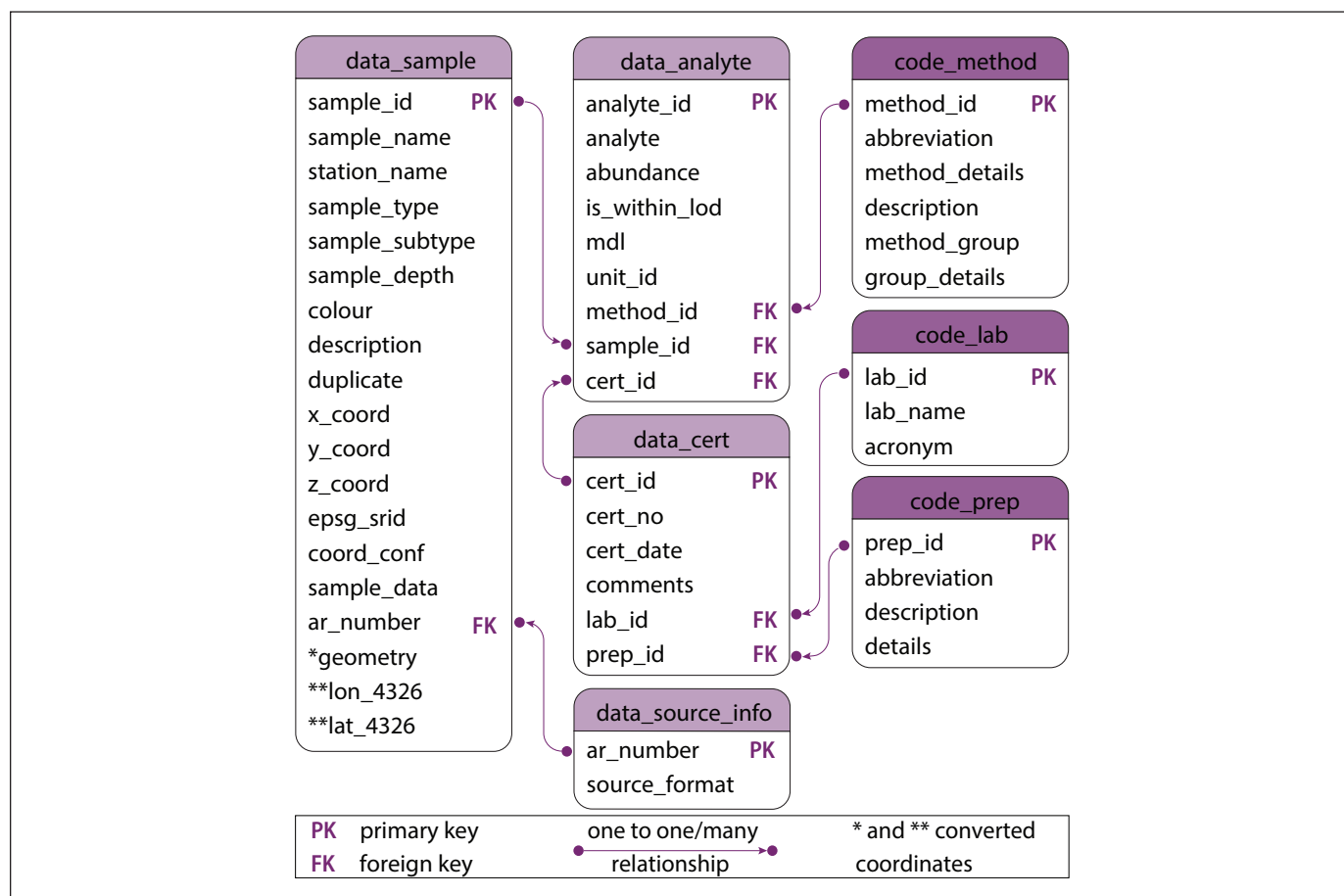
Figure 2. *Entity-relationship diagram of the Geopackage instance of GARDEd, adapted from Norris and Fortin (2019). Fields in data_sample table marked by an asterisk (*) contain longitude and latitude for sample locations converted to WGS84 (EPSG 4326) from those originally reported in assessment reports, compliant with the Geopackage specification for geospatial fields. The fields marked by two asterisks (**) are longitude and latitude stored in separate columns, facilitating their use in GIS software.*

provide a simplified, flat table version of the database, with certain data modified or removed compared to the Geopackage. For example, the CSV tables do not contain the original sample location coordinates and have element concentrations and units changed to match those specified in Table 1. In cases where abundance is reported as oxide concentrations, the measurements were recalculated into elemental concentrations. These modifications eliminate the need for an extra column to accommodate the same element reported in an oxide form or with a different unit, minimizing the width of the flat table by storing each measured element in a single column. This, however, may introduce data errors, especially in cases where the analytical unit was not explicitly stated in the assessment report and had to be inferred.

Table 1. *Standard units used to store analytical results within CSV flat tables. The originally reported analytical values and units are stored in the Geopackage version of GARDEd. Conversion to standardized units simplifies mapping of data from multiple sources; however, it may introduce errors if the original unit was incorrectly inferred during data extraction in reports that did not explicitly specify units.*

Unit	Elements
%	Al, Ca, Fe, K, Mg, Mn, Na, P, S, Si, Ti, TC (total carbon), TS (total sulfur), LOI (loss on ignition)
ppb	Au
ppm	Ag, As, B, Ba, Be, Bi, Br, Cd, Ce, Cl, Co, Cr, Cs, Cu, Dy, Er, Eu, Ga, Gd, Ge, Hf, Hg, Ho, In, Ir, La, Li, Lu, Mo, Nb, Nd, Ni, Pb, Pd, Pr, Pt, Rb, Re, Rh, Sb, Sc, Se, Sm, Sn, Sr, Ta, Tb, Te, Th, Tl, Tm, U, V, W, Y, Yb, Zn, Zr

The Geopackage GARDEd retains data as in the original assessment report and includes a view (a virtual table based on the result-set of a SQL query) named "wide_table" that can be used to generate CSV exports.

Database coverage

GARDEd was initially populated with data from samples within a 75 km radius of the Casino deposit to evaluate the data extraction procedures and assess the feasibility of the database. Data capture focused on recent ARs because these were available in a digital format. In general, ARs filed before 2005 were submitted in hard copy and subsequently scanned to PDF, so the digital file required optical character recognition (OCR), which posed data capture challenges. Once the initial test was completed and the Casino-area digital data were captured, efforts shifted to expanding sample coverage across the entire territory, while maintaining focus on digital data from relatively recent reports. The current release includes surficial geochemical data from 311 digital AR files, which taken together, is a dataset of 307 311 samples (Fig. 3). Most of the samples are located in the Dawson Range area. This concentration resulted from the initial focus on the 75 km radius around the Casino deposit, coupled with significant exploration work in the region between 2005 and 2018.

Data extraction and processing

Submitted assessment reports are stored in PDF format and may include spatial sample data and/or assay certificates as appendices in separate digital files of varying formats, making the data easily accessible; this is more common with newer reports. Reports created between the late 2000s and mid-2010s typically consist of a single PDF with all the data included in appendices within the report. Reports submitted prior to 2005 are almost always scans of hard copy reports; the quality of the scans generally decreasing in older reports. Extracting data from scanned reports requires more effort. The document must undergo OCR and the results must be reviewed before further processing is possible, and prior to adding it to the GARDEd database. Only a few scanned reports were included in the database to evaluate the required workload. As a result, the author focused on data capture from digital tables in newer ARs because these data could be captured relatively quickly and with fewer errors.

The author developed a custom tool to assist with data extraction and review. The tool is written in Python and is designed to capture tabulated data from custom tables and assay certificates generated by the laboratories. The tool heavily relies on libraries that can manipulate PDF, CSV and Microsoft Excel files; operate and analyze tables and interact with SQLite databases; and work with spatial data and operate with different coordinate systems to create dynamic maps. The tool expedites data extraction and applies quality assurance/quality control procedures to the extracted data. It automatically corrects minor inaccuracies (strips extra spaces in descriptive fields), creates dynamic sample maps showing the AR footprint overlain with the sample results that have been included or skipped in the geochemical data, and flags suspected errors for manual review.

Next steps

It is anticipated that GARDEd will be released in early 2024. It will be accessible under the Spatial Data and Compilations section of Yukon Geological Survey's Integrated Data System, available at https://data.geology.gov.yk.ca. The YGS encourages users to send the feedback to geology@yukon.ca to assess the usefulness of the dataset and determine how much effort should be invested to capture older, non-digital ARs.

Confidential assessment reports submitted to YGS have already had their data extracted. These data will be added to future releases of GARDEd following the expiration of the confidentiality period. The YGS encourages the inclusion of digital data with future AR submissions to streamline the integration of surficial geochemistry data into GARDEd.

Summary

This paper presents the development and upcoming release of the Geochemical Assessment Report Data Extracted Database (GARDEd), which contains geochemical data extracted from ARs based in the Yukon. The paper outlines the database structure and provides a snapshot of the data captured to date.

Although the initial release of GARDEd only contains approximately 10% of the geochemical data from
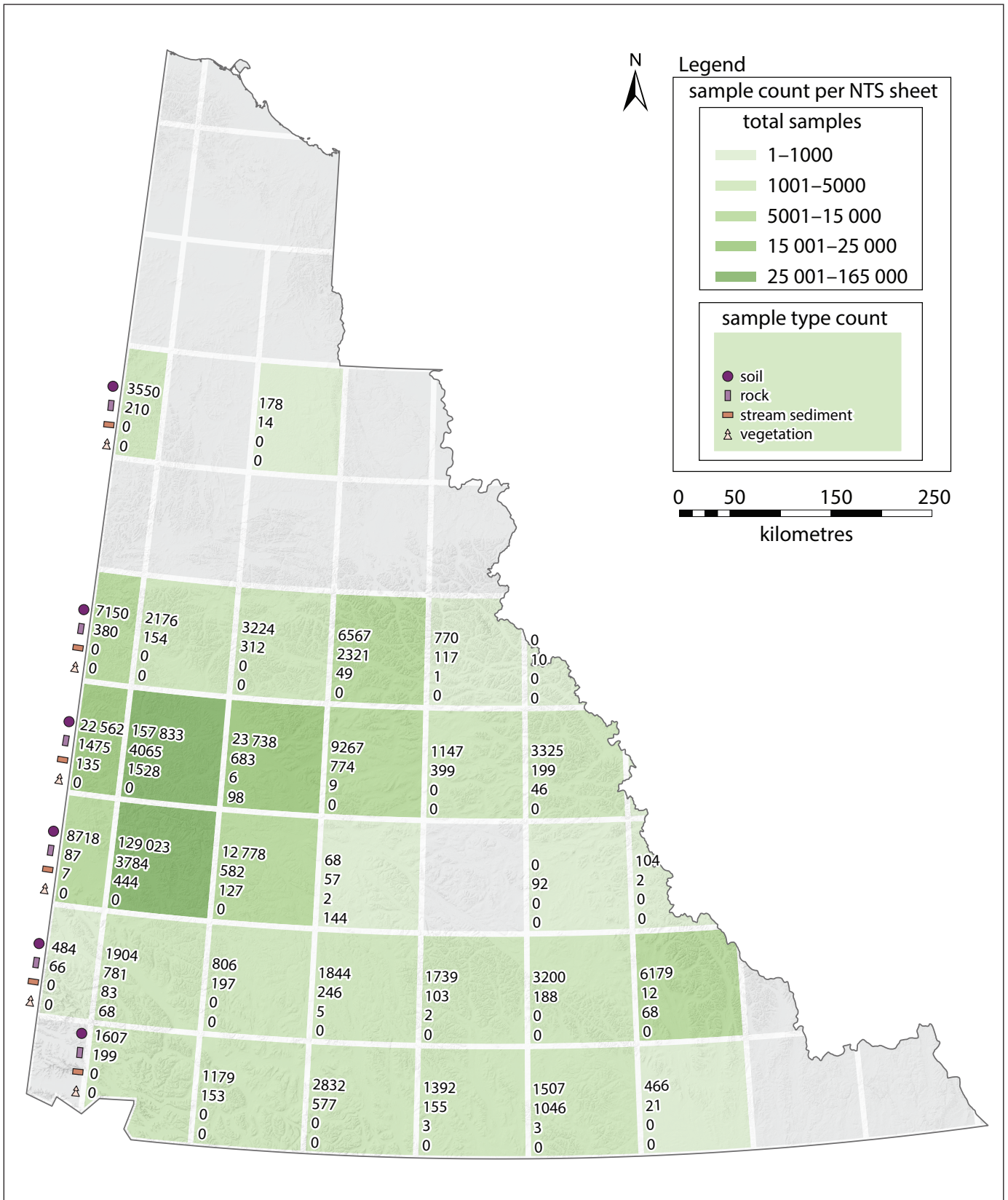
Figure 3. Count of extracted samples per NTS map sheet. The colour gradation applies to total count of samples. Labels within each NTS map sheet indicate the count for each sample type: soil, rock, stream sediment and vegetation.

surface samples within Yukon ARs, it serves as a valuable resource for researchers and exploration companies interested in the mineral potential of the Yukon. It provides centralized, standardized and internally consistent geochemical data for analysis and modelling. These data offer users valuable information for mineral exploration programs, allowing them to design custom maps and test different approaches to identify geochemical anomalies linked with known or potential mineralization. GARDEd is an evolving product that will be updated regularly with new data. Users are encouraged to provide feedback on their experience.

Acknowledgments

References

Grunsky, E.C. and de Caritat, P., 2020. State-of-the-art analysis of geochemical data for mineral exploration. Geochemistry: Exploration, Environment, Analysis, vol. 20, no. 2, p. 217–232. https://doi.org/10.1144/geochem2019-031.

Han, T., Rukhlov, A., Riddell, J. and Ferbey, T., 2019. A skeleton data model for geochemical databases at the British Columbia Geological Survey. *In*: Geological Fieldwork 2018, British Columbia Ministry of Energy, Mines and Low Carbon Innovation, British Columbia Geological Survey Paper 2019-01, p. 125–135.

Norris, J. and Fortin, G., 2019. Assessment report-sourced surface sediment geochemical database: Development and initial data release from the Interior Plateau. British Columbia Ministry of Energy, Mines and Low Carbon Innovation, British Columbia Geological Survey GeoFile 2019-04, p. 1–10.

Wang, J. and Zuo, R., 2022. Model averaging for identification of geochemical anomalies linked to mineralization. Ore Geology Reviews, vol. 146, article 104955, p. 1–12. https://doi.org/10.1016/j.oregeorev.2022.104955.

Preliminary site characterization for earthquake hazard assessment using ambient vibration techniques in Haines Junction, Yukon (parts of NTS 115A/11, 12, 13, 14)

Tess Leishman*
School of Earth and Ocean Sciences, University of Victoria

Jeremy M. Gosselin and Jan Dettmer
Department of Earth, Energy, and Environment, University of Calgary

John F. Cassidy
Geological Survey of Canada, Natural Resources Canada
School of Earth and Ocean Sciences, University of Victoria

Tae-Seob Kang
Division of Earth Environmental System Science, Pukyong National University, South Korea

Abstract

Regional mapping of soil stiffness improves understanding of seismic hazard in northern Canada, specifically southwestern Yukon, where local amplification hazards are largely unknown. Ambient vibration (AV) measurements record microtremor seismic noise used to calculate the horizontal-to-vertical spectral ratio (HVSR) and identify resonant frequencies at sites. *In-situ* estimation of fundamental frequency (f_0) is used to characterize sites and map local site amplification hazards. Furthermore, AV measurements permit the estimation of surface-wave propagation speeds at different frequencies (*i.e.*, dispersion). Dispersion measurements are used to infer profiles of shear-wave velocity as a function of depth. We present preliminary site characterization using AV measurements from 23 measured sites in Haines Junction, Yukon. The preliminary results suggest a spatial trend of fundamental frequency laterally, where higher frequencies are identified north of Haines Junction and lower f_0 values are identified in south-central Haines Junction. We attribute these observations to the proximity to the Dezadeash River basin.

Introduction

Haines Junction is located in southwestern Yukon, a region of complex active tectonics and abundant seismicity (Nelson et a*l*., 2013). Tectonics are governed by the oblique collision and subduction of the Yakutat microplate beneath the North American Plate (Bruhn et a*l*., 2012), which forms the high topography of the St. Elias Mountains in the region. The village of Haines Junction is at the base of this mountain range (Fig. 1). The St. Elias Mountains are heavily glaciated and characterized by large, crustal-scale faults with significant seismic activity (Doser and Rodriguez, 2011; Meighan et a*l*., 2013; Biegel et a*l*., 2023). The region

* tessleishman@uvic.ca
‡ jan.dettmer@ucalgary.ca
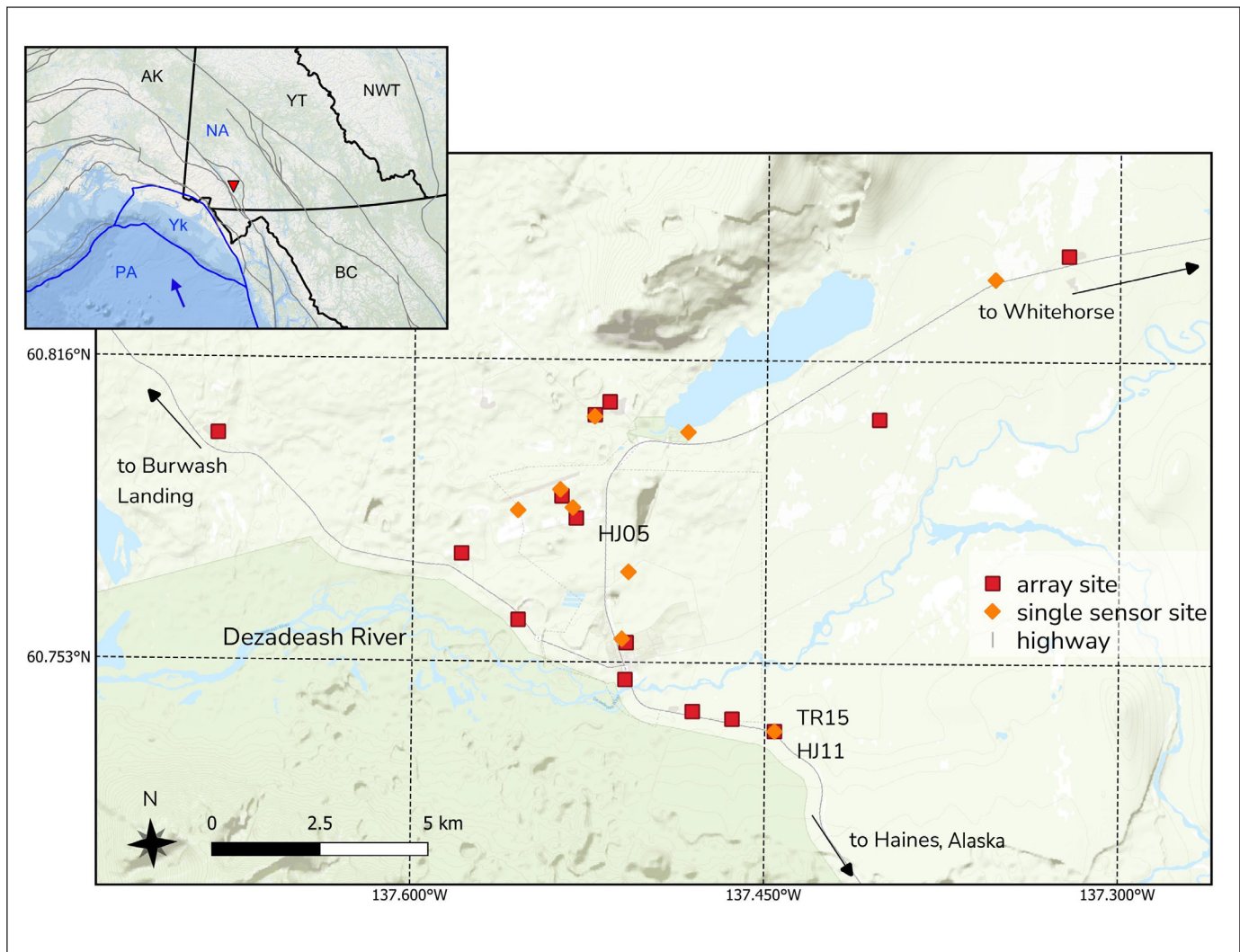
Figure 1. *Site locations for 23 passive seismic recordings in the Haines Junction area. Labelled sites HJ05, HJ11 and TR15 are discussed in the paper. Inset map shows the location of Haines Junction in southwestern Yukon (red triangle), a region of complex active tectonic interactions between the Pacific (PA), Yakutat (Yk) and North American (NA) plates. Tectonic boundaries and major regional faults are shown in blue and grey, respectively (after Yukon Geological Survey, 2020). Small blue arrow illustrates the plate vector of PA relative to NA (Kreemer et al., 2014). Political boundaries are shown in black.*

also exhibits high rates of uplift, erosion and exhumation (Enkelmann et al., 2009; Turner et al., 2016). As a result of these dynamic geological processes, the village of Haines Junction and the surrounding areas are susceptible to associated natural hazards. These include site-specific seismic amplification and resonance hazards, as well as liquefaction and landslide-related hazards. This paper presents preliminary investigations toward characterizing seismic site conditions using ambient vibration (AV) methods based on background seismic noise recordings from processes such as wind, waves and human activity.

Seismic hazard varies greatly across Canada, and the extent of our seismic hazard knowledge varies with geographic location and population density. Seismic hazard is modelled probabilistically by Natural Resources Canada based on seismic sources, fault types and site conditions (Adams et al., 2019; Kolaj et al., 2020). These models assume a given site classification and require adjustment based on local site conditions (V_{S30}, which is the time-averaged shear wave velocities in the upper 30 m of the crust); therefore, more detailed knowledge of local site effects is needed to accurately estimate the local seismic hazard. In densely populated regions, the local subsurface geology is relatively well

understood and seismic hazard is robustly modelled (Kolaj et a*l*., 2020). Regions of low population density are generally poorly understood; site characterization and seismic hazard estimation in these areas largely rely on sparse historical earthquake records and surface topography as proxies. This is especially true for Canada's northern territories and Arctic region, where the presence of a hard permafrost layer has led to the assumption that northern Canada is generally not at risk of amplified shaking (Lamontagne and Bent, 2021). Efforts have been made to identify fault sources to accurately model seismicity in and around the Yukon (Allen et a*l*., 2015); however, subsurface conditions remain broadly unknown, particularly in the more densely populated regions of Whitehorse and Haines Junction. Specifically, there has been no attempt to identify site effects in the Haines Junction area, despite local geological features that suggest the community is potentially at risk of laterally varying amplified and resonating earthquake shaking (Rampton and Paradis, 1979; Hunter and Crow, 2015).

The Yukon Geological Survey (YGS) has characterized surficial and bedrock geology in the Haines Junction region through multiple projects over decades to increase the granularity of mapping beyond regional work. The geology in southwestern Yukon is characterized by tectonic stacking of large rock assemblages dipping northeast (Israel et a*l*., 2017). Metamorphic and igneous rocks outcrop directly northeast of Haines Junction, whereas southwest, toward the Denali fault, there are sedimentary and volcanic outcrops. Repeated Pleistocene glaciation covered the Haines Junction area with complex assemblages of till, glaciolacustrine and glaciofluvial sediments (Rampton and Paradis, 1979). During the Holocene, permafrost aggraded sporadically in the region, and organic veneers formed in the wetter valley bottoms and on the cooler aspect slopes. Little Ice Age advances in the St. Elias Mountains repeatedly impounded the Alsek River and deposited silty glaciolacustrine sediments throughout the Haines Junction townsite as recently as 1848 CE (Clague and Rampton, 1982).

The distribution of permafrost is not well understood, and soil stiffness and site amplification are likely variable throughout the region. Water well records (Government of Yukon, 2002) indicate the presence of a small subsurface basin filled with soft sediment deposited by the Dezadeash River, which runs through central Haines Junction. In addition to surficial mapping, YGS attempted to identify subsurface permafrost in Haines Junction using electrical resistivity methods (P. Lipovsky, pers. comm., 2021). Resistivity data collected using these methods have identified several sites where permafrost is inferred to exist. The YGS has a network of boreholes for monitoring permafrost conditions in Haines Junction, ranging in depth from 2 to 27 m.

There is currently a lack of seismic hazard identification in the Yukon, including limited knowledge of local hazard variation based on soil conditions (Kolaj et a*l*., 2020; Lamontagne and Bent, 2021). Considering the notable seismicity in southwestern Yukon and potential for increased seismic hazard related to local site amplification (Rampton and Paradis, 1979; Hunter and Crow, 2015), communities in these regions face significant but unquantified levels of earthquake-related hazards. The horizontal-to-vertical spectral ratio (HVSR) technique (Nakamura, 1989) estimates the ratio between the horizontal and vertical components of ambient seismic noise. This technique is an established method for estimating the fundamental frequency (f_0) of a site to constrain the depth to significant seismic impedance contrasts (*i.e.*, soil layering structure) and, to a lesser extent, soil stiffness properties (Hunter and Crow, 2015). In this paper, we calculate HVSRs using recorded time series of microtremor waveforms to characterize sites in the Haines Junction region. We provide preliminary hazard assessments for 23 measured sites in the Haines Junction area (Fig. 1) as part of a larger study by YGS to accomplish a robust analysis of seismic hazard in the region using seismic response modelling. Low-frequency f_0 values (0.3–0.8 Hz) were identified at many sites, suggesting thick (*i.e.*, hundreds of metres) sequences of relatively soft sediment in certain areas, and associated risk of amplified shaking during an earthquake (Hunter and Crow, 2015). High-frequency HVSR peaks (10–50 Hz) were also identified at many sites, suggesting shallow, complex, soil-layering structures at depths of approximately 3–15 m. Furthermore, we measured surface-wave dispersion at 14 multi-instrument (array) sites throughout the region. Surface-wave dispersion data were used to probabilistically infer soil properties, and we present preliminary results from this analysis. Mapping these measurements improves our understanding of seismic hazard levels and distribution in southwestern Yukon.

Methods

Data collection

Data for this study were recorded at 23 sites in the Haines Junction region between July 2 and 6, 2023. Ambient vibration arrays (17 synchronous instruments) were deployed at 14 sites (Fig. 1), in cross-shape configurations with a 120 m diameter. The instruments used were Güralp 40T and Nanometrics Trillium Compact three-component (vertical, east and north) broadband seismometers. Figure 2a and b show array deployments at two sites, and Figure 2c shows a typical instrument installation. Ambient vibration recordings were taken at the remaining nine sites (Fig. 1) using a single three-component Tromino seismometer (Fig. 2d).
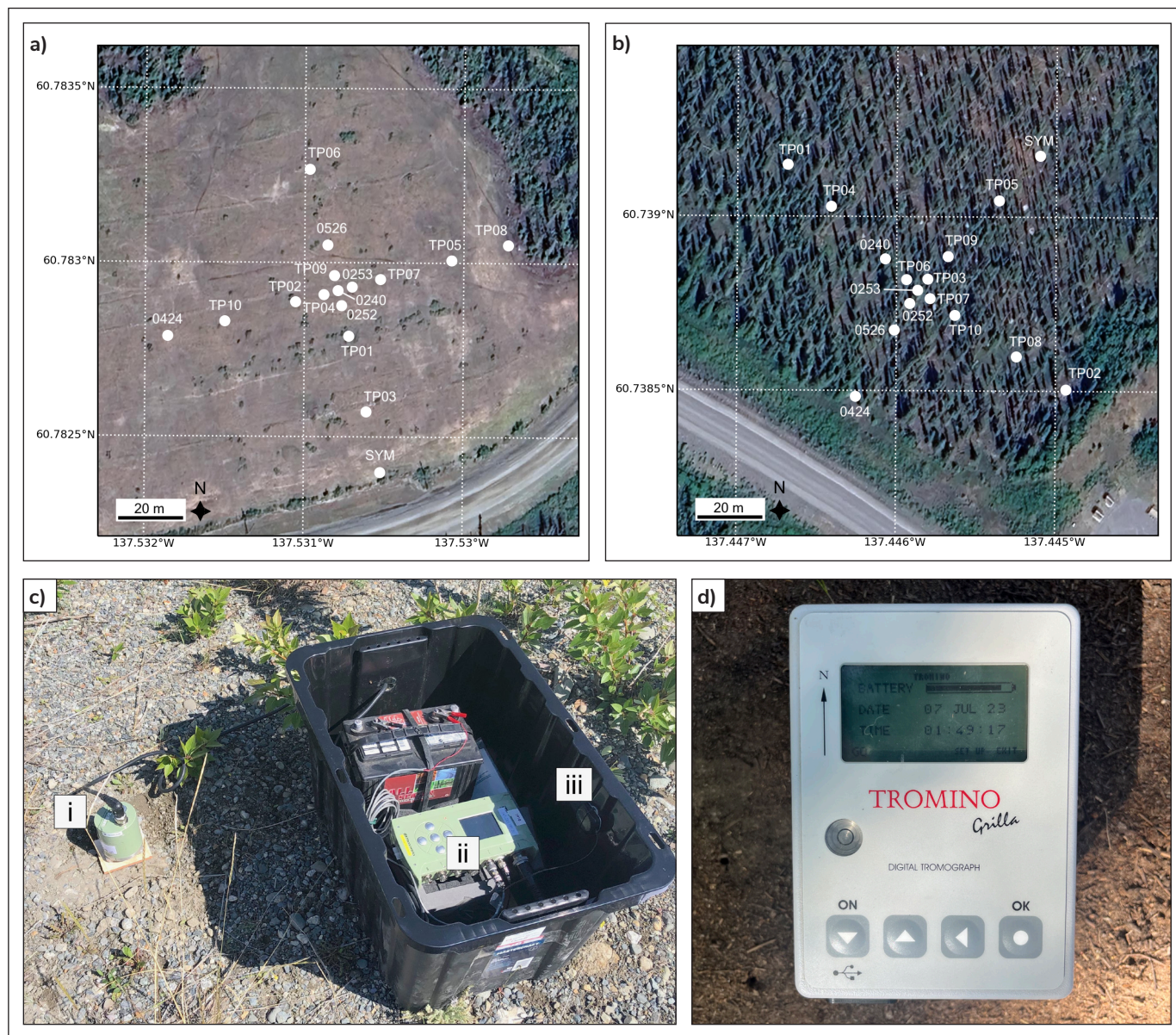
Figure 2. *Passive seismic array deployment configurations at sites* **a)** *HJ05 and* **b)** *HJ11. Individual instrument locations are shown in white. Recordings from instruments TP08 and SYM at both sites were not included in this work for technical reasons. Instruments are positioned along four arms/branches and are spaced at approximately 5, 15, 40 and 60 m from the centre of the array.* **c)** *Broadband seismograph deployment. Temporary, non-invasive installation includes a three-component sensor (seismometer) that is mechanically coupled to surficial soil using a ceramic plate (i); a digital recorder where data are saved (ii); and a GPS antenna to achieve exact, synchronous timing for data recording (iii).* **d)** *A three-component Tromino seismometer.*

Array AV recordings were approximately 2–3 h long with a sampling frequency of 100 Hz. These recordings captured broadband frequencies required for modelling purposes beyond the scope of this paper. Single-station Tromino recordings were 30 min long with a sampling frequency of 128 Hz to capture broadband frequencies excited by shallow and deep soil layering in the subsurface. These measurement criteria were chosen in accordance with SESAME (Site EffectS assessment using AMbient Excitations) guidelines for HVSR analysis (SESAME, 2004). Sites were selected based on various factors, including the presence of preliminary community-scale surficial geology mapping and results of electrical resistivity surveys provided by YGS (P. Lipovsky, pers. comm., 2021). Site selection was further guided by accessibility, availability and proximity to inhabited areas.

Horizontal-to-vertical spectral ratio processing

To obtain HVSR curves from AV recordings, time series from all three components (east, north and vertical channels) were extracted from each individual instrument. The ratios of horizontal and vertical recordings from each instrument were computed using Geopsy software (Wathelet et *al.*, 2020). Prior to calculating HVSR, recordings were corrected to account for the unique response of each instrument type. The signals, originally recorded in the time domain, were converted to the frequency domain as Fourier amplitude spectra for the three directional components using the discrete Fourier transform calculation (equation 1),

$$Y_k \; = \; \textstyle\sum_{j=0}^{n-1} X_j \exp\left(-2\pi \frac{\sqrt{-1}}{n} jk\right) \qquad (1)$$

where array Y, containing the frequency values indexed by $0 \leq k < n$, is computed for array X (a time series of length n) with complex exponents for the various frequencies (Frigo and Johnson, 2005). For a robust analysis, recordings were divided into many time windows (Fig. 3a) so that the frequency spectra of each time window (Fig. 3b–d) produced an individual HVSR measurement (Fig. 3e). Based on SESAME criteria (SESAME, 2004), the length and number of windows is directly related to the resolution quality of the lowest frequency of interest. With the assumption that frequencies of interest are above 0.1 Hz, signals recorded from all channels were divided into 120 s window lengths (Fig. 3a). A relative sampling threshold

of 75% was applied to exclude transient signals with abnormally high amplitudes. A 0.1 Hz high-pass filter was also applied to minimize the effect of tapering caused by windowing, which can distort the HVSR calculation in the presence of high-amplitude, low-frequency signals (SESAME, 2004). The HVSR (Fig. 3e) was then calculated by dividing the horizontal components of the 'windowed' frequencies by the vertical components to extract only the site response, eliminating the frequency response of the signal and the source (Nakamura, 1989). An average HVSR was computed from all the sensors at a site to produce a single representative HVSR curve. The HVSR curve of each sensor was analyzed individually to identify changes in resonant frequencies spatially over the site area. Sensors that produced outlier HVSR curves were removed from the calculation of the representative HVSR curve.

Surface-wave dispersion processing

Surface waves are seismic waves that propagate along Earth's free surface where it contacts the atmosphere. The propagation speed of these waves depends on the geophysical properties of the shallow subsurface (predominantly shear-wave velocity; V_S); however, the depth to which these waves are sensitive to site properties is a function of wavelength (or frequency). Low-frequency waves are sensitive to V_S at greater depths; consequently, surface waves with different frequencies will propagate (*i.e.*, disperse) at different velocities due to local vertically heterogeneous properties. The velocity–frequency relationship (*i.e.*, dispersion curve) can be used to infer profiles of geophysical site conditions, which is valuable for seismic site characterization. Surface-wave dispersion is generally more informative than HVSR curves for constraining site V_S conditions; however, the two provide complementary information (e.g., Gosselin et *al.*, 2022). Surface-wave dispersion is sensitive to depth-integrated V_S, whereas HVSR curves are sensitive to seismic impedance contrasts (*i.e.*, discrete layer boundaries).

Several techniques exist for estimating surface-wave dispersion at a site. Rayleigh waves (a surface wave polarized in the vertical plane) generally dominate background/ambient seismic noise (Shapiro and Campillo, 2004); therefore, an attractive approach to estimate dispersion is to extract fundamental-mode
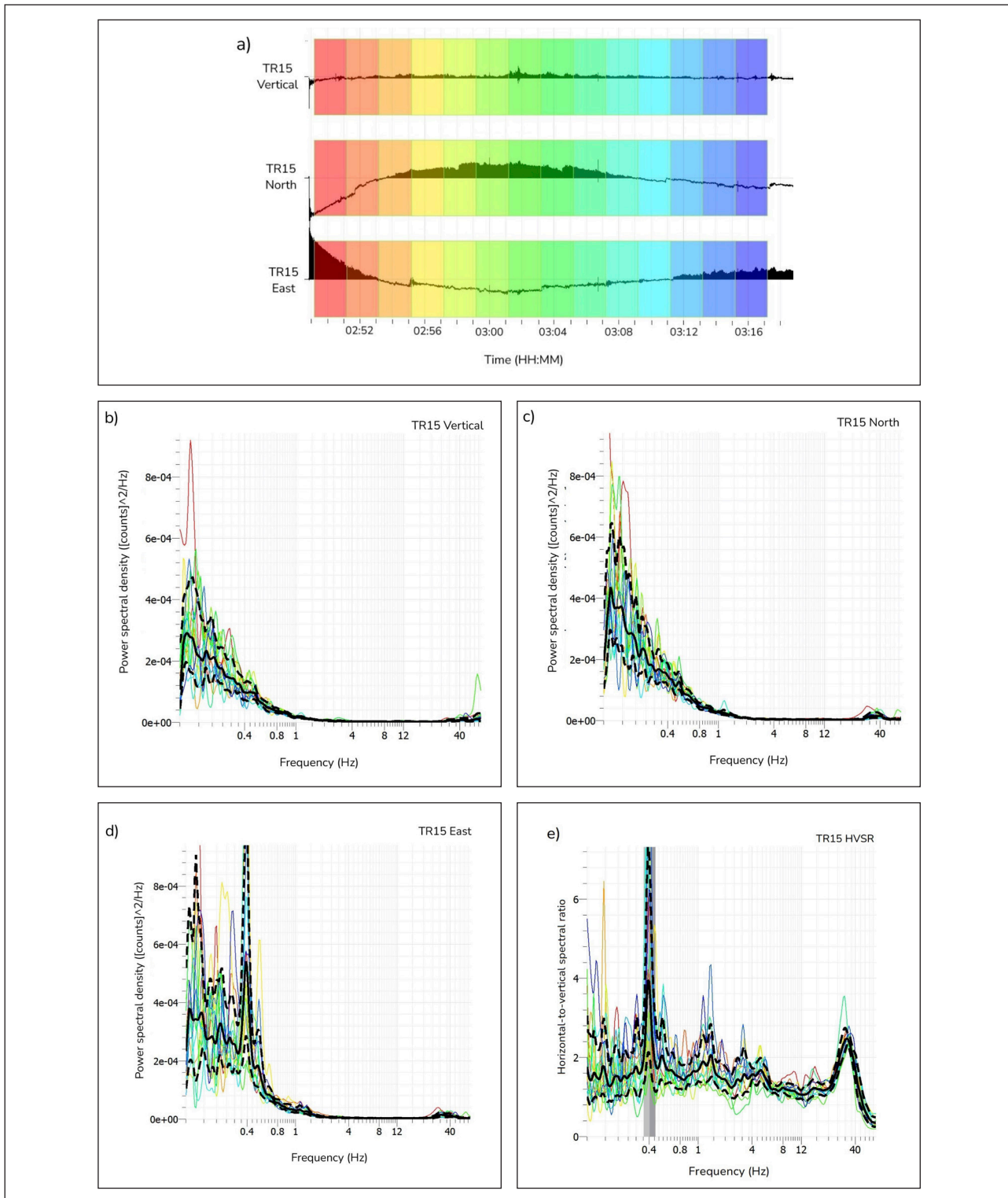
Figure 3. *Data analysis of site TR15.* **a)** *Time series windowing of site TR15 for spectra and horizontal-to-vertical spectral ratio (HVSR) calculations using 120 s windowing intervals of a 30 min Tromino recording. The colour of the recording windows corresponds with spectral and HVSR curves in* **b)**, **c)**, **d)**, *and* **e)**. **b)**, **c)**, **d)** *Fourier amplitude spectra in vertical, north and east components. The solid black line is the average of the spectra and the dashed line is the standard deviation.* **e)** *Horizontal-to-vertical spectral ratio (HVSR) curve; the vertical grey bar indicates the estimated fundamental frequency (f_0), where the thickness of the grey bar is the bounding error. The lighter grey band indicates the negative error, and the darker grey band positive error.*

Rayleigh wave signals from ambient seismic noise recordings (Aki, 1957; Wathelet et al., 2008; Molnar et al., 2010; Gosselin et al., 2018). In this study, we use frequency-wavenumber (f-k) processing to measure the phase velocity of Rayleigh waves at many frequencies (Lacoss et al., 1969). This technique requires synchronous recordings from instruments deployed in a 2D array (Fig. 2) because the propagation direction of background seismic signals is unknown and must be measured as part of the processing. All passive seismic recordings include three components; however, only vertical-component recordings are considered in this preliminary work because we can assume these are dominated by Rayleigh waves. The synchronous recordings are windowed according to the frequency (*f*) of interest. For each time window in f-k processing, the coherence of the Rayleigh wave signal across the array is estimated for various phase velocities and propagation directions (for the desired frequency band). This requires shifting individual windowed recordings in time based on a given wavenumber vector $\boldsymbol{k} = (k_x, k_y)$ and mapping the combined signal coherence on a 2D wavenumber grid. The location of maximum signal coherence on this wavenumber grid provides a single measurement of Rayleigh wave phase velocity (*c*) and propagation direction (*θ*) according to

$$c = \frac{2\pi f}{|\boldsymbol{k}|} \tag{2}$$

and

$$\theta = \arctan\left(\frac{k_x}{k_y}\right) \tag{3}$$

Each time window represents a single sample (estimates of *c* and *θ*). The ensemble of samples for all time windows, and across all frequencies, is considered to determine the dispersion curve (Fig. 4). We apply *f-k* processing to measure dispersion at 100 logarithmically spaced frequencies between 1 and 15 Hz; however, the actual frequency band over which dispersion can be measured is determined by the resolution and aliasing limits of the 2D array of the seismic instruments (Wathelet et al., 2008). The resolution and aliasing limits are functions of the distance between instruments and their geometries. The resolution limit defines the ability of a particular seismic array to distinguish waves propagating at similar wavenumbers (*i.e.,* distinguish peaks on the wavenumber grid). Aliasing limits occur due to finite,

discrete spatial sampling of the seismic wavefield. This introduces recurring peaks (side lobes) in the measured wavenumber grid, which can be summed incorrectly when determining signal coherence (Wathelet et *al.,* 2008, 2020). The use of several instrument spacing distances (Fig. 2a, b) enables wider resolution and aliasing limits (*i.e.,* wider frequency band). Although these limits are defined in terms of wavenumbers, they correspond to a frequency band of approximately 2–10 Hz for most array deployments in this study. Distributions of measured phase velocities at each frequency are often asymmetrical and contain outliers (Fig. 4); therefore, the dispersion curve is taken as the median phase velocity across the relevant frequency band. In this study, *f-k* processing for dispersion measurement was performed using Geopsy software (Wathelet et *al.,* 2020).

Preliminary soil shear-wave velocity inversion

Surface-wave dispersion data provide valuable constraints on soil V_S values, which are important for seismic hazard site classification and assessment. In this section, we present preliminary inferences of site soil properties based on measured dispersion data (see Surface-wave dispersion processing). Specifically, the dispersion data are inverted using a non-linear Bayesian methodology to estimate 1D models of site soil properties (Molnar et *al.,* 2010; Dettmer et *al.,* 2012; Gosselin et *al.,* 2017). Bayesian inversion is a probabilistic approach that considers the inversion solution as a probability density over model parameters (known as a posterior probability density). For simplicity, this preliminary paper assumes a two-layer model representative of unconsolidated sediment over bedrock. Furthermore, this paper assumes lateral heterogeneity over the array site, which may not be an accurate assumption at all sites (see Discussion for further details). Because this inversion problem is non-linear, we applied Markov-chain Monte Carlo sampling to generate an ensemble of model parameter combinations that agree with the data (Brooks et *al.,* 2011). The parameters of the model (layer V_S values and layer thicknesses) are restricted to geophysically realistic values; however, wide bounds are employed to ensure that the solution is primarily constrained by the dispersion data.
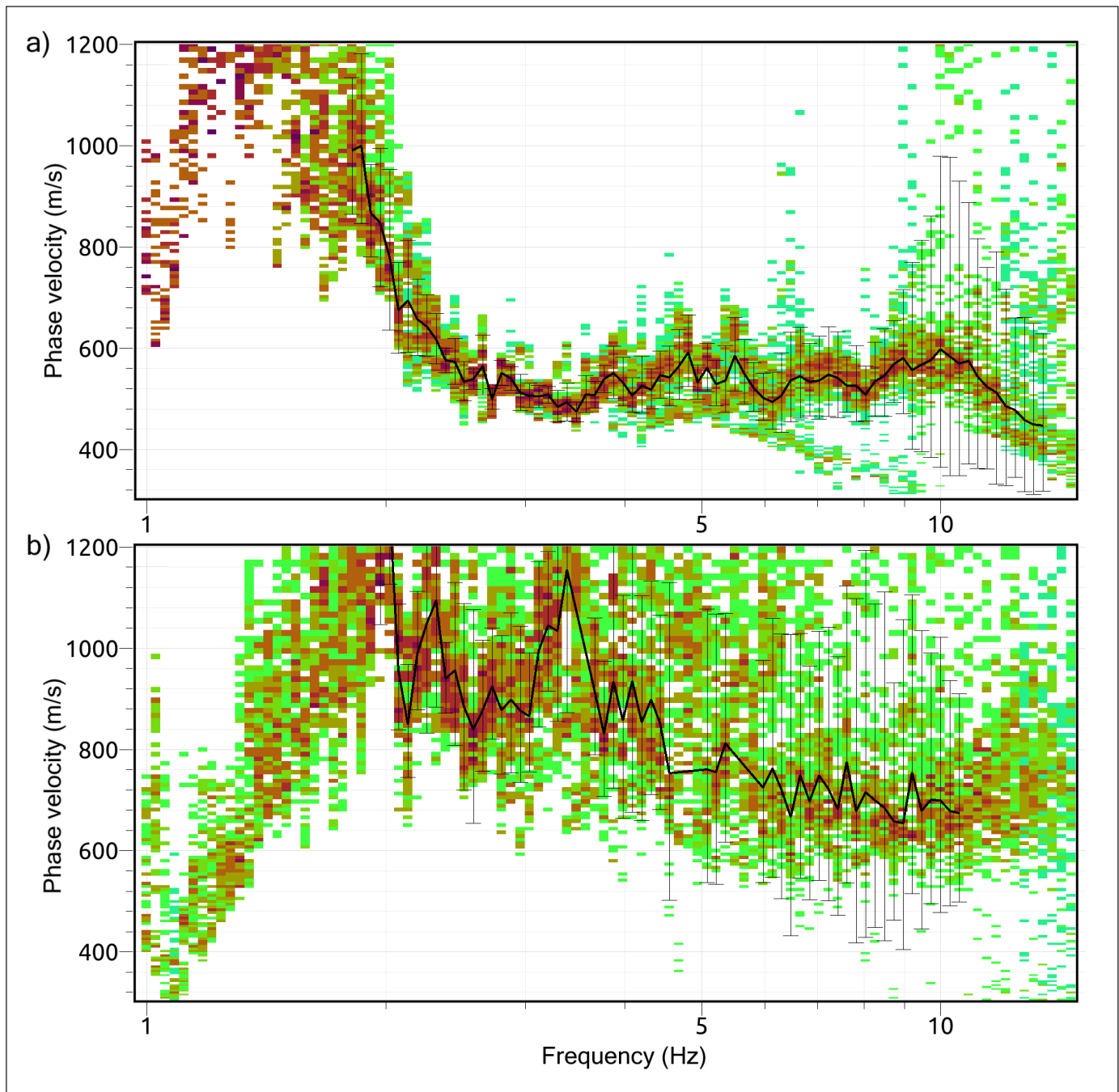
Figure 4. *Frequency-wavenumber processing of ambient seismic noise recordings at sites* **a)** *HJ05 and* **b)** *HJ11. The red and green bars represent high and low probability, respectively. Black lines illustrate the selected dispersion data. The histograms for HJ05 and HJ11 illustrate high and low-quality examples of frequency-wavenumber processing, respectively.*

Figure 5 illustrates estimated V_S as a function of depth at sites HJ05 and HJ11. The V_S estimates are presented as probability densities as a function of depth, where light colours indicate high probability. We observed that sediment velocities are generally lower at HJ05 than at HJ11. This is expected, given the difference in measured dispersion data (Fig. 4), which show that high-frequency (*i.e.*, shallow depth), surface-wave velocities are much higher at HJ11. Resolution in geophysical inversions typically degrades with increasing depth. Our results exhibit higher uncertainty in V_S at greater depths (Fig. 5). We also present

Figure 5. *Results for simple two-layer probabilistic inversions at sites* **a)** *HJ05, and* **b)** *HJ11. Depth marginal probability distributions of inferred shear-wave velocities* (V_s) *are shown, with yellow and blue representing high and low probability, respectively. Marginal probability distributions for inferred layer thickness (interface depth; $P(Z_0)$) are 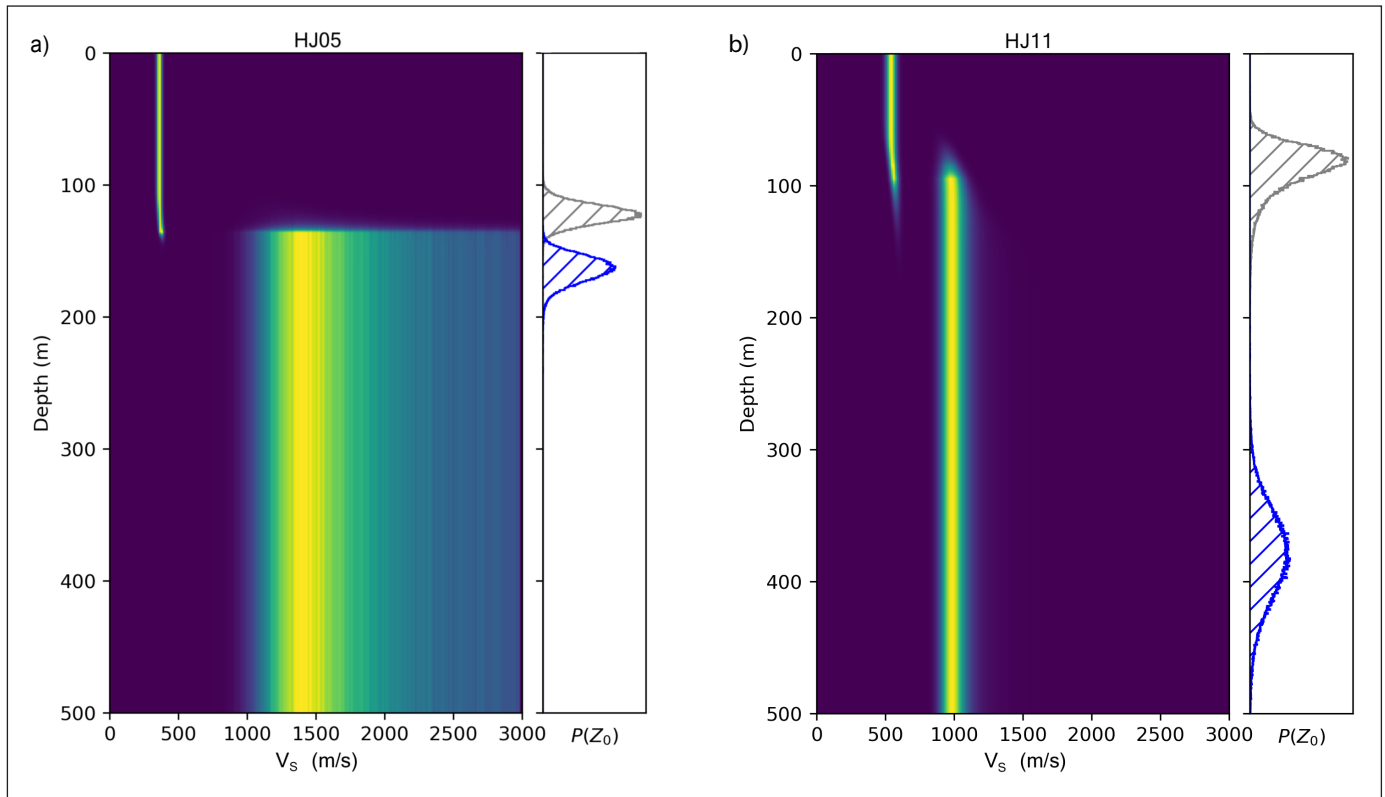shown in grey. The probability distribution of the inferred seismic impedance contrasts associated with f_0 in horizontal-to-vertical spectral ratio curves is shown in blue. Note that the distribution for depth is outside of the plot bounds for HJ11.*

marginal distributions of the thickness of the surficial layer, which can be interpreted as depth to bedrock; however, as will be discussed below, this assumption may not be true for all sites. Figure 6 illustrates the fit between measured and predicted surface-wave dispersion data. The measured data are those shown in Figure 4 (sites HJ05 and HJ11), whereas the predicted data represent a numerical simulation corresponding with a given inversion solution. Some complexities in the measured dispersion data are not fit by this simple, two-layer case (e.g., high-frequency data for site HJ05). This is expected given the simplicity of the model used in this preliminary analysis.

Discussion

Horizontal-to-vertical spectral ratio results

Fundamental frequencies were identified at each of the 23 measured sites and are summarized in Appendix A. Nine sites measured using the Tromino seismometer were excluded from these results due to poor recording quality, insufficient recording duration, complex geological site conditions, or a combination of these factors. Fundamental frequencies identified at sites recorded using Tromino seismometers and sensor arrays are illustrated in Figures 3e and 7, respectively. Fundamental frequencies identified throughout the study area range from 0.3 to 0.8 Hz, indicating that a thick layer of soft sediment overlies bedrock in the area (Nakamura, 2000). This suggests a potential for amplified shaking due to resonance effects caused by the significant velocity contrast between the bedrock layer and overlying sediment (Hunter and Crow, 2015). Figures 3e and 7d show HVSR results from co-located Tromino (site TR15) and array (site HJ11) recordings south of central Haines Junction (see Fig. 1 for site locations). The HVSR curves representative of this site demonstrate that both sensor types and calculations produce consistent results with a fundamental
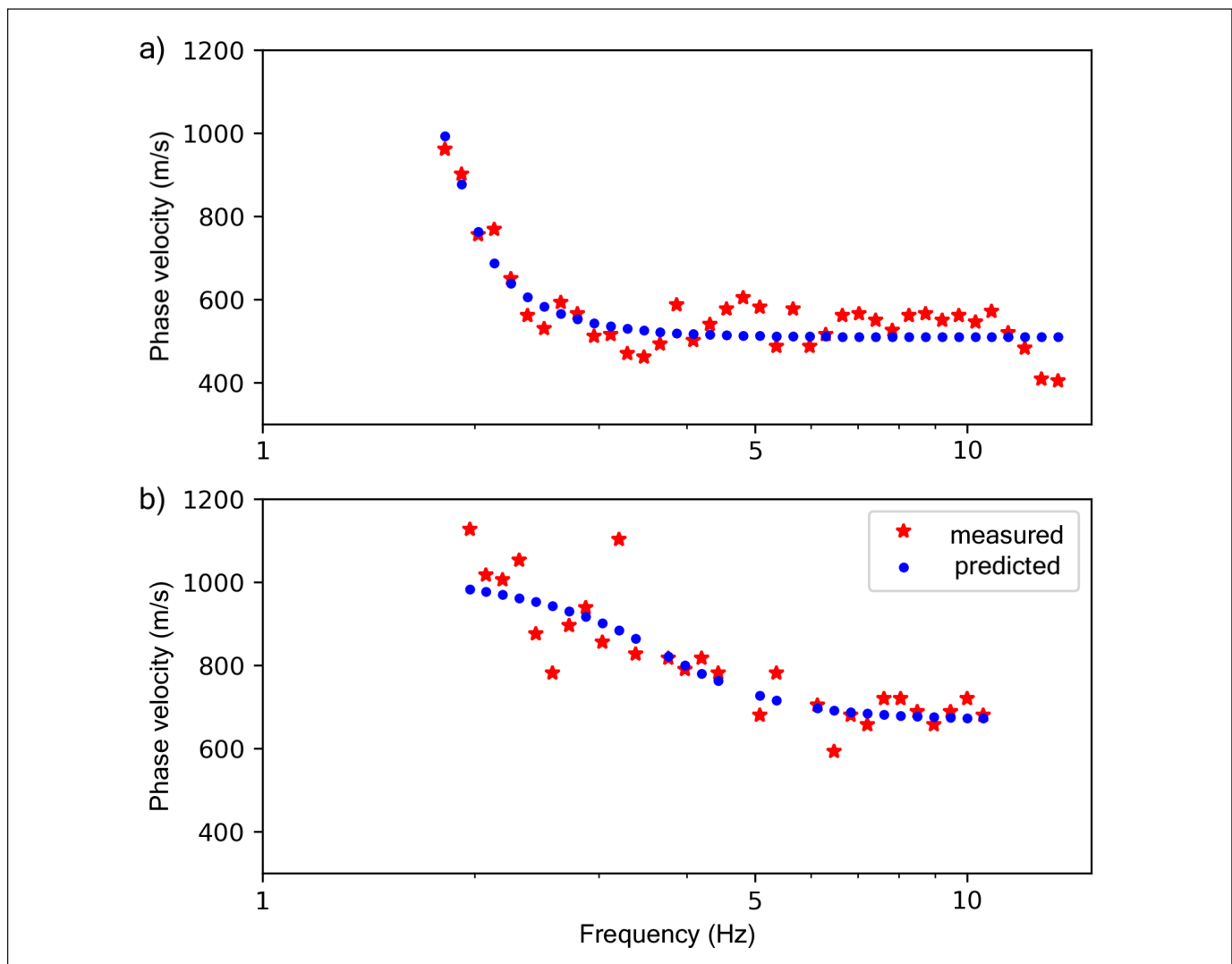
Figure 6. *Comparison of measured and predicted dispersion data for sites **a)** HJ05, and **b)** HJ11. Measured dispersion data are the same as shown in Figure 4. Predicted dispersion data are simulated using the solutions from the simplified two-layer probabilistic inversions.*

frequency of approximately 0.4 Hz and amplitude of approximately 4 to 5. Overall, average HVSR curves calculated from multiple sensors have a broader f_0 peak compared to single-station Tromino sites (see averaged HVSR curves in Fig. 7). This is likely due to instrumentation, seismic noise and lateral heterogeneity effects, which cause discrepancies between HVSR results from different sensors at a given array site. The multiple, narrow, shifted peaks seen in the stacked f_0 peaks identified at site HJ11 (Fig. 7c) suggest the sloped site has laterally varying subsurface geology over a scale of hundreds of metres (Molnar et al., 2022). Site HJ05 is located north of Haines Junction and has a higher fundamental frequency compared to the HJ11/ TR15 site, south of Haines Junction. This difference in

HVSR suggests that subsurface geology varies laterally over larger scales throughout the area.

Most sites demonstrate at least one high-frequency peak of 10–50 Hz (Appendix A). Additional peaks in HVSR curves are indicative of additional discrete sediment layering in the overburden between the surface and bedrock layer (Mihaylov et al., 2016). Because peak frequency values are inversely proportional to layer boundary depth (Nakamura, 2000), depth of the fundamental frequency can be estimated by dividing the V_S of the uppermost layer by the measured quarter-wavelength. Assuming the minimum V_S is approximately 250 m/s in the uppermost layer, peaks identified at high frequencies of approximately 25 Hz
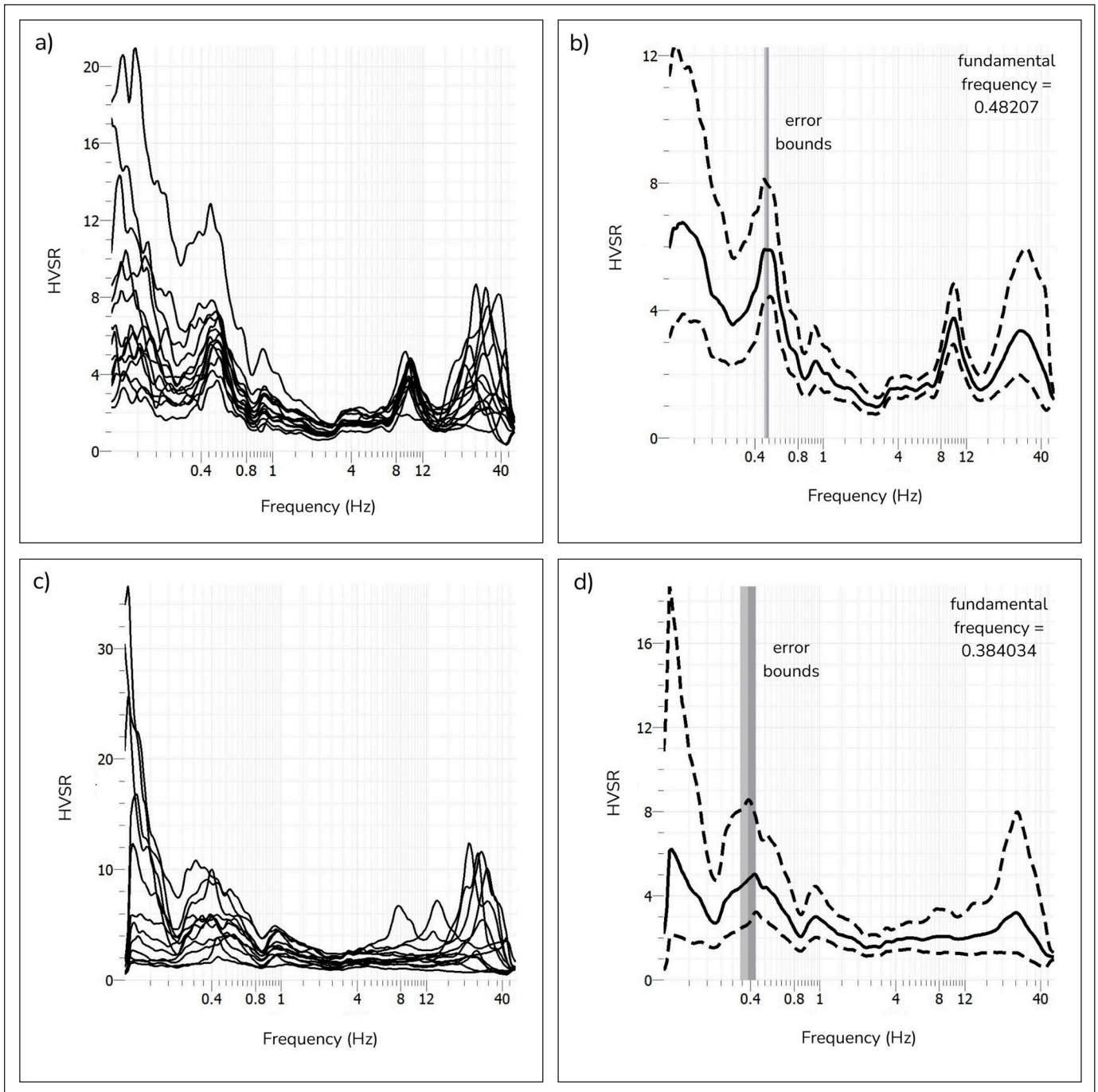
Figure 7. *Summarized and averaged horizontal-to-vertical spectral ratio (HVSR) curves from all sensors at array sites* **a**, **b)** *HJ05, and* **c**, **d)** *HJ11.* **a)** *and* **c)** *show stacked average HVSR curves calculated from each individual sensor recording.* **b)** *and* **d)** *show the average (solid line) and one standard deviation (dashed lines) HVSR curve for each site. Grey vertical error bars show the standard deviation of the average fundamental frequency. Sensors that produced anomalous HVSR curves were excluded, as indicated in Appendix A1.*

for sites HJ05, HJ11 and TR15 (Figs. 3e, 7) indicate sediment layering to be as shallow as approximately 2.5 m below the surface. Secondary or tertiary peaks identified at lower frequencies, for example, at approximately 9.5 Hz at site HJ05 (Fig. 7b), indicate that the interface of intermediate soil layers extends deeper into the subsurface, to 6–12 m deep.

The frequency, amplitude and number of high-frequency peaks vary among the studied sites (see Appendix A), suggesting complex sediment layering structure in the overburden that varies laterally. The multiple peaks at approximately 25 Hz, which shifted in frequency depending on the instrument (Fig. 7a, c), suggest that near-surface intermediate soil layers vary over the 120 m lateral extent of the array site (Molnar et al., 2022). Higher frequency peaks, consequently, are not well constrained at these sites. In comparison, the lower frequency secondary peak at site HJ05 (Fig. 7a, b) has a very similar frequency value (approximately 9.5 Hz) for almost all sensors, indicating that the boundary depth of this layer is more homogeneous across the site. Because permafrost is present but discontinuous throughout the Haines Junction region (Rampton and Paradis, 1979), it is possible that distinct overburden layers found at many of the measured sites are representative of an active permafrost layer. For example, the subsurface geology identified by HVSR results at site HJ05 (i.e., two distinct shallow layers) is consistent with nearby electrical resistivity tomography (ERT) conducted by YGS (P. Lipovsky, pers. comm., 2021) and may indicate the presence of a seasonally active shallow soil structure. Permafrost at HJ05 is likely discontinuous and degrading given the alterations to surficial vegetation cover (HJ05 is an agricultural field). In contrast, site HJ11 is in a wooded area on a gently sloping, north-facing incline with nearby geomorphological signatures of permafrost processes. It is difficult, however, to determine whether high-frequency peaks identified at many sites are produced by a discrete permafrost layer or other geological factors without additional data and/or seasonal monitoring.

Dispersion curve inversion results

As expected from inversion of surface-wave dispersion data, with an increase in depth, V_S generally increases, as does uncertainty in V_S profiles, and the estimated transition depth to bedrock is resolved. What is most reliable is the average V_S constrained over the depth

extent corresponding with the depth resolution capabilities of the array configuration used in this study. Average surficial sediment velocities and thicknesses with associated uncertainties, inferred from surface-wave dispersion data, are summarized in Appendix B for all array sites. The maximum depth resolution is a function of array geometry, which defines the low-frequency dispersion that can be measured (see Surface-wave dispersion processing). The depth resolution limit is also a function of geological conditions (soil V_S), which define the wavelength of these low-frequency seismic waves. The depth resolution limit is typically the maximum station separation distance (Park et al., 1999; Wathelet et al., 2008). This is 120 m for most sites considered in this study.

The wavelength limitations in HVSR measurements are defined by the recording parameters of the AV measurements (e.g., length of recording) and the sensitivity of the instrument (e.g., broadband or high frequency). In this study, HVSR measurements provide information over a significantly wider frequency band (0.1–50 Hz) compared to the measured dispersion; however, HVSR suffers from solution non-uniqueness between soil V_S and depth to impedance contrasts. To test the consistency between our simplified inversion results and HVSR observations, we calculated the depth associated with the f_0 peaks using sediment V_S values inferred from surface-wave dispersion. Uncertainties in both f_0 peaks and inferred V_S are propagated through this analysis; these depth estimates are summarized in Appendix B. Examples of this analysis are illustrated by the blue histogram in Figure 5a and b. At HJ05, the depth to bedrock inferred from the inversion is in relatively good agreement with the depth estimated from the f_0 peak. The discrepancy between the two distributions is likely attributed to the simplified velocity structure assumed for the inversion method. Alternatively, the discrepancy between bedrock depth estimates may be attributed to the simple quarter-wavelength assumption for HVSR measurements and the effects of high-frequency HVSR peaks (which are not considered in this simple analysis). At HJ11, the depth to bedrock estimated using the f_0 peak is much deeper than the interface inferred from dispersion data (approximately 380 ± 36 m). This suggests that the interface resolved in the inversion of dispersion data is not bedrock depth. Instead, this layer likely represents either a discrete intermediate sediment layer or a gradual increase in sediment V_S with increasing depth. This would also

explain why the distribution of V_S values in the deeper layer is much lower at HJ11 compared to HJ05 (Fig. 5). Future work will estimate more robust models of V_S structure by jointly inverting dispersion and HVSR data, and consider more complex models of soil-layering structure.

Regional observations

The average fundamental frequencies (f_0) for all single-station and array sites are mapped in Figure 8 to demonstrate site stiffness and/or sediment thickness as they vary spatially throughout the Haines Junction region. Eight sites in the south of our study area, including the colocated HJ11 array and TR15 single-station sites, demonstrate fundamental frequencies below 0.5 Hz. Meanwhile, eight sites in the north of our study area exhibit frequencies 0.5 Hz and above. These

observations suggest a shallower depth to bedrock, and/or stiffer (*i.e.*, higher seismic velocities) sediments, in the north of our study area compared with the south. The regional observations in HVSR fundamental frequencies are consistent with our interpretation of the inverted surface-wave dispersion curve results; however, dispersion data suggest higher sediment velocities in the south of our study area compared with the north (Fig. 5), as well as high variability in sediment V_S across the study area (see Appendix B). Interpreted together, these data imply that regional trends in measured f_0 are likely attributed to bedrock depth rather than site soil V_S properties. A possible explanation for deeper soft soil layers at southern sites is their proximity to the Dezadeash River running through central Haines Junction, which is associated with a sediment-filled river valley and associated basin in the subsurface. In comparison, northern sites in our
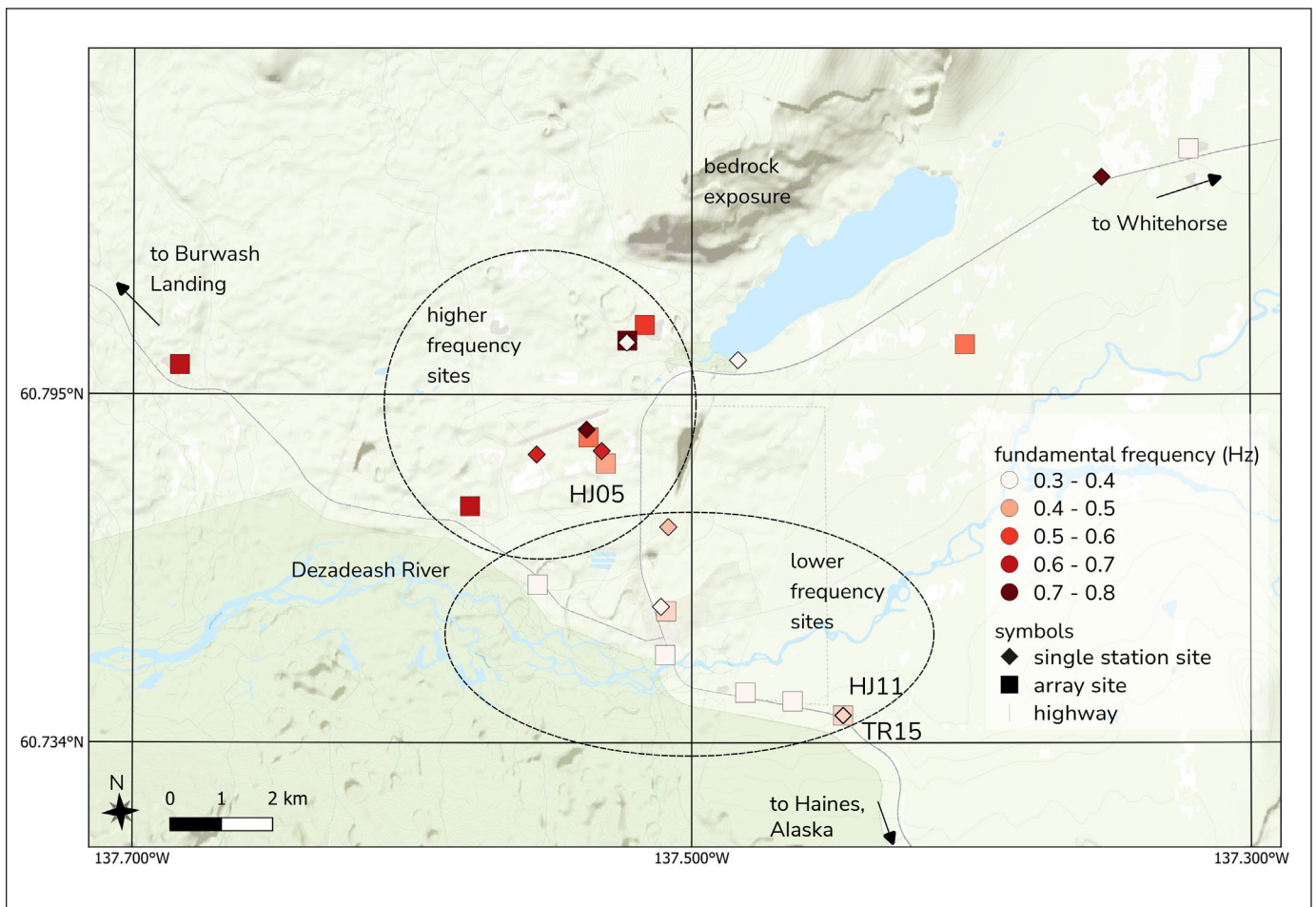

Figure 8. *Map of site locations in the Haines Junction area with identified fundamental frequencies from horizontal-to-vertical spectral ratio analysis. Labelled sites HJ05, HJ11 and TR15 are discussed in the text. Areas with relatively low (south) and high (north) fundamental frequencies are identified.*

study area are proximal to bedrock exposure (area of high topographic relief shown at the northern extent of our study region in Figs. 1 and 8). Proximity to bedrock supports our interpretation of a shallower depth to the sediment–bedrock interface. Sites located outside of these two subregions (circled in Fig. 8) exhibit varying fundamental frequencies, demonstrating the overall complexity in subsurface geology throughout the study area (Rampton and Paradis, 1979; Israel et al., 2017). They may also demonstrate site-specific hydrogeological and cryospheric processes.

Generally, sites with softer soils experience more amplified ground shaking during an earthquake compared to stiffer sediments or hardrock (Hunter and Crow, 2015). We do not comment on seismic hazard associated with regionally variable soil stiffness properties in this preliminary paper; however, site components of seismic hazard may also be attributed to subsurface basin structures that can significantly amplify and extend the duration of earthquake shaking (Bard and Bouchon, 1985). It is likely that central and south Haines Junction are at increased seismic hazard due to the presence of subsurface basin structures in the region.

Conclusion

Southwestern Yukon has abundant seismicity and complex active tectonics, and communities in the region are at risk of earthquake-associated hazards including shaking amplification and resonance. Although seismic hazard is elevated in southwestern Yukon, the contributions of local site effects to the overall hazard (within Canada's national hazard model) are largely unknown. To address this knowledge gap, preliminary site characterization was completed in the Haines Junction area using ambient vibration techniques. Passive seismic recordings were taken at 23 sites, including 9 single-station sites and 14 multi-instrument array sites. Time series recordings were processed to determine HVSR curves for all sites. Fundamental frequencies ranging from 0.3 to 0.8 Hz were readily identified; these values suggest regional variability in soil seismic properties, sediment depths and associated site-specific seismic hazards. Recordings from array sites were used to measure surface-wave dispersion, which was subsequently used to infer shallow soil V_s properties. When depth to bedrock is within array

depth resolution limits, inversion results are generally in agreement with HVSR observations.

Discrepancies between the results obtained from the two seismic data types may be due to lateral soil heterogeneity at sites, resolution limitations due to array aperture, the assumptions of the simplified (two-layer) inversion model, the simple quarter-wavelength assumption for HVSR measurements, and the effects of multiple HVSR peaks (which were not considered in this simple analysis). This paper provides preliminary site characterizations and mapping to identify local site effects and better understand seismic hazard in Haines Junction, Yukon. Future work will involve joint inversion of HVSR and measured surface-wave dispersion to obtain more robust V_s depth profiles, which will enable more complete site characterization, including seismic site classification, and amplification and resonance modelling.

Acknowledgments

References

Adams, J., Allen, T., Halchuk, S. and Kolaj, M., 2019. Canada's 6th generation seismic hazard model, as prepared for the 2020 National Building Code of Canada. *In*: 12th Canadian Conference on Earthquake Engineering, Canadian Association for Earthquake Engineering, paper 192-Mkvp-139, 8 p.

Aki, K., 1957. Space and time spectra of stationary stochastic waves, with special reference to microtremors. Bulletin of the Earthquake Research Institute, vol. 35, p. 415–456.

Allen, T., Adams, J., Halchuk, S. and Rogers, G., 2015. 5th generation seismic hazard model for north-western Canada. *In*: The 11th Canadian Conference on Earthquake Engineering, Canadian Association for Earthquake Engineering, paper 93782, 13 p.

Bard, P.Y. and Bouchon, M., 1985. The two-dimensional resonance of sediment-filled valleys. Bulletin of the Seismological Society of America, vol. 75, no. 2, p. 519–541. https://doi.org/10.1785/BSSA0750020519.

Biegel, K., Gosselin, J. and Dettmer, J., 2023. Preliminary double-difference relocation earthquake catalogue for southwestern Yukon centred along the Denali fault zone. *In*: Yukon Exploration and Geology 2022, K.E. MacFarlane (ed.), Yukon Geological Survey, p. 1–18, plus digital appendices.

Brooks, S., Gelman, A., Jones, G. and Meng, X.L. (eds.), 2011. Handbook of Markov Chain Monte Carlo (1st ed.). Chapman and Hall/CRC, New York, 619 p. https://doi.org/10.1201/b10905.

Bruhn, R.L., Sauber, J., Cotton, M.M., Pavlis, T.L., Burgess, E., Ruppert, N. and Forster, R.R., 2012. Plate margin deformation and active tectonics along the northern edge of the Yakutat terrane in the Saint Elias orogen, Alaska, and Yukon, Canada. Geosphere, vol. 8, no. 6, p. 1384–1407. https://doi.org/10.1130/GES00807.1

Clague, J.J. and Rampton, V.N., 1982. Neoglacial Lake Alsek. Canadian Journal of Earth Sciences, vol. 19, no. 1, p. 94–117. https://doi.org/10.1139/e82-008

Dettmer, J., Molnar, S., Steininger, G., Dosso, S.E. and Cassidy, J.F., 2012. Trans-dimensional inversion of microtremor array dispersion data with hierarchical autoregressive error models. Geophysical Journal International, vol. 188, no. 2, p. 719–734. https://doi.org/10.1111/j.1365-246X.2011.05302.x

Doser, D.I. and Rodriguez, H., 2011. A seismotectonic study of the southeastern Alaska region. Tectonophysics, vol. 497, no. 1–4, p. 105–113. https://doi.org/10.1016/j.tecto.2010.10.019

Enkelmann, E., Zeitler, P.K., Pavlis, T.L., Garver, J.I. and Ridgway, K.D., 2009. Intense localized rock uplift and erosion in the St Elias orogen of Alaska. Nature Geoscience, vol. 2, no. 5, p. 360–363. https://doi.org/10.1038/ngeo502

Frigo, M. and Johnson, S., 2005. The design and implementation of FFTW3. *In*: Proceedings of the IEEE, vol. 93, no. 2, p. 216–231. https://doi.org/10.1109/JPROC.2004.840301

Gosselin, J.M., Cassidy, J.F., Dosso, S.E. and Brillon, C., 2018. Probabilistic seismic-hazard site assessment in Kitimat, British Columbia, from Bayesian inversion of surface-wave dispersion. Canadian Geotechnical Journal, vol. 55, no. 7, p. 928–940. https://doi.org/10.1139/cgj-2017-0265

Gosselin, J.M., Dosso, S.E., Askan, A., Wathelet, M., Savvaidis, A. and Cassidy, J.F., 2022. A review of inverse methods in seismic site characterization. Journal of Seismology, vol. 26, no. 4, p. 781–821. https://doi.org/10.1007/s10950-021-10047-8

Gosselin, J.M., Dosso, S.E., Cassidy, J.F., Quijano, J.E., Molnar, S. and Dettmer, J., 2017. A gradient-based model parametrization using Bernstein polynomials in Bayesian inversion of surface wave dispersion. Geophysical Journal International, vol. 211, no. 1, p. 528–540. https://doi.org/10.1093/gji/ggx323

Government of Yukon, 2002. Haines junction borehole logging report. Water Resources Branch, Water Well Registry Open File 10337404. https://ftp-env-public.gov.yk.ca/WR/YWWR/101130001.pdf, [accessed December 2023].

Hunter, J.A. and Crow, H.L. (eds.), 2015. Shear wave velocity measurement guidelines for Canadian seismic site characterization in soil and rock. Geological Survey of Canada, General Information Product 110e, 226 p.

Israel, S., Friend, M. and Borch, A., 2017. Preliminary report on the bedrock geology of the Long Lake and Moraine Lake areas, southwestern Yukon (NTS 115A/15 and 115H/2 and 7). *In*: Yukon Exploration and Geology 2016, K.E. MacFarlane and L.H. Weston (eds.), Yukon Geological Survey, p. 87–102.

Kolaj, M., Adams, J. and Halchuk, S., 2020. The 6th generation seismic hazard model of Canada. *In*: The 17th World Conference on Earthquake Engineering, Sendai, Japan, Paper 1c-0028, 12 p.

Kreemer, C., Blewitt, G. and Klein, E.C., 2014. A geodetic plate motion and global strain rate model. Geochemistry, Geophysics, Geosystems, vol. 15, no. 10, p. 3849–3889. https://doi.org/10.1002/2014GC005407

Lacoss, R.T., Kelly, E.J. and Toksöz, M.N., 1969. Estimation of seismic noise structure using arrays. Geophysics, vol., 34, no. 1, p. 21–38. https://doi.org/10.1190/1.1439995

Lamontagne, M. and Bent, A.L., 2021. Earthquakes in the eastern Canadian Arctic: Past occurrences, present hazard, and future risk. Seismological Research Letters, vol. 92, no. 5, p. 2824–2837. https://doi.org/10.1785/0220210014

Meighan, L.N., Cassidy, J.F., Mazzotti, S. and Pavlis, G.L., 2013. Microseismicity and tectonics of southwest Yukon Territory, Canada, using a local dense seismic array. Bulletin of the Seismological Society of America, vol. 103, no. 6, p. 3341–3346. https://doi.org/10.1785/0120130068

Mihaylov, E.I., Naggar, M.H. and Dineva, S., 2016. Separation of high- and low-level ambient noise for HVSR: Application in city conditions for Greater Toronto Area. Bulletin of the Seismological Society of America, vol. 106, no. 5, p. 2177–2184. https://doi.org/10.1785/0120150389

Molnar, S., Dosso, S.E. and Cassidy, J.F., 2010. Bayesian inversion of microtremor array dispersion data in southwestern British Columbia. Geophysical Journal International, vol. 183, issue 2, p. 923–940. https://doi.org/10.1111/j.1365-246X.2010.04761.x

Molnar, S., Sirohey, A., Assaf, J., Bard, P.-Y., Castellaro, S., Cornou, C., Cox, B., Guillier, B., Hassani, B., Kawase, H., Matsushima, S., Sánchez-Sesma, F.J. and Yong, A., 2022. A review of the microtremor horizontal-to-vertical spectral ration (MHVSR) method. Journal of Seismology, vol. 26, no. 4. p. 653–685. https://doi.org/10.1007/s10950-021-10062-9

Nakamura, Y., 1989. A method for dynamic characteristics estimation of subsurface using microtremor on the ground surface. Quarterly Report of Railway Technical Research Institute, vol. 30, issue 1, p. 25–33.

Nakamura, Y., 2000. Clear identification of fundamental idea of Nakamura's technique and its applications. *In*: Proceedings of the 12th World Conference on Earthquake Engineering, Auckland, New Zealand. Paper no. 2656.

Nelson, J.L., Colpron, M. and Israel, S., 2013. The Cordillera of British Columbia, Yukon, and Alaska: Tectonics and metallogeny. *In*: Tectonics, Metallogeny, and Discovery: The North American Cordillera and Similar Accretionary Settings, M. Colpron, T. Bissig, B.G. Rusk, and J.F.H. Thompson (eds.), Society of Economic Geologists Special Publication, vol. 17, p. 53–109. https://doi.org/10.5382/SP.17.03

Park, C.B., Miller, R.D. and Xia, J., 1999. Multichannel analysis of surface waves. Geophysics, vol. 64, no. 3, p. 800–808. https://doi.org/10.1190/1.1444590

Rampton, V.N. and Paradis, S., 1979. Surficial geology and geomorphology, Pine Lake, Yukon Territory. Geological Survey of Canada, Open File Preliminary Map 16–1981, 1 sheet. https://doi.org/10.4095/119387

SESAME, 2004. Guidelines for the Implementation of the H/V Spectral Ratio Technique on Ambient Vibrations: Measurements, Processing and Interpretation. SESAME European Research Project WP12 - Deliverable D23.12, European Commission – Research General Directorate Project No. EVG1-CT-2000-00026 SESAME, 62 p.

Shapiro, N.M. and Campillo, M., 2004. Emergence of broadband Rayleigh waves from correlations of the ambient seismic noise. Geophysical Research Letters, vol. 31, no. 7, article L07614, 4 p., https://doi.org/10.1029/2004GL019491

Turner, D.G., Ward, B.C., Froese, D.G., Lamothe, M., Bond, J.D. and Bigelow, N.H., 2016. Stratigraphy of Pleistocene glaciations in the St Elias Mountains, southwest Yukon, Canada. Boreas, vol. 45, no. 3, p. 521–536. https://doi.org/10.1111/bor.12172

Wathelet, M., Chatelain, J.L., Cornou, C., Di Giulio, G., Guillier, B., Ohrnberger, M. and Savvaidis, A., 2020. Geopsy: A user-friendly open-source tool set for ambient vibration processing. Seismological Research Letters, vol. 91, no. 3, p. 1878–1889.

Wathelet, M., Jongmans, D., Ohrnberger, M. and Bonnefoy-Claudet, S., 2008. Array performances for ambient vibrations on a shallow structure and consequences over V_S inversion. Journal of Seismology, vol. 12, p. 1–19. https://doi.org/10.1007/s10950-007-9067-x

Yukon Geological Survey, 2020. A digital atlas of terranes for the northern Cordillera. Yukon Geological Survey, http://data.geology.gov.yk.ca/Compilation/2, [accessed November 20, 2023].

Appendix A

Average fundamental peak frequency (f_0) and higher order frequency peak (f_1) values for ambient vibration data collected from 23 sites (14 sensor arrays [HJ stations] and 9 single-sensor sites [TR stations]) in the Haines Junction area, Yukon. Error bounds are one standard deviation from the identified peak. F_1 peak error bounds are calculated for TR stations only.

Site name	Latitude WGS84 EPSG:4326	Longitude WGS84 EPSG:4326	F_0 peak (Hz)	F_0 peak error bounds (Hz)	F_0 amplitude, A_0	F_1 peak (Hz)	F_1 peak error bounds (Hz)	F_1 amplitude, A_1	Multiple high frequency peaks?
HJ01	60°50'17.02"N	137°19'18.78"W	0.35933	0.31622, 0.378437	4.51	42.686	–	2.32	no
HJ02	60°48'13.71"N	137°24'7.81"W	0.521971	0.504724, 0.539808	4.67	15.848	–	3.18	no
HJ03	60°48'25.91"N	137°31'0.80"W	0.599041	0.518735, 0.691779	8	40.762	–	4	no
HJ04	60°48'16.08"N	137°31'23.29"W	0.813822	0.657624, 1.00712	4.54	7.773	–	2.44	yes
HJ05	60°46'58.52"N	137°31'50.87"W	0.48207	0.465833, 0.498872	5.93	9.64	–	3.76	yes
HJ06	60°47'14.99"N	137°32'13.20"W	0.496907	0.471199, 0.524017	5.69	14.9616	–	2.12	uncertain
HJ07	60°45'25.43"N	137°30'32.95"W	0.38164	0.366159, 0.397776	5.67	14.191	–	2.47	no
HJ08	60°48'0.68"N	137°41'0.28"W	0.648612	0.618004, 0.680735	3.64	42.3887	–	3.46	no
HJ09	60°44'28.63"N	137°27'50.19"W	0.366304	0.333607, 0.402206	3.23	8.115	–	2.11	yes
HJ10	60°44'34.11"N	137°28'50.89"W	0.330034	0.290675, 0.374722	3.78	21.5663	–	2.88	no
HJ11	60°44'19.64"N	137°26'45.13"W	0.384301	0.339873, 0.434536	4.76	26.4391	–	3.26	no
HJ12	60°45'42.10"N	137°33'18.50"W	0.319797	0.302239, 0.338376	4.15	22.6249	–	3.07	no
HJ13	60°44'57.74"N	137°30'34.25"W	0.335154	0.31309, 0.358773	5.28	10.25	–	2.86	yes
HJ14	60°46'31.55"N	137°34'45.88"W	0.629003	0.581476, 0.680414	9.36	26.8211	–	4.27	uncertain

Average fundamental peak frequency (f_0) and higher order frequency peak (f_1) values for ambient vibration data collected from 23 sites (14 sensor arrays [HJ stations] and 9 single-sensor sites [TR stations]) in the Haines Junction area, Yukon. Error bounds are one standard deviation from the identified peak. F_1 peak error bounds are calculated for TR stations only. (continued)

Site name	Latitude WGS84 EPSG:4326	Longitude WGS84 EPSG:4326	F_0 peak (Hz)	F_0 peak error bounds (Hz)	F_0 amplitude, A_0	F_1 peak (Hz)	F_1 peak error bounds (Hz)	F_1 amplitude, A_1	Multiple high frequency peaks?
TR02	60°49'59.16"N	137°21'11.25"W	0.614592	0.505822, 0.746751	1.60	15.446	14.3309 and 16.6479	2.37	yes
TR05	60°48'14.85"N	137°31'23.81"W	0.290344	0.270237, 0.311947	8.88	28.9748	28.1074 and 29.869	2.76	no
TR07	60°47'6.41"N	137°31'56.23"W	0.596518	0.518478, 0.686306	2.53	none	n/a	n/a	n/a
TR08	60°48'3.67"N	137°29'0.48"W	0.29043	0.261372, 0.322717	2.56	24.0057	20.639 and 27.9217	1.73	no
TR09	60°47'19.90"N	137°32'15.68"W	0.655948	0.527858, 0.815119	2.97	19.8421	18.042 and 21.8218	1.70	yes
TR10	60°47'4.15"N	137°33'20.06"W	0.552875	0.463679, 0.659231	4.84	52.1615	50.1881 and 54.2126	2.50	no
TR11	60°45'28.21"N	137°30'39.70"W	0.377057	0.338841, 0.419584	1.79	4.57387	4.33866 and 4.82183	4.38	yes
TR15	60°44'19.64"N	137°26'45.13"W	0.405334	0.354963, 0.462852	3.91	33.681	32.4124 and 34.9993	2.48	no
TR20	60°46'18.49"N	137°30'30.36"W	0.45779	0.424018, 0.494252	1.51	14.6759	14.2999 and 15.0617	4.17	no

Appendix B

Summarized results of surface-wave dispersion inversions for data collected at 14 multi-sensor array sites in the Haines Junction area, Yukon.

Site name	Latitude WGS84 EPSG:4326	Longitude WGS84 EPSG:4326	Depth to layer boundary (m) calculated from surface-wave dispersion	Sediment velocity (m/s)	Depth to layer boundary (m) calculated from f_0
HJ01	60°50'17.02"N	137°19'18.78"W	63 ± 2	213 ± 6	116 ± 4
HJ02	60°48'13.71"N	137°24'7.81"W	149 ± 9	346 ± 21	139 ± 9
HJ03	60°48'25.91"N	137°31'0.80"W	54 ± 4	331 ± 23	118 ± 8
HJ04	60°48'16.08"N	137°31'23.29"W	46 ± 3	113 ± 10	31 ± 3
HJ05	60°46'58.52"N	137°31'50.87"W	122 ± 8	382 ± 22	164 ± 10
HJ06	60°47'14.99"N	137°32'13.20"W	160 ± 10	400 ± 50	167 ± 21
HJ08	60°45'25.43"N	137°30'32.95"W	162 ± 19	484 ± 521	162 ± 176
HJ09	60°48'0.68"N	137°41'0.28"W	87 ± 12	377 ± 30	202 ± 17
HJ10	60°44'28.63"N	137°27'50.19"W	70 ± 4	452 ± 22	263 ± 15
HJ11	60°44'34.11"N	137°28'50.89"W	87 ± 17	738 ± 68	380 ± 36
HJ13	60°44'19.64"N	137°26'45.13"W	81 ± 6	380 ± 20	218 ± 12
HJ14	60°45'42.10"N	137°33'18.50"W	108 ± 12	469 ± 35	161 ± 12
HJ13	60°44'57.74"N	137°30'34.25"W	0.335154	0.31309, 0.358773	5.28
HJ14	60°46'31.55"N	137°34'45.88"W	0.629003	0.581476, 0.680414	9.36

Hydrothermal modelling of Takhini Hot Springs (NTS 105D/14)

Xavier Léveillée-Dallaire*
Institut national de la recherche scientifique

Jasmin Raymond
Institut national de la recherche scientifique

Abstract

The Takhini Hot Springs, located northeast of Whitehorse, Yukon, exhibits significant geothermal potential with a surface water temperature of 46°C. To address the limited geological knowledge in the region, a 500 m deep well was strategically drilled in this area and intercepted warm groundwater (25°C) at a depth of 450 m. The objective of this study was to assess the geothermal potential of the Takhini Hot Springs area using 2D subsurface flow and heat transfer simulations to numerically replicate the observed temperature and gain a better understanding of heat transfer mechanisms affecting the geothermal resource. Inclined permeable layers such as contacts between fractured sedimentary units appear to facilitate groundwater circulation, creating a path for geothermal fluids to rise. A fault that is assumed to be subvertical is present in the area but does not impact the model's water circulation. A sensitivity analysis was conducted to define the impact of each model parameter on the hot springs temperature and on temperature profiles simulated in the Takhini well. The analysis revealed that boundary conditions, including basal heat flux and surface recharge, as well as rock thermal conductivity and permeability, are the most influential parameters in the model.

Introduction

The Yukon Territory in northwestern Canada shows substantial geothermal potential due to its proximity to the Pacific Ring of Fire, the abundance of plutonic rocks, the presence of major crustal-scale structures such as the Tintina and Denali faults, extensive sedimentary rock deposits and the existence of numerous hot springs. Studies on Curie depth (Witter et a*l.*, 2018), radiogenic heat generation potential from granitoid rocks (Colpron, 2019), and rock thermohydraulic properties (Langevin et a*l.*, 2020a), indicate that southern Yukon is expected to have the highest geothermal potential in the territory. Unfortunately, few detailed geothermal studies have been conducted, so sparse geoscientific data are available for an in-depth understanding of the available geothermal resources. To address this data gap, the Yukon Geological Survey (YGS) launched a geothermal-focused research initiative to integrate geological, geochemical and geophysical data, and collect additional subsurface temperature data through drilling in specific geological contexts. The wells drilled as part of this initiative are instrumental in acquiring temperature gradient measurements, contributing to a more comprehensive understanding of the region's geothermal potential.

* xavier.leveillee-dallaire@inrs.ca

This paper presents an assessment of the geothermal potential of the Takhini Hot Springs area using well data acquired by YGS in 2017 from YGS-17-01, referred to here as the 'Takhini well'. Insights from regional geological investigations and rock thermohydraulic property analysis were combined to conduct finite element simulations of subsurface flow and heat transfer using the COMSOL Multiphysics software (COMSOL, 2023). Our objective was to better understand heat transfer mechanisms that facilitate warm groundwater to seep at surface. Innovative concepts supported by 2D numerical simulations of deep subsurface temperature are presented to explain the origin of the Takhini Hot Springs. The simulations aimed to identify conditions under which the geothermal gradient measured in the Takhini well can be reproduced and provide insights into the presence of 46°C groundwater at the Takhini Hot Springs by considering the thermohydraulic properties of the surrounding rock formations. Knowledge gained through this assessment can benefit renewable energy development in the Yukon with a better understanding of the geothermal potential of the area. The Takhini Hot Springs is a major tourist attraction; understanding its origin can promote sustainable development and responsible resource management.

Project background

Previous geothermal studies

The Government of Yukon aims to achieve a 45% reduction in greenhouse gas emissions by 2030, primarily by reductions in fossil fuel use in transportation, heating, electricity generation, and industrial activities (Government of Yukon, 2022). Geothermal energy is presented as a source of green energy as part of the government's strategy to combat climate change, although little work to date has been done to better understand the Yukon's green energy resources. The YGS geothermal research program was launched in 2016 as part of the Government of Yukon's initiative to find green energy solutions. Initial studies focused on regional assessment of geothermal potential, including potential radiogenic heat production (RHP; Colpron, 2019) and regional mapping of Curie depths (Witter et al., 2018; Fraser et al., 2019). The YGS also drilled two 500 m deep temperature gradient wells to further characterize the geothermal gradient in target areas. One of these wells (YGS-17-01), which is the focus of this paper, was drilled in the vicinity of the Takhini River,

approximately 2 km west of Takhini Hot Springs (Fig. 1). This area is adjacent to a granitoid intrusion with an average potential RHP value of 4.1 $\mu W/m^3$, which is slightly higher than the average value of 2.5 $\mu W/m^3$ (Artemieva et al., 2017; Colpron, 2019). Drilling operations were conducted on a parcel of Settlement Land of the Ta'an Kwäch'än Council and were carried out in collaboration with the Da Daghay Development Corporation.

Comprehensive details and findings of the YGS' Takhini geothermal well drilling program are presented in Fraser et al. (2019). After drilling, a thermistor cable with sensors at 50 m intervals was installed in the well and temperature was measured periodically over a six-month period. After re-equilibration, the top 450 m of the well featured a geothermal gradient of 16.5°C/km, and the final 50 m showed a substantial gradient of 250°C/km (Fig. 2). This drastic gradient change is interpreted to have resulted from warm groundwater flowing along permeable rock layers.

Geological setting

At a regional scale, the Yukon can be divided into two major geological domains: rocks of the North American continental margin, and terranes that accreted to the western margin of North America in the Mesozoic–Cenozoic (Hart, 1997; Monger and Price, 2002). These two domains are roughly separated by the northwest-striking Tintina fault, a dextral strike-slip fault with approximately 430 km of early Cenozoic displacement (Gabrielse et al., 2006).

The Whitehorse trough, where the Takhini Hot Springs occur, is a northwest-elongated sedimentary basin southwest of the Tintina fault that extends from northern British Columbia to the Yukon (Hart, 1997). The basin is characterized by Lower to Middle Jurassic sedimentary rocks of the Laberge Group that include a mixture of marine and fluvial sedimentary rocks and minor volcanic rocks (Fig. 3). Rocks of the Whitehorse trough were deposited in a synorogenic basin that overlaps Stikinia and the Cache Creek allochthonous terrane (Colpron et al., 2015, 2022).

Near the Takhini well site, rocks of the Whitehorse trough (Laberge Group) consist of marine sandstone and shale of the Richthofen formation and intercalated volcaniclastic rocks of the Nordenskiöld facies (Colpron
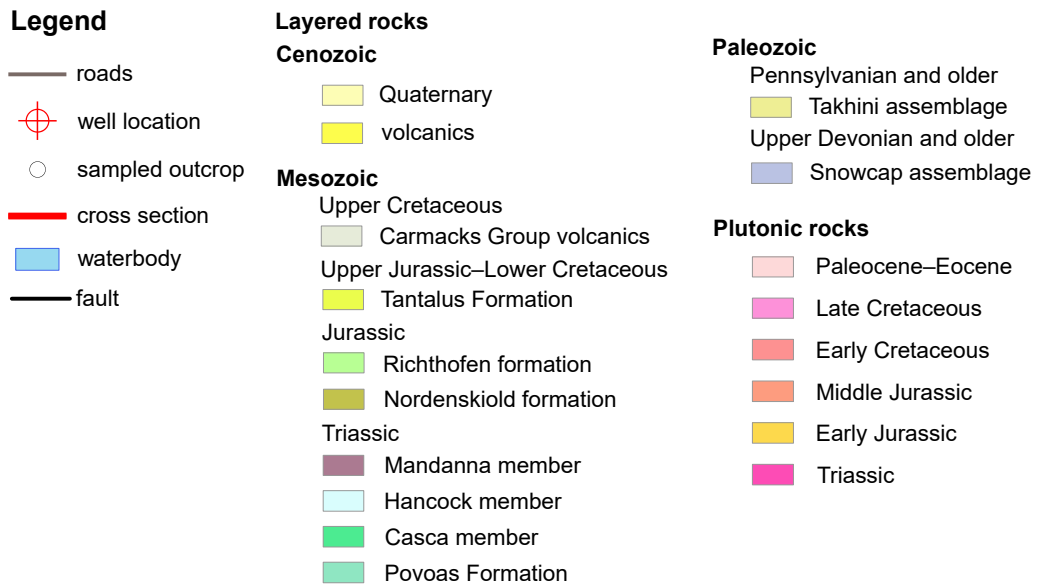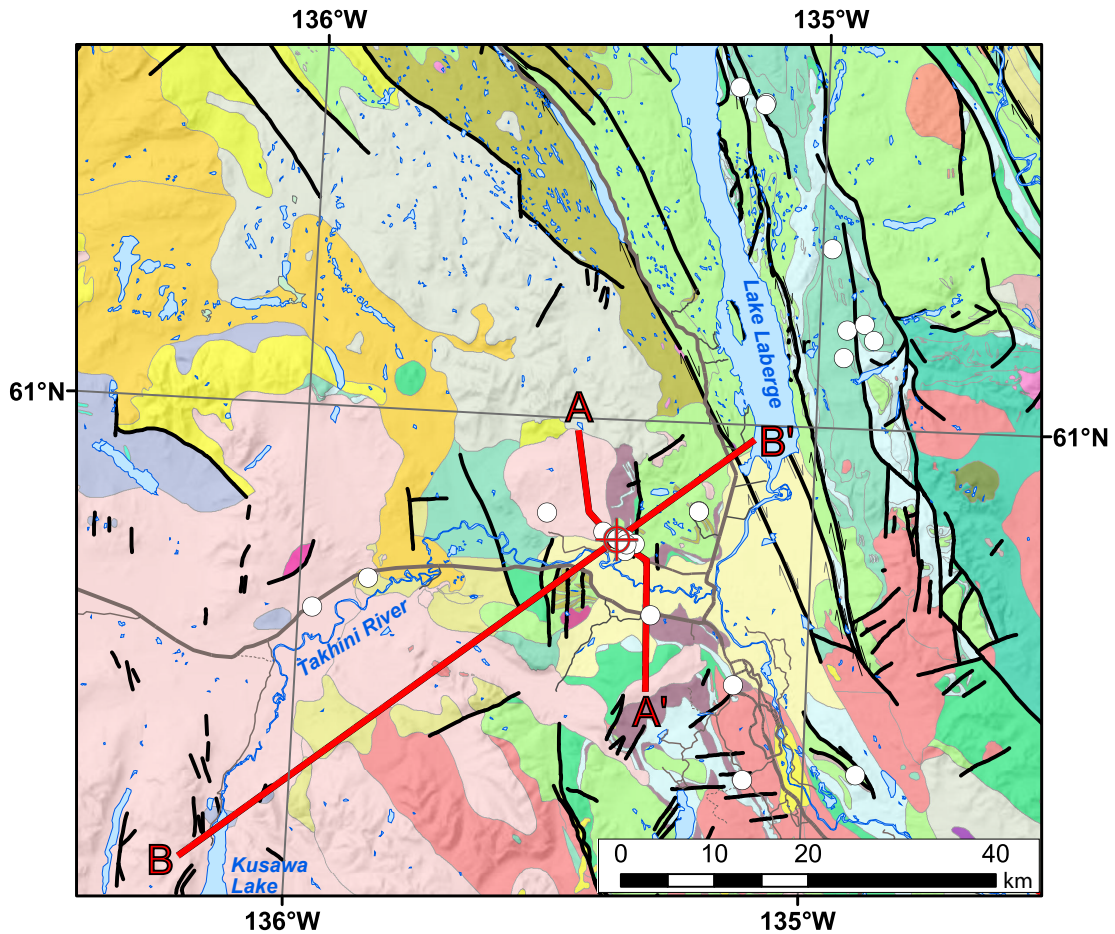
Figure 1. *Geological map of the Takhini Hot Springs area showing the locations of cross sections A–A' and B–B' from Langevin et al. (2020a). Geology from Yukon Geological Survey (2022, 2023).*
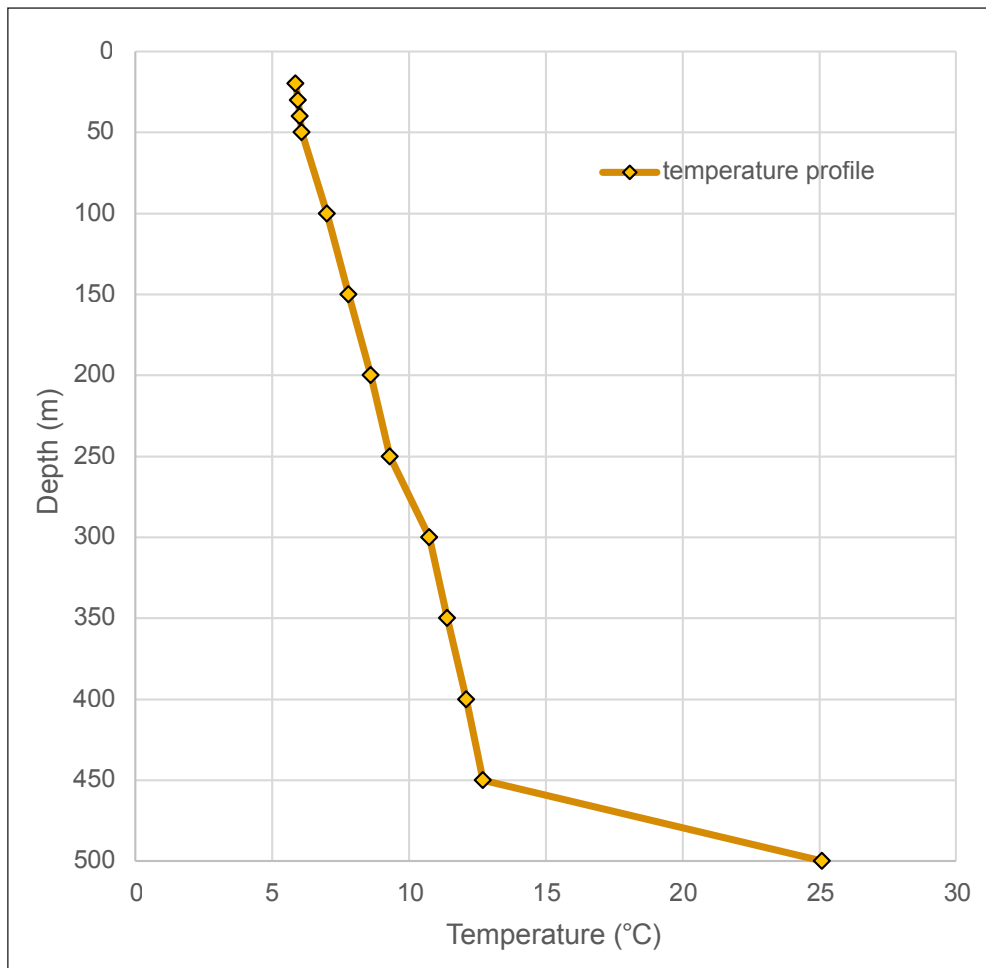
Figure 2. *Downhole temperature profile measured in the Takhini well (YGS-17-01); after Fraser et al. (2019) in Langevin et al. (2020a).*

these two publications are summarized here for context.

Logging of the Takhini well core was undertaken at the YGS H.S. Bostock Core Library in Whitehorse using hand samples and thin sections. Representative samples were also taken from relevant outcrops in the vicinity of the well to aid in interpretation. The Takhini well intercepted Lower Jurassic volcaniclastic rocks of the Nordenskiöld facies and marine siliciclastic strata of the Richthofen formation (Laberge Group). At surface, strata strike approximately 162 degrees north and dip approximately 75 degrees to the southwest. In the vertical wellbore, the dip angles on bedding vary from 45 to 85 degrees from horizontal. The well can be divided into six main lithostratigraphic units, labelled A to F in Figure 4. Unit A (55.0–82.9 m depth) mainly consists of volcaniclastic sandstone, basaltic tuff and mafic dikes. Unit B (82.9–167.1 m) consists of medium and coarse-grained volcaniclastic sandstone and minor shale. Unit C (167.1–258.1 m) consists of coarser grained version of unit B, with local pervasive carbonate alteration. Unit D (258.1–347.0 m) consists of a bluish-grey, medium to very coarse grained volcaniclastic sandstone, minor siltstone, shale and brecciated fault zones. Unit E (347.0–462.5 m) is a shale unit cut by a series of mafic and felsic dikes. Unit F (462.5–500.0 m) consists of a coarse-grained volcaniclastic sandstone succession cut by an intermediate dike.

et al., 2015; van Drecht et al., 2022). The Laberge Group rocks overlie the Upper Triassic siliciclastic (Casca and Mandanna members) and carbonate rocks (Hancock member) of the Lewes River Group (Hart, 1997). Middle Jurassic to Paleogene granitoid plutons intrude the Whitehorse trough and underlying terranes. Notably, an Eocene granite pluton (ca. 54 Ma; Hart, 1997) occurs approximately 2 km west of the Takhini drill site (Figs. 1, 3). To the southwest, rocks of the Takhini assemblage (upper Paleozoic volcanic rocks of Stikinia) are intruded by the Annie Ned batholith (ca. 57 Ma; Hart, 1997).

Thermohydraulic rock properties and heat generation

Rock thermohydraulic properties evaluated by Langevin et al. (2020a, b) were used to define the numerical model parameters in this study. Pertinent results from

Two cross sections were constructed through the Takhini well area to gain a better understanding of the groundwater flow and heat transfer in the region
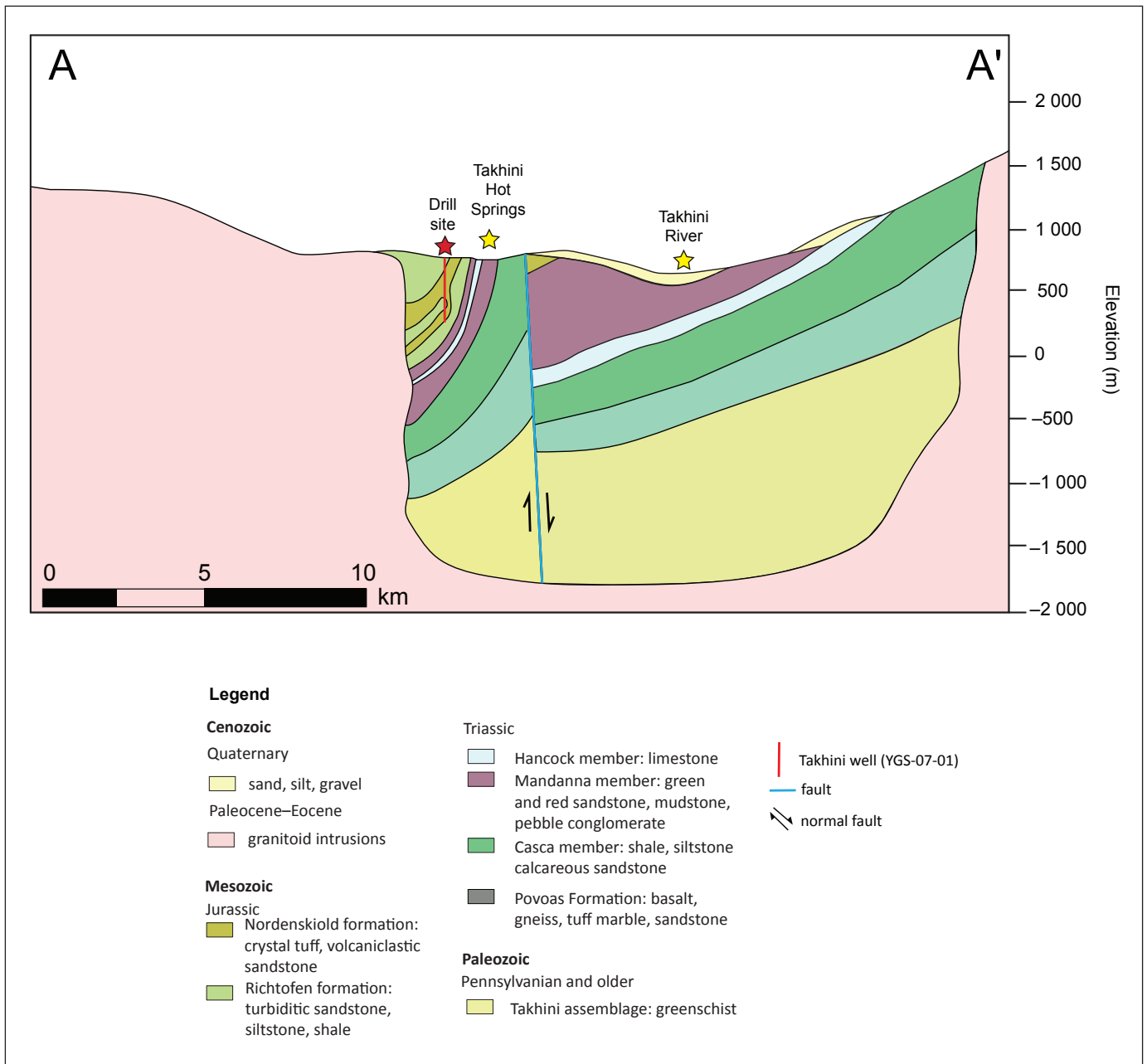
Figure 3. *Cross section A–A' showing geological interpretations in the vicinity of the Takhini well (YGS-17-01; from Langevin et al., 2020a). Geology after Hart (1997) and Colpron et al. (2015).*

(Figs. 1, 3). These cross sections were constrained using existing geological maps, core samples from the Takhini well and specific outcrop samples. Our work is based on cross section A–A' of Langevin et al. (2020a; Fig. 3), which was used to define the geometry of strata, faults, contacts and rock types in our model. Basement rocks consist of variably deformed and metamorphosed greenschist of the Takhini assemblage, unconformably overlain by Upper Triassic to Jurassic sedimentary and volcaniclastic sequences. The sedimentary rocks are cut

by steeply dipping normal faults that were developed during regional tectonic activity in the Cretaceous (Hart, 1997). Extrapolation of faults and bed thicknesses at depth are speculative.

Thermohydraulic analyses were conducted on both well core and field samples. A total of 43 well samples were analyzed for thermal conductivity at the Laboratoire ouvert de géothermie at the Institut national de la recherche scientifique (INRS) in Québec City, Quebec.
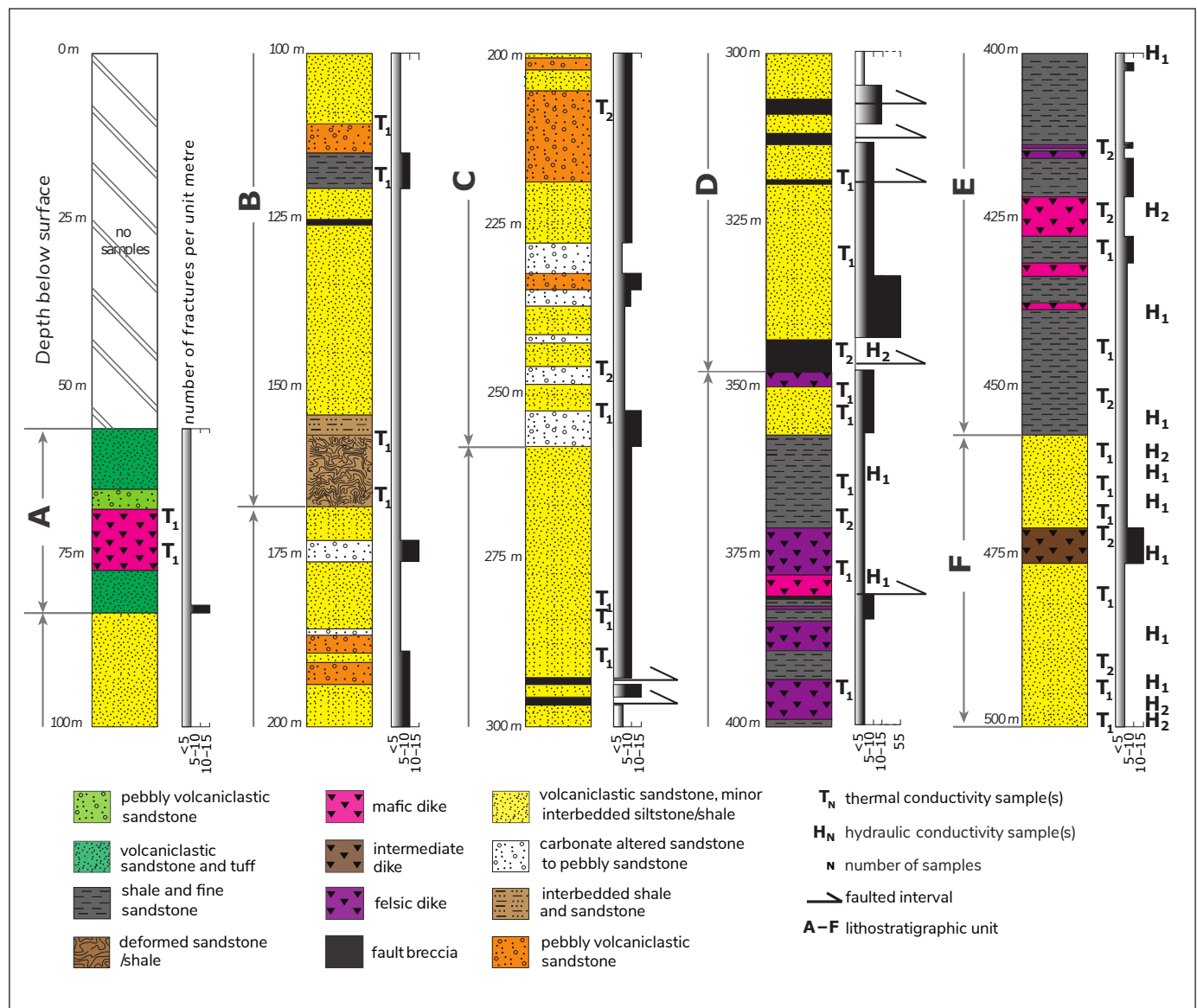
Figure 4. *Lithostratigraphy of the Takhini well (YGS-17-01) including fracture density and locations of samples taken for thermal and hydraulic conductivity analyses (after Langevin et al., 2020a).*

Thermal conductivity values in the well range from 0.63 to 4.19 W/(m·K) (Fig. 5). The highest average value was measured in the deformed sandstone and shale unit (3.81 W/(m·K)). The lowest average value was found in the breccia unit (0.98 W/(m·K) ; Langevin et al., 2020a). Analysis of thermal conductivity also included three samples from the Flat Creek pluton and two samples from the Annie Ned batholith (Ruby Range suite), which yielded average values of 2.53 and 2.39 W/(m·K), respectively. The radiogenic heat production was also measured, with an average of 3.00 μW/m^3 for the Flat Creek pluton and 1.66 μW/m^3 for the Annie Ned batholith (Langevin et al., 2020b)

Hydraulic conductivity was measured on three groups of rocks: consolidated rocks (19 core and 16 outcrop samples); unconsolidated fragments of core samples; and fractured rocks (core fractures). Analyses were made using a transient gas permeameter for consolidated core plugs and outcrop samples (PPP-250; Core Lab Instruments, 2016); grain size distribution determination for unconsolidated rock fragments (Alvarado Blohm et al., 2016); and fracture aperture and spacing using the cubic law (Witherspoon et al., 1980). Measurements indicate a general hydraulic conductivity of less than 9.6 × 10^{-9} m/s for consolidated rock matrix, with a maximum of 1.6 × 10^{-7} m/s, whereas
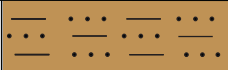
Lithology	Lithology graphic	Average thermal conductivity (W/(m·K))	Thermal conductivity [low; high] (W/(m·K))	Number of samples
deformed sandstone and shale		3.81	[3.43; 4.19]	1
carbonate altered sandstone to pebbly sandstone		3.47	[3.05; 3.89]	3
felsic dike		3.38	[3.18; 3.58]	5
interbedded shale and sandstone		3.28	[2.95; 3.61]	1
shale and fine sandstone		3.16	[2.32; 4.00]	7
pebbly volcaniclastic sandstone		3.16	[3.02; 3.30]	3
intermediate dike		3.06	[3.04; 3.08]	2
volcaniclastic sandstone, minor interbedded siltstone and shale		2.94	[2.64; 3.24]	14
mafic dike		2.39	[2.15; 2.63]	5
fault breccia		0.98	[0.63; 1.33]	2
pebbly volcaniclastic sandstone		-	-	0
volcaniclastic sandstone and mafic tuff		-	-	0

Figure 5. *Thermal conductivity of rock formations in the Takhini well (YGS-17-01; after Langevin et al., 2020a).*

brecciated (unconsolidated) rock samples had an average hydraulic conductivity of 5.6×10^{-4} m/s (Fig. 6). Lithologies shown in Figure 6 correspond to the ones shown in Figures 4 and 5. Intervals of fractured rock resulted in values on the order of 10^{-14} to 10^{-10} m/s for superfine apertures, 10^{-10} to 10^{-6} m/s for fine apertures, and 10^{-6} to 10^{-1} m/s for moderate to large apertures.

From these studies, it was determined that the Takhini area is prone to conductive and forced convective heat transfer typical of an orogenic belt (Moeck, 2014; Langevin et al., 2020a). In these settings, forced convective heat transfer is generally found in steeply dipping crustal faults and permeable structures, which act as conduits for rising warm groundwater.

Numerical heat transfer model

Conceptual model and assumptions

A 2D conceptual model, simplified from the model proposed by Langevin et al. (2020a, b), is presented in Figure 7. The model has three rock types, including sedimentary rocks in the centre, the Flat Creek Eocene granite to the north and the Annie Ned batholith (granite) to the south. The model also includes four permeable layers (green lines), which represent boundaries between sedimentary units, as well as a subvertical fault (blue line). The lateral boundaries of the basin were simplified with straight vertical lines at the margin of both plutons.
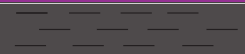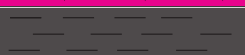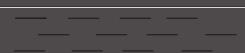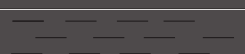
Rock type	Lithology	Well depth (m)	Hydraulic conductivity (m/s)
Consolidated		302.83–303.07	$<9.6 \times 10^{-9}$
		325.16–325.34	$<9.6 \times 10^{-9}$
		363.17–363.32	$<9.6 \times 10^{-9}$
		378.89–379.09	$<9.6 \times 10^{-9}$
		401.86–402.08	$<9.6 \times 10^{-9}$
		423.03–423.18	$<9.6 \times 10^{-9}$
		424.58–424.76	$<9.6 \times 10^{-9}$
		439.86–440.00	1.6×10^{-7}
		455.00–455.25	7.4×10^{-8}
		459.27–459.43	$<9.6 \times 10^{-9}$
		461.44–461.59	$<9.6 \times 10^{-9}$
		462.85–463.00	$<9.6 \times 10^{-9}$
		467.00–467.15	$<9.6 \times 10^{-9}$
		475.00–475.28	$<9.6 \times 10^{-9}$
		485.95–486.10	$<9.6 \times 10^{-9}$
		493.10–493.25	$<9.6 \times 10^{-9}$
		496.40–496.50	$<9.6 \times 10^{-9}$
		497.00–497.15	$<9.6 \times 10^{-9}$
		497.84–498.00	$<9.6 \times 10^{-9}$
Unconsolidated		345.32–345.52	1.8×10^{-5}
		346.00–346.20	2.0×10^{-5}

Figure 6. *Hydraulic conductivity of consolidated and unconsolidated rocks in the Takhini well (YGS-17-01; after Langevin et al., 2020a).*

The Takhini Hot Springs are situated in sedimentary rocks between two permeable layers, approximately 2 km southeast of the Takhini well and 2 km north of the subvertical fault in the model. The Takhini well in the model intersects a permeable layer at approximately 450 m depth, aiming to recreate the Takhini well temperature gradient change with numerical simulations (Fig. 2; Fraser et al., 2019). The Takhini River is located approximately 2 km south of the subvertical fault in the model.

Governing equations

The model was developed using the subsurface flow module available in the COMSOL Multiphysics software (COMSOL, 2023). Steady state groundwater flow was simulated using the finite element method based on Darcy's law coupled with heat transfer in porous media, allowing us to simulate convective heat transfer, mainly occurring along permeable layers. Darcy's law is expressed as

$$\boldsymbol{u} = -\frac{k}{\mu}\nabla P \qquad (1)$$

where $\boldsymbol{u}$ represents the fluid velocity within the porous medium in m³/s, k is the permeability of the medium in m², μ is the dynamic viscosity of the fluid in kg/(m·s), and ∇P represents the pressure gradient in Pa/m. Velocity vectors found with the flow solution are used to compute heat transfer according to

$$\lambda_{\mathrm{b}} \left(\frac{\partial^2 T}{\partial x^2} + \frac{\partial^2 T}{\partial z^2} \right) - \rho_{\mathrm{f}} C_{\mathrm{f}} \left(u_{\mathrm{x}} \frac{\partial T}{\partial x} + u_{\mathrm{z}} \frac{\partial T}{\partial z} \right) + A = 0 \quad (2)$$

where λ_{b} is the bulk thermal conductivity in W/(m·K), T represents the temperature in K, ρ_{f} is the density of the fluid in kg/m³, C_{f} is the heat capacity of the fluid in J/(kg·K) and A is the internal heat generation from the decay of radiogenic elements in μW/m³.

Geometry and subsurface properties

Geometry

The modelled section, referred to as E–E', is 31 km long (Fig. 8) and 4 km deep (Fig. 7). The model was chosen to incorporate the regional valleys and topographic highs and includes both the location of the Takhini Hot Springs and the projected Takhini well. The model also includes the subvertical normal fault that was mapped approximately 2 km east of the hot springs (projected

to the south of the hot springs in our model). The dimensions of the pluton and dip of the sedimentary units follow the interpretation of Langevin et al. (2020a, cross section A–A'; Fig. 3). The Flat Creek pluton occupies the northern 8.9 km of our model, whereas the Annie Ned batholith fills the southern part of the model, from 21.6 to 31 km. Sedimentary units dip at approximately 50 degrees to the north. The thickness and geometry of sedimentary units were mostly determined by trial and error, until simulations showed an appropriate well temperature profile and hot springs temperature. A 1D observation line was set approximately 2 km north of the hot springs, at the location of Takhini well, to evaluate temperature at depth. Sedimentary units and granitic rocks were defined as low-permeability 2D units. Faults and permeable layers are defined as 1D linear elements superimposed onto the 2D porous medium. The model geometry allowed the fluid to travel along faults and permeable layers.

Hydrothermal properties and radioactive heat generation

All model input parameters for rock and fault properties are shown in Figure 7 and Table 1. The geology was simplified in the model to facilitate numerical development and computations, especially in sedimentary units. Geo1 and Geo2 represent the most
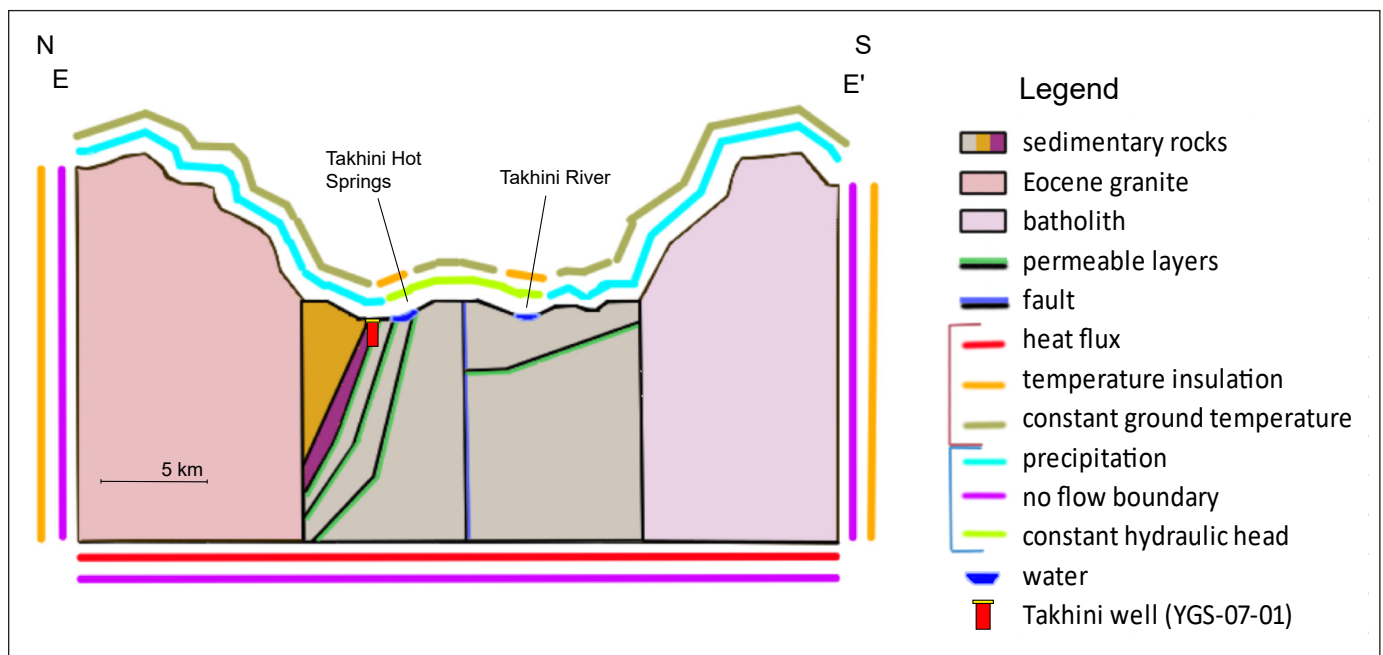
Figure 7. *Conceptual model of the Takhini Hot Springs. BC: boundary condition.*
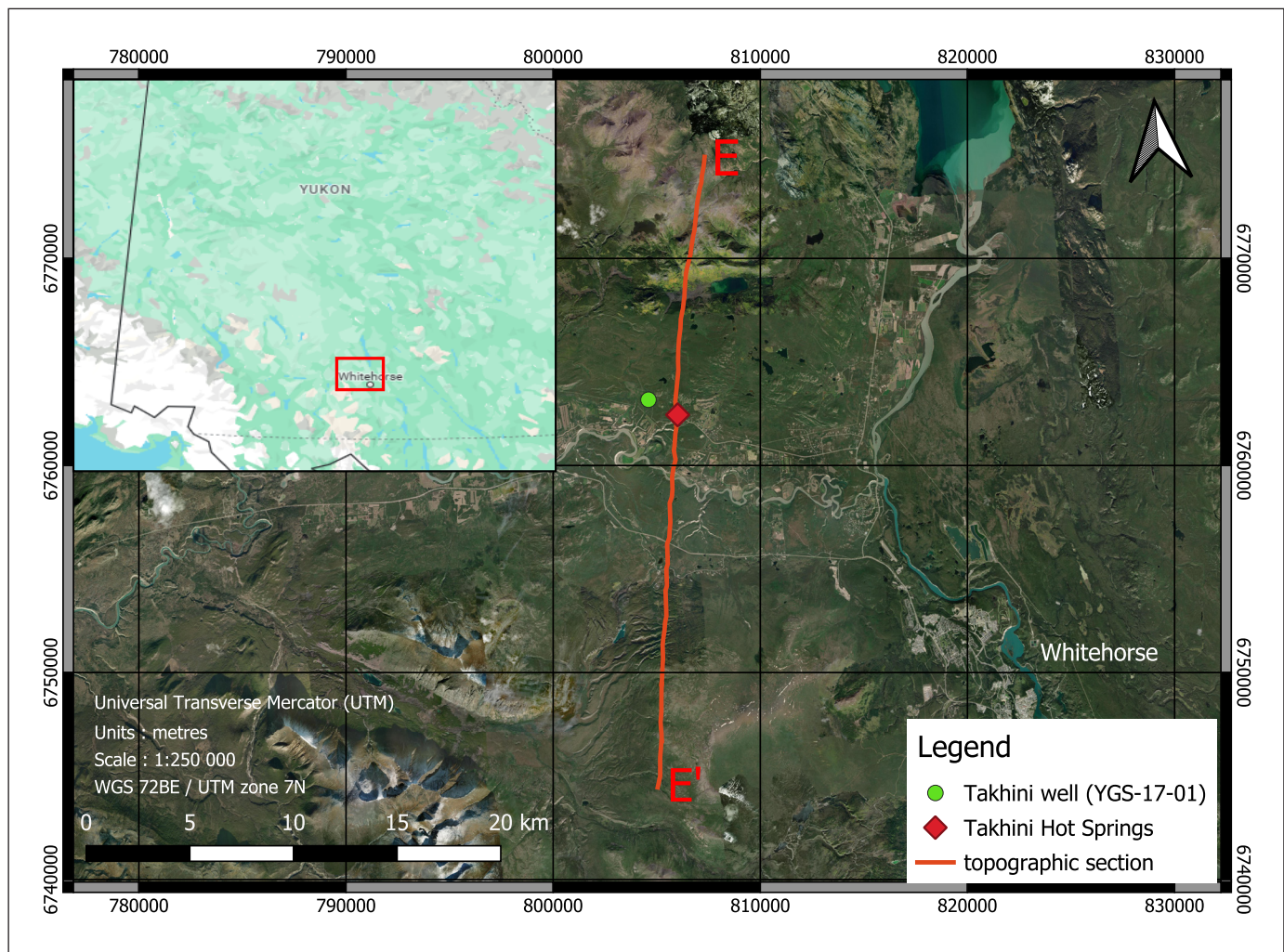
Figure 8. *Location of topographic section E–E', used to define the surface of the model (Esri Canada, 2023).*

common sedimentary rock types, namely deformed sandstone and volcaniclastic sandstone, respectively. All properties were assumed constant and not variable with depth.

Thermal conductivity and permeability for the fault and permeable layer were initially based on the work of Langevin et al. (2020a) from the analysis of two fault breccia samples that resulted in an average thermal conductivity of 0.98 W/(m·K) and an average hydraulic conductivity of 7.05×10^{-4} m/s. Although our initial model was based on these values, both properties changed when calibrating the model to reproduce the Takhini well temperature profile. High permeability was attributed to the permeable layers to create corridors ensuring water circulation. The calibrated model properties are listed in Table 1.

Boundary conditions

Flow

A surface constant hydraulic head of 640 m was applied to the whole valley, including both the river and the hot springs, to allow groundwater to exit through Takhini Hot Springs and the Takhini River. An infiltration rate of 18 mm/year was assigned to the surface boundary outside of the valley bottom, which is equal to approximately 7% of annual precipitation in the Whitehorse area (262 mm/year; Government of Canada, 2023). Water recharge diverges from annual precipitation because it specifically reflects the portion of precipitation that infiltrates the ground to replenish aquifers, accounting for factors like evapotranspiration and surface runoff. The recharge specified here is thought to be characteristic of deep aquifers. Regional groundwater flow is simulated and superficial aquifers

Table 1. *Model input parameters for rock and fault properties in the Takhini Hot Springs area. Colours match those in Figure 5.*

Material	Permeability (m^2)	Thermal conductivity of solids (W/(m·K))	Porosity	Radiogenic heat generation (μW/m^3)	Thickness (m)
Eocene granite	3.05×10^{-15}	2.5*	0.016	6.00**	–
batholith	9.78×10^{-15}	2.4*	0.016	1.66*	–
Geo1	2.00×10^{-14}	5	0.016	0	–
Geo2	2.37×10^{-13}	2.3	0.016	0	–
shale	8.00×10^{-18}	0.4	0.016	0	–
permeable layer	7.00×10^{-7}	0.6	0.2	0	0.05
fault	2.75×10^{-8}	0.6	0.1	0	0.01

* from Langevin et a*l*. (2020b); ** from Colpron et a*l*. (2019)

that could be found in Quaternary deposits are not represented in the model. The left, right and bottom boundaries are impermeable (Fig. 7) allowing for groundwater flow to follow the natural topography with recharge in mountains and discharge in the valley.

Heat transfer

Bottom heat flux was set to 0.05 W/m^2, based on heat flow values in the area (Witter et a*l*., 2018) and then adjusted by trial and error. Surface ground temperature was set according to equation 3:

$$T(K) = 278.15 - 0.0065 \times (z - 830) \qquad (3)$$

where z represents the elevation of every point on the upper boundary, in metres. The equation assumes a constant surface ground temperature of 278.15 K at an altitude of 830 m, with a temperature gradient of –0.0065 K/m to simulate lower temperatures at higher elevation. The surface ground temperature equation was applied on the whole upper boundary, except for the Takhini Hot Springs and the Takhini River, which are insulated boundaries where temperature is calculated according to the model solution.

Mesh

A mesh is a computational grid or network of interconnected elements used to discretize and represent the geometry of a domain for numerical simulations. Refinement of the mesh increases from bottom to top and close to the faults and contacts to avoid convergence problems (Fig. 9). Groundwater flow mostly follows permeable layers, highlighting the importance of refining the surroundings of permeable layers to allow for accurate computations. The mesh is composed of extremely fine free triangles applied on the entire geometry and consists of 143 280 elements. The average skewness of the mesh is 0.8948, meaning that the mesh elements have shapes closer to their ideal configurations, contributing to improved numerical stability and reliability of the simulations.

Sensitivity analysis

A sensitivity analysis was conducted once input parameters were adjusted to reproduce the Takhini well temperature profile and the temperature of Takhini Hot Springs. This calibrated model, where input parameters are adjusted to reproduce the observed temperature, is the base case scenario used as the foundation for
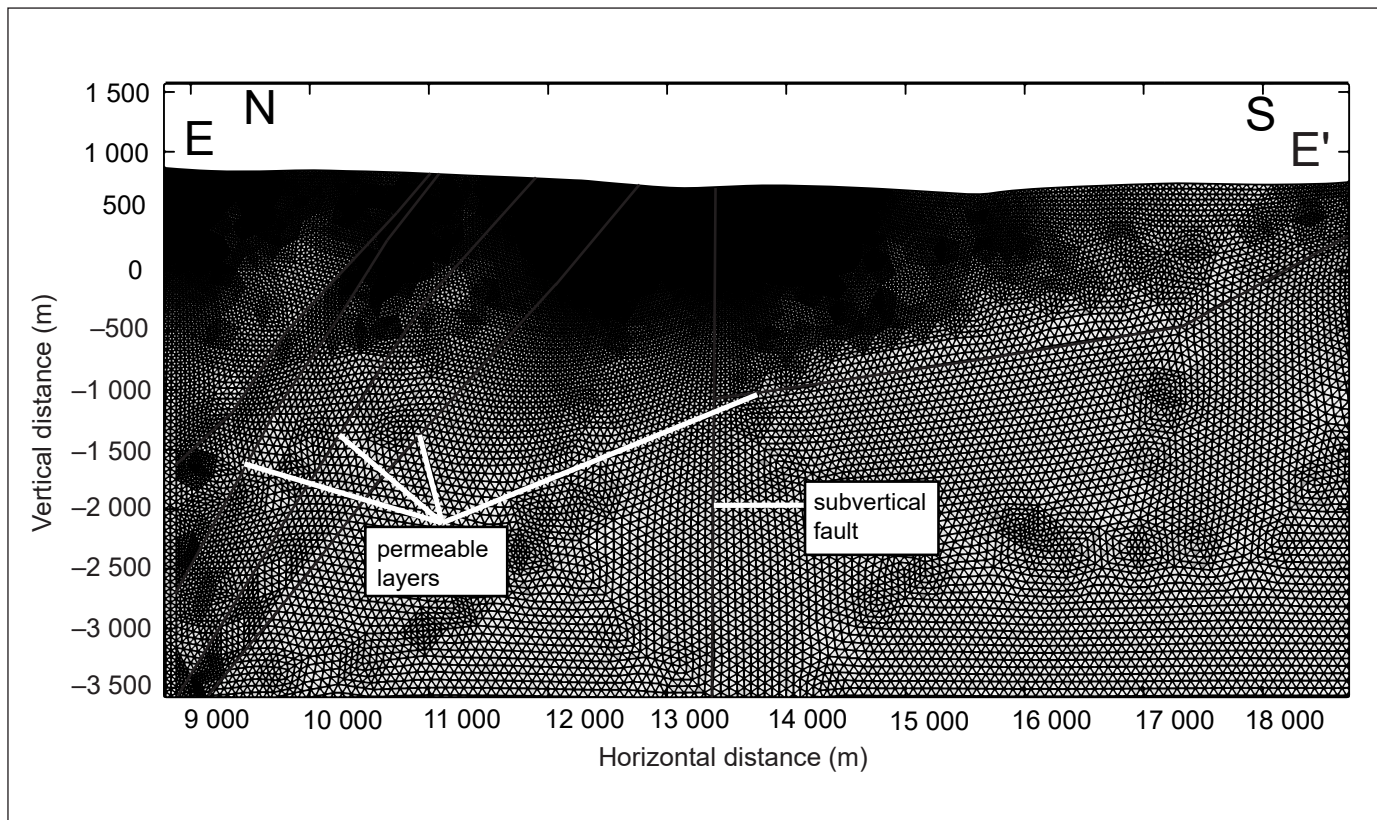
Figure 9. *Finite element mesh of the 2D numerical model for the Takhini Hot Springs area.*

subsequent simulations of the sensitivity analysis. The goal was to define the impact of each parameter on the simulated hot springs temperature and the temperature profile in the Takhini well. For every parameter, hot springs temperature and a well temperature profile was calculated and compared with the base case scenario. The parameters were grouped into three categories: material properties (red), model geometry (green) and boundary conditions (blue). Ultimately, thermal conductivity, permeability, radiogenic heat production, thickness of fractures, dip of layers, presence of a subvertical fault, recharge and heat flux were varied (Table 2).

Results

Temperature distribution and flow velocity

Figures 10 and 11 show temperature distribution with flow velocity vectors and hydraulic head distribution obtained with the calibrated model, respectively. Most of the groundwater on the north side of the model travels through the permeable layers. Heat accumulates in the sedimentary units below the shale layer and near the hot springs. In comparison, the ground below the Takhini River, located to the south of the subvertical fault, is not as hot as the north side of the fault due to its distance (approximately 3 km) from the inclined permeable layers.

Well temperature profile

The Takhini well temperature profile reported by Fraser *et al.* (2019) is compared to the simulated Takhini well temperature for the base case scenario in which parameters were adjusted to fit observations (Fig. 12). The simulated temperature gradient in the upper portion of the well shows a linear trend. This is due to the simplified model units and geometry used to save computational time. Local variations in the temperature gradient are not reproduced, though the effect of the permeable layer is clearly seen at the base of the well, where there is a steep change in temperature gradient.

Table 2. Model parameters that were varied for sensitivity analysis.

	Parameter	Units	Initial value	Variation
material properties	thermal conductivity (Geo1 / Geo2)	W/(m·K)	5 / 2.3	± 1
	permeability (Geo1/Geo2)	m^2	2.4e−14 / 2.37e−13	÷ 100, × 100
	radiogenic heat generation (Flat Creek / Annie)	$\mu W/m^3$	6 / 1.66	± 50%
model geometry	thickness of fractures	m	0.05	÷ 10, × 10
	angle of layers	degrees	50	± 25
	presence of a subvertical fault	–	–	–
boundary conditions	recharge	mm/year	18 (6.87% of Whitehorse annual precipitation)	± 13 (± 5% of Whitehorse annual precipitation)
	heat flux	W/m^2	0.05	± 0.015

Sensitivity analysis

Takhini well temperature profile

The simulated temperatures for the 500 m well are presented in Figure 13, showing the impact of individual parameters on ground temperature compared to the base case scenario. The sum of squared differences between temperature profiles with respect to that of the base case was calculated for all variations in parameters in the sensitivity analysis (Table 3).

The ranking of parameter impact (high to low) on the Takhini well temperature profile is as follows: 1) steeply dipping permeable layers, 2) recharge, 3) heat flux, 4) rock thermal conductivity, 5) rock permeability, 6) radiogenic heat generation, 7) thickness of permeable layers, 8) shallow-dipping permeable layers and 9) the presence of a subvertical fault at the centre of the model. Results indicate that both recharge and heat flux (boundary conditions) significantly influence the overall temperature of the model; rock thermal conductivity (input parameter) is also a notable factor.

Steeply dipping permeable layers reduce the overall temperature in the model, whereas the shallow-dipping model exhibits a profile similar to the base case scenario. Increasing rock permeability has more impact than decreasing it.

Takhini Hot Springs temperature

The range of simulated hot springs temperature for all parameters is shown in Figure 14. The ranking of parameter impact (high to low) on the hot springs temperature is 1) heat flux, 2) rock thermal conductivity, 3) permeability, 4) recharge, 5) radiogenic heat generation, 6) thickness of permeable layers, 7) angle of permeable layers and 8) the presence of a sub-vertical fault. Results indicate that heat flux and recharge (boundary conditions), rock thermal conductivity and rock permeability (input parameters) significantly influence the hot springs temperature, whereas other parameters barely affect the water temperature. Increasing or reducing a single parameter would be sufficient to obtain a temperature of 46.5°C.
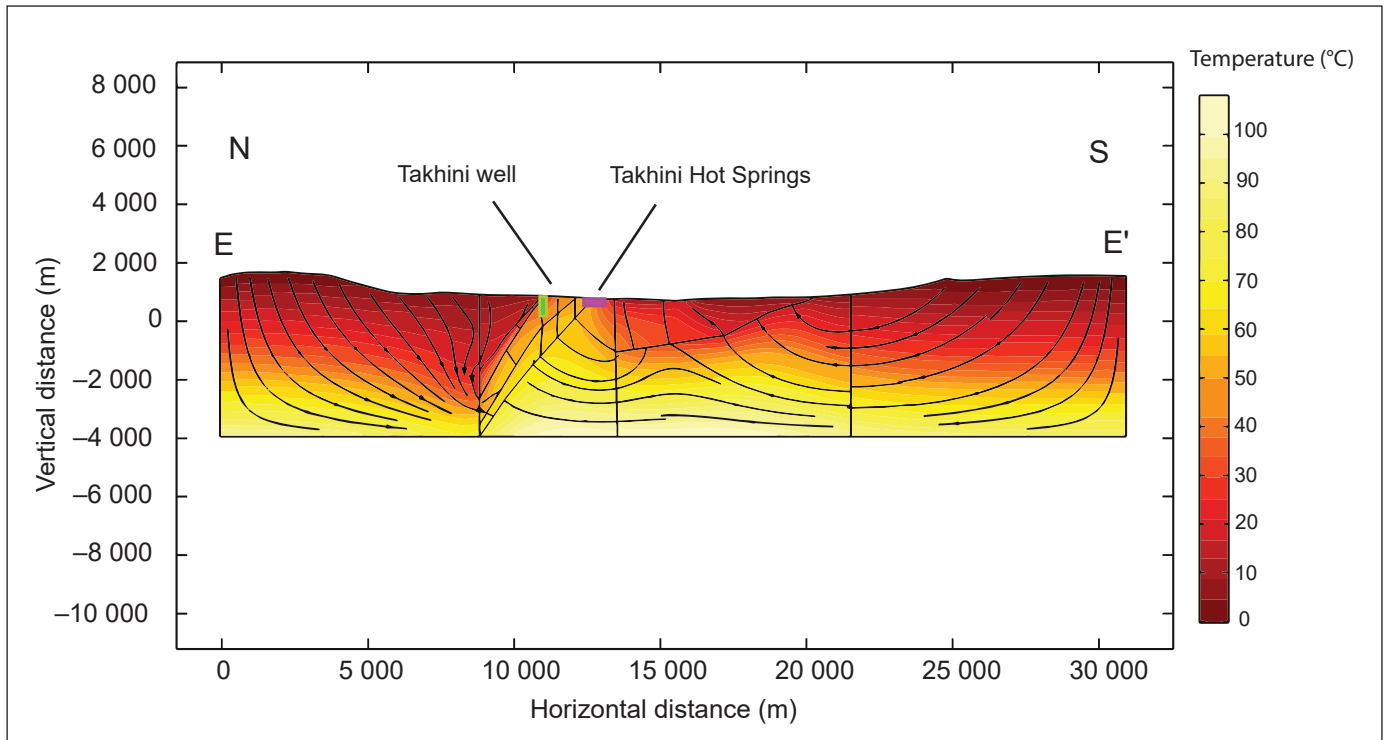
Figure 10. *Simulated temperature distribution and flow lines for topographic section E–E' in the Takhini Hot Springs area.*
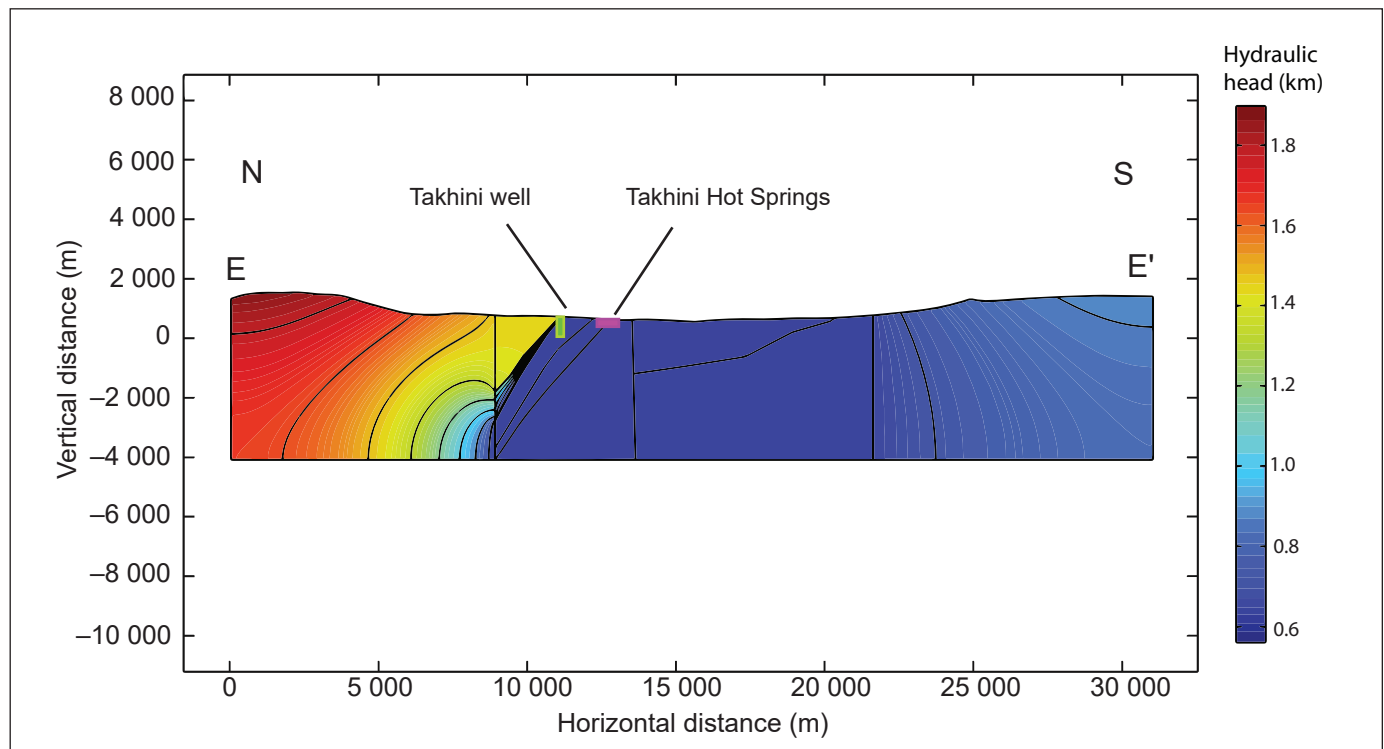
Figure 11. Simulated hydraulic head for topographic section E–E' in the Takhini Hot Springs area.
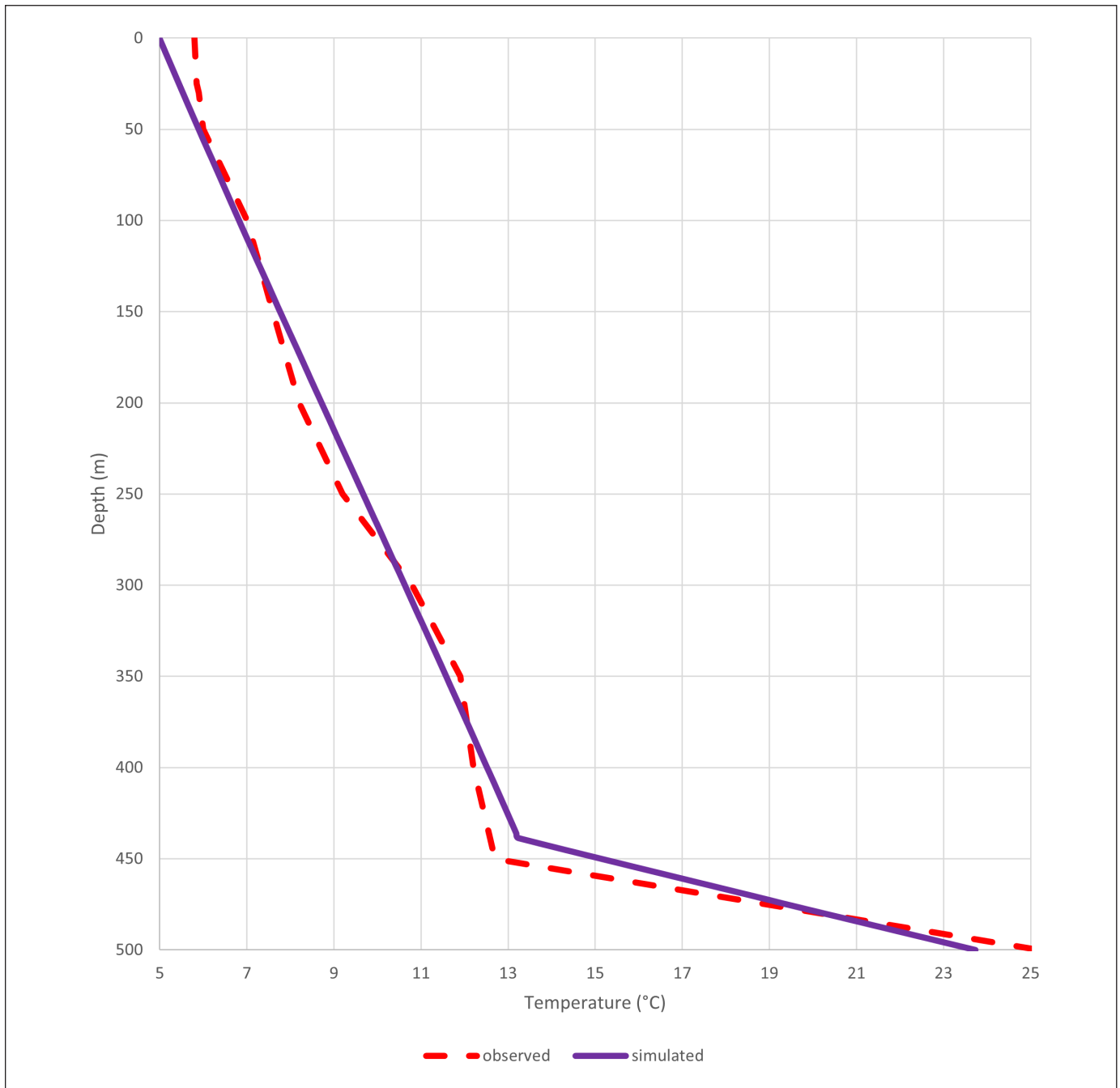
Figure 12. Comparison of observed (Fraser et al., 2019) and simulated (this study) temperature in the Takhini well (YGS-17-01) for the base case scenario.

Discussion

Critical parameters such as heat flux, recharge, and rock thermal conductivity and permeability have substantial influence in our model of the Takhini Hot Springs geothermal system. These parameters mainly control the temperature's behaviour and dictate the overall thermal dynamics at the well and the hot springs'

locations. Heat flux and recharge influence the system's energy input and output, which have an important impact on the overall water temperature. Rock thermal conductivity and permeability are the main controllers of heat transfer and fluid flow, shaping the temperature distribution and the paths taken by the groundwater.
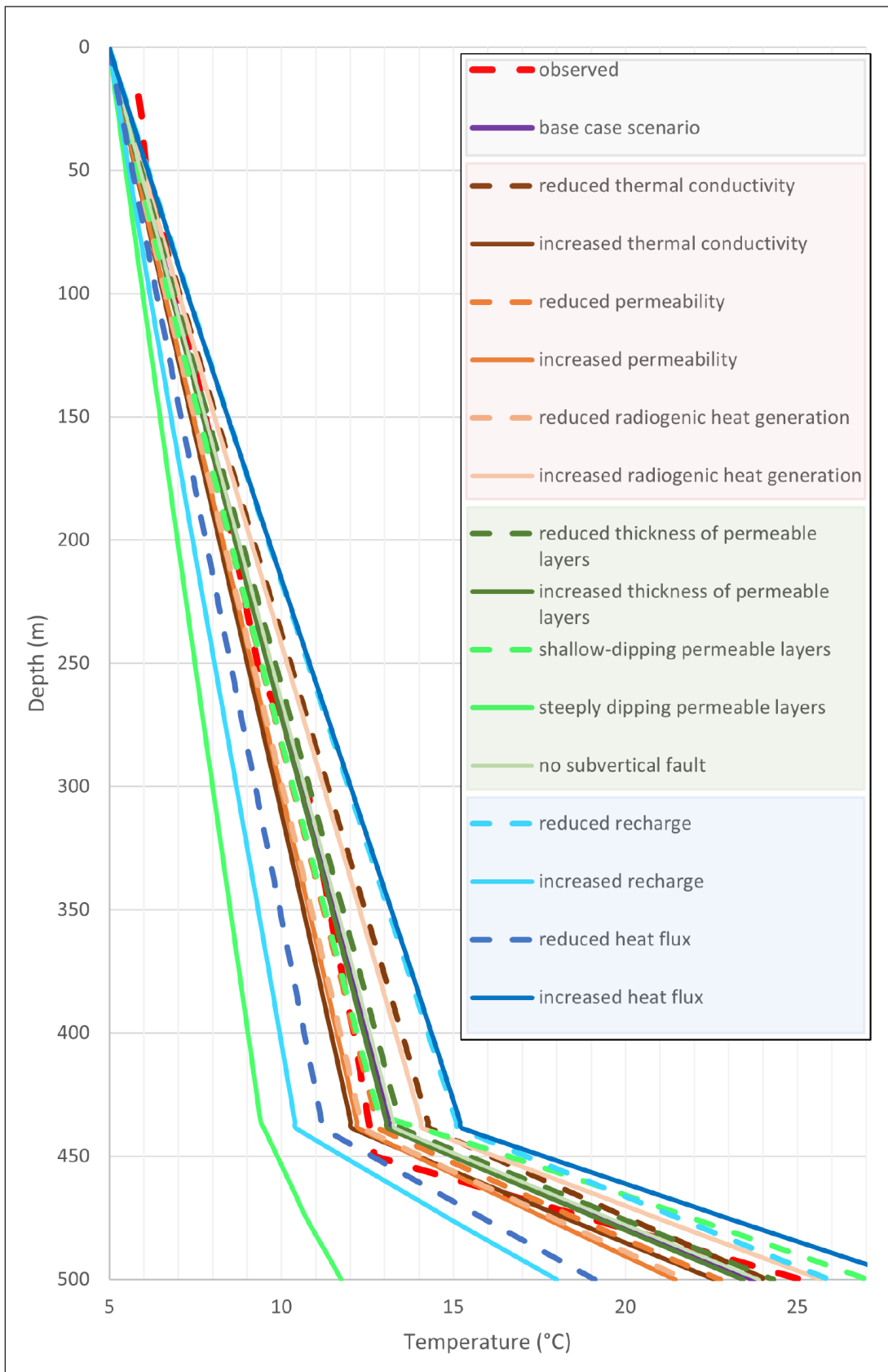
Figure 13. Simulated well temperature profiles for all parameters of the sensitivity analysis.

Table 3. Sum of squared differences for all scenarios with varying parameters of the sensitivity analysis. All parameters are compared to the base case scenario. Positive values imply an overall increase in the temperature profile, whereas negative values suggest a decrease in temperature..

Parameter	Sum of squared difference
reduced thermal conductivity	15.24
increased thermal conductivity	−21.02
reduced permeability	−4.80
increased permeability	−22.70
reduced radiogenic heat generation	−17.89
increased radiogenic heat generation	17.89
reduced fractures thickness	1.59
increased fractures thickness	−0.43
shallow-dipping beds	−27.44
steeply dipping beds	−466.81
no subvertical fault	0.11
reduced recharge	60.75
increased recharge	−172.47
reduced heat flux	−96.85
increased heat flux	96.85

The model shows that groundwater seepage toward the surface can be caused by highly permeable layers of inclined sedimentary rocks. This results in high temperature in the Takhini Hot Springs area, allowing the hot water to circulate freely. It also shows the importance of low-permeability layers (shale), which tend to act as an insulator to the underlying reservoir. The steeply and shallowly dipping permeable layers exhibit distinct differences in their flow path. This geometric variation poses a challenge when attempting to evaluate its impact compared to that of other parameters; however, it is possible to adjust the geometry so that the observed temperature profile can be reproduced. The simulated well temperature reveals that shallow-dipping permeable layers allow a better circulation of the water from the surrounding mountains to the bottom of the valley, with hot water circulation along this path. Such geological settings are, therefore, more likely to create the high temperature gradient measured at the base of the Takhini well. Subvertical permeable layers do not significantly impact water circulation in the Takhini Hot Springs area but allow deeper and hotter water to directly reach the surface. The dip of the permeable layers in the model is opposite to the groundwater flow direction, creating a significant hydraulic head difference from the bottom to the top of the layers and allowing groundwater to rise.

The model geometry and input parameters are based on geological characteristics of the Takhini Hot Springs area. Calibrations based on field measurements, such as the Takhini well temperature profile and actual hot springs water temperature, ensure that the model is grounded in empirical data and not just based on theoretical inputs. The alignment between the simulations and field observations emphasizes the reliability of the model's predictions. The sensitivity analysis, which involved varying key parameters, highlighted model uncertainty that could be reduced with additional field observations.

This study provides new knowledge that can assist geothermal exploration in the Whitehorse trough. The identification of critical parameters, such as heat flux, recharge, and rock thermal and hydraulic conductivity—and their impact on the hydrothermal system—can provide guidelines for geothermal exploration. We believe that hot water circulation is caused by permeable layers in sedimentary units intercepting regional groundwater flow. Identifying
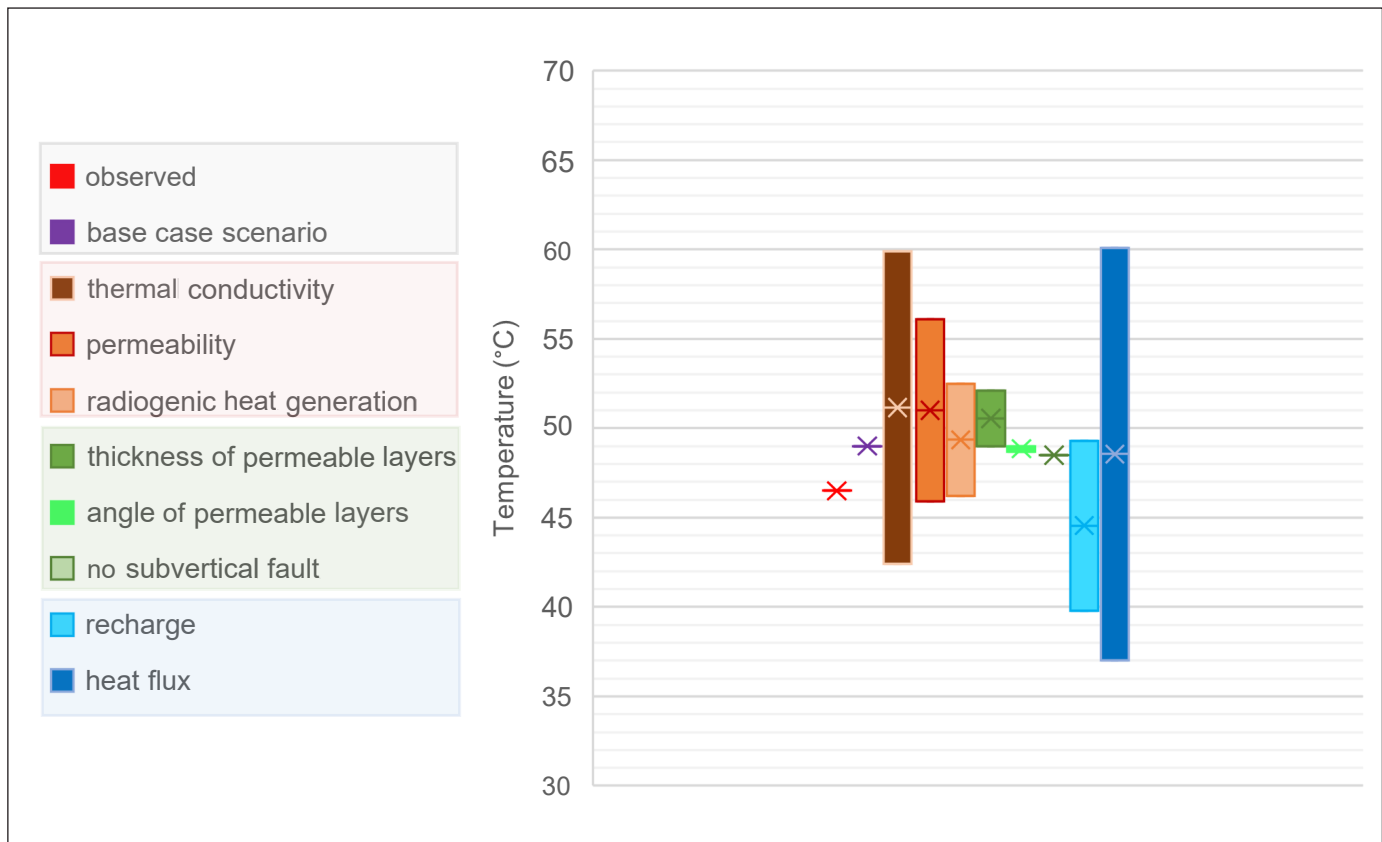
Figure 14. *Simulated and observed (Fraser et al., 2019) temperatures at Takhini Hot Springs.*

the pathways for fluid movement can help predict temperature gradients, as well as identify new targets in similar regions characterized by inclined sedimentary units that dip away from regional groundwater flow, as observed on the north side of the model. These areas can exhibit a favourable hydraulic head contrast between the base and top of the sedimentary layers, facilitating an efficient upward flow of hot water. Other locations in the Whitehorse trough could have similar characteristics, although few springs are observed at surface.

The simplified model facilitated our understanding of the flow and heat transfer mechanisms influencing the temperature distribution in the Takhini Hot Springs geothermal system. The thermal conductivity and permeability were assumed to be uniform for all units and they did not evolve with increasing temperature and pressure. This simplification favours convection over conduction. Having well data from only a single location is an important limitation in our study. Better knowledge of the dip angle, thickness and

fracture density of sedimentary units would allow a better representation of the geological model. It is difficult to identify a single rock type responsible for transporting water to surface because the model is based on simplified geology. We also simplified the basin lateral boundaries with straight vertical margins for both plutons, which differs from the hydrothermal interpretation of Langevin et al. (2020a). The overall geometry is, therefore, not an accurate representation of the Takhini Hot Springs area, but it gives a general idea of its shape and hydrothermal interactions. Previous studies indicated that the Whitehorse area has a moderate heat flux, reaching up to 60 mW/(m^2) (Grasby et al., 2012; Witter et al., 2018), which affected the temperature distribution of the entire model. A thicker pluton with higher concentrations of radiogenic elements could contribute significantly to the overall radiogenic heat generation, whereas a higher heat flux enhances the rate of heat production. Although the heat flux at the base of the model and the internal heat generation rate of plutons are likely linked, the depth of our model is insufficient for confirmation. To assess

the relationship between these factors and determine whether surrounding intrusions could represent heat sources, a deeper model that includes information on pluton thickness is required.

Conclusions

Our 2D groundwater flow and heat transfer model of the Takhini Hot Springs area was used to explore the role of key parameters—heat flux, recharge, and rock thermal conductivity and permeability—in defining the thermal dynamics of the Takhini Hot Springs geothermal system. These factors strongly affect flow and heat transfer in the basin, influencing both the simulated well and the hot springs temperatures. The model emphasizes the importance of permeable layers that facilitate hot water circulation below a low-permeability shale layer acting as an insulator to the underlying geothermal reservoir.

Built from field observations, the model is empirical and offers a good degree of accuracy, validated through calibration and a sensitivity analysis on various parameters. The study proposes a comprehensive understanding of the influence of the geometry of sedimentary units and interaction of surrounding plutons on hydrothermal flow. Although our model offers a better understanding of the Takhini Hot Springs geothermal system, it is limited by simplifications involving uniform unit properties and relying on an interpreted geological cross section. Geophysical surveys to image geological structures at depth and infer rock properties could help better constrain the model. Nevertheless, the study contributes to the understanding of Takhini Hot Springs, providing practical guidelines for exploring geothermal resources in the Whitehorse trough and beyond, and contributes to the Government of Yukon's larger initiative to identify green energy solutions.

Acknowledgments

References

Alvarado Blohm, F.J., Urzua, A., Ebel, J. and Kafka, A., 2016. Determination of hydraulic conductivities through grain-size analysis. MSc thesis, Boston College University, Chestnut Hill, United States, 102 p.

Artemieva, I.M., Thybo, H., Jakobsen, K., Sørensen, N.K. and Nielsen, L.S.K., 2017. Heat production in granitic rocks: Global analysis based on a new data compilation GRANITE2017. Earth Science Reviews, vol. 172, p. 1–26. https://doi.org/10.1016/j.earscirev.2017.07.003

Colpron, M., 2019. Potential radiogenic heat production from granitoid plutons in Yukon. Yukon Geological Survey, Open File 2019-16, 1 map and data.

Colpron, M., Crowley, J.L., Gehrels, G.E., Long, D.G.F., Murphy, D.C., Beranek, L.P. and Bickerton, L., 2015. Birth of the northern Cordilleran orogen, as recorded by detrital zircons in Jurassic synorogenic strata and regional exhumation in Yukon. Lithosphere, vol. 7, no. 5, p. 541–562. https://doi.org/10.1130/L451.1

Colpron, M., Sack, P.J., Crowley, J.L., Beranek, L.P. and Allan, M.M., 2022. Late Triassic to Jurassic magmatic and tectonic evolution of the Intermontane terranes in Yukon, northern Canadian Cordillera: Transition from arc to syn-collisional magmatism and post-collisional lithospheric delamination. Tectonics, vol. 41, no. 2, article e2021TC007060. https://doi.org/10.1029/2021TC007060.

COMSOL, 2023. COMSOL Multiphysics, version 6.1, COMSOL AB, Stockholm, Sweden. https://www.comsol.com/comsol-multiphysics [accessed November 5, 2023]

Core Lab Instruments, 2016. PPP-250 Portable probe permeameter operations manual. Core Lab Instruments. Tulsa, United States, 6 p.

Esri Canada, 2023. Satellite Image of Yukon, scale 1:250 000, ESRI, Redlands.

Fraser, T., Colpron, M. and Relf, C., 2019. Evaluating geothermal potential in Yukon through temperature gradient drilling. *In:* Yukon Exploration and Geology 2018, K.E. MacFarlane (ed.), Yukon Geological Survey, p. 75–90.

Gabrielse, H., Murphy, D.C. and Mortensen, J.K., 2006. Cretaceous and Cenozoic dextral orogeny parallel displacements, magmatism and paleogeography, north-central Canadian Cordillera. *In:* Paleogeography of the North American Cordillera: Evidence For and Against Large-Scale Displacements, J.W. Haggart, J.W.H. Monger and R.J. Enkin (eds.), Geological Association of Canada, Special Paper 46, p. 255–276.

Government of Canada, 2023. Canadian Climate Normals 1981–2010 Station Data for Whitehorse. https://climate.weather.gc.ca/climate_normals/results_1981_2010_e.html?searchType=stnName&txtStationName=whitehorse&searchMethod=contains&txtCentralLatMin=0&txtCentralLatSec=0&txtCentralLongMin=0&txtCentralLongSec=0&stnID=1617&dispBack=0 [accessed June 19, 2023]

Government of Yukon, 2022. Our Clean Future: 2021 Annual Report. Government of Yukon, Whitehorse, Canada, 82 p. https://our-clean-future.service.yukon.ca/sites/default/files/2023-10/env-our-clean-future-2021-annual-report.pdf

Grasby, S.E., Jessop, A., Kelman, M., Ko, M., Chen, Z., Allen, D.M., Bell, S., Ferguson, G., Majorowicz, J., Moore, M., Raymond, J. and Therrien, R., 2012. Geothermal energy resource potential of Canada. Geological Survey of Canada, Open File 6914, 322 p., https://doi.org/10.4095/291488.

Hart, C.J.R., 1997. A transect across northern Stikinia: Geology of the northern Whitehorse map area, southern Yukon Territory (105D/13-16). Exploration and Geological Services Division, Yukon, Indian and Northern Affairs Canada, Bulletin 8, 112 p.

Langevin, H., Fraser, T. and Raymond J., 2020a. Assessment of thermo-hydraulic properties of rock samples near Takhini Hot Springs, Yukon. *In:* Yukon Exploration and Geology 2019, K.E. MacFarlane (ed.), Yukon Geological Survey, p. 57–73.

Langevin, H., Fraser, T.A. and Raymond, J., 2020b. Assessment of the thermo-hydraulic properties of rock samples near Takhini Hot Springs and in the Tintina fault zone, Yukon. Yukon Geological Survey, Miscellaneous Report 19, 30 p.

Moeck, I.S., 2014. Catalog of geothermal play types based on geologic controls. Renewable and Sustainable Energy Reviews, vol. 37, p. 867–882. https://doi.org/10.1016/j.rser.2014.05.032

Monger, J.W.H. and Price, R.A., 2002. The Canadian Cordillera: Geology and tectonic evolution. Canadian Society of Exploration Geophysicists Recorder, vol. 27, p. 17–36.

van Drecht, L.H., Beranek, L.P., Colpron, M. and Wiest, A.C., 2022. Development of the Whitehorse trough as a strike-slip basin during Early to Middle Jurassic arc-continent collision in the Canadian Cordillera. Geosphere, vol. 18, no. 5, p. 1538–1562. https://doi.org/10.1130/GES02510.1.

Witherspoon, P.A., Wang, J.S.Y., Iwai, K. and Gale, J.E., 1980. Validity of Cubic law for fluid flow in a deformable rock fracture. Water Resources Research, vol. 16, issue 6, p. 1016–1024. https://doi.org/10.1029/WR016i006p01016.

Witter J.B., Miller C.A., Friend, M. and Colpron, M., 2018. Curie point depths and heat production in Yukon, Canada. Proceedings, 43rd Workshop on Geothermal Reservoir Engineering, Stanford University, Stanford, California, February 12–14, 2018, 11 p.

Yukon Geological Survey, 2022. Yukon digital bedrock geology. Yukon Geological Survey, https://data.geology.gov.yk.ca/Compilation/3, [accessed January 3, 2024]

Yukon Geological Survey, 2023. Surficial geology dataset. Yukon Geological Survey, https://data.geology.gov.yk.ca/Compilation/33, [accessed January 3, 2024]

Preliminary report on the bedrock geology southwest of Big Salmon Lake (parts of NTS 105F/3, 4, 5, 6), south-central Yukon

David Moynihan *
Yukon Geological Survey

Abstract

Two contrasting lower Paleozoic units underlie the region southwest of Big Salmon Lake in south-central Yukon. The lower unit comprises dolomitic quartzite, quartzite, dolostone, dolomitic shale, siltstone and sandstone, and their metamorphosed equivalents. Two-holed crinoid ossicles indicate an Early–Middle Devonian age for the dolostone. These dolomitic rocks are overlain by largely carbonate-free, dark, fine-grained and siliceous strata. Rock types include graphitic phyllite, siltstone, metachert and porphyroblastic metapelitic schist. The two units are correlated with the Askin and Earn groups, respectively. An interval of metabasaltic schist locally marks the boundary between the Askin and Earn groups. Mafic and ultramafic rocks are intermittently exposed beneath the Askin Group in parts of the region.

The lower Paleozoic metasedimentary units are crosscut by deformed Devonian–Mississippian two-mica augen gneiss and by largely undeformed mid-Cretaceous megacrystic biotite granite to monzogranite. Deformation prior to the mid-Cretaceous produced close to tight folds that trend northwest. The associated axial-planar cleavage/schistosity dips northeast at moderate to steep angles, away from the crest of a major antiformal structure.

Introduction

The Yukon Geological Survey began mapping part of the southern Big Salmon Range at 1:50 000 scale in 2020. The study area includes parts of the Teslin Lake (NTS 105D), Quiet Lake (NTS 105F) and Laberge (NTS 105E) map areas. Its boundaries include the Teslin fault in the southwest, Big Salmon Lake in the northeast, and the South Canol Highway in the southeast (Fig. 1). Preliminary observations from southwestern parts of this region are presented in Moynihan and Crowley (2022) and Moynihan (2023). This paper summarizes observations made during the summer of 2023 in northeastern parts of the study area. Two areas were mapped: the region southwest of Big Salmon Lake (Figs. 1 and 2), and a small area in the headwaters of the Boswell River (Fig. 1).

Previous work and regional geology

Wheeler et *al.* (1960) carried out preliminary bedrock mapping of the Quiet Lake map area (NTS 105F) at a scale of 1:250 000. Tempelman-Kluit led more extensive work during the 1970s and a revised map of the Quiet Lake area was released (Tempelman-Kluit, 1977). Related information on the geology of the area became publicly available when an early draft of a manuscript, initially intended as a Geological Survey of Canada memoir, was released as an open file (Tempelman-Kluit, 2012).

The southwestern part of the Quiet Lake map area is dominated by the Quiet Lake batholith, which occupies

* david.moynihan@yukon.ca
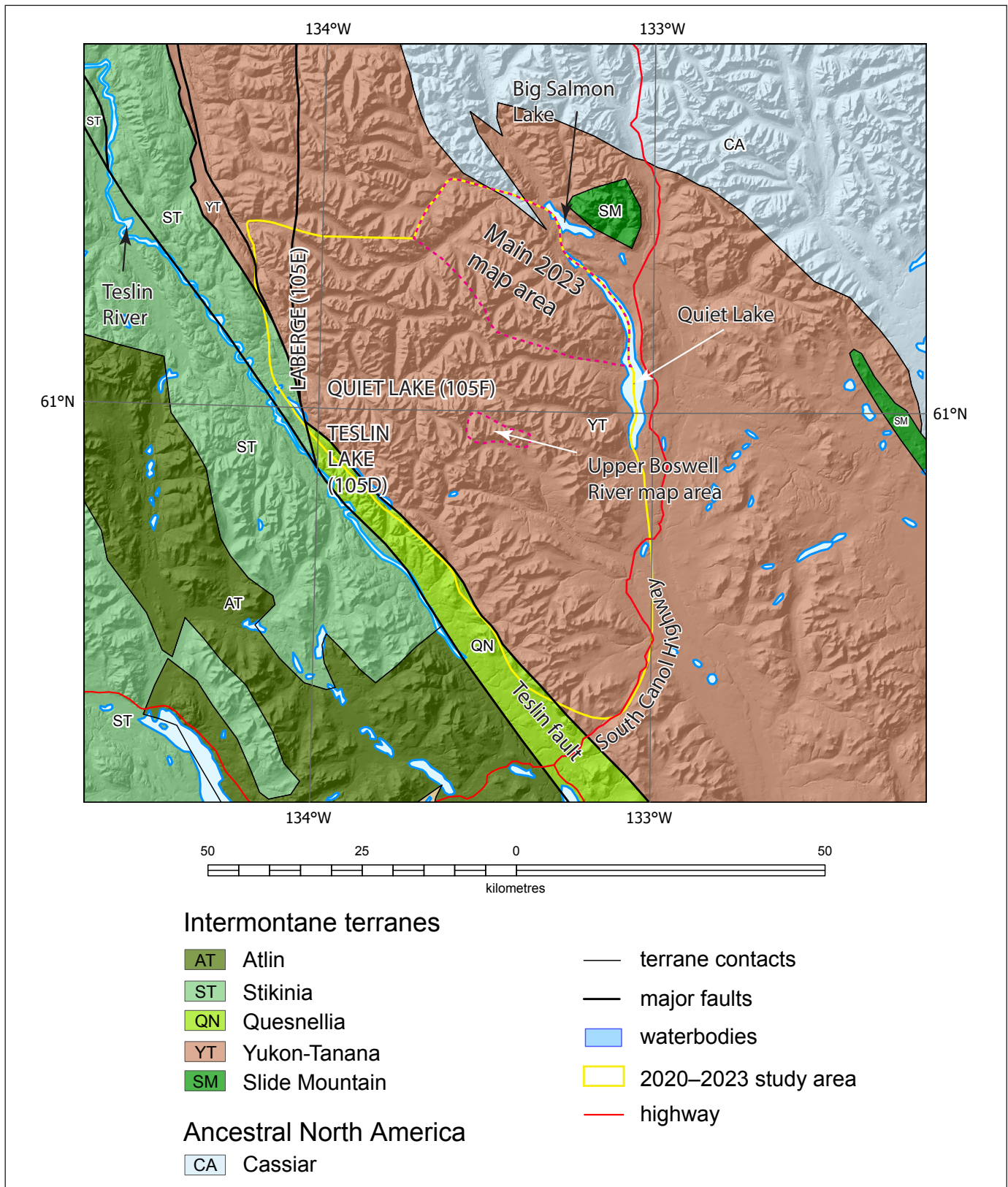
Figure 1. *Location of the 2020–2023 study region. Areas mapped in 2023 are outlined by dashed magenta lines. The base map shows the interpreted terrane assignment for this part of southern Yukon (Yukon Geological Survey, 2023). Inclusion of the 2023 mapping area in Yukon-Tanana terrane follows the interpretation of Westberg (2010).*

the core of a structural arch (Tempelman-Kluit, 2012). Most of the country rock in the area is highly deformed and metamorphosed, but Wheeler et al. (1960) noted an area of 'unmetamorphosed' rocks southwest of Big Salmon Lake, from which they recovered non–age-diagnostic fossils. Wheeler et al. (1960) recognized two units with sedimentary protoliths, which they traced across the Pelly Mountains (Cassiar platform). The older of the two is dominated by dolomitic rocks

and quartzite (their unit 4; Silurian–Devonian) and is overlain by dark fine-grained clastic rocks (their unit 5; Devonian–Mississippian). Tempelman-Kluit (2012) included all of these rocks in his Silurian–Devonian Askin Group. Informally named subunits that are exposed in the study area include the Hogg formation (dolomitic sandstone and orthoquartzite) and the Nasina formation (dark, fine-grained clastic rocks with lenses of carbonate/quartzite). Westberg (2009, 2010)
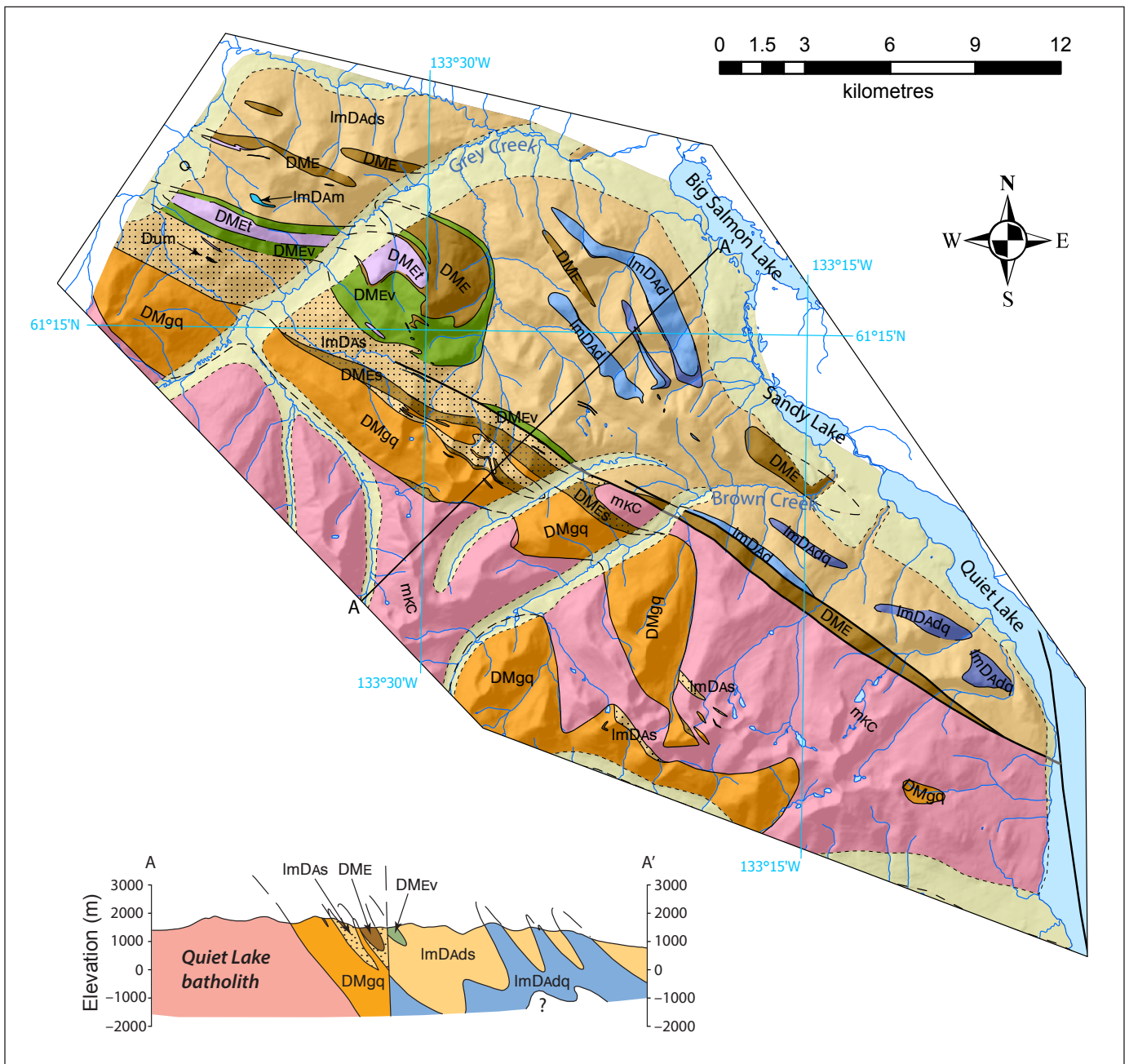
Figure 2a. *Simplified geological map and cross section of the area southwest of Big Salmon Lake.*

mapped equivalent clastic and mixed clastic-carbonate rocks in the area along strike to the northwest; she interpreted the rocks as part of the Yukon-Tanana terrane rather than the Cassiar terrane, in contrast with earlier works.

The revised terrane assignment of Westberg (2010) is not adopted here because rocks in the study area are lithologically identical to, and apparently physically continuous with, those elsewhere in the Cassiar terrane. Following Tempelman-Kluit (1977, 2012),

Cretaceous

mKC   CASSIAR SUITE: porphyritic to megacrystic biotite granite

Devonian–Mississippian

DMgq   GRASS LAKES SUITE: granitic 2-mica orthogneiss with potassium feldspar augen

Quaternary

Q   unconsolidated glacial, glaciofluvial and glaciolacustrine sediments; fluvial silt, sand and gravel deposits; volcanic ash; partly covered by soil and organic deposits

Middle–Upper Devonian

DME   EARN GROUP: rusty weathering, siliceous shale, phyllite; black siltstone; commonly contains abundant siliceous layers and lenses; minor metachert; minor thin blue-grey calcareous horizons; minor chert-granule conglomerate

DMEv   EARN GROUP: greenschist and amphibolite; tuffaceous metasiltstone and sandstone

DMEt   EARN GROUP: metachert; typically grey or black and white; locally pale green; compositionally banded, with thin micaceous folia between siliceous layers

DMEs   EARN GROUP: coarse-grained schist; commonly contains porphyroblasts of garnet and andalusite

___ fault

___ stratigraphic contact

----- covered contact

········· limit of Quaternary cover

Lower–Middle Devonian

lmDAd   ASKIN GROUP: dark grey, laminated and thin- to medium-bedded bioclastic dolostone; crinoidal debris typically dominant but includes shelly layers; pale grey, variably recrystallized fossiliferous dolostone; chert; dolomitic quartzite

lmDAds   ASKIN GROUP: dark grey, weakly dolomitic shale, siltstone and fine sandstone; forms distinctive blue-grey talus; weathered surfaces are grey to tan, locally orange-brown; fissile; blue-grey dolostone; minor medium to thick beds of quartz-rich sandstone, minor fossiliferous sandstone;

lmDAs   ASKIN GROUP: fissile dolomitic phyllite and schist; garnet and amphibole-bearing calc-silicate; typically schistose and banded; quartzite and dolomitic quartzite

lmDAm   ASKIN GROUP: marble; mostly pale to medium grey, locally also buff to cream

lmDAdq   ASKIN GROUP: white to cream, medium- to thick-bedded dolomitic quartzite; quartzite; thin- to medium-bedded dolomitic sandstone and siltstone

Dv   SUB-ASKIN BASEMENT: greenschist and/or amphibolite; commonly banded, local epidote alteration

Dum   SUB-ASKIN BASEMENT: ultramafic rocks, now mostly serpentinite; locally composed of garnet, talc and nephrite

Figure 2b. *Legend for Figures 2a and 5.*

dolomitic and quartzite-rich units are referred to as the Askin Group, whereas the fine-grained clastic rocks are assigned to the Earn Group (Campbell, 1967), based on their stratigraphic position and lithology. Gabrielse (1998) and Gordey and Makepeace (1999) correlated similar rocks elsewhere in the Cassiar platform region with the Earn Group. The term 'Nasina formation' (Tempelman-Kluit, 2012) is not used here because this name is currently applied to rocks of the Yukon-Tanana terrane in western Yukon (Mortenson, 1992; Colpron et al., 2006).

Rock units

Askin Group

Pale-grey and white-weathering dolomitic and/or quartz-rich rocks are exposed in the cores of anticlines southwest of Big Salmon, Sandy and Quiet lakes (lmDAdq and lmDAd; Fig. 2). These are overlain by finer grained, mixed siliciclastic-dolomitic rocks, which underlie much of the area between the lakes and the Quiet Lake batholith (lmDAds; Figs. 2, 3).

Dolomitic quartzite (lmDAdq; equivalent to the Hogg formation of Tempelman-Kluit [2012]) forms thick to very thick, resistant intervals that are white, pale grey and cream weathering (Fig. 4a, b). Very thick beds have some planar-laminated tops but are otherwise structureless, whereas cross-bedding is developed in some of the thick beds. A pitted texture and faint to distinct ribbing parallel to layering results from differential weathering of dolomitic cement (Fig. 4b). Calc-silicate minerals (tremolite, diopside) are locally developed within this unit.

Where well preserved, dolostone is medium to dark grey, mostly thin to medium-bedded, commonly planar-laminated dolomitic wackestone and grainstone that contains abundant fossil detritus (lmDAd; Fig. 4c). Most layers are dominated by crinoid fragments, but in rare cases layers are composed almost entirely of shelly debris with convex surfaces that systematically face downward. Thin to medium-bedded rocks mostly contain fragments less than 5 mm in diameter, but some thicker layers contain intact crinoid stems up to 5 cm long and 1 cm in diameter, as well as larger
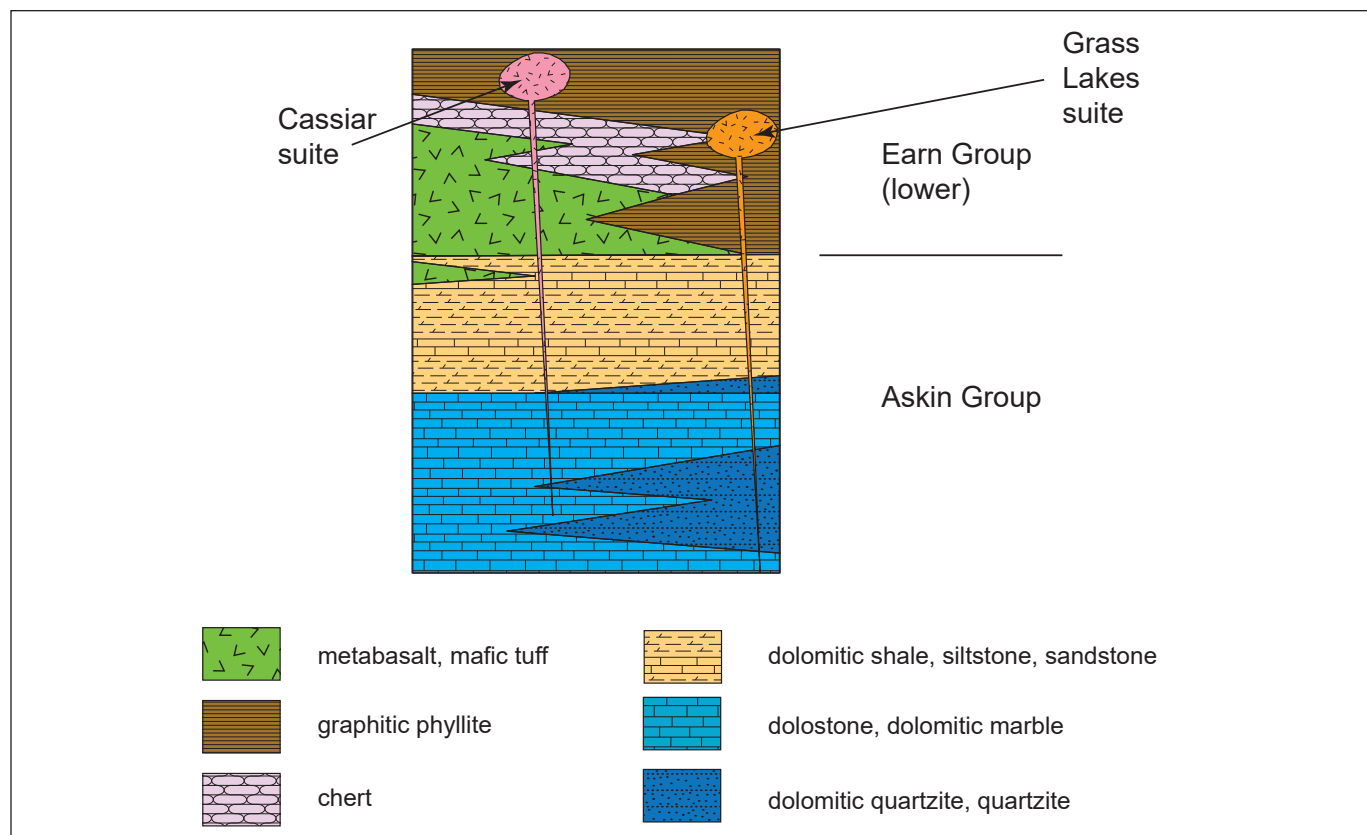
Figure 3. *Schematic stratigraphy of the area southwest of Big Salmon Lake. Not to scale.*
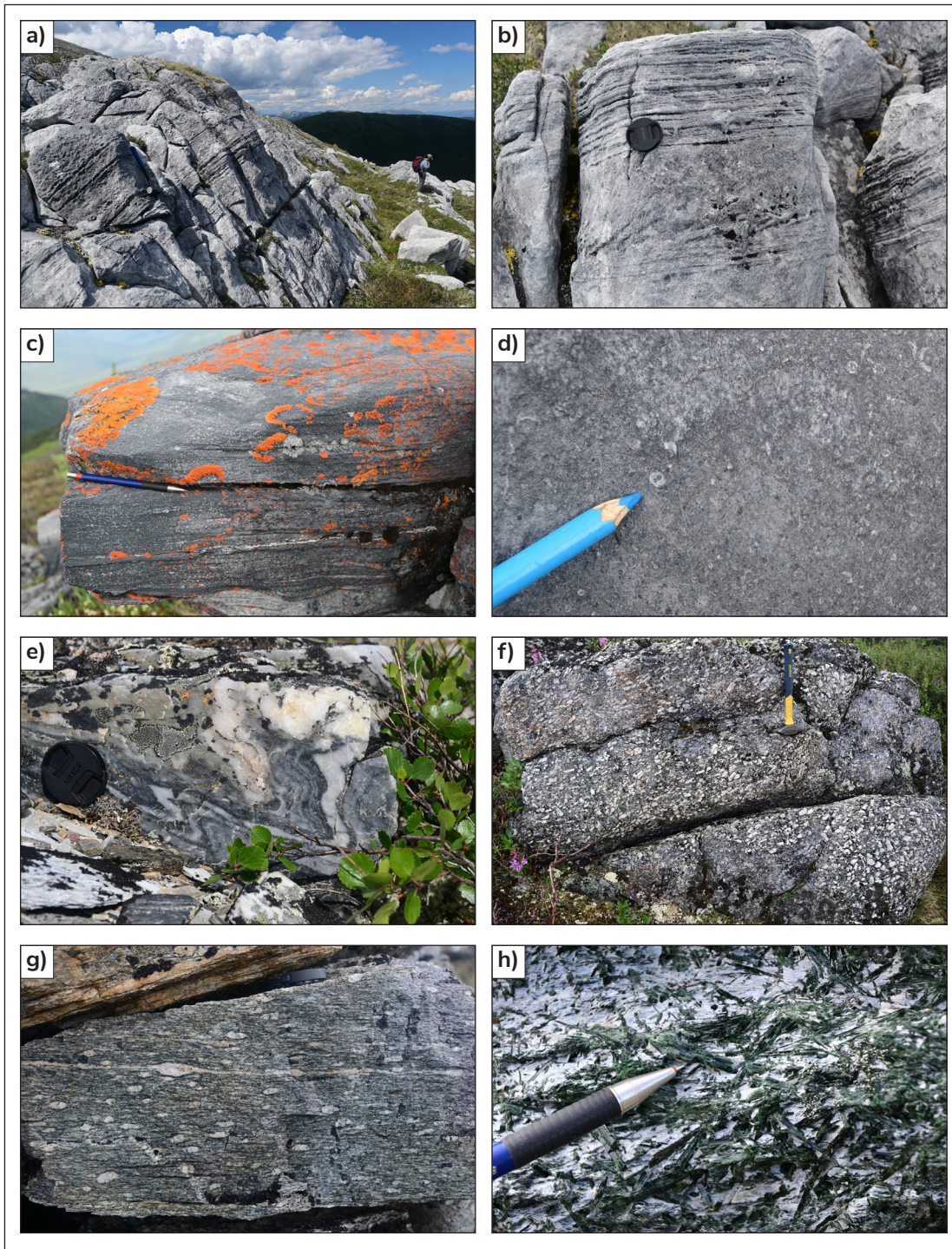
Figure 4. Representative photographs of rock units in the study area: **a)** resistant, pale-weathering dolomitic quartzite of the Askin Group (person for scale); **b)** close-up view of the outcrop in **a)**; planar laminations and cross-bedding are accentuated by variations in carbonate content (lens cap for scale); **c)** dark grey bioclastic dolomitic wackestone with abundant crinoidal debris (pencil for scale); **d)** two-holed crinoid ossicles are common in well-preserved dolostone (pencil for scale); **e)** folded layering in metachert from the lower part of the Earn Group (lens cap for scale); **f)** megacrystic phase of the mid-Cretaceous Quiet Lake batholith (hammer for scale); **g)** deformed two-mica orthogneiss with K-feldspar porphyroclasts (augen; lens cap on its side for scale); **h)** jade-green nephrite (amphibole) and talc in altered ultramafic rock northwest of Grey Creek (pencil for scale).

unidentified fossil fragments. Two-holed crinoid ossicles are common in many well-preserved outcrops, which indicates an Early–Middle Devonian age (Fig. 4d; Johnson and Lane, 1969; Nelson, 1975). Well-preserved dolostone grades laterally into more recrystallized, white-weathering dolostone with sugary texture. Fossil outlines in these rocks are indistinct and chert layers/lenses with irregular outlines are common.

The stratigraphic relationship between dolomitic quartzite (lmDAdq) and dolostone (lmDAd) is complex (Fig. 3). Dolomitic quartzite (lmDAdq) is the stratigraphically lowest unit present in the area immediately southwest of Big Salmon Lake (Fig. 2), but similar rock types locally form part of higher stratigraphic levels (Fig. 3). In several locations, a discrete interval rich in quartzite and dolomitic quartzite approximates the boundary between pale-weathering, relatively resistant dolostone (lmDAd) and overlying, finer-grained units (lmDAds). Beds in this interval range from thick to thin in upward-fining sequences. Medium and thin beds exhibit planar and cross-lamination, whereas thick beds are weakly graded. Grading in dolomite content results in variation in colour and resistance across individual beds and through multi-bed packages. Dolomitic quartzite commonly has a pitted texture and weathers white, grey, cream and tan, whereas relatively pure quartzite is pale grey and weathers white and grey to pale brown. A distinctive variety is composed of large (>1 cm) fossil fragments in a medium to coarse sandstone with a weakly dolomitic matrix; this has resulted in a pockmarked appearance on weathered surfaces. Dolomitic quartzite and quartzite is interbedded with dolomitic shale and siltstone, which weathers tan, brown, cream and grey. These finer-grained intervals are planar and locally cross-laminated and are compositionally heterogeneous. They commonly contain lamellae and lenses of siltstone to sandstone, which form resistant ribs; these resistant silty and sandy layers die out up section into the overlying unit.

The upper part of the Askin Group comprises relatively recessive, weakly dolomitic shale, siltstone and lesser fine sandstone (lmDAds). These rocks have a dull lustre and are typically medium to dark grey on fresh surfaces. In some alpine exposures, weathered surfaces are tan, buff, brown or creamy orange and differential weathering accentuates the compositional layering; elsewhere the rocks weather grey or black. Talus slopes below creek cuts and other cliffs have a

distinctive blue-grey colour. The rocks are laminated and thin bedded; locally, some minor cross-bedding is also developed. Dolomitic argillite and lesser siltstone dominate this unit, but some intervals of dolomitic siltstone to fine sandstone are also preserved. The unit contains scattered layers of dark fetid dolostone, mostly less than 1 m thick, and rare layers of olive-green–brown to grey-weathering sandstone. A single example of pockmarked, fossil-rich, weakly dolomitic sandstone/quartzite, similar to that developed in the underlying unit (lmDAdq), was also observed. Cleaved and recrystallized varieties of this unit are brown, locally chloritic, fissile, crumbly carbonate-bearing phyllite.

As noted by Wheeler et al. (1960), rocks southwest of Big Salmon Lake, though deformed, have undergone relatively little recrystallization. Rocks closer to the Quiet Lake batholith are more highly deformed and have undergone complete recrystallization during higher-grade metamorphism. Rocks of the Askin Group in this region are represented by calc-silicate schist and marble. Calc-silicate schist typically contains varying proportions of quartz, plagioclase, green amphibole, biotite, garnet and minor minerals. Amphibole ranges from less than 1 mm to greater than 1 cm and forms radiating splays on some surfaces. Calc-silicate rocks commonly have a strongly banded appearance and weather pale green to grey. Marble is coarse grained, pale-grey/white to cream weathering and locally contains calc-silicate minerals such as tremolite and diopside.

Earn Group

Dark, fine-grained, non–carbonate-bearing rocks that overlie dolomitic units are assigned to the lower part of the Devonian–Mississippian Earn Group (DME). The group is dominated by rusty weathering, dark grey to black siliceous phyllite, siltstone and metachert.

The base of the group includes an interval of foliated mafic metavolcanic and minor intrusive rocks (DMEv) on either side of Grey Creek (Fig. 2); elsewhere, siliceous rocks are in direct contact with dolomitic siltstone/calc-silicate schist of the upper Askin Group. The metavolcanic rocks are greenschist or epidote amphibolite, which locally host small metagabbro bodies. They are medium to dark green and weather grey green.

Some thin layers of pale-green chlorite schist, biotite-bearing greenschist, and compositionally banded biotite-magnetite–bearing greenschist are in contact with calc-silicate rocks of the Askin Group outside of the main belt of metavolcanic rocks. The stratigraphic position of these layers is difficult to determine due to multiple structural repetitions, but they appear to be part of a gradational boundary between the Askin Group and the metavolcanic unit. The upper contact of the greenschist with overlying rocks is sharp. Tempelman-Kluit (2012) included the mafic metavolcanic rocks in the 'Grey Creek formation', a local unit of presumed Cambrian age that was not recognized elsewhere. Westberg (2009) included similar rocks along strike in a 'greenstone-quartzite' unit, which she interpreted to be Mississippian or younger.

Metachert directly overlies metavolcanic rocks northwest of Grey Creek and passes laterally into siliceous slate and phyllite to the southeast. Siliceous phyllite and siltstone is dark grey to black, laminated, and contains abundant white siliceous layers and lenses. These are typically approximately 1 mm to 1 cm thick. Outcrops commonly have a rusty weathering rind, and some weather to pale blue. Some varieties of metachert exhibit grey to white, fine colour banding (Fig. 4e), whereas others are uniformly white to pale green. In each case, micaceous folia are regularly spaced less than 1 cm apart. Yellow-weathering, siliceous rock (quartzite or metachert) is common at the contact between greenschist and overlying metachert.

Resistant porphyroblastic meta-pelitic schist adjacent to the Quiet Lake batholith is interpreted as a more highly metamorphosed part of the Earn Group. Garnet porphyroblasts or their pseudomorphed remnants are ubiquitous and some rocks also contain slender andalusite porphyroblasts in a matrix composed of biotite, muscovite, quartz, plagioclase and accessory minerals. Most garnet is replaced by chlorite and other secondary minerals.

Ultramafic and mafic rocks in contact with the Askin Group

Northwest of Grey Creek, altered ultramafic rock (Dum) is exposed adjacent to a band of dolostone (Askin Group). The rock weathers jade green to white and is mostly composed of serpentinite, talc and nephrite. The body is cut by a mesh-textured network composed entirely of pale-pink garnet. A zone of acicular nephrite crystals in a talc-rich matrix is prominent on its upper boundary with pale-green, chlorite-rich Askin Group schist (Fig. 4h). Dolostone with well-preserved crinoidal detritus is preserved approximately 30 m downslope from the ultramafic rock.

Dark, rusty-weathering siliceous schist (Earn Group) and grey to pale green, amphibole and biotite-bearing calc-silicate schist (Askin Group) are exposed near the headwaters of the Boswell River (Fig. 5). The Askin Group dips under a band of epidote amphibolite (Dv), whose upper contact is with altered ultramafic rock (mostly dun-weathering serpentinite). The boundary between the amphibolite and calc-silicate appears gradational, as it is characterized by thin to medium interbeds of clastic, volcaniclastic and carbonate metasedimentary rocks This band of mafic schist extends approximately 30 km to the northwest, along the southwestern margin of the Quiet Lake batholith; it is in contact with, and ostensibly marks the base of, the Askin Group throughout this region.
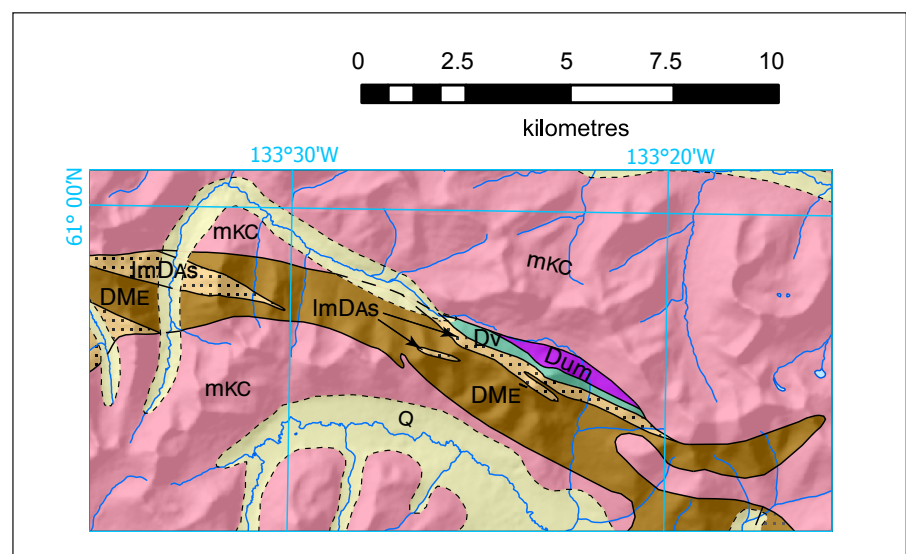

Figure 5. *Simplified geology of the headwaters of the Boswell River. A thin band of metabasalt separates altered ultramafic rock from calc-silicate schist of the Askin Group. See Figure 2b for legend.*

Quiet Lake batholith

The Quiet Lake batholith is dominated by coarse-grained, typically porphyritic biotite granite and quartz monzonite of the mid-Cretaceous Cassiar suite (mKC; Fig. 4f). These rocks are not penetratively foliated, but locally there is a scaly cleavage and weak alignment of K-feldspar phenocrysts. Phenocrysts are typically 1–2 cm long, but are locally up to 5 cm. On the Tower claims, near the eastern boundary of the Quiet Lake batholith, pegmatite is rich in tourmaline and garnet, and also contains yellow-green beryl (Jilson, 2007). This pegmatite is located along or near the contact between megacrystic granite of the Cassiar suite and a screen of metasedimentary rock. Dikes and small plutons of fine to medium-grained hornblende-biotite (grano-)diorite were noted within and adjacent to the main phase of the Quiet Lake batholith. They are equigranular and have matted intergrown mafic phases and quartz-filled amygdules.

The Cassiar suite intrudes deformed orthogneiss along much of its eastern boundary. The orthogneiss (DMgq) is mostly grey and brown weathering and typically contains two micas. Rounded to rectangular K-feldspar porphyroclasts (augen) are characteristic (Fig. 4g), though they are sparsely distributed in some areas. A less voluminous phase is white to pale-grey weathering, finer grained, and only mildly porphyritic. The augen gneiss is correlated with the Grass Lakes suite of the Finlayson district (Mortensen, 1992) and similar intrusive rocks that are exposed in para-autochthonous regions of western Yukon (Ryan et al., 2021). Westberg (2010) obtained several preliminary U-Pb laser ablation–inductively coupled plasma–mass spectrometry (LA-ICP-MS) dates from these intrusions in the area along strike to the northwest. The dates range from 360.5 ± 3.7 Ma (weighted mean of four analyses) to 348.0 ± 3.8 Ma (weighted mean of six analyses). Gallagher previously reported a U-Pb zircon thermal ionization mass spectrometry (TIMS) date of 359 ± 7 Ma from the same area.

Structure

The structure of the area is dominated by close to tight, northwest-trending folds. The main cleavage/foliation is axial-planar to these folds and mostly dips steeply to moderately steeply to the northeast, away from the axial trace of a major antiformal structure called the Quiet

Lake arch (Tempelman-Kluit, 2012). This deformation affected all units except Cretaceous intrusions.

The boundary zone of the Quiet Lake batholith is irregular due to numerous northeast-dipping screens of metasedimentary rock and orthogneiss in the area northwest of Brown Creek (Fig. 2). In contrast, southeast of Brown Creek the boundary is straight and sharp. The batholith is interpreted to be truncated by a steeply dipping, northwest-trending fault that coincides with a prominent aeromagnetic low. Crinoidal dolo-wackestone (lmDAd) is in direct contact with siliceous phyllite of the Earn Group across this fault, unlike elsewhere, where these two units are separated by dolomitic shale, siltstone and fine sandstone (lmDAds).

Summary and future work

Metasedimentary rocks on the northeastern side of the Quiet Lake batholith are interpreted to correlate with the lower Paleozoic Askin and Earn groups. These units, which form the Cassiar platform, are widely distributed in the Pelly Mountains. Geochronological, geochemical and paleontological studies on samples from the area are underway; the information gathered will be used to test this correlation and refine stratigraphic interpretations.

Acknowledgments

References

Campbell, R.G., 1967. Reconnaissance geology of Glenyon map area, Yukon Territory (105L). Geological Survey of Canada, Memoir 352, 92 p.

Colpron, M., Nelson, J.L. and Murphy, D.C., 2006. A tectonostratigraphic framework for the pericratonic terranes of the northern Cordillera. *In*: Paleozoic Evolution and Metallogeny of Pericratonic Terranes at the Ancient Pacific Margin of North America, Canadian and Alaskan Cordillera, M. Colpron and J.L. Nelson (eds.), Geological Association of Canada, Special Paper 45, p. 1–23.

Gabrielse, H., 1998. Geology of the Cry Lake and Dease Lake map areas, north-central British Columbia. Geological Survey of Canada, Bulletin 504, 147 p.

Gordey, S.P. and Makepeace, A.J. (comp.), 1999. Yukon digital geology. Exploration and Geological Services Division, Yukon Region, Indian and Northern Affairs Canada, Open File 1999-1(D).

Jilson, G., 2007. Assessment report on prospecting, line establishment and soil sampling the Tower claims. Yukon Energy, Mines and Resources Assessment Report 094632, 15 p.

Johnson, J.G. and Lane, N.G., 1969. Two new Devonian crinoids from central Nevada. Journal of Paleontology, vol. 43, no. 1, p. 69–73.

Mortenson, J.K., 1992. Pre-mid-Mesozoic tectonic evolution of the Yukon-Tanana terrane, Yukon and Alaska. Tectonics, vol. 11, p. 836–853. https://doi.org/10.1029/91TC01169

Moynihan, D., 2023. A preliminary geological interpretation of the Mount Grant–Evelyn Creek area, southern Yukon (parts of 105C/11, 12, 13, 14). *In*: Yukon Exploration and Geology 2022, K.E. MacFarlane (ed.), Yukon Geological Survey, p. 93–107.

Moynihan, D. and Crowley, J.L., 2022. Preliminary observations on the geology of the southern Big Salmon Range, south-central Yukon (parts of NTS 105C/13, 14, 105F/4 and 105E/1). *In*: Yukon Exploration and Geology 2021, K.E. MacFarlane (ed.), Yukon Geological Survey, p. 217–265.

Nelson, S.J., 1975. Paleontological field guides, northern Canada and Alaska. Bulletin of Canadian Petroleum Geology, vol. 23, no. 3, p. 428–683.

Ryan, J.J., Zagorevski, A., Cleven, N.R., Parsons, A.J. and Joyce, N.L., 2021. Architecture of pericratonic Yukon-Tanana terrane in the northern Cordillera. *In*: Northern Cordillera geology: A synthesis of research from the Geo-mapping for Energy and Minerals program, British Columbia and Yukon, J.J. Ryan and A. Zagorevski (eds.), Geological Survey of Canada, Bulletin 610, p. 67–93. https://doi.org/10.4095/326062

Tempelman-Kluit, D.J., 1977. Geology of Quiet Lake and Finlayson map-areas, Yukon Territory. Geological Survey of Canada, Open File 486, 1:250 000 scale.

Tempelman-Kluit, D.J., 2012. Geology of the Quiet Lake and Finlayson Lake map areas, south-central Yukon – an early interpretation of bedrock stratigraphy and structure. Geological Survey of Canada, Open File 5487, 103 p. https://doi.org/10.4095/291931

Westberg, E., 2009. Geological map of the 'Mendocina Creek' area (parts of 105E/8 and 105F/5). Yukon Geological Survey, Open File 2009-44, 1:50 000 scale.

Westberg, E., 2010. The tectonometamorphic and structural evolution of the Yukon-Tanana and Cassiar terranes in the Mendocina Creek area: Implications for the tectonic framework of south-central Yukon. Unpublished MSc thesis, Simon Fraser University, Vancouver, British Columbia, 148 p.

Wheeler, J.O., Green, L.H. and Roddick, J.A., 1960. Quiet Lake. Geological Survey of Canada, Preliminary Map 7-1960, 1:250 000 scale.

Yukon Geological Survey, 2023. A digital atlas of terranes for the northern Cordillera. Yukon Geological Survey, http://data.geology.gov.yk.ca/Compilation/2, [accessed November 2023].

Preliminary data from the establishment of long-term ground temperature reference sites in five Yukon communities

Moya Painter*
Yukon Geological Survey

Derek Cronmiller
Yukon Geological Survey

Panya Lipovsky
Yukon Geological Survey

Abstract

A drilling program was conducted in fall 2023 to install deep (up to 35 m) ground temperature monitoring boreholes in communities at risk from permafrost thaw. These boreholes will serve as long-term reference sites in both undisturbed and developed locations within or adjacent to communities. These boreholes also filled knowledge gaps that included the thickness of permafrost, and temperature data at the bottom of permafrost. Prior to this program, only 3 of the 34 permafrost-monitoring boreholes managed by the Yukon Geological Survey recorded temperatures through to the bottom of permafrost; furthermore, none of these boreholes are in the extensive discontinuous or continuous permafrost zones. Fifteen boreholes were drilled in five different communities across the Yukon: Dawson City, Mayo, Ross River, Beaver Creek and Haines Junction. Permafrost was encountered in 10 of the 15 boreholes, and the bottom of permafrost, or bedrock, was reached in at least one borehole in each community.

Introduction

In October 2023, the Yukon Geological Survey (YGS) drilled 15 boreholes in 5 Yukon communities. Boreholes were drilled in Dawson City, Mayo, Ross River, Beaver Creek and Haines Junction (Fig. 1). The primary purpose of these boreholes is to establish deep, long-term ground temperature monitoring stations to provide insight into how permafrost conditions (i.e., temperature and thickness) are changing in and adjacent to these communities. Geotechnical analysis of cores extracted from the boreholes also help characterize local permafrost properties such as ice content, sediment texture and genetic material. Prior to the installation of these sites, YGS was managing 34 permafrost-

monitoring stations, primarily in communities or along major transportation corridors. Only 4 of the existing sites are deeper than 10 m, and none are more than 20 m deep.

The Yukon has a sub-arctic continental climate, and has regional variation depending on latitude, topography and continentality (Smith et a*l*., 2004). Large mountain ranges acting as orographic barriers play a major role in variability of precipitation. Annual precipitation ranges from 3500 mm on the coastal Alaska side of the St. Elias Mountains, to as little as 200 mm in the North Slope region (Smith et a*l*., 2004). Annual mean temperatures
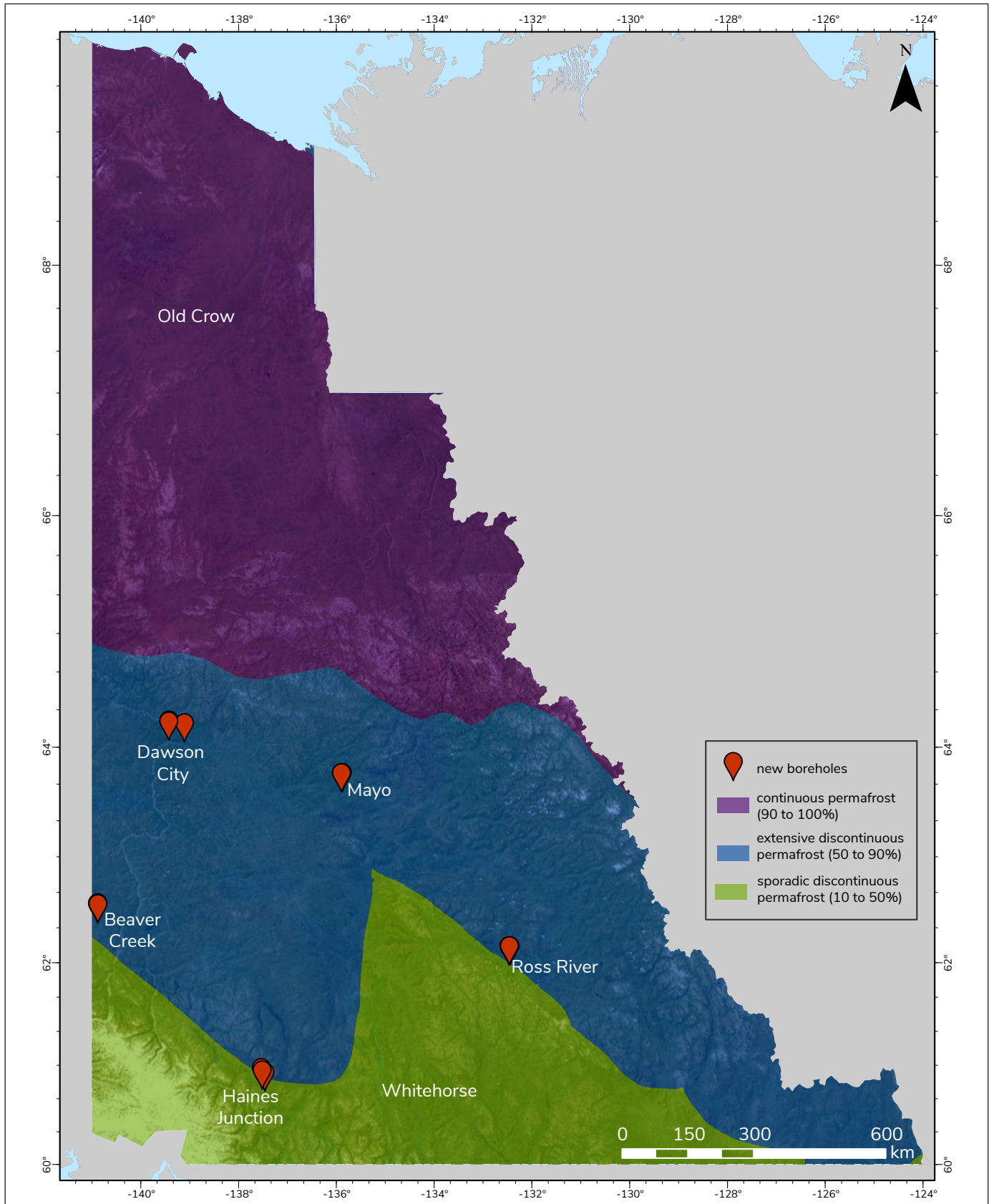
* moya.painter@yukon.ca

Figure 1. Map illustrating new borehole locations and permafrost distribution in the Yukon.

vary from approximately –2°C in the south to –10°C along the North Slope (Smith et a*l.,* 2004). Although there is spatial and temporal variation, there has been an overall increasing trend of precipitation and air temperature. The annual average temperature over northern Canada increased by 2.3°C between 1948 and 2016, and is expected to continue rising (Bush and Lemmen, 2019).

Permafrost in the territory ranges from continuous to sporadic discontinuous, depending largely on latitude and elevation (Fig. 1; Heginbottom et a*l.,* 1995). Smaller-scale controls include vegetation, slope angle, aspect, site moisture, surficial geology, precipitation and disturbance. Permafrost is warming and thawing across the Arctic, primarily due to rising air temperatures driven by climate change (Smith et a*l.,* 2022). The YGS' new monitoring sites will track changes in ground temperature across the territory as air temperatures continue to rise.

Methodology

The approach for this project was modelled, where possible, on best practices for ground temperature monitoring as proposed by Noetzi et a*l.* (2021), including recommendations for site selection, strategy for temperature sampling, and drilling procedures.

The five communities were selected to provide geographical distribution across the territory, while prioritizing areas having potentially thick permafrost (i.e., >10 m), and ease of access for future site visits. Sites within each community were selected based on the assumed presence of permafrost. Access for the drill rig and areas sited for future development were also considered. It was important that each site is broadly representative of the permafrost conditions of the region.

The boreholes were drilled with a sonic drill by Northern Sonic Drilling and Consulting (Northern Sonic) between October 6 and 16, 2023 (Fig. 2). The sonic drill used low-pressure tracks and an elevated working platform to minimize site disturbance during the drilling process. Each borehole was drilled with a four-inch diameter bit, cased with one-inch schedule 80 PVC pipe. The boreholes were backfilled primarily with bentonite chips, except for the top two feet, which was backfilled with sand. The casings at the

surface are housed in lockable aluminum covers, which protrude approximately one metre from the ground surface (Fig. 3). Boreholes were drilled without the use of water, whenever possible, to minimize the thermal disturbance to permafrost; however, the vibration of the sonic drill generated excess heat during drilling, particularly in coarse materials. This disturbance means ground temperatures will take time to recover from the thermal effect of drilling, especially where permafrost temperatures are near 0°C. Estimates of ground thermal conditions presented in this paper are preliminary, and may not have completely recovered from the initial drilling.

Nearly continuous intact cores were recovered during drilling. Preliminary core logging was completed on site to document material thickness, texture, colour, thermal state, ice content, cryostructures and moisture. Drill cores displaying complex stratigraphy were taken to the YGS Core Library for detailed logging and photography. Samples were collected from representative intervals to analyze ice content. Metadata collected at each site included location, elevation, slope, aspect, site drainage, vegetation, disturbance and surface morphology. Samples of buried organic carbon were collected for radiocarbon dating where the results would yield useful information about site chronology. Radiocarbon ages were not available in time for publication of this report. Temporary data loggers and thermistor strings were installed in most boreholes with the intention of recording preliminary ground temperature data to inform the configuration of custom, site-specific, thermistor strings for long-term deployment. A list of monitoring sites, including the location, elevation and depth of borehole, is found in Table 1.

Site descriptions and preliminary results

Dawson City

Dawson City is the most northern community in the Yukon that is accessible by road year-round and is the most populated community in the Yukon after Whitehorse (Yukon Bureau of Statistics, 2023). The town is located at the confluence of the Yukon and Klondike rivers and is within an unglaciated region of the territory. Mean annual air temperature in Dawson City is –3.8°C, based on data from the Dawson City meteorological station between 1991 and 2020

Figure 2. *Northern Sonic Drilling and Consulting's sonic drill at site YGS_BeaverCreek_BH4 in Beaver Creek.*

Figure 3. *Completed site at YGS_BeaverCreek_BH4 in Beaver Creek.*

Table 1. *List of monitoring sites, including location, elevation and depth of borehole.*

Site	Location	Elevation (m)	Depth (m)
YGS_Moosehide	64.07088, −139.42291	352	28.0
YGS_DawsonRec	64.06197, −139.42914	321	10.9
YGS_YDA	64.04677, −139.10792	352	14.9
YGS_Mayo_School	63.59790, −135.89438	513	35.0
YGS_Mayo_GroupHome	63.59740, −135.87889	519	15.5
Mayo_WRB_Admin	63.59592, −135.89528	519	14.0
YGS_RR_Lagoon	61.97849, −132.46902	683	26.5
YGS_RR_LagoonRd	61.97901, −132.46124	663	17.3
YGS_RR_Hwys	61.97732, −132.44720	653	11.2
YGS_BC_Ptarmigan	62.38028, −140.88485	669	21.2
YGS_BC_Brown	62.38855, −140.88160	659	16.0
YGS_BC_Hwys	62.37973, −140.87811	667	12.1
YGS_HainesRd	60.74084, −137.46242	634	16.3
YGS_HJ_AirportRdDeep	60.78581, −137.53599	638	26.8
HJ_WRB_CO	60.76194, −137.51859	617	26.2

(Environment Canada, 2023). Dawson is located in the extensive discontinuous permafrost zone, that is, 50–90% of the area is underlain by permafrost (Heginbottom et a*l.*, 1995). Ice-rich permafrost is common in the Dawson City region and is susceptible to degradation, which has caused extensive damage to many buildings in the area.

YGS_Moosehide

Borehole YGS_Moosehide is located at the north end of town on the prehistoric Moosehide landslide deposit (Fig. 4a). The lower portion of the landslide deposit, where the borehole is located, consists of frozen, rubbly colluvium, which is creeping downslope (Brideau et al., 2007). The borehole is approximately 120 m east of, and 40 m higher in elevation than the Yukon River. The organic mat at this site is thin and discontinuous. Site vegetation includes white spruce (*Picea glauca*), soapberry (*Shepherdia canadensis*) and various grasses. The YGS_Moosehide borehole is 28 m deep. Drilling did not penetrate through the bottom of the landslide deposit, and materials in the borehole range from fine grained to rubbly colluvium (Fig. 5a; Appendix A1). The top one metre of diamict is enriched in organic content, likely in part from ongoing slope deformation. At approximately 20 m depth, the estimated ice content averaged 40% in ice lenses thicker than 1 cm and ice coatings on grains throughout the bottom 8 m of the core. Preliminary temperature data collected a month after installation indicates that the top of permafrost is at 7 m depth. Although the temporary thermistor string only extends to 21 m, extracted core was frozen to the bottom of the borehole, indicating that permafrost is at least 21 m thick.

YGS_DawsonRec

Borehole YGS_DawsonRec is located in the parking lot of the Art and Margaret Fry Recreation Centre on a Yukon River fluvial terrace (Fig. 4a). This borehole was drilled in collaboration with Yukon Water Resources Branch (WRB) to expand on their Yukon Observation Well Network (YOWN). The borehole is approximately 30 m north of the building and 5 m from the fence of a neighbouring residential property. The site is clear of vegetation and has been covered with gravel fill. Plans are in place to build a new recreation facility because thawing permafrost has limited the use of the current recreation centre. The borehole contains a two-inch PVC pipe that houses WRB's instrumentation and an adjacent one-inch PVC pipe that houses

YGS' permafrost monitoring instrumentation. The YGS_DawsonRec borehole is 10.9 m deep and surficial sediments are predominantly composed of gravel (Fig. 5b; Appendix A2). No visible ice was found in the core, but ground temperature data indicates the top of permafrost is at approximately 5 m depth.

YGS_YDA

Borehole YGS_YDA is located on a Klondike River fluvial terrace, approximately 180 m east of the north end of the Dawson City Airport (Fig. 4b). Evidence of permafrost degradation at this site includes thermokarst ponds and leaning trees. Vegetation at the site includes black spruce (*P. mariana*), dwarf birch (*Betula nana*), Labrador tea (*Rhododendron groenlandicum*) and a mossy organic mat. A cross-slope drainage ditch, installed to redirect snowmelt away from the airport, is located 65 m upslope of the site. Plans to construct helicopter pads approximately 100 m west of the drill site will include clearing of trees and ground compaction, which may have minor thermal impacts on the site in the future. The YGS_YDA borehole is 15 m deep and is instrumented with a thermistor string to 14.9 m depth. This borehole intersected bedrock at 14.5 m. The predominant surficial material at this site is gravel (Fig. 5c; Appendix A3). Drill core contained up to 20% visible ice over an interval of 1 m including ice lenses up to 5 cm thick. Ground temperature data retrieved approximately one month after installation indicated that permafrost is present from 1 m depth to the bottom of the borehole, confirming that permafrost is at least 14 m thick at this site.

Mayo

The Village of Mayo is located at the confluence of the Mayo and Stewart rivers and is within the limit of the McConnell glaciation, the most recent glaciation in the territory. Mean annual air temperature in Mayo is −2.4°C, based on data from the Mayo A meteorological station between 1981 and 2010 (Environment Canada, 2023). Mayo is situated within the extensive discontinuous permafrost zone. Those areas within the Village of Mayo that are underlain by fine-grained glaciolacustrine sediments are commonly ice rich (Northern Climate Exchange, 2011), and infrastructure in these areas has experienced damage due to permafrost thaw-induced subsidence, particularly in the Lower East End Subdivision.
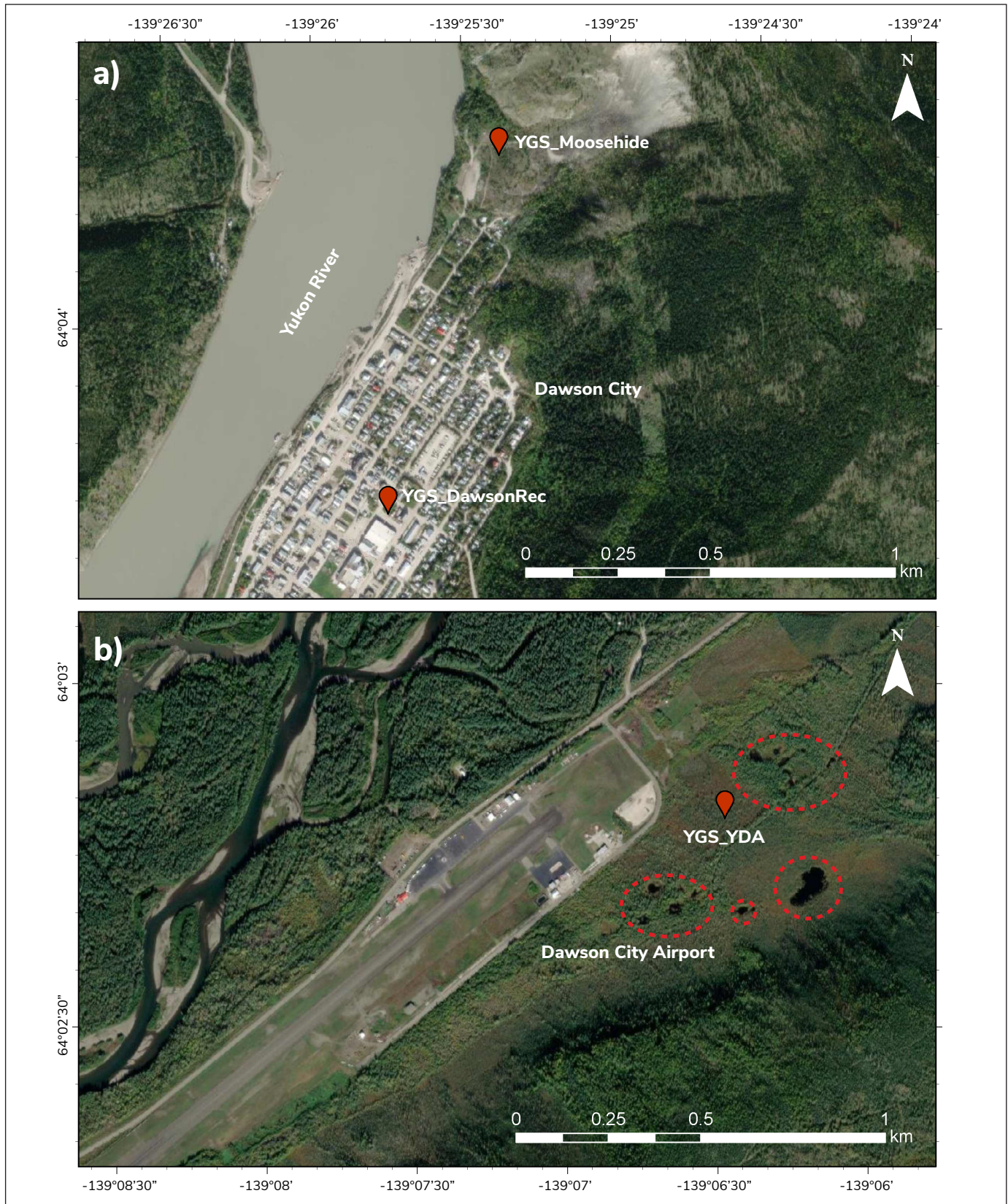
Figure 4. *Dawson region monitoring site locations:* **a)** *Dawson City (YGS_Moosehide and YGS_DawsonRec); and* **b)** *Dawson City Airport (YGS_YDA); thermokarst ponds delineated by red dashed lines.*
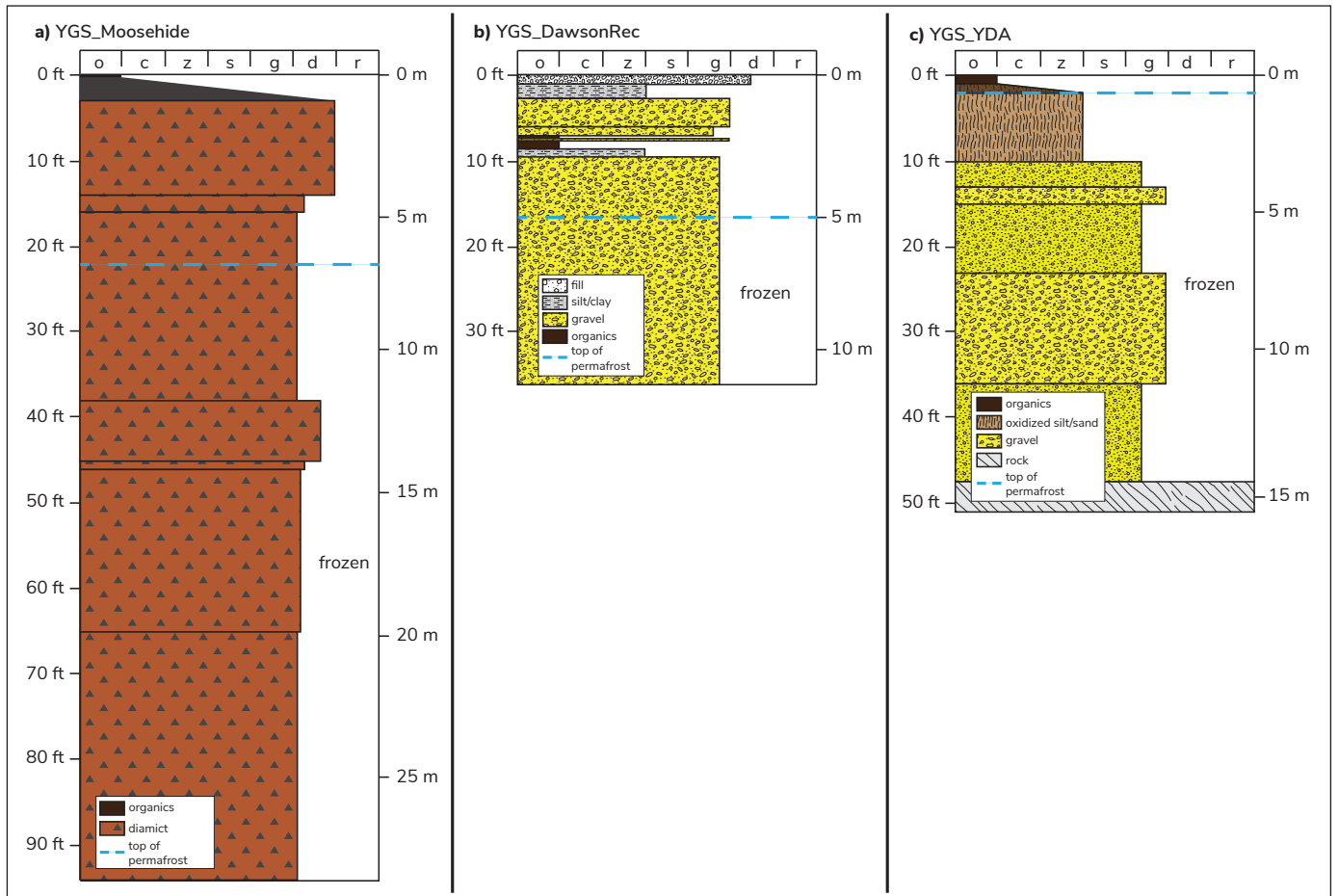
Figure 5. *Borehole logs for Dawson region:* **a)** *YGS_Moosehide;* **b)** *YGS_DawsonRec; and* **c)** *YGS_YDA.*
o: organic; c: clay; z: silt; s: sand; g: gravel; d: mixed fragments; r: rubble.

YGS_Mayo_School

Borehole YGS_Mayo_School is located adjacent to a cutline approximately 100 m northeast of the school (Fig. 6). This site was selected because it is located in a relatively undisturbed forest close to the Village of Mayo, and likely represents typical permafrost conditions for the community. Additionally, an electrical resistivity tomography (ERT) survey completed in 2011 (Northern Climate Exchange, 2011) showed a deep zone of high-resistivity material at this site, which was interpreted as thick permafrost. The vegetation at this site is predominantly white spruce and black spruce, willow shrubs, Labrador tea and a mossy organic mat. Borehole YGS_Mayo_School is 35 m deep, and is the deepest borehole drilled during this project. The surficial materials at this site are primarily glaciolacustrine sediments of silty clay to fine sand, overlain by a few metres of sandy gravel near the surface (Fig. 7a; Appendix A4). Preliminary temperature data and

drilling observations indicate that permafrost is 20.5 m thick and extends from 8.5 to 29 m depth. Ice lenses ranging from 1 to 5 cm thick were present in the core between 14 and 20 m.

YGS_Mayo_GroupHome

Borehole YGS_Mayo_GroupHome is located on the north side of the Group Home Road approximately 450 m east of the intersection with the Mayo Elsa Road (Fig. 6). Permafrost thaw has occurred in the area as is evidenced by the development of tension cracks from ground subsidence and abundant thermokarst ponds. Vegetation at this site includes birch (*Betula* sp.), black and white spruce and moss. Borehole YGS_Mayo_GroupHome is 15.5 m deep and is instrumented to 15 m. Surficial deposits at this site are primarily glaciolacustrine clay (Fig. 7b; Appendix A5). Preliminary data suggest the top of permafrost is at 6 m depth and the bottom of permafrost is at 12.5 m. Ice lenses up to
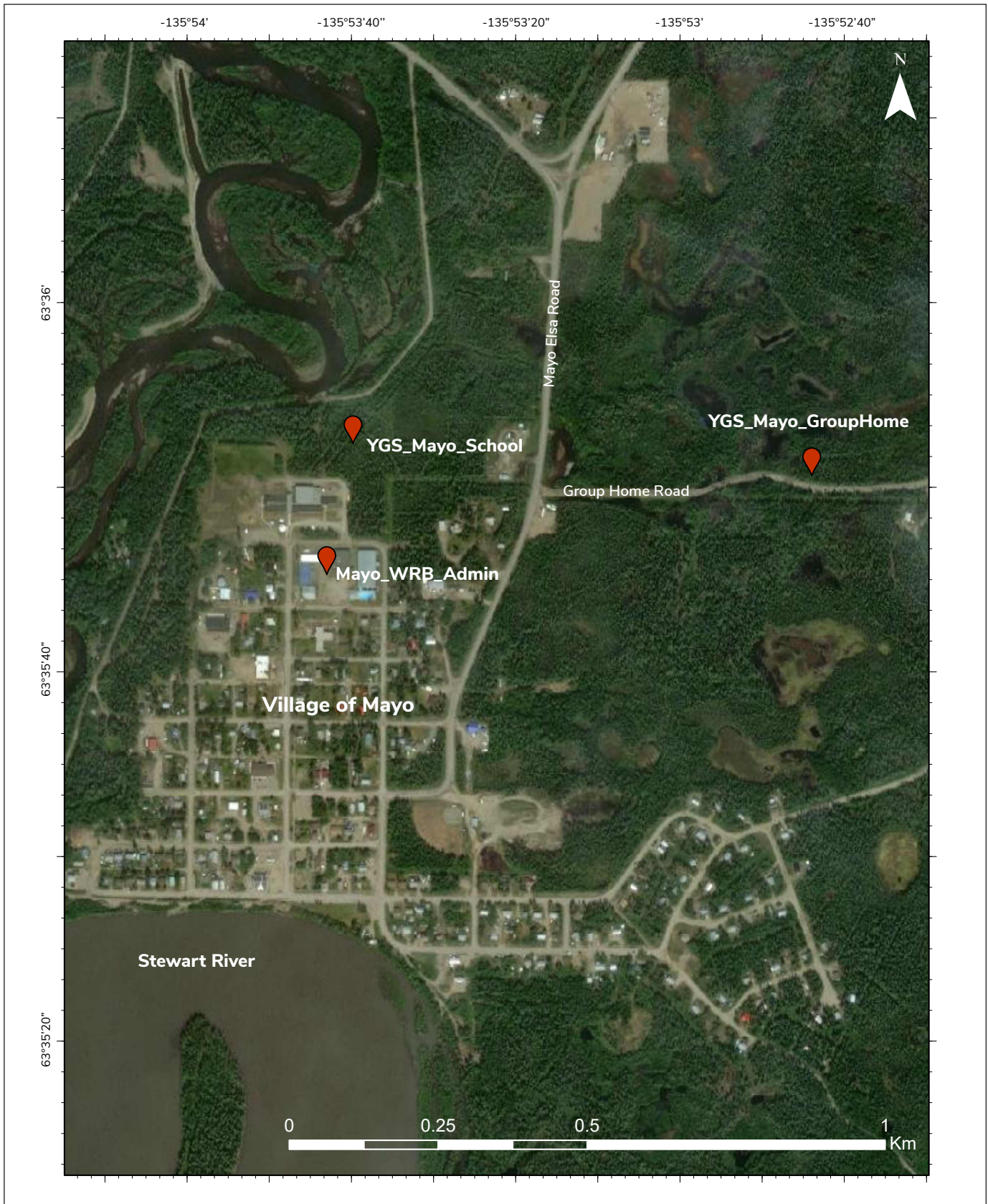
Figure 6. *Mayo monitoring site locations.*
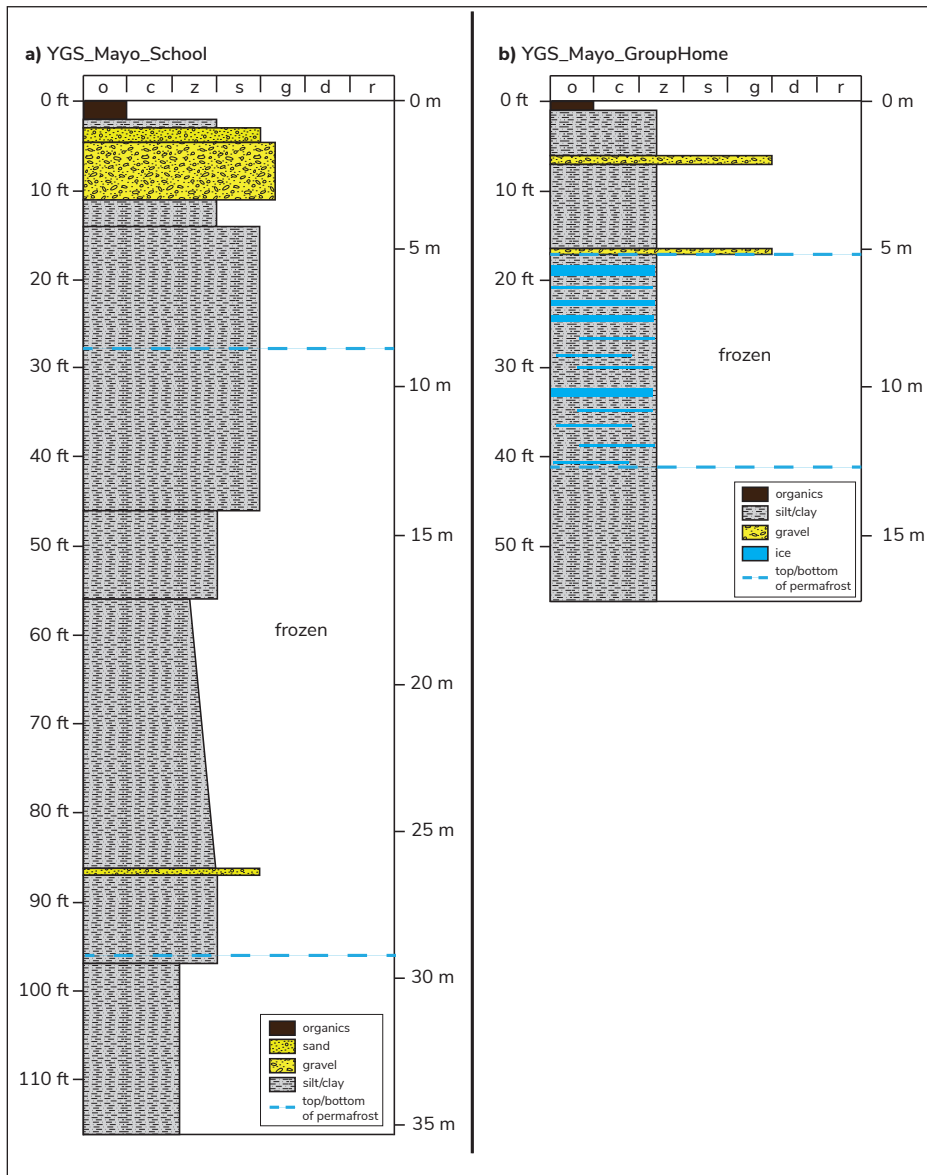
Figure 7. *Borehole logs for Mayo:* **a)** *YGS_Mayo_School; and* **b)** *YGS_Mayo_ GroupHome. o: organic; c: clay; z: silt; s: sand; g: gravel; d: mixed fragments; r: rubble.*

is 14 m deep and surficial materials consist of 5.5 m of gravel overlying a silty clay unit. The deposits are interpreted as fluvial gravel overlying glaciolacustrine sediment. No permafrost was encountered during drilling, and the borehole was not cased or instrumented for ground temperature monitoring.

Ross River

Ross River is located along the Canol Road, on a fluvial terrace above the Pelly River. The terrace is composed of fluvial sediments underlain by a thick unit of fine-grained glaciolacustrine material, which was deposited by a glacial lake that was present at the end of the McConnell Glaciation approximately 12 000 ka ago (Jackson, 1994; Bond, 1999). Mean annual air temperature in Ross River is −4.5°C, based on historical data between 1976 and 2005 (Prairie Climate Centre, 2019). Ross River is on the border between the extensive discontinuous permafrost zone (50–90% underlain by permafrost) and the sporadic discontinuous permafrost zone (10–50% underlain by permafrost) (Heginbottom et al., 1995). Widespread infrastructure damage has occurred in the community due to permafrost thaw (e.g., the damage at Ross River School), suggesting that ice-rich permafrost is likely pervasive in the area (Calmels et al., 2016).

20 cm thick were observed between 5 and 12.5 m, and ice content reached a maximum of 80% from 5 to 8 m.

Mayo_WRB_Admin

Borehole Mayo_WRB_Admin is located in the parking lot behind the Village of Mayo's main administrative building and was drilled by WRB as a YOWN site for long-term groundwater monitoring in the community (Fig. 6). There are several buildings at this site, some as close as 10 m from the borehole. The borehole

YGS_RR_Lagoon

Borehole YGS_RR_Lagoon is located approximately 110 m south of the southern corner of the Ross River wastewater treatment facility (Fig. 8). The site is approximately 10 m from a small road and 50 m from a
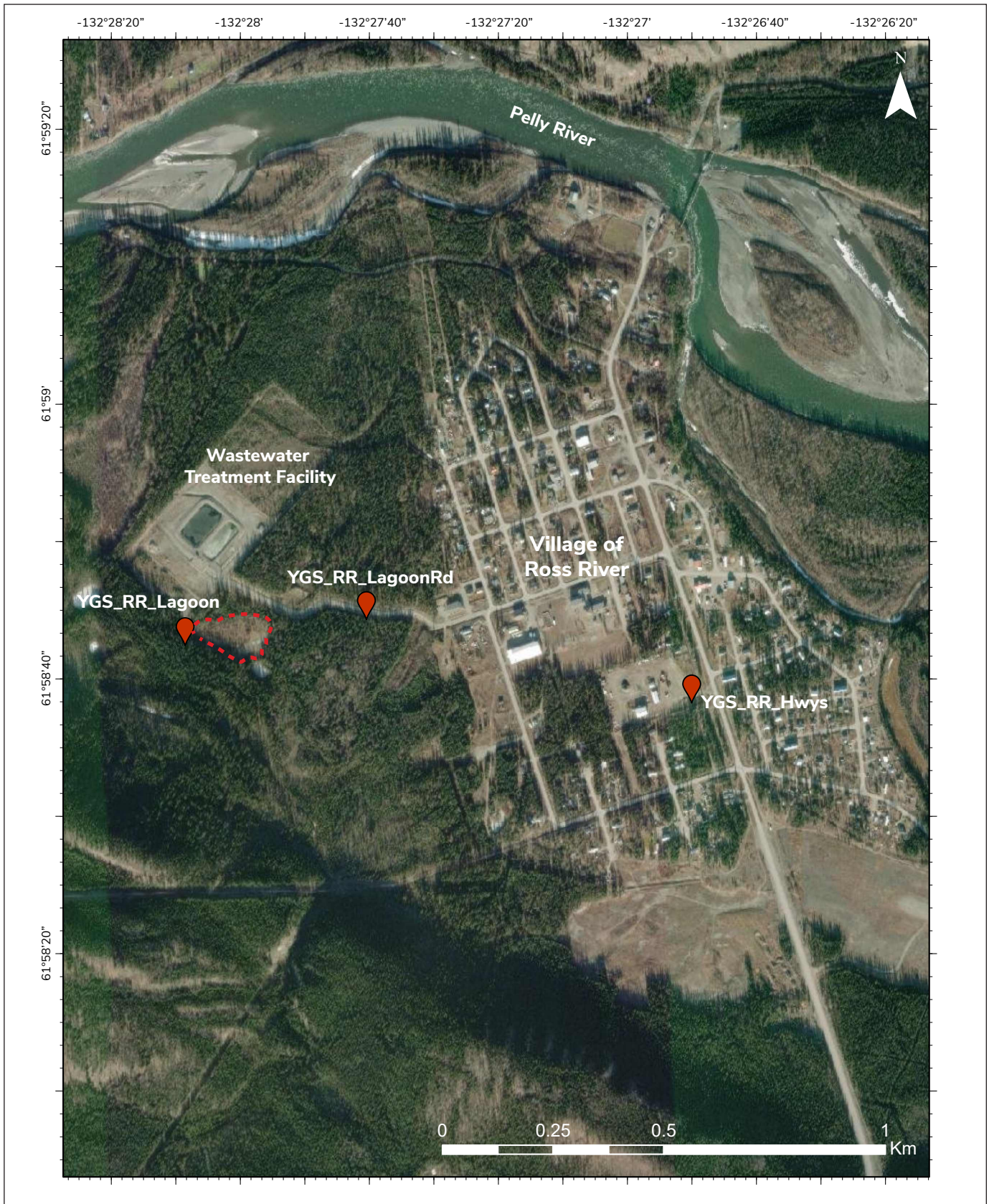
Figure 8. *Ross River monitoring site locations. Drained thermokarst pond delineated by red dashed line.*

drained thermokarst pond (Fig. 8). Vegetation consists predominantly of black and white spruce and moss. The borehole is 26.5 m deep and is instrumented to 20 m. Surficial materials at this site consist predominantly of clay overlain by unfrozen gravel (Fig. 9a; Appendix A6). These deposits are interpreted as fluvial gravel overlying glaciolacustrine sediment. Drill core suggests that permafrost is 18.4 m thick and permafrost extends from 3.5 m to 21.9 m depth. Core from this site contained up to 90% ice over some 3 m intervals (e.g., from 11 m to 14 m depth; Fig. 9a).

YGS_RR_LagoonRd

Borehole YGS_RR_LagoonRd is located in a forested area on the south side of the road leading into the wastewater treatment facility (Fig. 8). Vegetation includes black and white spruce, aspen (*Populus* sp.), willow shrubs (*Salix* sp.) and moss. The borehole is 17.3 m deep. The surficial materials at this site consist of 5.8 m of sandy gravel underlain by clay to the bottom of

the borehole (Fig. 9b; Appendix A7). These deposits are interpreted as fluvial gravel overlying glaciolacustrine sediment. Less ground ice was observed in the core from this borehole compared with YGS_RR_Lagoon. Rare ice lenses up to 3 cm thick were present from 5.7 to 10.9 m. The top of permafrost was encountered at 3.3 m depth; it is at least 14 m thick and extends beyond the bottom of the borehole.

YGS_RR_Hwys

Borehole YGS_RR_Hwys is located in the Yukon Highways and Public Works compound adjacent to a YOWN groundwater monitoring well, which intersected permafrost (Fig. 8). The site is located in the southeast corner of the compound, approximately 10 m from the perimeter fence, and 80 m from the closest building structure. The site was clear of vegetation. The borehole was cased and drilled to a depth of 11.2 m. The top of permafrost was encountered at 8.2 m. The upper half of the borehole was predominantly gravel,
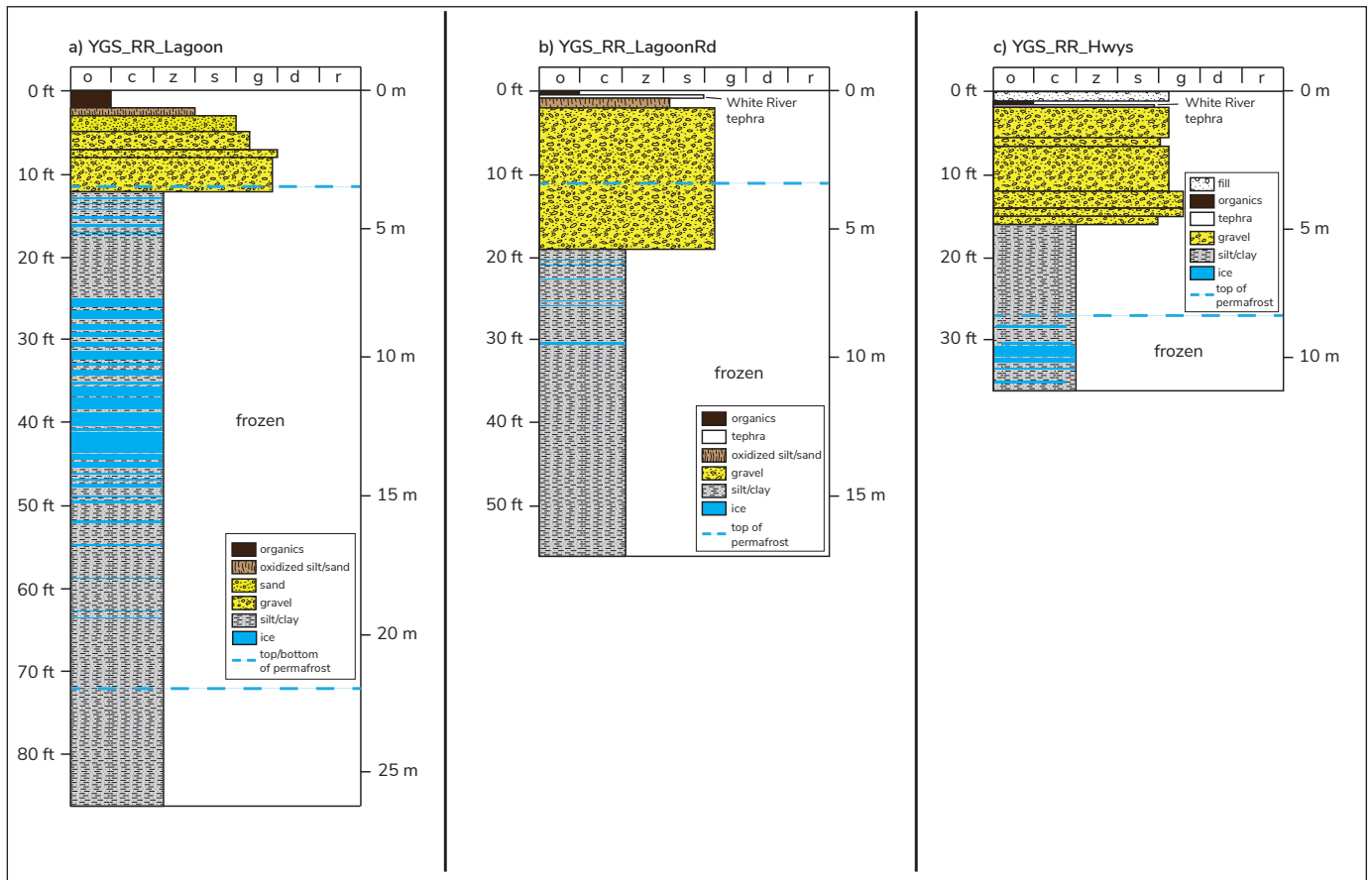
Figure 9. *Borehole logs for Ross River:* **a)** *YGS_RR_Lagoon;* **b)** *YGS_RR_LagoonRd;* *and* **c)** *YGS_RR_Hwys.* o: *organic;* c: *clay;* z: *silt;* s: *sand;* g: *gravel;* d: *mixed fragments;* r: *rubble.*

which was underlain by clay to the bottom of the hole. (Fig. 9c; Appendix A8). These sediments are interpreted as fluvial gravel overlying glaciolacustrine sediment. Ice lenses of variable thicknesses were observed from 8.2 m depth to the bottom of the borehole. This site is not currently instrumented.

Beaver Creek

Beaver Creek is located on the Alaska Highway, approximately 30 km south of the Alaska border. Beaver Creek was glaciated during the Reid and Gladstone glaciations, but is approximately 15 km beyond the limit of the McConnell glaciation (Duk-Rodkin, 1999). The town site is located on a McConnell-aged glacial outwash plain. Mean annual air temperature in Beaver Creek is –4.9°C, based on data from the Beaver Creek A meteorological station between 1981 and 2010 (Environment Canada, 2023). Beaver Creek is located in the extensive discontinuous permafrost zone (Heginbottom et al., 1995). Although permafrost is expected to be present under most of the community, the coarse-grained surficial materials underlying most of the town are generally ice-poor and thaw stable.

YGS_BC_Ptarmigan

Borehole YGS_BC_Ptarmigan is located on the north side of Ptarmigan Road (Fig. 10). Vegetation at the site consists of black and white spruce trees averaging 10 m high. Most of the forest in Beaver Creek has been thinned for wildfire management, but there is extensive regrowth of black and white spruce approximately one metre tall. The presence of widespread leaning trees suggests some permafrost degradation is occurring in the area. The borehole is 21.2 m deep and is instrumented to 20 m. The predominant sediment observed in core is gravel, and compact diamict below 17 m depth (Fig. 11a; Appendix A9). Surficial sediments at this site are interpreted as Gladstone and McConnell-aged glaciofluvial outwash overlying Gladstone-aged till. Because the surficial sediments at this site are predominantly coarse and dry, most of the core came out hot from drilling. For this reason, none of the retrieved core was frozen, but extrapolated preliminary temperature data downloaded from the data logger suggest that permafrost is 6 m thick, and extends from 3 m to 9 m depth.

YGS_BC_Brown

Borehole YGS_BC_Brown is located 40 m west of the cul-de-sac at the end of Brown Street (Fig. 10). Black and white spruce at the site are approximately 20 m tall, and have been thinned for fuel abatement purposes. The understory consists of willow, dwarf birch and Labrador tea, and the moss mat is approximately 30 cm thick. The site is located in a 30 by 30 m depression up to 2 m deep. Borehole YGS_BC_Brown was drilled to a depth of 17 m, but was only cased and instrumented to 16 m. The surficial geology at this site is similar to the Ptarmigan Road site; most of the core comprises gravel and diamict below 15.8 m (Fig. 11b; Appendix A10). Surficial deposits at this site are interpreted as Gladstone and McConnell-aged glaciofluvial outwash overlying Gladstone-aged till. Both the core and the initial temperature profiles indicate that there is no permafrost at this site.

YGS_BC_Hwys

Borehole YGS_BC_Hwys was drilled as a YOWN groundwater monitoring well, located along the fence in the Yukon Highways and Public Works compound, approximately 70 m from the main building (Fig. 10). A ground temperature monitoring casing (one-inch PVC pipe) was installed adjacent to the groundwater monitoring casing (two-inch PVC pipe) in the same borehole; however, permafrost-monitoring instrumentation was not installed at the time of drilling. This site has been cleared of vegetation. The borehole is 12.1 m deep and the surficial sediments are almost entirely gravel, except for a thin layer of diamict at a depth between 5.8 and 6.4 m (Figure 11c; Appendix A11). Surficial deposits at this site are interpreted as Gladstone-aged advance and retreat glaciofluvial outwash bracketing Gladstone-aged till. This package is overlain by McConnell-aged glaciofluvial outwash. There was no evidence of permafrost observed during drilling, but the site will be instrumented in the future to confirm the presence or absence of permafrost.

Haines Junction

Haines Junction is the most southern community in Yukon chosen for this monitoring program. The area was inundated at least once by Glacial Lake Champagne at the end of the McConnell glaciation. During the Little Ice Age, which occurred between the 16th and 19th centuries, Neoglacial Lake Alsek repeatedly flooded
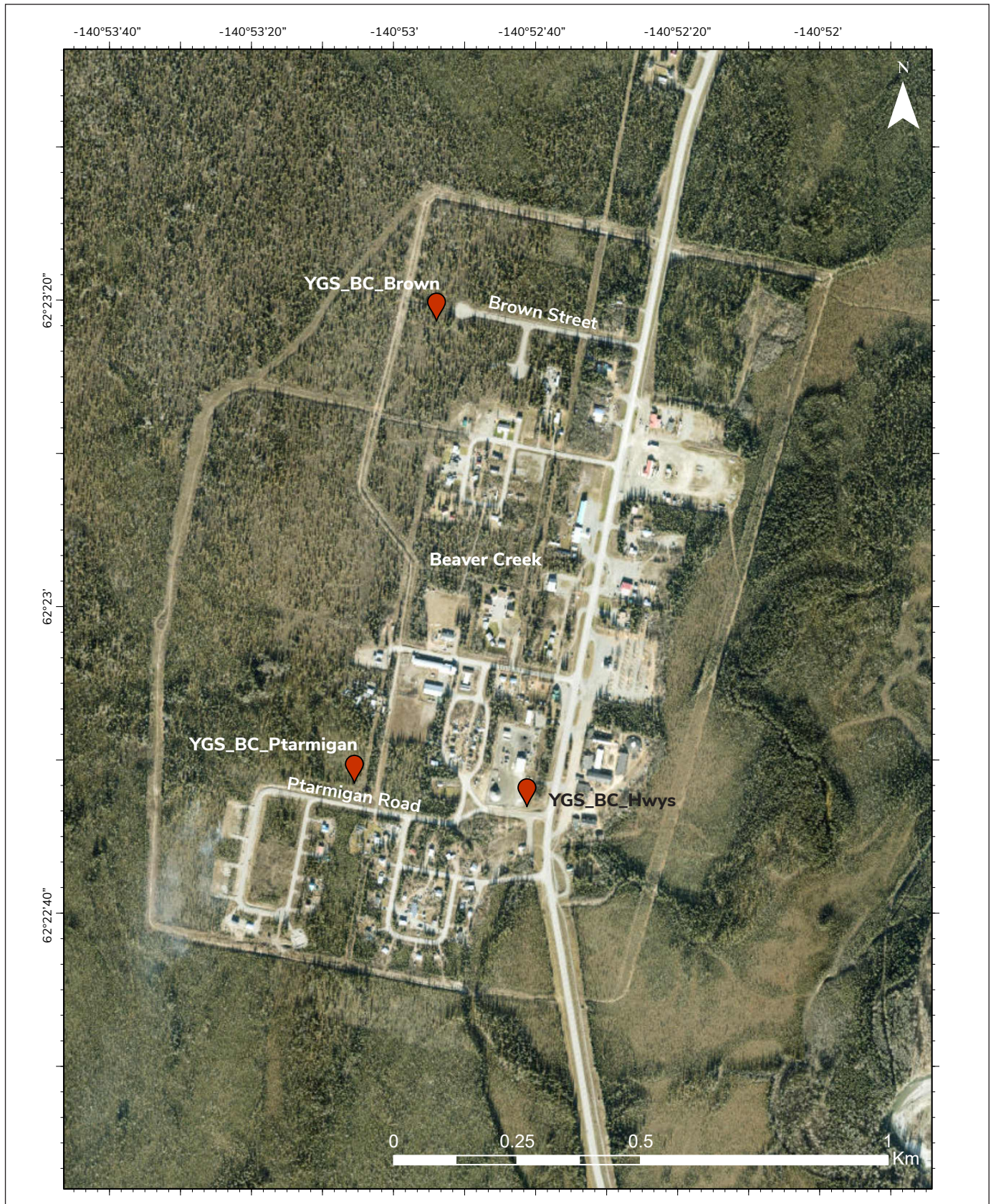
Figure 10. *Beaver Creek monitoring site locations.*
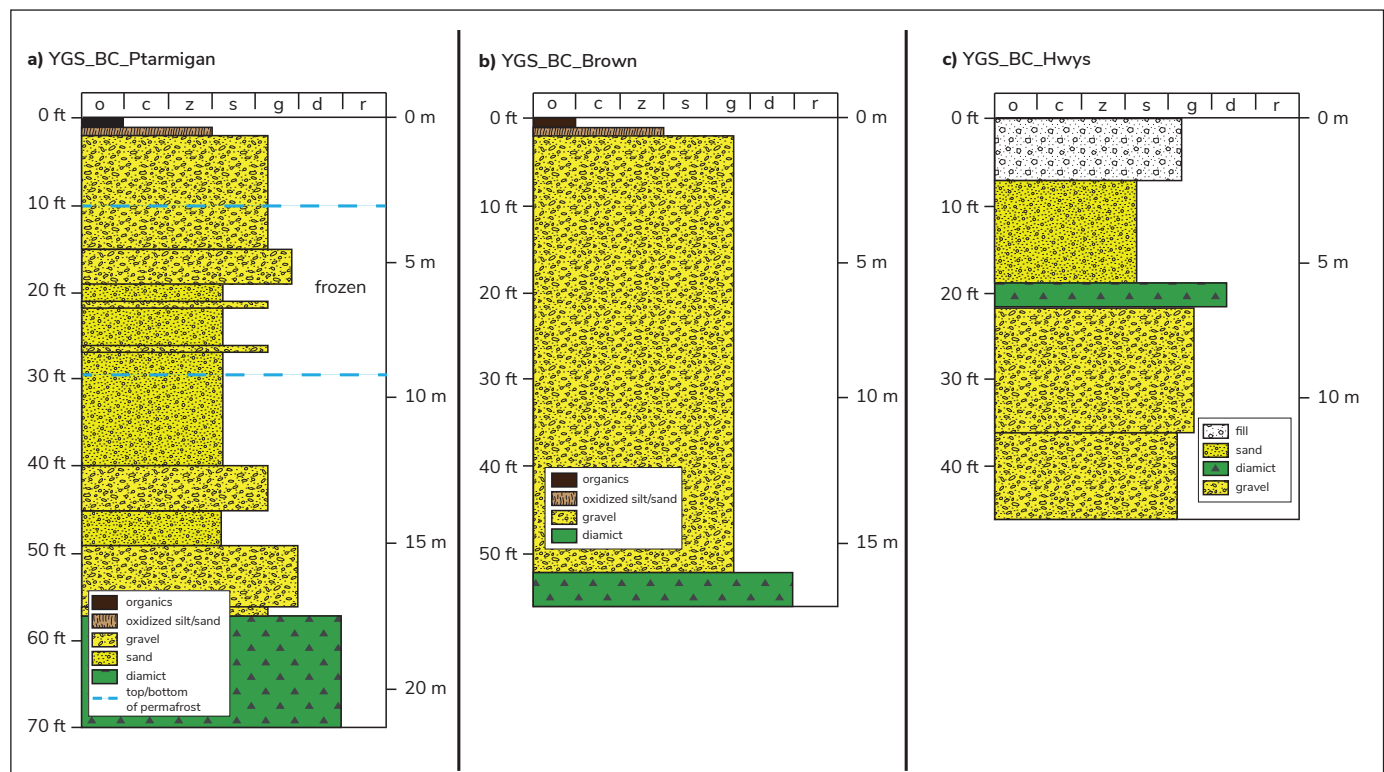
Figure 11. *Borehole logs for Beaver Creek:* **a)** *YGS_BC_Ptarmigan;* **b)** *YGS_BC_Brown; and* **c)** *YGS_BC_Hwys. o: organic; c: clay; z: silt; s: sand; g: gravel; d: mixed fragments; r: rubble.*

the area (Clague and Rampton, 1982). Surficial deposits in the region consist of complex sequences of glaciolacustrine, till, fluvial and glaciofluvial sediments (Rampton and Paradis, 1979), which are currently being mapped in detail by YGS. Mean annual air temperature in Haines Junction is −2.1°C, based on historical data between 1976 and 2005 (Prairie Climate Centre, 2019). Haines Junction is within the sporadic discontinuous permafrost zone, meaning 10–50% of the area is expected to be underlain by permafrost (Heginbottom et al., 1995). In this region, permafrost is found primarily in low-lying areas and on north-facing slopes.

YGS_HainesRd

Borehole YGS_HainesRd is located near a forestry cut block approximately 3 km southeast of Haines Junction along the Haines Road (Fig. 12). This site shows widespread evidence of permafrost degradation including small thaw ponds and a drunken black spruce forest. Yukon University's YukonU Research Centre Permafrost and Geoscience group completed an ERT survey at this site prior to drilling. The survey

line ran roughly southwest and was 160 m long. The ERT profile suggested that the area most likely to be frozen occurred at 110 m along the survey line. The borehole was drilled approximately 40 m along the ERT line due to access constraints. The YGS_HainesRd borehole is 16.3 m deep and is instrumented to 16 m. Surficial sediments at this site consist of alternating layers of diamict and gravel (Fig. 13a; Appendix A12). These deposits are interpreted as a complex sequence of till interstratified with glaciofluvial outwash gravel. Although surface features and vegetation were typical of permafrost environments, there was no permafrost observed during drilling and core inspection. This was confirmed by ground temperatures downloaded approximately three weeks after the borehole was drilled, suggesting that permafrost at this site has completely degraded.

YGS_HJ_AirportRdDeep

Borehole YGS_HJ_AirportRdDeep is located 400 m south of the Haines Junction Airport (Fig. 12). A 10 m deep ground temperature monitoring borehole (YGS_HJ_BH6) drilled in early 2023 is located approximately
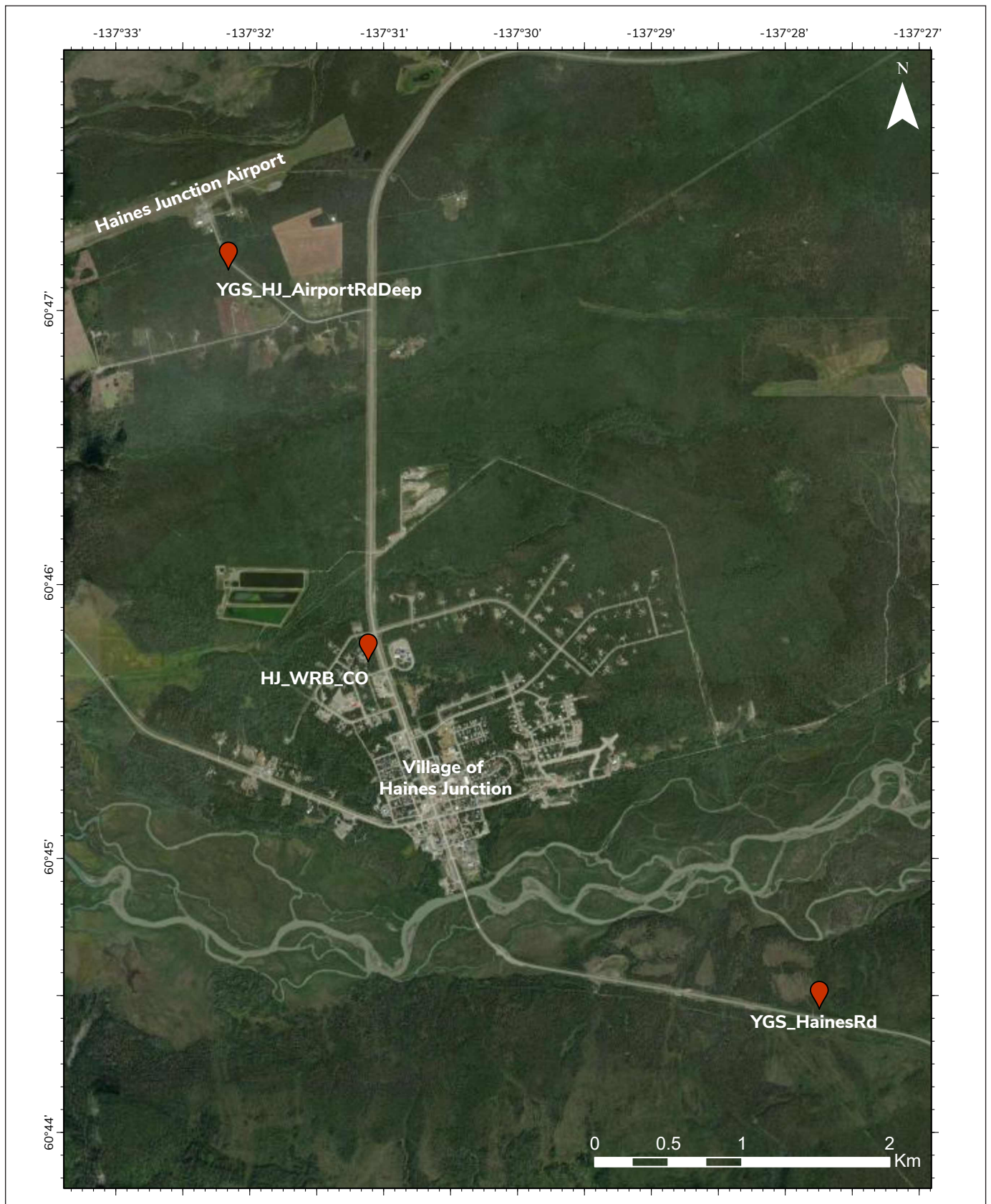
Figure 12. Haines Junction monitoring site locations.
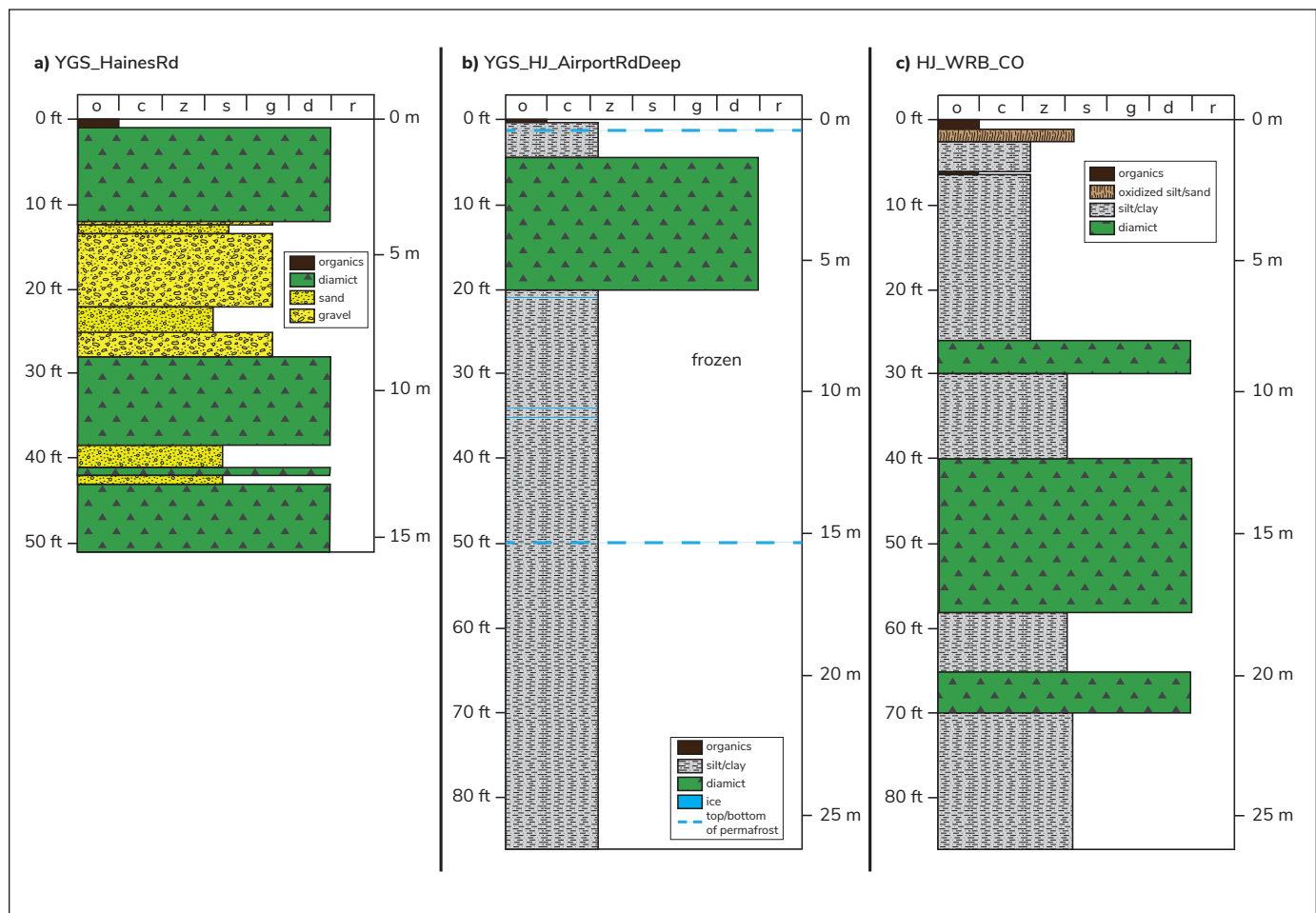
Figure 13. *Borehole logs for Haines Junction:* **a)** *YGS_HainesRd;* **b)** *YGS_HJ_AirportRdDeep; and* **c)** *HJ_WRB_CO.*
o: organic; c: clay; z: silt; s: sand; g: gravel; d: mixed fragments; r: rubble.

100 m north of borehole YGS_HJ_AirportRdDeep, and ground temperatures measured in this hole indicated that the bottom of permafrost exceeds 10 m depth. The YGS_HJ_AirportRdDeep site was selected to expand our understanding of permafrost in this area, and to determine the true thickness of the permafrost. Permafrost is inferred at the site based on the presence of a drunken black spruce forest in the surrounding area. Understory vegetation includes willow and soapberry, and the ground surface is covered with moss. The borehole is 26.8 m deep and is instrumented to 20 m. The surficial sediments at this site are predominantly silty clay containing a layer of diamict from 1.4 to 5.9 m depth (Fig. 13b; Appendix A13). The stratigraphy is interpreted as Glacial Lake Champagne glaciolacustrine sediments overlain by a McConnell-aged re-advance till, capped by Neoglacial Lake Alsek sediments. The top of permafrost was encountered at 1 m depth, and the bottom is located between 15 m and 20 m depth

based on ground temperature data (estimated at <17 m in the drill logs). Intact ice lenses up to 1.5 cm thick were observed between 6 m and 10 m depth. The core was frozen from 10 to 17 m depth, but there was no visible ice.

HJ_WRB_CO

Borehole HJ_WRB_CO is a YOWN groundwater monitoring well located at the southeast edge of the Haines Junction Conservation Officer's compound, approximately 15 m from the perimeter fence and 25 m from the main building (Fig. 12). The site is cleared of vegetation. The HJ_WRB_CO borehole is 26.2 m deep. The surficial sediments encountered at this site are primarily alternating silty clay and diamict (Figure 13c; Appendix A14). The series of diamict layers are interpreted to represent till deposited at a fluctuating ice front. These till units are interstratified with lacustrine

sediments from Glacial Lake Champagne. The till-lacustrine package is overlain by what is interpreted to be a sequence of Neoglacial Lake Alsek sediments interbedded with organics. A thin veneer of eolian loess caps the entire package. Permafrost was not encountered at this site during drilling, and permafrost-monitoring instrumentation was not installed in the borehole.

Future work

In spring 2024, customized instrumentation will be installed at selected borehole locations to match the depth of key permafrost horizons. At this time, ground-surface temperature loggers will be installed at the sites outside and adjacent to the borehole. An additional shallow borehole will also be drilled at each site to determine how much of a thermal effect the drill disturbance and borehole housing has on near-surface ground temperatures.

Data and interpretations from each site will inform future development in the area and each site will serve as a reference of how ground temperatures respond to changes in air temperature and precipitation in different regions of the Yukon. Geotechnical data, including volumetric and gravimetric ice-content measurements, will provide more information on extent of ground subsidence expected as permafrost thaws and what the implications might be for existing and future development.

Conclusions

Fifteen boreholes were drilled in five communities in October 2023. Borehole depths ranged from 10.9 m to 35.0 m. Permafrost was encountered in 10 boreholes and 5 boreholes penetrated the bottom of permafrost. Drilling observations and ground temperature data collected to date provide preliminary estimates of local permafrost and active layer thicknesses. In Dawson City, permafrost is at least 21 m thick on the lower portion of Moosehide Slide and at least 14 m thick near the airport, and the top of permafrost is quite deep (5–7 m) at the disturbed sites (e.g., Moosehide and the recreation centre), and shallow (1 m) at the undisturbed site near the airport. In the two Mayo boreholes, permafrost was 6.5 m and 20.5 m thick, and the top of permafrost was estimated from drill core to be at 5 m and 8.5 m depth,

respectively. In Ross River, permafrost was greater than 14 m and 18.4 m thick at the two undisturbed sites; active layers are approximately 3.5 m thick. In one of three Beaver Creek boreholes, permafrost is 6 m thick and has a 3 m thick active layer. Near Haines Junction airport, permafrost is approximately 16 m thick and has a 1 m thick active layer.

Long-term ground temperature monitoring is planned to begin in 2024 and will document permafrost change at both relatively undisturbed and developed sites in these communities. These monitoring sites fill critical gaps in the existing ground temperature monitoring network. Additional site information and monitoring data will be available in the Yukon Permafrost Database (https://service.yukon.ca/permafrost/) in 2024.

References

Bond, J.D., 1999. The Quaternary history and till geochemistry of the Anvil District, east-central Yukon. In: Yukon Exploration and Geology 1998, C.F. Roots and D.S. Emond (eds.), Exploration and Geological Sciences Division, Yukon Region, Indian and Northern Affairs Canada, p. 105–116.

Brideau, M.A., Stead, D., Roots, C. and Orwin, J., 2007. Geomorphology and engineering geology of a landslide in ultramafic rocks, Dawson City, Yukon. Engineering Geology, vol. 89, no. 3–4, p. 171–194.

Bush, E. and Lemmen, D.S. (eds.), 2019. Canada's Changing Climate Report. Government of Canada, Ottawa, ON, 444 p. https://changingclimate.ca/synthesis/chapter/report/ [accessed December 31, 2023].

Calmels, F., Horton, B., Roy, L.P., Lipovsky, P. and Benkert, B., 2016. Assessment of risk to infrastructure from permafrost degradation and a changing climate, Ross River. Northern Climate ExChange, Yukon Research Centre, Yukon College, 87 p.

Clague, J.J. and Rampton, V.N., 1982. Neoglacial Lake Alsek. Canadian Journal of Earth Sciences, vol. 19, no. 1, p. 94–117.

Duk-Rodkin, A., 1999. Glacial limits map of Yukon. Exploration & Geological Services Division, Yukon Region, Indian & Northern Affairs Canada, Geoscience Map 1999-2., scale 1:1 000 000.

Environment Canada, 2023. Historical climate data. Environment Canada, Ottawa, Ontario, https://climate.weather.gc.ca/climate_normals/index_e.html [accessed December 31, 2023].

Heginbottom, J.A., Dubreuil, M.A. and Harker, P.A., 1995. Canada, permafrost. The National Atlas of Canada. Natural Resources Canada, Geomatics Canada, MCR Series no. 4177 (ed. 5), one map sheet, scale 1:7 500 000. https://doi.org/10.4095/294672

Jackson, L.E., 1994. Terrain inventory and Quaternary history of the Pelly River area, Yukon Territory. Geological Survey of Canada Memoir 437, 47 p.

Noetzli, J., Arenson, L.U., Bast, A., Beutel, J., Delaloye, R., Farinotti, D., Gruber, S., Gubler, H., Haeberli, W., Hasler, A., Hauck, C., Hiller, M., Hoelzle, M., Lambiel, C., Pellet, C., Springman, S.M., Vonder Muehll, D. and Phillips, M., 2021. Best practice for measuring permafrost temperature in boreholes based on the experience in the Swiss Alps. Frontiers in Earth Science, Sec. Cryospheric Sciences, vol. 9, article 607875. https://doi.org/10.3389/feart.2021.607875

Northern Climate Exchange, 2011. Mayo Landscape Hazards: Geological Mapping for Climate Change Adaptation Planning. Yukon Research Centre, Yukon College, 64 p.

Prairie Climate Centre, 2019. The Climate Atlas of Canada, version 2. https://climateatlas.ca [accessed December 31, 2023].

Rampton, V.N. and Paradis, S., 1979. Surficial geology and geomorphology of Pine Lake, Yukon Territory. Geological Survey of Canada, Preliminary Map 16-1981, scale 1:100 000.

Smith, C.A.S., Meikle, J.C. and Roots, C.F. (eds.), 2004. Ecoregions of the Yukon Territory: Biophysical properties of Yukon landscapes. Agriculture and Agri-Food Canada, PARC Technical Bulletin No. 04-01, Summerland, British Columbia, 313 p.

Smith, S.L., O'Neill, H.B., Isaksen, K., Noetzli, J. and Romanovsky, V.E., 2022. The changing thermal state of permafrost. Nature Reviews Earth & Environment, vol. 3, no. 1, p. 10–23.

Yukon Bureau of Statistics, 2023. Population Report, First Quarter, 2023. Yukon Bureau of Statistics, Government of Yukon, 4 p. https://yukon.ca/en/population-report-q1-2023 [accessed December 31, 2023].

Appendix A

Appendix A1. *Detailed borehole log for YGS_Moosehide.*

Start (m)	End (m)	Grain size*	Description	Permafrost	Ice description
0.0	0.2	o	organics	no	n/a
0.2	0.9	od	organic-enriched coarse diamict	no	n/a
0.9	1.8	d	diamict; grey	no	n/a
1.8	2.3	d	diamict; boulder at 2.0 m	no	n/a
2.3	3.5	d	diamcit; boulder from 2.3 to 3.4 m	no	n/a
3.5	4.3	d	no return	no	n/a
4.3	4.9	d	sandy rubble	no	n/a
4.9	7.0	d	sandy rubble; grey	no	n/a
7.0	7.9	d	sandy rubble; grey	yes	n/a
7.9	11.6	d	diamict; more fines than previous interval; grey	yes	n/a
11.6	13.7	d	clay-rich diamict; light grey to buff	yes	n/a
13.7	16.5	d	clay-rich diamict; grey to buff; dark grey from 13.7 to 14.0 m	yes	n/a
16.5	20.1	d	rubbly diamict; rare boulders; moist to wet; mottled light grey and buff; oxidized from 19.5 to 19.8 m	yes	n/a
20.1	23.2	d	muddy to sandy rubbly diamict; medium grey; highly oxidized from 23.6 to 24.4 m	yes	ice is bonding core,~40% ice in distinct lenses >1 cm, ice coating grains
23.2	28.7	d	sandy diamict; abrupt colour changes: dark grey to black from 25.0 to 26.2 m; brown from 26.2 to 27.4 m; green/grey from 27.4 to 28.7 m	yes	visible ice coating grains

* o: organic; c: clay; z: silt; s: sand; g: gravel; d: mixed fragments; r: rubble

Appendix A2. *Detailed borehole log for YGS_DawsonRec.*

Start (m)	End (m)	Grain size*	Description	Permafrost	Ice description
0.0	0.3	sg	backfill gravel; buff colour	no	n/a
0.3	0.8	ozcg	organic-enriched, silty to clay-rich gravel; ~30% clasts; grading from lighter to darker brown	no	n/a
0.8	1.8	szg	gravel; sandy-silt matrix; pebbles and cobbles; light brown	no	n/a
1.8	2.1	czsg	clay-rich, silty to sandy gravel; grey	no	n/a
2.1	2.2	o	organics	no	n/a
2.2	2.3	sg	sandy gravel; grey	no	n/a
2.3	2.6	o	fibric organics	no	n/a
2.6	2.9	cz	clay-rich silt; no clasts; grey	no	n/a
2.9	3.4	zsg	sandy to silty gravel; pebbles and cobbles; grey	no	n/a
3.4	5.0	zsg	coarse sand and gravel, some silt; cobbles up to 20 cm; grey	no	n/a
5.0	5.8	zsg	coarse sand and gravel, some silt; cobbles up to 20 cm; grey	yes	no visible ice
5.8	6.1	zsg	sandy to silty gravel; mostly pebbles; grey	yes	no visible ice
6.1	7.9	zsg	silty to sandy gravel; mostly pebbles; wet and dry alternating layers; grey and buff	yes	no visible ice
7.9	11.0	zsg	variable gravel, mainly pebbles, a few cobbles up to 12 cm, grey; pebble lens at ~10.7 m; light brown	yes	no visible ice

* o: organic; c: clay; z: silt; s: sand; g: gravel; d: mixed fragments; r: rubble

Appendix A3. Detailed borehole log for YGS_YDA.

Start (m)	End (m)	Grain size*	Description	Permafrost	Ice description
0.0	0.3	oz	fibric organics	no	n/a
0.3	0.6	oz	humic organics grading to organic-rich silt	no	n/a
0.6	3.0	oz	organic-rich silt	yes	ice lenses 2–5 cm thick, ~15% visible ice
3.0	4.0	zg	silty, pebble gravel	yes	20% visible ice, coating particles
4.0	4.6	sg	sandy gravel, dry	yes	no ice visible
4.6	7.0	g	gravel	yes	ice coating particles
7.0	11.0	g	gravel	yes	n/a
11.0	14.5	czg	muddy gravel, brown/grey; dry silt lenses	yes	n/a
14.5	15.5	r	weathered schist	yes	n/a

* o: organic; c: clay; z: silt; s: sand; g: gravel; d: mixed fragments; r: rubble

Appendix A4. *Detailed borehole log for YGS_Mayo_School.*

Start (m)	End (m)	Grain size*	Description	Permafrost	Ice description
0.0	0.6	o	fibric to mesic organics	no	n/a
0.6	0.9	z	silt; grey	no	n/a
0.9	1.4	zs	silty sand; grey/buff	no	n/a
1.4	1.8	sg	poorly sorted, sandy pebble gravel; fining upward	no	n/a
1.8	3.4	sg	sandy gravel; coarse sand and pebbles; water at the top of the interval	no	n/a
3.4	4.3	zc	sticky clay; dense; wet; grey	no	n/a
4.3	4.9	zs	silty fine sand	no	n/a
4.9	7.9	zs	silty fine sand	no	n/a
7.9	8.5	zs	silty fine sand; grey	no	n/a
8.5	11.0	zs	silty fine sand; grey	yes	no visible ice
11.0	14.0	zs	silty fine sand; more fines and wetter from 11.3 to 11.6 m	yes	no visible ice
14.0	17.1	z	silt; dry; grey	yes	ice lens at 15.2 m, ~1 cm thick
17.1	20.1	zsc	rhythmite – alternating lenses of clay and silty fine sand; each about 1 cm thick	yes	clay lenses often not frozen; ice lens at 19.5 m, ~2 cm thick; chunks of ice up to 5 cm thick
20.1	23.2	cz	rhythmite – silt lenses getting thicker	yes	relatively ice poor
23.2	26.2	cz	fining upward; becomes more massive; silts at the bottom of the interval	yes	no visible ice
26.2	29.0	z	silt; 5 cm well-sorted sand lens at 26.2 m	yes	n/a
29.0	29.3	z	silt	no	n/a
29.3	36.0	cz	clay-rich silt; soft and sticky; pebble at 35.4 m	no	n/a

* o: organic; c: clay; z: silt; s: sand; g: gravel; d: mixed fragments; r: rubble

Appendix A5. *Detailed borehole log for YGS_Mayo_GroupHome.*

Start (m)	End (m)	Grain size*	Description	Permafrost	Ice description
0.0	0.3	o	fibric organics	no	n/a
0.3	0.6	cz	clay-rich silt; dense; wet; grey/brown	no	n/a
0.6	1.2	z	silt; dry; very powdery	no	n/a
1.2	1.8	scz	clay-rich silt; dense; wet; coarse sand lenses up to 3 cm thick	no	n/a
1.8	2.1	g	cobble gravel; clasts up to 10 cm; saturated	no	n/a
2.1	5.0	zc	mostly clay, some silt; dense, stiff, dry	no	n/a
5.0	5.2	g	thin gravel lens	no	n/a
5.2	5.8	zc	silty clay; some gravel at the bottom of the interval	yes	ice lenses
5.8	7.9	zc	silty clay; clay layers are unfrozen	yes	ice lenses from 5.2 to 7.9 m; occasional ice lenses up to 20 cm thick containing suspended sediment
7.9	11.0	zc	silty clay with ice lenses	yes	ice lenses, up to 20 cm thick; unfrozen between lenses
11.0	12.5	zc	silty clay with ice lenses; clay lenses are thawed	yes	ice lenses
12.5	14.0	cz	stiff clay	no	n/a
14.0	17.1	szc	stiff clay and silt; some fine sand lenses	no	n/a

* o: organic; c: clay; z: silt; s: sand; g: gravel; d: mixed fragments; r: rubble

Appendix A6. Detailed borehole log for YGS_RR_Lagoon.

Start (m)	End (m)	Grain size*	Description	Permafrost	Ice description
0.0	0.6	o	fibric organics; White River ash ~3 cm thick at 0.6 m	no	n/a
0.6	0.9	z	silt; some oxidation; loose, buff colour	no	n/a
0.9	1.5	zs	silty sand; fining upwards; grey/brown at the top, colour change to dark grey at the bottom	no	n/a
1.5	2.1	zsg	sandy pebble gravel, some silt; first 0.2 m wetter, bottom 0.2 m dry and loose; grey	no	n/a
2.1	2.4	sg	open-work cobble gravel	no	n/a
2.4	3.4	zsg	poorly sorted gravel; pebbles and cobbles	no	n/a
3.4	3.7	msg	muddy, coarse sand and gravel	yes	top of permafrost in gravel ~3.5 m
3.7	4.9	zc	silty clay; sticky; stiff; dark grey	yes	ice lenses ~1 cm starting at 3.8 m; ice lenses up to 8 cm thick
4.9	7.3	zc	silty clay; dark grey; pebbles and coarse sand from 7.0 to 7.3 m	yes	ice lenses variable thickness; ~15 cm ice lens near bottom of interval
7.3	11.0	zc	mostly ice with lenses of stiff frozen silty clay; dark grey	yes	high ice content; large sections pure ice starting at ~7.6 m
11.0	14.0	zc	mostly ice; lenses of silty clay up to 20 cm thick	yes	~90% ice
14.0	17.1	zc	alternating lenses of pure ice and silty clay; ice thickness ranging from 20 to 50 cm; more clay lenses than previous unit	yes	~50–60% ice over whole section
17.1	20.1	zc	stiff clay; trace silt; dry, dark grey; more clay than ice in this unit	yes	~10% ice; small ice lenses ~0.5 cm thick; ice lens at 17.4 m ~20 cm thick
20.1	23.2	zc	stiff, silty clay; more moisture below ~21.3 m where thawed	yes	thawed at 21.9 m; very little visible ice in frozen section
23.2	26.2	zc	clay, trace silts; well-bonded; dark grey	no	n/a

* o: organic; c: clay; z: silt; s: sand; g: gravel; d: mixed fragments; r: rubble

Appendix A7. *Detailed borehole log for YGS_RR_LagoonRd.*

Start (m)	End (m)	Grain size*	Description	Permafrost	Ice description
0.0	0.2	o	fibric organics	no	n/a
0.2	0.2	-	White River ash	no	n/a
0.2	0.6	sz	sandy silt; oxidized; darker orange at the top fading to light brown at the bottom	no	n/a
0.6	1.8	zsg	silty to sandy gravel; pebbles and cobbles up to 10 cm; loose and dry; mottled light grey and brown colour	no	n/a
1.8	3.4	zsg	silty to sandy gravel; 80% pebbles, 20% smaller cobbles (~7 cm); saturated; light grey	no	n/a
3.4	4.9	zsg	silty to sandy gravel; 80% pebbles, 20% smaller cobbles (~7 cm); saturated; light grey	yes	n/a
4.9	5.8	zsg	silty to sandy gravel; pebbles and cobbles; wet; grey	yes	ice likely melted from drilling
5.8	7.9	zc	silty clay; stiff; dark grey	yes	small (<0.5 cm) ice lenses; at 7.3 and 7.6 m ice lenses ~2 cm each; a lot of core has no visible ice
7.9	11.0	zc	silty clay	yes	bottom 1.5 m has no visible ice; 1 cm ice lens at 8.2 m; 3 cm ice lens at 9.4 m; 90% of core has no visible ice
11.0	17.1	zc	silty clay; rare sand lenses	yes	no visible ice

* o: organic; c: clay; z: silt; s: sand; g: gravel; d: mixed fragments; r: rubble

Appendix A8. Detailed borehole log for YGS_RR_Highways.

Start (m)	End (m)	Grain size*	Description	Permafrost	Ice description
0.0	0.3	g	backfill gravel	no	n/a
0.3	0.5	zso	silty to sandy organics; some pebbles; dry; brown	no	n/a
0.5	0.5	-	White River ash	no	n/a
0.5	1.7	zsg	silty to sandy pebble gravel; loose and dry; grading from light brown at the top to light grey at the bottom	no	n/a
1.7	2.0	czsg	clay-rich silty to sandy pebble gravel; powdery; light grey	no	n/a
2.0	3.7	sgF	coarse, sandy gravel; mostly pebbles; some moisture	no	n/a
3.7	4.3	g	gravel	no	n/a
4.3	4.6	czg	clay-rich, silty pebble gravel; dark grey	no	n/a
4.6	7.9	zc	clay; trace silt; stiff; dark grey	no	n/a
7.9	11.0	c	clay; stiff; dark grey	yes	frozen starting at 8.2 m; ice lenses of varying thickness (0.5–5 cm) all the way to 11.0 m; top of permafrost is ice rich, up to 90% ice

* o: organic; c: clay; z: silt; s: sand; g: gravel; d: mixed fragments; r: rubble

Appendix A9. *Detailed borehole log for YGS_BC_Ptarmigan.*

Start (m)	End (m)	Grain size*	Description	Permafrost	Ice description
0.0	0.3	o	fibric organics; 25 cm moss mat	no	n/a
0.3	0.6	szg	fine sand to silty gravel; 40% rounded pebbles; dark brown; saturated	no	n/a
0.6	2.1	zsg	silty-sandy gravel; rounded pebbles; loose and dry; light grey	no	n/a
2.1	4.6	zsg	silty-sandy gravel; poorly sorted; rounded pebbles; coarser sand from 4.0 to 4.6 m; saturated from 4.3 to 4.6 m	undetermined	n/a
4.6	4.9	zsg	silty-sandy gravel; dry	undetermined	n/a
4.9	5.8	zsg	silty-sandy gravel; matrix fining downwards; saturated first 0.5 m, then damp to 5.5 m; 5.5–5.8 m dry and loose	undetermined	n/a
5.8	12.2	gzs	fine sand and silt, massive; dense, dry, well-bonded; layer of rounded pebbly gravel from 6.4 to 6.7 m; silty fine sand with rounded pebbles and some coarse sand from 7.9 to 8.2 m	undetermined	n/a
12.2	13.7	sg	well-sorted pebble gravel and coarse sand	no	n/a
13.7	14.9	zs	silty fine sand; massive with a few pebbles; saturated at 14.6 m	no	n/a
14.9	17.1	zsg	poorly sorted, silty, sandy gravel; loose; large cobble at 16.5 m; silty, fine sand lens at 15.8 m; wet and sticky below 16.5 m	no	n/a
17.1	19.2	d	matrix-supported diamict; saturated; sticky; brown	no	n/a
19.2	20.7	d	matrix-supported diamict; silty sand matrix; 60% pebbles ranging from rounded to sub-angular; moderately dense; dark grey	no	n/a
20.7	21.3	d	matrix-supported diamict; silty sand matrix; pebbles to cobbles; very dense	no	n/a

* o: organic; c: clay; z: silt; s: sand; g: gravel; d: mixed fragments; r: rubble

Appendix A10. *Detailed borehole log for YGS_BC_Brown.*

Start (m)	End (m)	Grain size*	Description	Permafrost	Ice description
0.0	0.3	o	fibric organics	no	n/a
0.3	0.6	sz	dense, sandy silt; oxidized; pebbles at the bottom of unit	no	n/a
0.6	2.1	zsg	silty-sandy gravel; 40% clasts: 70% pebbles, 30% cobbles; clasts are subangular to subround; dry and loose; light grey	no	n/a
2.1	3.7	sg	sandy pebble gravel; medium-grained sand; 80% pebbles	no	n/a
3.7	15.2	zsg	silty-sandy gravel; 70% pebbles, 30% cobbles; grey, dry, powdery; lenses of fines and damp gravel from 5.2 to 5.8 m; muddy layer at 5.5 m	no	n/a
15.2	15.8	zsg	silty-sandy gravel; loose and damp; 70% clasts: 40% granules, 40% pebbles, 20% cobbles; clasts are rounded to subrounded	no	n/a
15.8	17.1	d	matrix-supported diamict; silty-sand matrix; 60% clasts: 40% granules, 60% pebbles; clasts are rounded to subangular; crumbly, damp, moderately compact	no	n/a

* o: organic; c: clay; z: silt; s: sand; g: gravel; d: mixed fragments; r: rubble

Appendix A11. *Detailed borehole log for YGS_BC_Hwys.*

Start (m)	End (m)	Grain size*	Description	Permafrost	Ice description
0.0	2.1	g	backfill gravel	no	n/a
2.1	5.8	szg	silty-sandy gravel; mostly pebbles, some cobbles; clasts are subround; brown near top to light grey near bottom	no	n/a
5.8	6.4	d	matrix-supported diamict; sandy silt matrix; cohesive but not dense; 50% clasts: 70% pebbles, 30% cobbles, rounded to subrounded; damp; brown	no	n/a
6.4	11.0	zsg	silty-sandy gravel; 60% clasts: 70% pebbles, 30% cobbles; fewer clasts below 9.4 m, water table at ~10.7 m	no	n/a
11.0	14.0	sg	sandy pebble gravel; saturated	no	n/a

* o: organic; c: clay; z: silt; s: sand; g: gravel; d: mixed fragments; r: rubble

Appendix A12. *Detailed borehole log for YGS_HainesRd.*

Start (m)	End (m)	Grain size*	Description	Permafrost	Ice description
0.0	0.3	ozs	0–0.2 m fibric organics; 0.2–0.3 m mesic organics	no	n/a
0.3	3.7	d	matrix-supported diamict; sandy, silt matrix; 0.3–0.9 m looser, mixed with organics; 0.9–3.7 m grey and sticky; increased moisture toward bottom of unit	no	n/a
3.7	8.5	zsg	silty to sandy pebble gravel; finer layer at 3.8–4.0 m; well-sorted medium sand; 6.0–6.7 m fine to coarse sand, coarsening upward, a few small pebbles at the top; 6.7-7.6 m silty fine sand, no cobbles, well-sorted; pebble-cobble gravel from 7.9-8.5 m	no	n/a
8.5	11.0	d	matrix-supported diamict; silty, fine sand matrix; 15% clasts; pebbles and cobbles; moderately dense	no	n/a
11.0	11.7	d	matrix-supported diamict; fine sand and silt matrix; ~10% clasts, granules and pebbles; dry and dense	no	n/a
11.7	12.5	s	well-sorted, fine to medium-grained sand; fining downward; occasional pebble; damp, grey	no	n/a
12.5	15.5	d	diamict; ~10% clasts at top, increasing to 40% at the bottom of the unit	no	n/a

* o: organic; c: clay; z: silt; s: sand; g: gravel; d: mixed fragments; r: rubble

Appendix A13. *Detailed borehole log for YGS_HJ_AirportRdDeep.*

Start (m)	End (m)	Grain size*	Description	Permafrost	Ice description
0.0	1.4	zc	silty clay; some laminations; very sticky; damp; tan colour	yes	n/a
1.4	6.1	d	matrix-supported diamict; silty to fine-sand matrix; at 4.9 m coarser sand lens ~10 cm thick; 5.0–6.1 m crumbly brown silt and clay matrix with angular pebbles and granules	yes	n/a
6.1	26.2	cz	silty clay; massive, no laminations; 6.1–7.5 m: very few clasts <5%, very dense; 7.5–7.9 m: dry, very dense, pebbles and granules ~5%; colour change at 6.1 m from brown to grey; fines upward	yes	ice lens ~1.5 cm at 10.4 m; ice lens ~1 cm at 10.8 m

* o: organic; c: clay; z: silt; s: sand; g: gravel; d: mixed fragments; r: rubble

Appendix A14. *Detailed borehole log for HJ_WRB_CO.*

Start (m)	End (m)	Grain size*	Description	Permafrost	Ice description
0.0	0.3	o	organics	no	n/a
0.3	0.8	sz	fine to sandy silt; oxidized in bottom half	no	n/a
0.8	1.8	cz	silt and clay; no clasts; first 0.3 m crumbly then compact	no	n/a
1.8	7.9	cz	same as above, stickier; organics at ~1.9 m; occasional clasts, pebbles starting at 7.0 m, <5%; some laminations visible at 3.0 m, and from 7.3 to 7.9 m	no	n/a
7.9	9.1	czd	matrix-supported diamict; 40% clasts: 20% granules, 70% pebbles, 10% cobbles; no cobbles in bottom 0.6 m; clasts are subangular to subround	no	n/a
9.1	12.2	czd	matrix-supported diamict; 5–10% pebbles; brown	no	n/a
12.2	17.7	d	matrix-supported diamict; clay-rich, silty to fine sand matrix; 25–30% clasts: 90% pebbles, 10% cobbles; no obvious structure; grey, very compact	no	n/a
17.7	19.8	sz	fine, sandy-silt with very few clasts, <5% pebbles	no	n/a
19.8	21.3	d	matrix-supported diamict; clay-rich, silty fine sand matrix; 15–20% clasts	no	n/a
21.3	26.2	zs	silty fine sand; some fine laminations at 22.7 m, thixotrophic; wet at 22.9 m and 24.1 m	no	n/a

* o: organic; c: clay; z: silt; s: sand; g: gravel; d: mixed fragments; r: rubble

Preliminary observations of the Mesoproterozoic Pinguicula Group in the Coal Creek inlier, Yukon (parts of NTS 116B/11, 14)

Lucy C. Webb [*]
Department of Earth and Planetary Sciences, Stanford University

Tyler K. Ambrose [‡]
Yukon Geological Survey

Abstract

Proterozoic strata in central Yukon are exposed in the Coal Creek, Hart River and Wernecke inliers. The Paleoproterozoic and Neoproterozoic strata are well correlated across the inliers; however, correlation of the Mesoproterozoic units remains ambiguous. We present two stratigraphic logs of Mesoproterozoic units PP1 and PP2 (previously termed PR1 and PR2, respectively) in the Coal Creek inlier. PP1 is dominantly siltstone and sandstone, whereas PP2 is mostly dolostone. In one section where the contact is well exposed, PP2 gradationally overlies PP1, suggesting that these units, at least locally, are conformable. Based on similarities in the stratigraphy and contact relationships with underlying and overlying units, we suggest that PP1 and PP2 are correlative with the Pinguicula Group formally defined in the Hart River and Wernecke inliers. Resolving how PP1 and PP2 correlate with Proterozoic strata exposed in other inliers provides insight into basin development along northwest Laurentia during the Meso–Neoproterozoic.

Introduction

Proterozoic strata are exposed across central Yukon in a series of erosional inliers that are separated from each other by younger Phanerozoic rocks (Fig. 1). Mapping, stratigraphic analysis, and geochronology have been used to correlate strata between these inliers. Correlation of the late Paleoproterozoic Wernecke Supergroup in these inliers across the Yukon is well established (Delaney, 1981; Abbott, 1997; Thorkelson, 2000; Furlanetto et a*l*., 2016). Analysis of the Neoproterozoic Fifteenmile Group in the Coal Creek inlier (Macdonald et a*l*., 2011, 2012; Halverson et a*l*., 2012) has provided convincing evidence for its correlation with the Hematite Creek Group (Mackenzie Mountains Supergroup) in the Wernecke inlier (Eisbacher, 1981; Thorkelson, 2000; Turner, 2011). However, compared

to Paleoproterozoic and Neoproterozoic strata, correlation of Mesoproterozoic strata across the Yukon is less well understood. In particular, correlating units PP1 and PP2 in the Coal Creek inlier to the other inliers farther east has remained controversial (Fig. 2; Medig et a*l*., 2010, 2014; Macdonald et a*l*., 2012). Resolving the age and correlation of these units is necessary to understand the history of basin development along the northwestern margin of Laurentia (present-day coordinates) in the Proterozoic.

This paper presents two measured stratigraphic sections of PP1 and PP2 in the Coal Creek inlier (NTS 116B/11, 14). Section W2313 was measured through strata mapped as PR1 and PR2 by Thompson et a*l*. (1994);

[*] lcwebb@stanford.edu
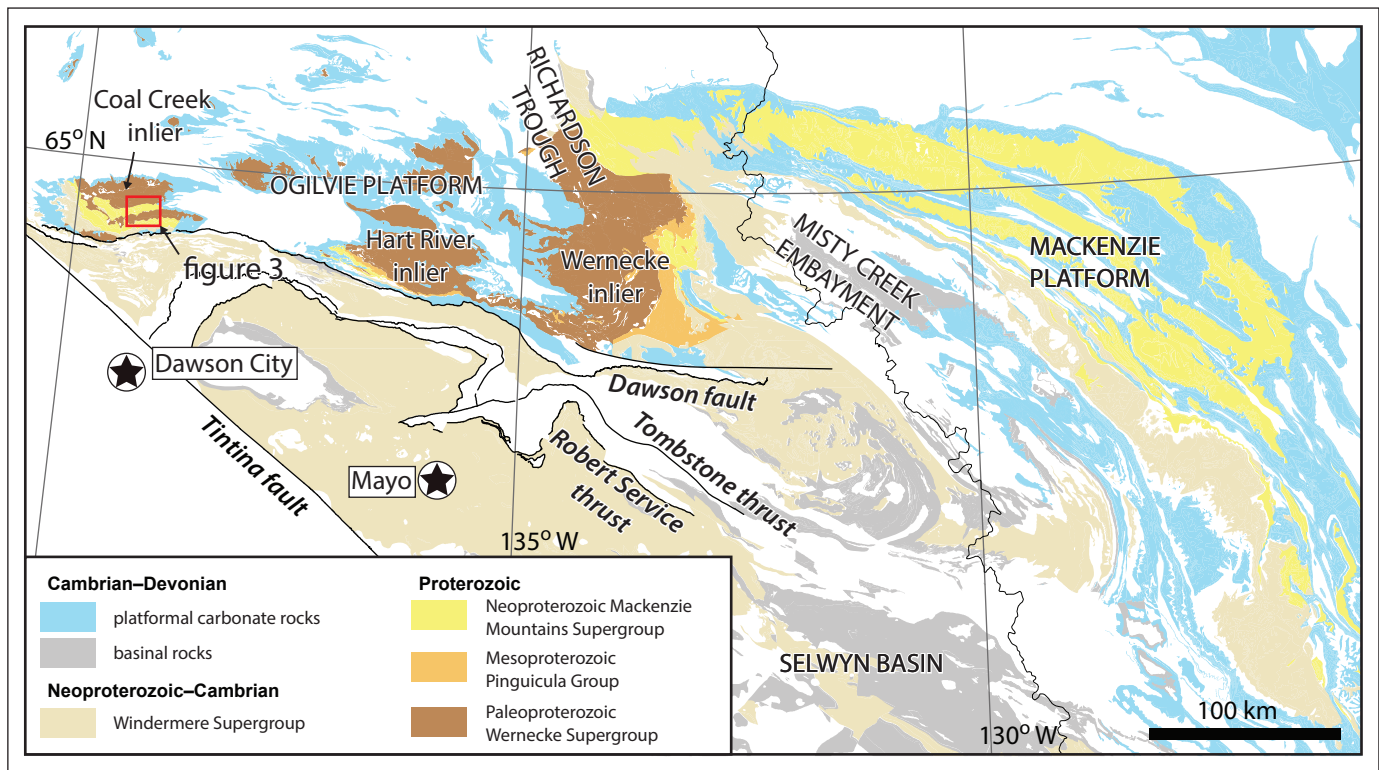[‡] tyler.ambrose@yukon.ca

Figure 1. *Simplified geological map showing the distribution of Proterozoic strata in the Yukon and Northwest Territories (after Moynihan et al., 2019). The study area (outlined in red box) is located in the Coal Creek inlier. White areas are Devonian and younger strata. Geology is from Yukon Geological Survey (2022).*

Figure 2. *Summary of terminology used and proposed correlations for units PR1/PP1 and PR2/PP2 by Thompson et al. (1994), Medig et al. (2010, 2016), Macdonald et al. (2012), Strauss et al. (2014), and this paper. Thompson et al. (1994) did not correlate these units to the Pinguicula Group. Medig et al. (2016) did not correlate PR1 with the Pinguicula Group and instead proposed that PR1 was deposited during an earlier basin-forming event based on the results of Medig et al. (2014).*

PR1 and PR2 were later termed PP1 and PP2, respectively, by Strauss et a*l.* (2014). Section W2316 was measured through strata mapped as the Quartet and Gillespie Lake groups (Wernecke Supergroup) by Thompson et a*l.* (1994) but are interpreted here as PP1 and PP2 based on field observations made during summer 2023. In this paper we suggest that PP1 and PP2 are correlative with the Pinguicula Group in the Wernecke and Hart River inliers to the east, in agreement with some previous work (Medig et a*l.,* 2010; Halverson et a*l.,* 2012; Macdonald et a*l.,* 2012; Strauss et a*l.,* 2014). Field observations reported here do not support the hypothesis that PP1 was deposited in a separate, earlier, basin-forming event (Medig et a*l.,* 2014, 2023).

Previous work

The Coal Creek inlier was first mapped at a reconnaissance scale of 1:250 000 by Green (1972). Building on this initial work, Thompson et a*l.* (1994) mapped the Coal Creek inlier at a more detailed 1:50 000 scale and divided the Proterozoic strata into the Wernecke Supergroup, the lower Fifteenmile Group (PR1–PR5), the upper Fifteenmile Group and the Mount Harper Group. As in the Hart River and Wernecke inliers (Delaney, 1981), the Wernecke Supergroup in the Coal Creek inlier is divided, from oldest to youngest, into the Fairchild Lake, Quartet and Gillespie Lake groups (Thompson et a*l.,* 1994). Here, we focus on the sedimentary units PR1 and PR2 (termed PP1 and PP2 here, building on recent work), which unconformably overlie the Wernecke Supergroup and underlie units PR3–PR5.

Since Thompson et a*l.* (1994), units PR1 and PR2 have been assigned and correlated to different groups (Fig. 2). Based on similar stratigraphy and contact relationships with the underlying Wernecke Supergroup and Wernecke Breccia, Medig et a*l.* (2010) tentatively correlated PR1 and PR2 with the Pinguicula Group in the Wernecke and Hart River inliers (Fig. 2). Macdonald et a*l.* (2011) measured section E1003 through PR1 and PR2 and referred to those units as 'Fifteenmile Group undifferentiated'. Macdonald et a*l.* (2012) agreed with Medig et a*l.* (2010) and correlated units PR1 and PR2, as well as PR3, with the Pinguicula Group, and assigned PR4 and PR5 to the newly defined and informal 'lower' assemblage of the Fifteenmile Group. Halverson et a*l.*

(2012) agreed that PR1 and PR2 are correlative with the Pinguicula Group and informally divided units PR3–5 in the lower Fifteenmile Group into the Gibben formation, equivalent to PR3, PR4 and PR5a, and the Chandindu Formation, equivalent to PR5 (formalized in Kunzmann et a*l.,* 2014).

The correlations between PR1 and the Pinguicula Group were challenged by Medig et a*l.* (2014). Based on the presence of a near unimodal ca. 1499 Ma detrital zircon population from a sandstone within PR1, which is distinct from the Pinguicula Group in the Hart River and Wernecke inliers, Medig et a*l.* (2014, 2023) proposed that PR1 records a separate, older basin-forming event and is not correlative with the Mount Landreville Formation of the Pinguicula Group. Furthermore, they proposed that the contact between PR1 and PR2 is unconformable and that PR2 is still possibly correlative to the Rubble Creek Formation of the Pinguicula Group.

In their updated compilation map of the Coal Creek inlier, Strauss et a*l.* (2014) renamed PR1 and PR2 to PP1 and PP2, respectively, and this is the terminology that we will use here. Notably, throughout these changes in unit names and correlation schemes, the lithological descriptions of the units have remained consistent (Table 1). PP1 is described as a siltstone to shale-dominated unit with large dolostone blocks interpreted as olistoliths and siliciclastic conglomerates interpreted as debris flows. PP2 is a dolostone-dominated unit with dolostone grainstone, micrite and boundstone. PP2 is locally stromatolitic and has minor shale and siltstone intervals (Medig et a*l.,* 2014; Strauss et a*l.,* 2014).

Stratigraphy

Section W2313

Section W2313 was measured along the same ridge as section E1003, which was previously measured and described in Macdonald et a*l.* (2011) as part of broader work to correlate all Neoproterozoic strata in the Coal Creek inlier (Figs. 3, 4). The purpose of remeasuring and describing this section here is to 1) focus on these units in light of new observations on the Pinguicula Group in the Hart River and Wernecke inliers (Medig et a*l.,* 2016, 2023); 2) collect samples for isotopic, geochemical and geochronological analyses; and 3) provide a comparison with section W2316 (described below).

Table 1. *Description of units PR1–PR5 from Thompson et al. (1994) and updated terminology and descriptions from Strauss et al. (2014).*

Thompson et al. (1994)		Strauss et al. (2014)	
PR5	shale; pebbly mudstone; gritty mudstone; stromatolitic limestone; quartz sandstone	Chandindu Fm	basal maroon shale and siltstone with abundant mud cracks; transitions upward into cyclic shale, siltstone, and dolostone intervals with grainstone, stromatolites, or microbialaminite; local stromatolitic bioherms and poorly sorted, massive coarse-grained sandstone beds; upper part contains large carbonate olistoliths (possibly correlative with Katherine and Hematite Creek groups; Halverson et al., 2012; Long and Turner, 2012; Macdonald et al., 2012; Kunzmann et al., 2014)
PR4	medium grey dolostone breccia, oolitic packstone, uncommon stromatolitic dolostone	Gibben Fm	grey ribbon-bedded dolostone, oolitic grainstone, stromatolitic dolostone, and microbialaminite with tepee structures; thickens northward into several hundred metres of grey to black shale that transition up-section into pink ribbon-bedded limestone (possibly correlative with Katherine and Hematite Creek groups; Halverson et al., 2012 ; Long and Turner, 2012; Macdonald et al., 2012)
PR3	recessive weathering grey medium-bedded dolomite with mudstone interbeds		
PR2	medium to thick-bedded dolomitic mudstone; dolostone breccia; massive, medium crystalline dolostone	PP2	orange to light blue weathering dolostone grainstone, micrite, and boundstone; locally stromatolitic with morphospecies *Minjaria* and *Conophyton*; locally upper black shale and minor dolomicrite with green weathering, planar-laminated siltstone and minor coarse-grained quartz arenite (equivalent to PR2 of Medig et al. [2014])
PR1	shale, silty dolomite with common dolostone olistoliths	PP1	weakly foliated, brown to grey-coloured siltstone, shale, and phyllite with irregularly dispersed large dolostone blocks and conglomerate interpreted as olistoliths and debris flows (Macdonald et al., 2012; equivalent to PR1 of Medig et al. [2014[)

The base of section W2313 is placed at a minor fault that separates orange-weathering dolostone to the north and dark grey siltstone to the south (Figs. 4, 5a, b and 6a). The dolostone below the fault consists of alternating beds of finely laminated, micritic dolostone, and dolostone with granule to pebble-sized, micritic dolomite intraclasts (Fig. 5a). Stromatolites and tepee structures are also present. Consistent with previous mapping of this area, we interpret this dolostone as part of the Gillespie Lake Group.

Above the faulted contact, the basal 280 m of section W2313 is composed of heavily cleaved siltstone (Fig. 6b) and sandstone. Aside from current ripple cross-lamination in sandstone (Fig. 6c), sedimentary structures are limited. Thin beds of very coarse sandstone are present but rare in the first 275 m of the section. The interval from 280 to 310 m is dominantly

medium to very coarse grained sandstone (Fig. 6d). From 310 to 370 m, the exposure is poor and is mostly recessive subcrop interpreted as siltstone. At approximately 340 m, an orange-weathering dolostone olistolith, several metres wide and several metres tall with conical stromatolites, is present (Fig. 6e, f). Additional olistoliths, up to several tens of metres in size, were observed in this same siltstone interval along ridges to the east and southeast.

Approximately 665 m of grey-weathering dolostone is present above the basal 370 m of siltstone and sandstone. The lower 170 m of dolostone consists of alternating beds of dolomite intraclast conglomerate and planar-laminated micritic dolostone (Fig. 7a). The dolomite intraclast conglomerate contains granule to cobble-sized clasts. Above the lower 170 m, intraclast conglomerate beds are absent and the grey-weathering
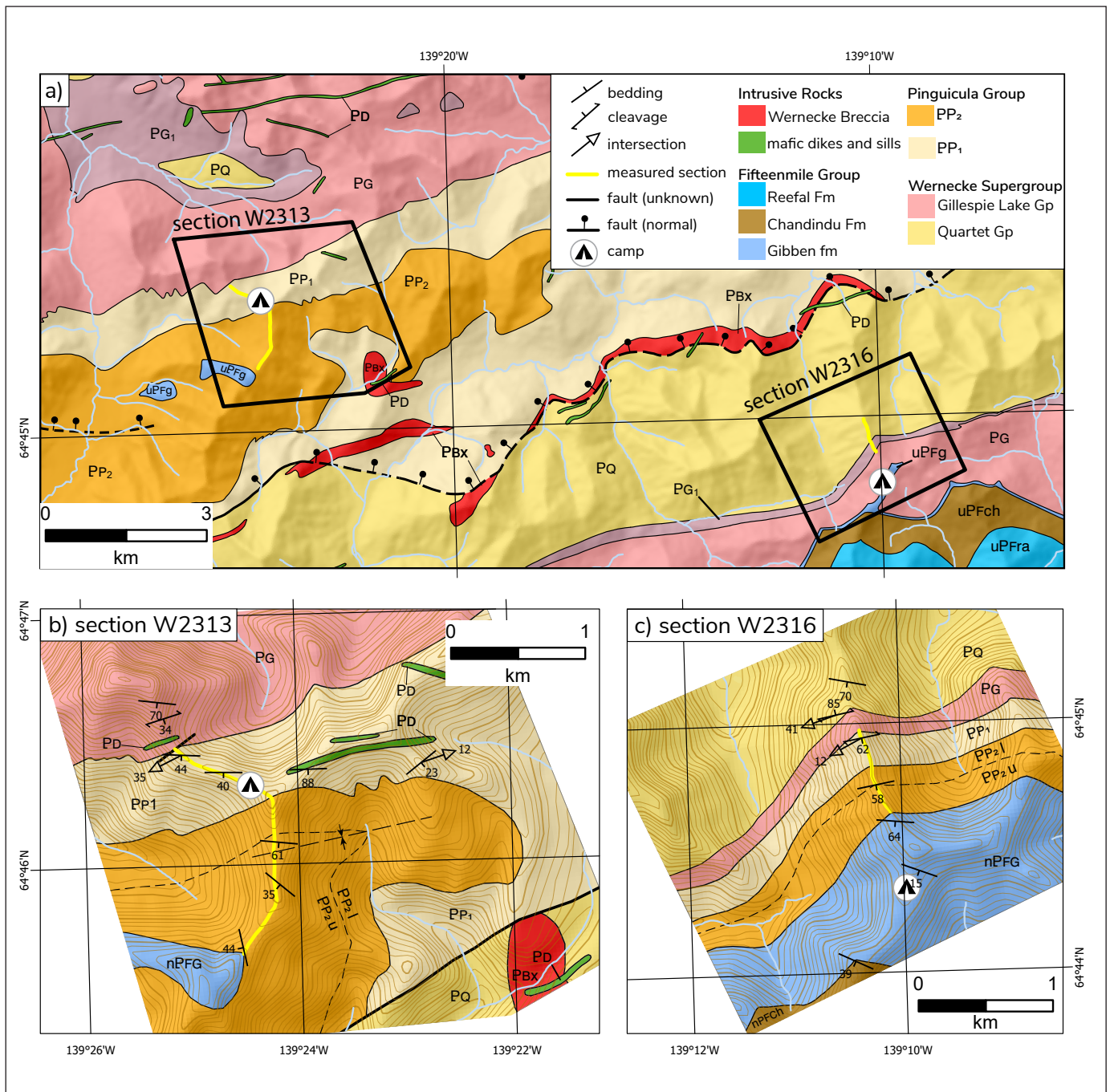
Figure 3. a) Geological map of the study area showing the location (yellow lines) of the two stratigraphic sections we present in this paper (geology from Strauss et al. [2014] and Thompson et al. [1994]). **b)** Geology of the area at section W2313 modified from Strauss et al. (2014). The original map of Thompson et al. (1994) and subsequent update by Strauss et al. (2014) mapped the Wernecke Breccia (PBx) in the southeastern part of the area as cross-cutting PP1/PR1; however, the Wernecke Breccia has since been dated at ca. 1.6 Ga (Thorkelson et al., 2001), indicating that the host rocks are the older ca. 1.65 Ga Wernecke Supergroup (Furlanetto et al., 2016). Given that these rocks are siliciclastic, they most likely belong to the Quartet Group and the contact with PP1 is now interpreted as a fault. **c)** Geology of the area at section W2316. As seen in panel a), the rocks transected by this section were originally mapped as the Quartet and Gillespie Lake groups. However, as discussed in the text, we interpret only a thin interval of Gillespie Lake Group near the base of our section that is underlain by the Quartet Group and is overlain by PP1, PP2 and the Fifteenmile Group. In panels b) and c), the contact between our upper (PP2u) and lower (PP2l) is indicated by a dashed line.
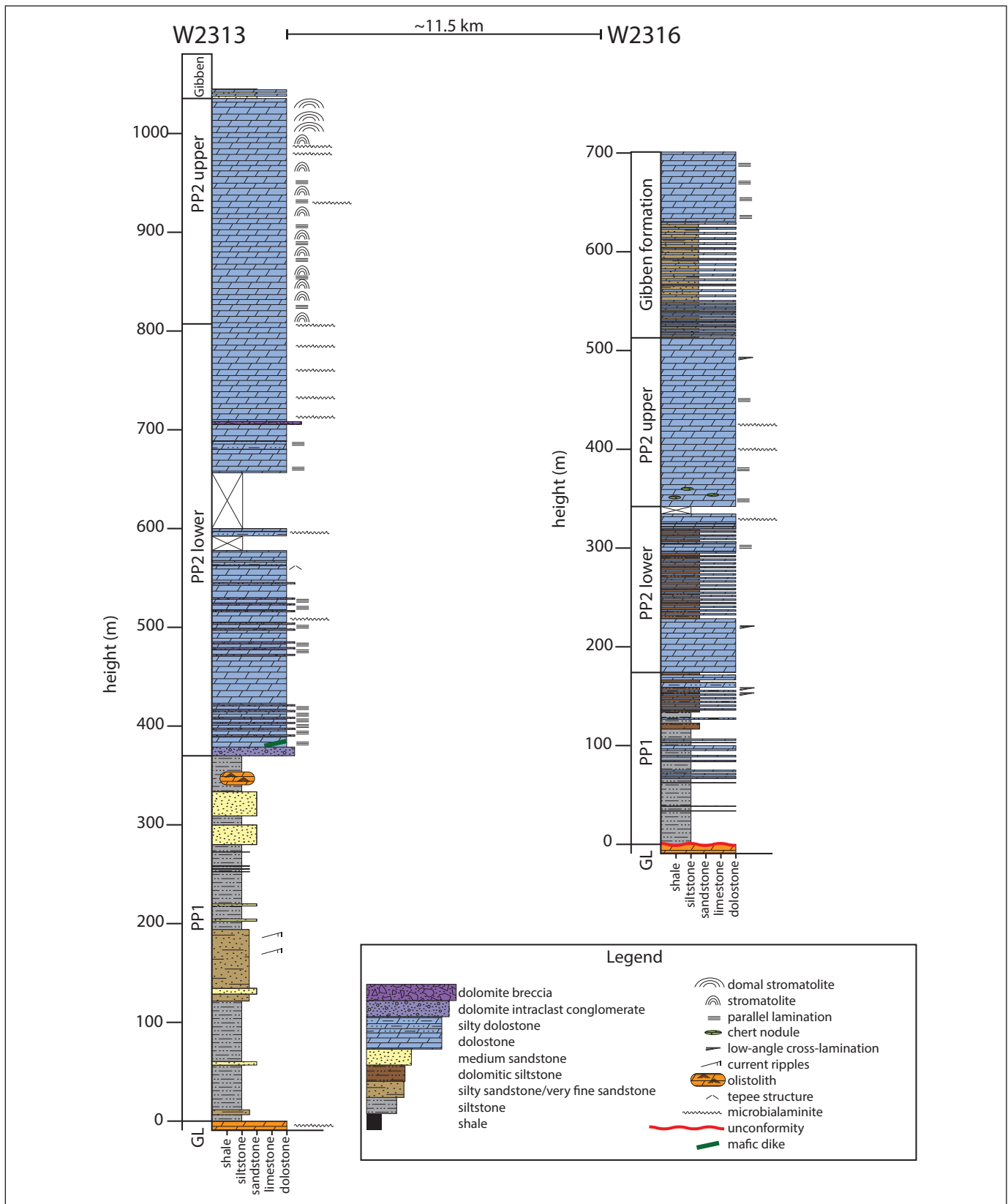
Figure 4. *Stratigraphic logs of sections W2313 and W2316 measured through PP1 and PP2. GL: Gillespie Lake Group. The base of section W2313 is located at 64.774502°N, 139.417783°W and section W2316 is approximately 11.5 km away at 64.749551°N, 139.172991°W.*
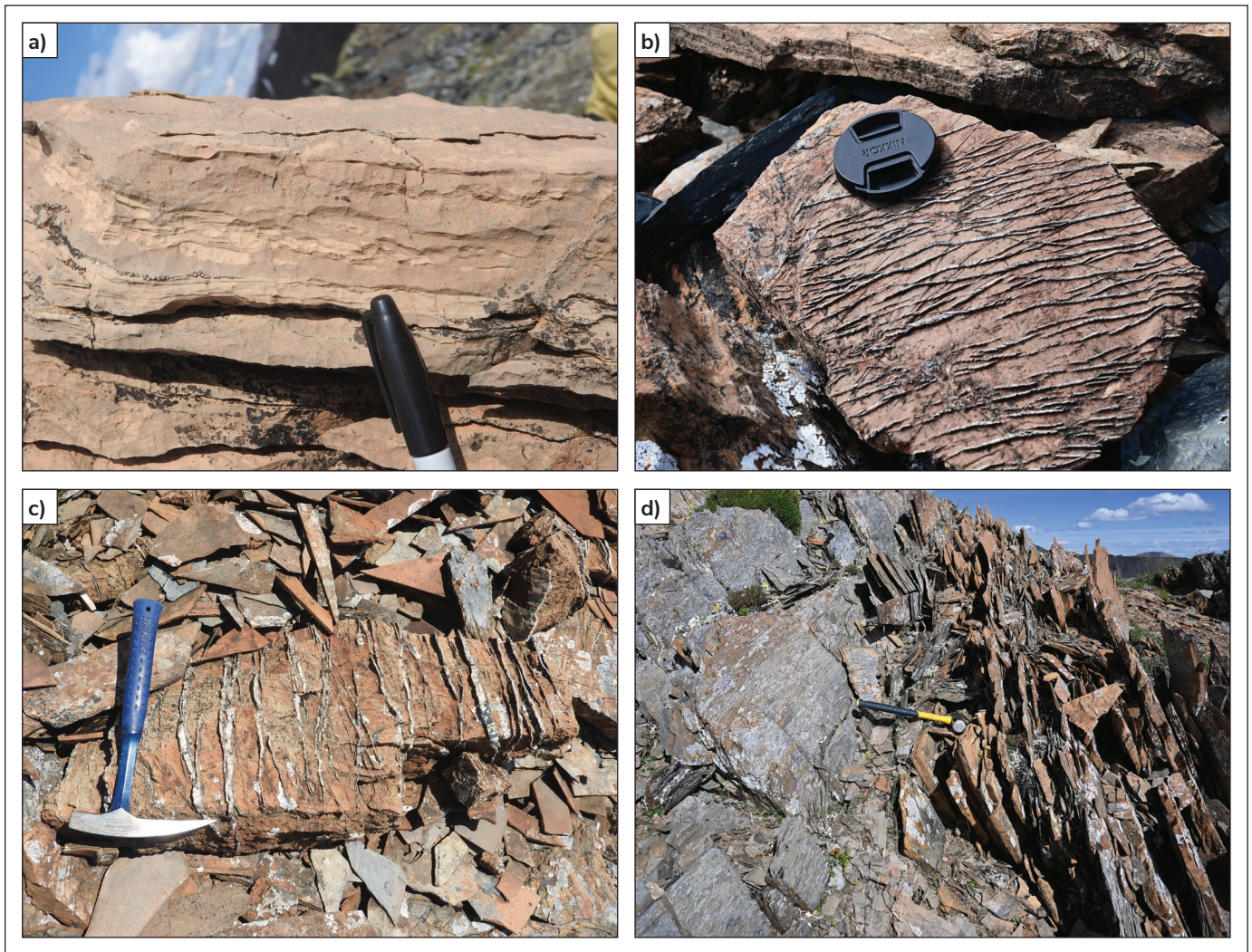
Figure 5. *Field photographs of the Gillespie Lake Group at sections W2313 (**a, b**) and W2316 (**c, d**): **a)** dolostone with micritic intraclasts immediately below the base of W2313; **b)** and **c)** silicified veins in dolostone blocks from float below the base of **b)** W2313 and **c)** W2316. Typically, veins in PP2 dolostone are carbonate rather than the silica common in the Gillespie Lake Group shown here; **d)** siltstone and thinly bedded orange-weathering dolostone immediately below the base of W2316 (stratigraphic up is to the right).*

dolostone is dominantly thinly laminated and wavy bedded with occasional teepee structures (Fig. 7b, c). Within this dolostone interval, crinkly lamination interpreted as microbialaminite is common, with more microbialaminite observed as stratigraphic height increases.

At approximately 810 m of total stratigraphic height, the dolostone becomes stromatolitic (Fig. 7d–f). Stromatolitic dolostone alternates with planar, finely laminated dolostone. The stromatolitic beds contain columnar stromatolites that are a few centimetres in width and up to tens of centimetres in height (Fig. 7d, e). The stromatolitic and laminated dolostone

alternate in approximately 5 to 10 m intervals. Columnar stromatolites are the dominant form for the first 200 m of the stromatolitic interval, and large, domal stromatolitic buildups approximately 30 cm wide and 1 m tall dominate the remaining 40 m (Fig. 7f).

Interbedded orange-weathering carbonate (mostly dolostone but limestone in places) and blue-weathering sandstone overlies the large domal stromatolites (Fig. 8a, b). The contact between the stromatolites and the interbedded siltstone and carbonate is poorly exposed. Approximately 50 m of the interbedded sandstone and dolostone is exposed between the basal contact and the top of the hill.
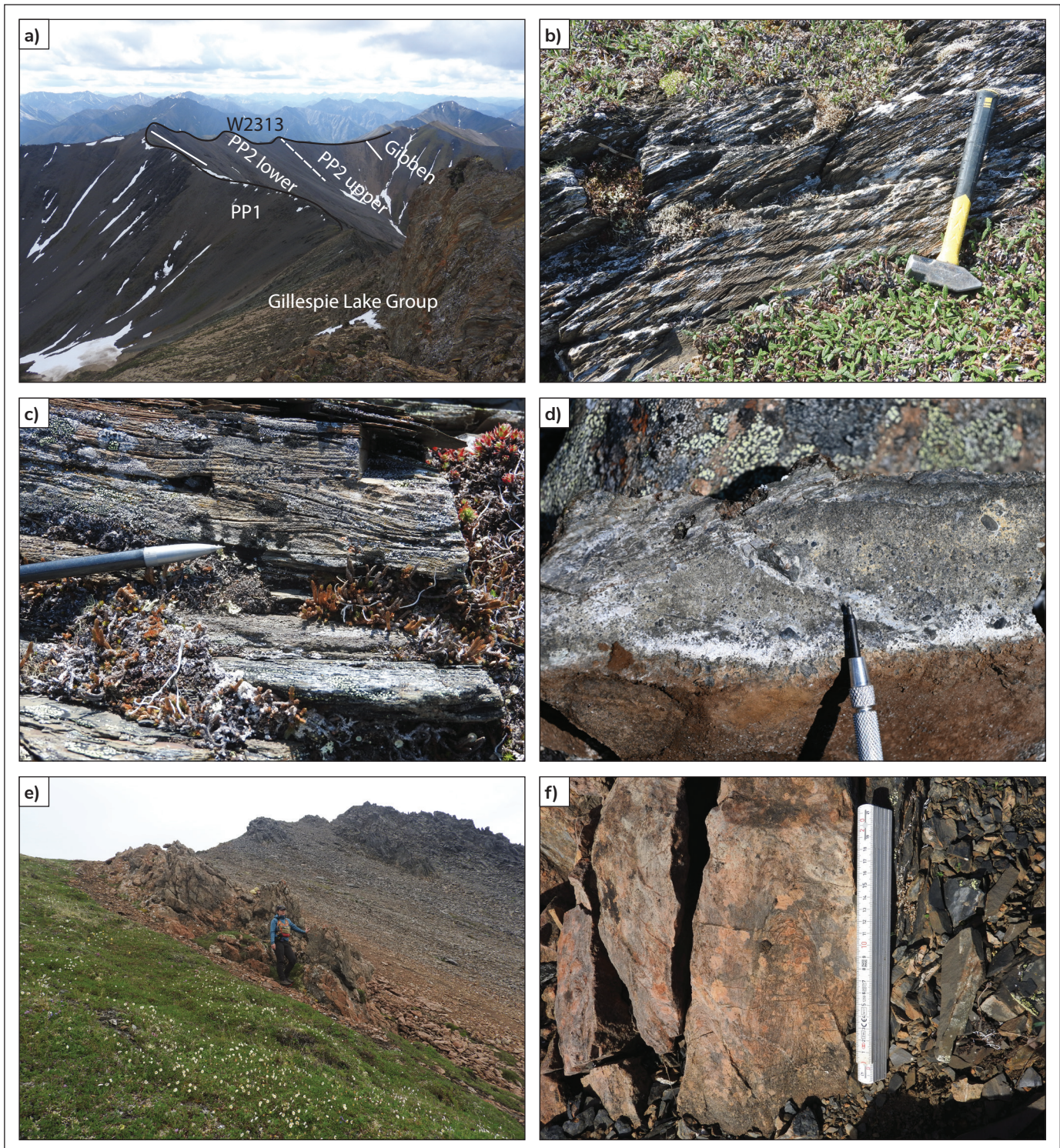
Figure 6. *Field photographs of PP1 from section W2313:* **a)** *ridge that W2313 was measured along with proposed contacts identified with white lines. In section W2313, PP1 is exposed along a ridge that is nearly parallel to strike;* **b)** *cleaved siltstone within PP1;* **c)** *current ripple cross-lamination in sandstone at 172 m of stratigraphic height,* **d)** *very coarse, gritty sandstone from sandstone interval between 280 and 330 m;* **e)** *orange-weathering dolostone olistolith in siltstone subcrop near the top of PP1 (person for scale);* **f)** *conical stromatolite from within a dolostone olistolith in PP1 (oriented in the same direction as ruler). This photograph is from an olistolith within PP1 along the ridge to the east of section W2313. Collapsible metre stick with cm markings for scale.*
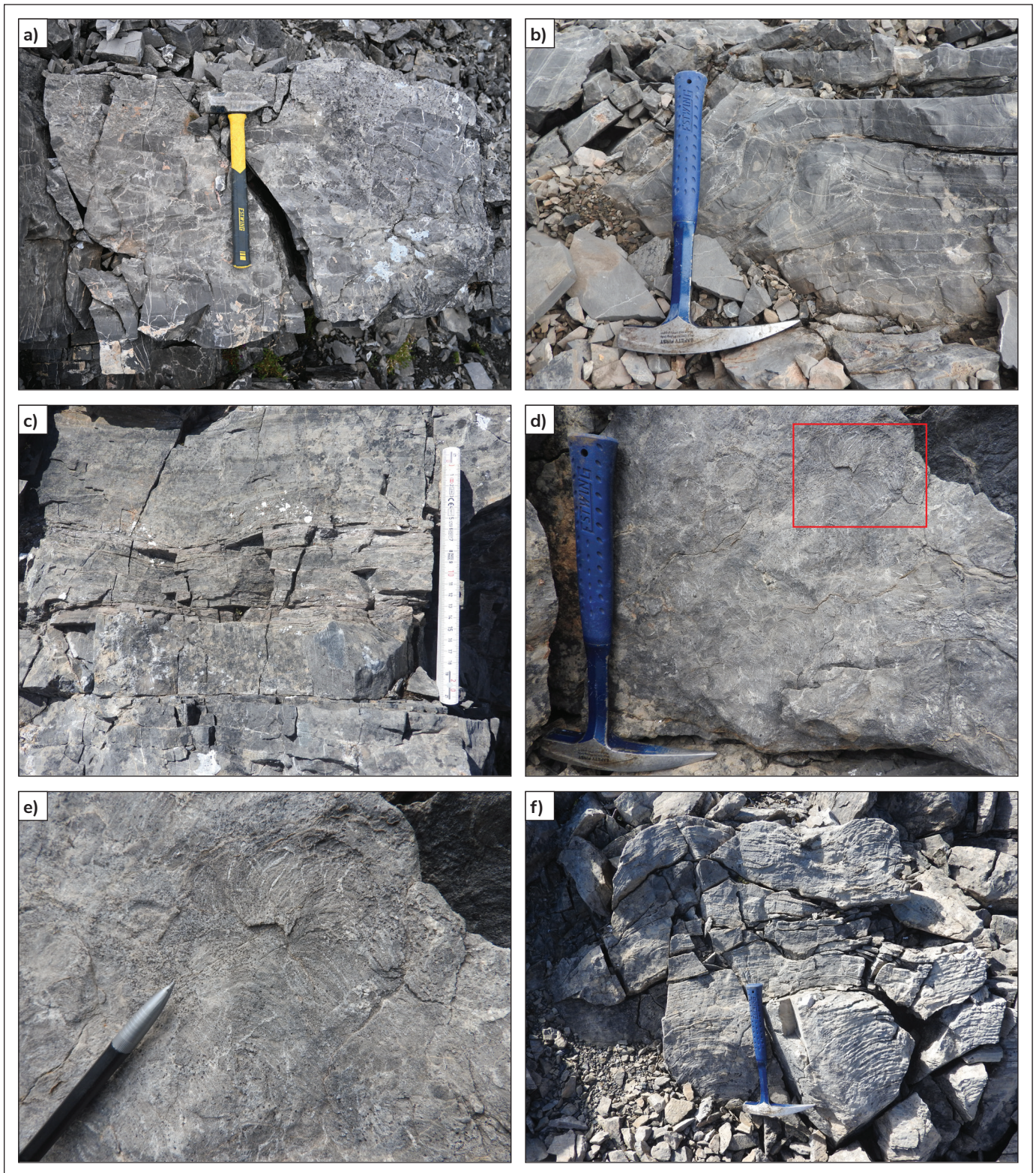
Figure 7. *Field photographs of PP2 from section W2313:* **a)** *dolostone intraclast conglomerate. This facies is more common in the base of PP2 lower;* **b)** *tepee structure in dolostone from PP2 lower;* **c)** *thinly bedded to thinly laminated dolostone with wavy bedding from PP2 lower;* **d)** *columnar stromatolites in dolostone from PP2 upper. Red box marks the area shown in part* **e)**; **e)** *columnar stromatolite that is 3–5 cm wide;* **f)** *larger, domal stromatolites from the top of PP2 upper near the contact with the Gibben formation.*

Figure 8. *Field photographs of stratigraphic units above PP1 and PP2 at section W2313* **(a, b)** *and W2316* **(c, d, e, f)**: **a)** *approximately 50–100 m of alternating dark grey sandstone and orange-weathering dolostone above the large domal stromatolites at the top of PP2 upper at section W2313. Above this, exposure of this unit is lost. This interbedded siliciclastic and dolostone unit is interpreted as the Gibben formation and the contact between it and PP2 upper is drawn as a white line;* **b)** *alternating sandstone and dolostone of the Gibben formation above PP2 upper at W2313;* **c)** *al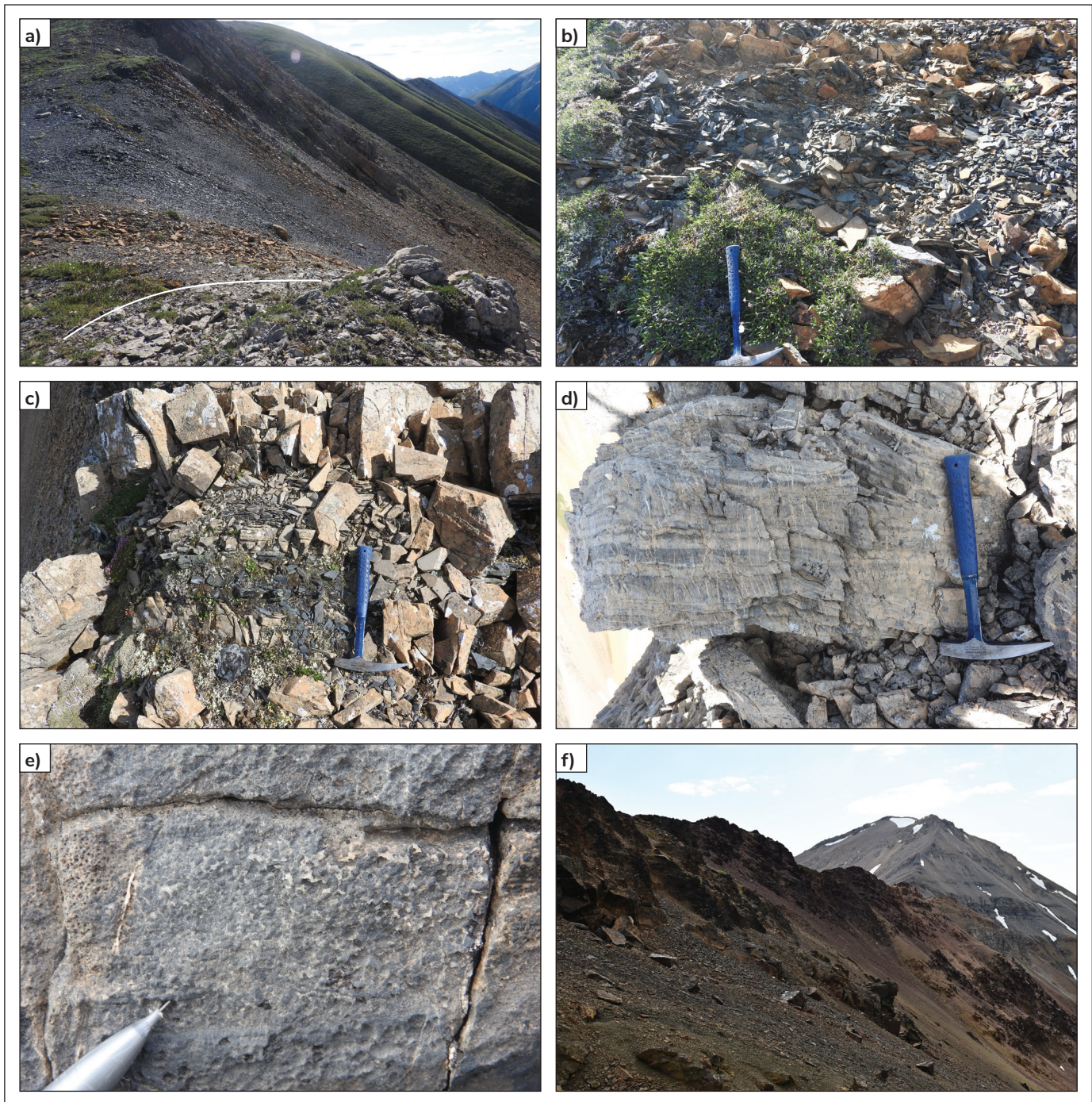ternating siltstone and orange-weathering dolostone above the grey-weathering wispy laminated dolostone of PP2 upper at W2316. The alternating siltstone and dolostone is interpreted as the Gibben formation;* **d)** *thinly bedded dolostone with alternating darker and lighter beds. The centimetre-scale beds contain laminations stratigraphically above the interbedded siltstone and dolostone at section W2316;* **e)** *ooid and coated grain packstone stratigraphically above the thinly bedded dolostone;* **f)** *pebble to cobble conglomerate, coarse sandstone, and maroon-weathering siltstone stratigraphically above the oolitic dolostone. This is interpreted as the Chandindu Formation.*

Interpretation

We suggest that the contact between PP1 and PP2 is at the transition from dominantly siltstone to dominantly dolostone at 370 m of stratigraphic height. This is consistent with the descriptions of PP1 and PP2 from Thompson et a*l*. (1994), Medig et a*l*. (2010, 2014) and Strauss et a*l*. (2014). We tentatively divide PP2 into lower and upper units with a contact at the transition from wavy bedded and thinly laminated dolostone to dominantly stromatolitic dolostone at 810 m of stratigraphic height. Macdonald et a*l*. (2011) interpreted the shift to stromatolitic dolostone as a lateral facies change and, therefore, did not separate these units, referring to PP2 instead as Pinguicula B/C. Halverson et a*l*. (2012) proposed that the stromatolitic dolostone, here termed 'PP2 upper', was correlative with the Rubble Creek Formation in the Hart River and Wernecke inliers. Whether PP2 lower and upper, as described here, can be separated as distinct mappable units will require additional sections.

Broadly, there is a shallowing upward trend within this section. We interpret PP1 as a relatively deep-water, mid to outer ramp environment. Although full Bouma sequences are absent from this section, the overall thickness of siltstone and sandstone in this section, current ripple cross-stratification, absence of features indicative of shallow-water conditions, and coarser event beds are consistent with a turbiditic environment below storm-weather wave base as suggested in Medig et a*l*. (2014). The presence of olistoliths in the upper portion of PP1 is consistent with deposition along a slope and suggests that the basin was tectonically active during deposition. We interpret PP2 as a shallow, peritidal, inner ramp environment due to the presence of tepee structures and carbonate intraclast conglomerates in PP2 lower. Columnar and domal stromatolites in PP2 upper, typically found in subtidal to intertidal environments, also support the interpretation of a shallow, peritidal, inner ramp environment. This environmental interpretation is consistent with those presented in Macdonald et a*l*. (2011) and Medig et a*l*. (2014).

Section W2316

Section W2316 is located approximately 11 km to the southeast of section W2313 along a roughly north-trending ridge that is perpendicular to strike (Figs. 3, 4 and 9a). The base of section W2316 is at a sharp contact between orange-weathering dolostone and dark grey weathering siltstone. Immediately below the base of W2316, the laminated, orange-weathering dolostone is heavily silicified. We interpret the orange-weathering dolostone as the Gillespie Lake Group (Fig. 5c, d).

The first 30 m of section W2316 consists of siltstone (Fig. 9b) with occasional intervals of finer grained shale beds. Above 30 m, thin orange-weathering dolostone beds are present every 5 to 10 m. The interval from 50 to 130 m consists of interbedded siltstone and thinly bedded, parallel-laminated, orange-brown weathering dolostone (Fig. 9c). Above 130 m, the siltstone becomes dolomitic and is interbedded with laminated dolostone. At approximately 180 m, the interbedded dolostone and siltstone transitions to a 55 m thick interval of dominantly orange-brown weathering dolostone (Fig. 9d) before returning to interbedded dolomitic siltstone and dolostone for another approximately 110 m.

Above the relatively recessive siltstone and dolostone, at 342 m total stratigraphic thickness, there is a 173 m section of resistant, grey-weathering, microbialaminite and wispy-laminated dolostone with wavy bedding and low-angle cross-stratification (Fig. 9e). Chert occurs as bedding-parallel nodules, up to a few centimetres wide, at the base of this interval and as thin (<1 cm) layers within the dolostone farther up section (Fig. 9f).

Above this interval of dominantly dolostone, at 515 m of total stratigraphic thickness, there is 145 m of interbedded brown-orange weathering, laminated dolostone and dark grey-weathering, laminated, very fine sandstone to siltstone (Fig. 8c). At the start of this 145 m thick stratigraphic package, the siltstone intervals are 10 cm thick for every 0.5 to 1 m of dolostone. As stratigraphic height increases, the siltstone intervals thicken to approximately 1 m. A 40 m interval of grey-weathering, laminated, thin to medium-bedded dolostone (Fig. 8d) was measured above the interbedded siltstone and dolostone before stopping the log at a total thickness of 701 m. Stratigraphically above the end of the log, there is grey-weathering laminated dolostone and oolitic/coated grain packstone (Fig. 8e) that is overlain by maroon-weathering siltstone, pebble conglomerate, and sandstone (Fig. 8f).
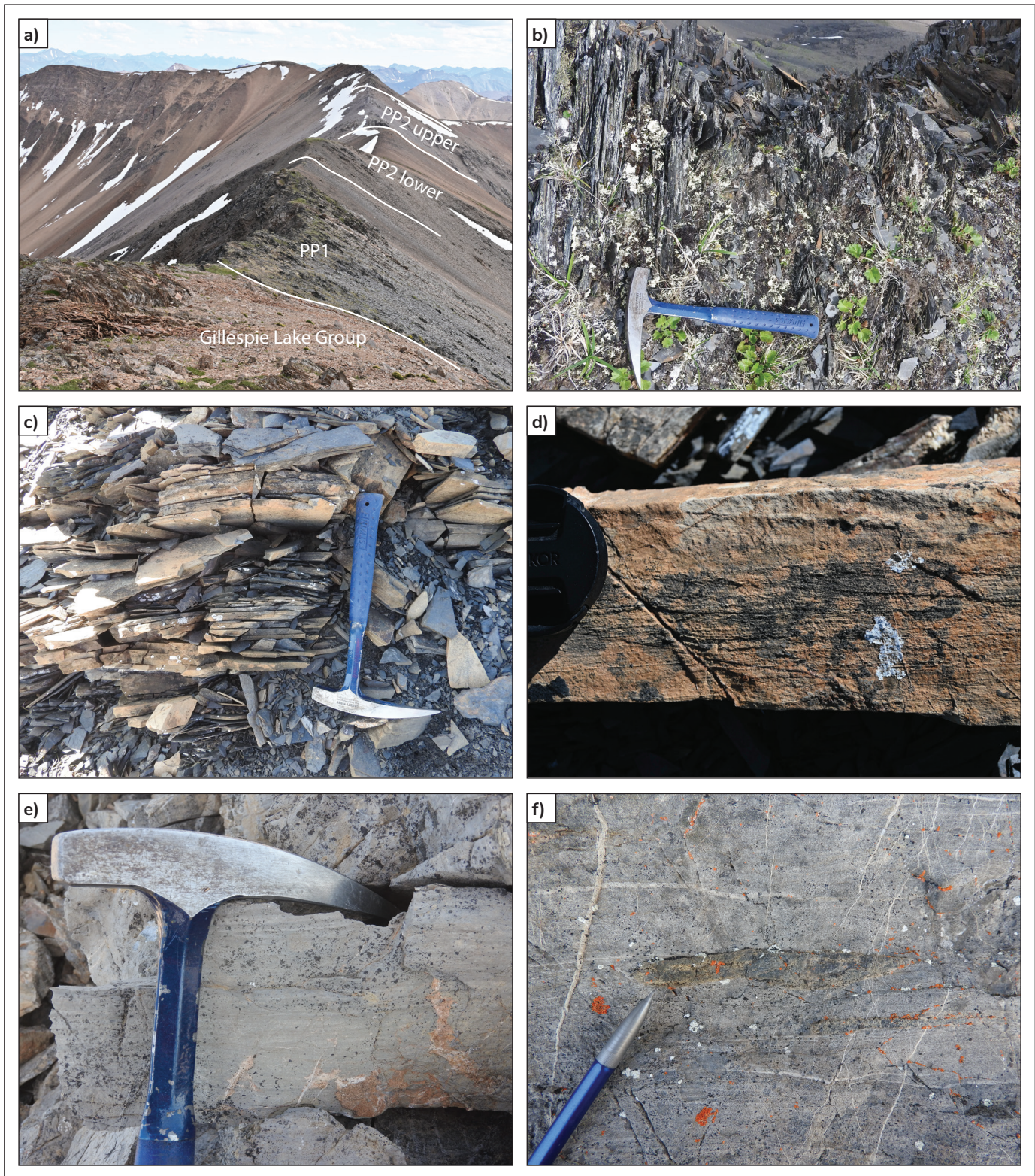
Figure 9. *Field photographs of PP1 and PP2 from section W2316:* **a)** *ridge that W2316 was measured along with proposed contacts identified with white lines;* **b)** *dark grey-weathering siltstone from the base of PP1 (stratigraphic up is to the right);* **c)** *interbedded siltstone and dolostone from the gradational contact between PP1 and PP2 lower;* **d)** *orange-brown weathering, laminated dolostone in PP2 lower;* **e)** *grey weathering, wispy and thinly laminated dolostone from PP2 upper;* **f)** *bedding-parallel chert nodule from the base of PP2 upper.*

Interpretation

Similar to section W2313, orange-weathering dolostone is overlain by an interval of dark grey-weathering, fine-grained siliciclastic rocks that pass up section to a laminated, grey-weathering dolostone. The units that overlie the dolostone at the top of W2316 are consistent with the descriptions of the Fifteenmile Group elsewhere in the Coal Creek inlier (Macdonald et *al.*, 2011, 2012; Halverson et *al.*, 2012; Kunzmann et *al.*, 2014). Specifically, the laminated thin to medium-bedded dolostone and oolitic/coated grain packstone above the interbedded siltstone and dolostone is interpreted as the Gibben formation here, consistent with the descriptions of the middle of the Gibben formation in Halverson et *al.* (2012). The sharp contact between the dolostone above the oolitic/coated grain packstone and the maroon-weathering siltstone and granule to cobble conglomerate is interpreted here as the contact between the Gibben and Chandindu formations (Halverson et *al.*, 2012; Kunzmann et *al.*, 2014). Based on these similar stratigraphic relationships, we interpret our section as spanning PP1 and PP2, with the underlying orange dolostone as the Gillespie Lake Group and the overlying siliciclastic and carbonate strata as the Fifteenmile Group.

The contact between the Gillespie Lake Group and PP1 at the base of W2316 is unconformable. The contact between PP1 and PP2 is gradational and is placed at the transition from interbedded dolomitic siltstone and siltstone to dominantly dolostone at 180 m. The PP2 lower to PP2 upper contact within W2316 is at the base of a strongly resistant, grey-weathering dolostone above the interbedded dolostone and dolomitic siltstone at 342 m. We interpret the interbedded siltstone and dolostone as the base of the Gibben formation at 515 m. This contact with PP2 upper and the Gibben formation is gradational.

Our interpretation differs from Thompson et *al.* (1994), who mapped this ridge as Quartet Group overlain by Gillespie Lake Group. Thompson et *al.* (1994) and Strauss et *al.* (2014) did recognize Gibben formation (PR4) up section from the Gillespie Lake Group. However, they map it as unconformably overlying the Gillespie Lake Group. A section that was measured during the mapping reported in Thompson et *al.* (1994) but published in 2015 describes maroon siltstone and heterolithic conglomerate interpreted as the Gibben

formation at a sharp, unconformable contact with the Gillespie Lake Group (Thompson and Roots, 2015).

Although our interpretations differ from the work by Thompson et *al.* (1994) and Thompson and Roots (2015), the interpretation of the Gibben and Chandindu formations here is consistent with more recent descriptions of these units elsewhere in the Coal Creek inlier (Halverson et *al.*, 2012; Kunzmann et *al.*, 2014). Additionally, the interpretation of the units PP1 and PP2 here is consistent with the overall description of PP1 and PP2 as a basal siliciclastic unit and overlying carbonate unit stratigraphically above the Wernecke Supergroup and below the Fifteenmile Group. Though our interpretation of the units as PP1, PP2 and Gibben formation differs from the interpretation of these units as the Gillespie Lake Group in Thompson and Roots (2015), we agree with Thompson and Roots (2015) that the contacts between units here are gradational.

Here, PP1 is identified and interpreted as a deep-water mid to outer-ramp environment due to the absence of cross-stratification or other sedimentary structures that would be consistent with a shallower environment. Unlike in section W2313, no olistoliths were identified in PP1 in section W2316. PP2 at section W2316 likely records a deeper environment than PP2 at W2313 because it is mostly wispy-laminated dolostone. Tepee structures, intraclast conglomerates, and stromatolites are absent.

Discussion

The two sections discussed here are separated by approximately 11 km and, though broadly similar, exhibit some key differences. Section W2313 is approximately 500 m thicker than section W2316. Numerous olistoliths are present near the top of PP1 in section W2313; however, they are absent in W2316. In section W2316, PP2 is relatively featureless and composed of microbialaminite and wispy-laminated dolostone. In contrast, PP2 in section W2313 contains tepee structures, intraclast conglomerates, wavy bedding and stromatolites. The olistoliths in W2313 are consistent with active tectonism during deposition. The lateral variation in sedimentary facies and stratigraphic thickness would be also expected in a tectonically active basin. Macdonald et *al.* (2012) noted that the overlying Fifteenmile Group is laterally variable in thickness as a

result of small fault-bounded sub-basins and that the pattern of variance was similar to what they observed in PP1 and PP2. Additional sections are required to better understand the lateral variation in these units, and how the variation relates to tectonism in the basin at the time of deposition of PP1, PP2 and the overlying Fifteenmile Group.

As discussed above, the correlation of PP1 and PP2 with other units farther east is ambiguous. Previous work has suggested that PP1 and PP2 are correlative with the Pinguicula Group in the Hart River and Wernecke inliers (Fig. 2; Medig et a*l.*, 2010; Macdonald et a*l.*, 2012; Strauss et a*l.*, 2014). However, Medig et a*l.* (2014) challenged this correlation based on detrital zircon analyses from a sandstone in PP1, which suggest that PP1 recorded a separate, earlier basin-forming event possibly correlative with the Belt Supergroup. Medig et a*l.* (2014) also suggested that PP2 unconformably overlies PP1 and could be correlative with the uppermost formation of the Pinguicula Group, the Rubble Creek Formation. Based on the field observations presented here, PP2 conformably overlies PP1 at section W2316 because the contact is gradational. This conformable relationship between PP1 and PP2 challenges the suggestion from Medig et a*l.* (2014) that PP1 and PP2 record separate basin-forming events. Further, in section W2316, the contact between PP2 and the overlying Gibben formation appears to be gradational. This suggests that there is not much time missing between the deposition of these two units.

In the Hart River and Wernecke inliers, the Pinguicula Group is stratigraphically above the Wernecke Supergroup and below the Mackenzie Mountains Supergroup, and records deposition along a ramp (Medig et a*l.*, 2016). The base of the Pinguicula Group, the Mount Landreville Formation, is a dominantly siliciclastic unit with turbidites interpreted as being deposited in a deep-water environment, below storm-weather wave base (Medig et a*l.*, 2016, 2023). The overlying Pass Mountain Formation is dominantly carbonate and was deposited on the outer ramp near storm-weather wave base. The overlying Rubble Creek Formation is also carbonate dominated and was deposited above fair-weather wave base in places (Medig et a*l.*, 2016). In the sections described here from the Coal Creek inlier, PP1 is a dominantly siliciclastic unit deposited in a deep-

water environment below storm-weather wave base. PP2 is composed of carbonates deposited in a shallow subtidal to peritidal environment in section W2313 and a deeper environment near storm-weather wave base in section W2316. The relative stratigraphic position and transition from a deep-water siliciclastic unit to shallower water carbonate unit support the proposed correlations between PP1 and PP2 and the Pinguicula Group, and that PP1 and PP2 were deposited during the same basin-forming event (Medig et a*l.*, 2010; Macdonald et a*l.*, 2012). The field observations and interpretations presented here do not agree with the hypothesis that PP1 records an earlier basin-forming event that is distinct from PP2 (Medig et a*l.* 2014, 2023). Additional sections, mapping and geochronology are required to confidently establish these correlations and test tectonic models.

Acknowledgments

References

Abbott, G., 1997. Geology of the upper Hart River area, eastern Ogilvie Mountains, Yukon Territory (116A/10, 11). Exploration and Geological Services Division, Yukon Region, Indian and Northern Affairs Canada, Bulletin 9, 92 p.

Delaney, G.D., 1981. The mid-Proterozoic Wernecke Supergroup, Wernecke Mountains, Yukon Territory. *In*: Proterozoic Basins of Canada, F.H.A. Campbell (ed.), Geological Survey of Canada, Paper 81-10, p. 1–23. https://doi.org/10.4095/109384

Eisbacher, G.H., 1981. Sedimentary tectonics and glacial record in the Windermere Supergroup, Mackenzie Mountains, northwestern Canada. Geological Survey of Canada, Paper 80-27, 40 p.

Furlanetto, F., Thorkelson, D.J., Rainbird, R.H., Davis, W.J., Gibson, H.D. and Marshall, D.D., 2016. The Paleoproterozoic Wernecke Supergroup of Yukon, Canada: Relationships to orogeny in northwestern Laurentia and basins in North America, East Australia, and China. Gondwana Research, vol. 39, p. 14–40. https://doi.org/10.1016/j.gr.2016.06.007

Green, L.H., 1972. Geology of Nash Creek, Larsen Creek, and Dawson map areas, Yukon Territory. Geological Survey of Canada, Memoir 364, p. 1–172. https://doi.org/10.4095/100697

Halverson, G.P., Macdonald, F.A., Strauss, J.V., Smith, E.F., Cox, G.M. and Hubert-Théou, L., 2012. Updated definition and correlation of the lower Fifteenmile Group in the central and eastern Ogilvie Mountains. In: Yukon Exploration and Geology 2011, K.E. MacFarlane and P.J. Sack (eds.), Yukon Geological Survey, p. 75–90.

Kunzmann, M., Halverson, G.P, Macdonald, F.A., Hodgskiss, M., Sansjofre, P.D., Schumann, D. and Rainbird, R.H., 2014. The early Neoproterozoic Chandindu Formation of the Fifteenmile Group in the Ogilvie Mountains. In: Yukon Exploration and Geology 2013, K.E. MacFarlane, M.G. Nordling and P.J. Sack (eds.), Yukon Geological Survey, p. 93–107.

Long, D.G.F and Turner, E.C., 2012. Formal definition of the Neoproterozoic Mackenzie Mountains Supergroup (Northwest Territories), and formal stratigraphic nomenclature for terrigenous clastic units of the Katherine Group. Geological Survey of Canada, Open File 7113, 40 p. https://doi.org/10.4095/292168

Macdonald, F.A., Halverson, G.P., Strauss, J.V., Smith, E.F., Cox, G., Sperling, E.A. and Roots, C.F., 2012. Early Neoproterozoic basin formation in Yukon, Canada: Implications for the make-up and break-up of Rodinia. Geoscience Canada, vol. 39, no. 2, p. 77–100.

Macdonald, F.A., Smith, E.F., Strauss, J.V., Cox, G.M., Halverson, G.P. and Roots, C.F., 2011. Neoproterozoic and early Paleozoic correlations in the western Ogilvie Mountains, Yukon. In: Yukon Exploration and Geology 2010, K.E. MacFarlane, L.H. Weston and C. Relf (eds.), Yukon Geological Survey, p. 161–182.

Medig, K.P.R., Thorkelson, D.J. and Dunlop, R.L., 2010. The Proterozoic Pinguicula Group: Stratigraphy, contact relationships and possible correlations. In: Yukon Exploration and Geology 2009, K.E. MacFarlane, L.H. Weston and L.R. Blackburn (eds.), Yukon Geological Survey, p. 265–278.

Medig, K.P.R., Thorkelson, D.J., Davis, W.J., Rainbird, R.H., Gibson, H.D., Turner, E.C. and Marshall, D.D., 2014. Pinning northeastern Australia to northwestern Laurentia in the Mesoproterozoic. Precambrian Research, vol. 249, p. 88–99. https://doi.org/10.1016/j.precamres.2014.04.018

Medig, K.P.R., Thorkelson, D.J., Turner, E.C., Rainbird, R.H., Gibson, H.D. and Marshall, D.D., 2023. Mesoproterozoic basins (Yukon, Canada) in the evolution of supercontinent Columbia. Canadian Journal of Earth Sciences, vol. 60, p. 912–973. https://doi.org/10.1139/cjes-2022-0055

Medig, K.P.R., Turner, E.C., Thorkelson, D.J. and Rainbird, R.H., 2016. Rifting of Columbia to form a deep-water siliciclastic to carbonate succession: The Mesoproterozoic Pinguicula Group of northern Yukon, Canada. Precambrian Research, vol. 278, p. 179–206. https://doi.org/10.1016/j.precamres.2016.03.021

Moynihan, D.P., Strauss, J.V., Nelson, L.L. and Padget, C.D., 2019. Upper Windermere Supergroup and the transition from rifting to continent-margin sedimentation, Nadaleen River area, northern Canadian Cordillera. GSA Bulletin, vol. 131, no. 9–10, p. 1673–1701. https://doi.org/10.1130/B32039.1

Strauss, J.V., Roots, C.F., MacDonald, F.A., Halverson, G.P., Eyster, A. and Colpron, M., 2014. Geological map of the Coal Creek Inlier, Ogilvie Mountains (NTS 116B/10-15 and 116C/9, 16). Yukon Geological Survey, Open File 2014-15, scale 1:100 000.

Thompson, R.I., Roots, C.F. and Mustard, P.S., 1994. Geology of Dawson map area (116B,C) (northeast of Tintina Trench). Geological Survey of Canada, Open File 2849, scale 1: 50 000. https://doi.org/10.4095/194830

Thompson, R.I. and Roots, C.F., 2015. Twenty-six archival stratigraphic sections in Paleoproterozoic to Neoproterozoic strata from the Coal Creek inlier, southern Ogilvie Mountains, Yukon. Geological Survey of Canada, Open File 7925, 36 p. https://doi.org/10.4095/296977

Thorkelson, D.J., 2000. Geology and mineral occurrences of the Slats Creek, Fairchild Lake and "Dolores Creek" areas, Wernecke Mountains (106D/16, 106C/13, 106C/14), Yukon Territory. Exploration and Geological Services Division, Yukon Region, Indian and Northern Affairs Canada, Bulletin 10, 73 p.

Thorkelson, D.J., Mortensen, J.K., Davidson, G.J., Creaser, R.A., Perez, W.A. and Abbott, J.G., 2001. Early Mesoproterozoic intrusive breccias in Yukon, Canada: The role of hydrothermal systems in reconstructions of North America and Australia. Precambrian Research, vol. 111, p. 31–55. https://doi.org/10.1016/S0301-9268(01)00155-3

Turner, E.C., 2011. Stratigraphy of the Mackenzie Mountains Supergroup in the Wernecke Mountains, Yukon. *In*: Yukon Exploration and Geology 2010, K.E. MacFarlane, L.H. Weston and C. Relf (eds.), Yukon Geological Survey, p. 207–231.

Yukon Geological Survey, 2022. Yukon Digital Bedrock Geology. Yukon Geological Survey, http://datatest.geology.gov.yk.ca/Compilation/3, [accessed November 2023].

Yukon Geological Survey

Yukon Geological Survey staff are located in two buildings in Whitehorse: the Elijah Smith Building at 300 Main Street, room 102, and the H.S. Bostock Core Library at Mile 918 on the Alaska Highway.

Operations

H.S. Bostock Core Library

Relf, Carolyn – Director, (867) 667–8892 ....carolyn.relf@yukon.ca

Vacant – Manager, Finance & Operations

Bedrock Geology

H.S. Bostock Core Library

Colpron, Maurice – Head, Bedrock Geology, (867) 667–8235 .... maurice.colpron@yukon.ca

Ambrose, Tyler – Project Geologist, (867) 667–5175 ....tyler.ambrose@yukon.ca

Cobbett, Rosie – Project Geologist, (867) 455–2802 .... rosie.cobbett@yukon.ca

Moynihan, David – Project Geologist, (867) 455–2805 .... david.moynihan@yukon.ca

Skipton, Diane – Project Geologist, (867) 667–5175 .... diane.skipton@yukon.ca

Surficial Geology

H.S. Bostock Core Library

Cronmiller, Derek – acting Head, Surficial Geology, (867) 332–4961 .... derek.cronmiller@yukon.ca

Lipvosky, Panya – Surficial Geologist, (867) 667–8520 .... panya.lipovsky@yukon.ca

Kennedy, Kristy – Surficial Geologist, (867) 393–7188 .... kristy.kennedy@yukon.ca

Elijah Smith Building

van Loon, Sydney – Placer Geologist, (867) 667–3408 .... sydney.vanloon@yukon.ca

Minerals Geology

H.S. Bostock Core Library

Sack, Patrick – acting Head, Minerals Geology, (867) 667–3203 .... patrick.sack@yukon.ca

Ellis, Sarah – Economic Geologist, (867) 332–9263 .... sarah.ellis@yukon.ca

Emberley, Justin – Core Library Manager, (867) 393–6492 .... justin.emberley@yukon.ca

Elijah Smith Building

Klyukin, Yury – Economic Geologist, (867) 332–2530 .... yury.klyukin@yukon.ca

Technical Services & Outreach

Elijah Smith Building

Elliot, Brett – acting Head, Technical Services, (867) 667–8481 .... brett.elliot@yukon.ca

Cote, Chad – Geological Spatial Database Administrator, (867) 393–7186 .... chad.cote@yukon.ca

Staffen, Bailey – GIS Technician/Web Manager, (867) 456–6801 .... bailey.staffen@yukon.ca

H.S. Bostock Core Library

Weston, Leyla – Outreach Geologist, (867) 393–7187 ....leyla.weston@yukon.ca

O'Connor, Amanda – Outreach Geologist, (867) 332–9376 ....amanda.oconnor@yukon.ca

Yukon Geological Survey
Energy, Mines and Resources
Government of Yukon